The University Of Sheffield.

Department of Electronic & Electrical Engineering

A Study on Frequency Reconfigurable Antennas for Applications in Frequency Agile Radio and mm-Wave.

PhD Thesis

Sergio Pedro Rodriguez-Albarran

First Supervisor: Professor Richard J. Langley

Second Supervisor: Professor. K. Lee Ford

Submitted in accordance with the requirements for the degree of Doctor of Philosophy.

ABSTRACT.

As the current technologies in mobile communications are constantly growing it is becoming a necessity for researchers to investigate and deliver novel, versatile and agile devices providing adaptive performance in order to fulfil the ever changing requirements for communication engineering standards in the next and currently developing generation of mobile communications known as 5G. The current technologies in adaptive antennas have provided optimal numbers using comprehensive technologies that are compatible with the past generations of mobile communications. However, the increasing amounts of data exchanged by mobile devices nowadays require multiple services to be covered by reduced number of devices. In order to overcome this inconvenience, the use of reconfigurable antennas, specifically frequency reconfigurable antennas introduce an adaptive and innovative concept for versatile devices with applications in radio agility that overcomes the limitations of the current devices that are unable to cover multiple services by a single antenna.

Two different kinds of frequency reconfigurable antennas are discussed in this work. The design, simulations, manufacture, and measurements for the discussed antennas are developed in this thesis. The first discussed designs are three prototypes of 1×2 triple-slotted antennas with different positions in the board. These boards offered independent frequency tuning using varactor-loaded slots that are electrically tunable by voltages from 0 – 25 V offering a fully tunable frequency range from 0.57 GHz and up to 2.73 GHz. The commented antennas offered independent metrics for frequency response and radiation patterns as well as good agreement between simulations and measurements. Moreover, the three slot antenna prototypes were object of a study in diversity metrics as they present spatial diversity schemes. The simulated and measured diversity parameters observed agreed on optimal numbers for frequencies above 750 MHz for the three prototypes with correlations well below 0.3 and diversity gains near the ideal value of 10 dB which allows reduction of required power in multi-antenna systems and determines its capacity to operate in MIMO systems for 5G. The second kind of antennas discussed in this is a dielectric resonant antenna (DRA) designed to operate at 28 GHz using bioplastics with relatively low dielectric constants and filled by different materials in order to achieve frequency reconfiguration including electrically tunable substances such as graphene oxide covering a frequency range from 26.3 GHZ to 28.3 GHz presenting good agreement between measured and simulated reflection coefficients and radiation patterns.

ACKNOWLEDGEMENTS.

The presented research in this work was funded by the National Council of Science and Technology of Mexico (CONACyT), the Engineering and Physical Sciences Research Council of the United Kingdom (EPSRC) and Communications and Networking (COMMNET^2).

The measurements of the antenna metrics in this thesis were assisted by the technical support staff of the Communications Research group of the Electronic and Electrical Engineering Department of the University of Sheffield. The measurements were assisted and supervised by Mr. Steve Marsden.

The material used for the development of the antennas in Chapter 5 were facilitated by the silk fibroin research group of the Chemical and Biological Engineering Department of the University of Sheffield (CBE) as well as the preparations of the specialised chemical materials were carried out by Dr. David Alexander and PhD candidate Ms Ana Jiménez Franco.

DEDICATION.

To my family, for supporting me to have chosen this path more than 5 years ago, for standing next to me despite the distance, for encouraging me to follow my dreams, for guiding me through the toughest times and celebrating the finest. All my unconditional love for them.

To my partner and her family, for all the love and support they gave me, for the guidance and assistance provided during the years as research student, for adopting me as one of their own and making me fell home always. Eternally grateful with all of you.

To my friends for making me part of a strong group full of support, help and respect, for the good times enjoyed during my time as an international student making this an unforgettable experience. All the best for you.

¡Muchas Gracias!

Sergio

CONTENTS.

FIGURES AND TABLES.

CHAPTER 1. INTRODUCTION

The constant growing of emerging technologies for 5G requires novel and versatile devices that fulfil the new standards of the new generation of mobile communications, where large amounts of data are expected to be exchanged between devices at a high speed and a large bit rate, this demands devices able to manage these amounts of information with a low latency. These trends aim for adaptable devices, capable of modify their structure either internally or externally in order to offer a performance according to the changing environment.

1.1. Setting the scene.

Reconfigurable antennas are devices that offer a controlled performance, this allows a feature of adaptability which is achievable using typical techniques used on electronic systems as well as mechanical modifications. Essentially, reconfiguration in terms of antennas means the current distribution on the surface of the radiator will be controlled. Passive and active elements are commonly used in the structure antennas with a view to redirect the surface current and therefore change the performance of the system. The adaptive performance of reconfigurable antennas varies in terms of the parameters that can be controlled, in some cases one can control several of these at the same time [1], however, it is more common to find antennas that reconfigure a parameter solely. Frequency reconfigurable antennas are the most typical among the tunable devices [2]–[5] , followed by pattern reconfigurable antennas which control their beam by changing mechanically the structure of the system [6], [7] . Furthermore, novel antennas offering features compatible with the new trends on mobile communications and emerging technologies are the dielectric resonant antennas (DRA) a technology seen for the first time in the early 50's that is now being reconsidered as it is highly suitable due to their performance in high frequencies given dielectric materials present low and very low metallic losses [8]–[11] such as ceramics. The constant increment of data exchange involved in the current mobile communication networks suggests that the next generation will provide devices offering novel features of quick adaption to the changing mobile networks. 5G is expected to offer latencies lower than 5 ms, high energy efficiencies and support simultaneous connection of multiple devices simultaneously connected [12], [13]. With a view to meeting future 5G requirements such as always provide connectivity for a large number of users many reconfigurable antennas can be used simultaneously which yields to the use of tunable antenna arrays. Another technology which is turning a key feature for 5G is MIMO (Multiple-Input,

Multiple Output) which is scheme that studies the advantages of large numbers of antennas operating simultaneously and increasing spectrum efficiency. MIMO, and particularly the method of using multiple radiators, has helped the development of many standards of wireless communications which rule the current devices such as 802.11n and 802.11ac for Wi-Fi, WiMAX and LTE [14], [15]. In order to adapt MIMO technologies to 5G requirements it is essential to meet with diversity parameters which describe the interaction between antennas in a MIMO scheme [16].

Overall these novel systems provide adaptation to the medium in which they work, they are versatile devices presenting attractive functionalities such as multiband operation and their size is reduced which makes them discrete, nevertheless, one of the most challenging task is to achieve multiple operating modes as this is a feature that allows a single device to cover multiple services which leads to reducing the number of antennas in a device and consequently the miniaturisation and cost reduction of mobile communication devices. Nevertheless, the next generation of mobile communications 5G demands devices optimal to work within its new standards and requirements and the current technologies present some limitations. This project aims to provide innovative antennas either independently tunable over several different frequency bands or using state of the art technologies in order to meet future 5G requirements for communications systems.

1.2. Motivation, 5G technologies, requirements, and standards.

What is 5G technology and how is it different from 4G/LTE? The new generation of mobile communications will go beyond improving access to mobile internet data and will reach the innovative concept known as “Internet of Things” (IoT) [17]. This concept aims to a full automatization of the home appliances connected in a network that controls their operation, this requires a quick response time in each of the connected items, this is only achievable by low latencies. In 5G latencies are expected to be considerably lower than in 4G/LTE in order to ensure an optimal real time interaction between devices and cloud services. This would be a key advantage in the foreseeable application on smart vehicles which will require a remote interaction with crucially depending on low latencies [12], [18] . Another noticeable difference between 5G and 4G is the energy consumption, 5G technologies aim to reduce the consumption of devices with a view to ensure that equipment will remain connected for extended periods of time (months/years) without the human intervention to be required [19]. 5G technologies will be ruled by the following specifications:

- Data rates up to 10 Gbps (10-100 times higher than 4G).
- Latencies of 1ms.
- Broadband 1000 times faster than 4G per area unit.
- Capacity of up to 100 devices connected simultaneously per area unit.
- Availability of 99.99999%.
- 100% coverage.
- 90% reduction of energy consumption.
- Up to 10 years of battery duration on IoT low power devices.

5G will focus on IoT and critical communications, in terms of foreseeable launches of such applications, big companies are predicting the following schedule:

- Fixed wireless access from late 2018 and onwards.
- Improved mobile broadband from late 2019.
- Massive M2M / IoT from 2021, 2022.
- Ultra-low latency communications from 2024, 2025.

Highlights of key features of each generation of mobile communications:

- 1G mobile networks offered mobility to analogic voice data services.
- 2G mobile networks brought digital cellular technology, basic data services such as SMS, WAP internet access and roaming through mobile networks, leading years later to improved mobile data services such as GPRS and EDGE.
- 3G mobile networks improved mobile internet services increasing data rates and adapting massive data services and offering friendly data applications.
- 4G released IP (voice and data) services, fast internet broadband access with unified network architectures and protocols, then LTE duplicated data exchanges rates.
- 5G will expand wireless broadband services beyond mobile internet access towards IoT and M2M communications.

5G networks will be able to fulfil all of the communication systems requirements i.e. Local area networks (LAN) and wide area networks (WAN) will have the proper speed / latency configuration by allowing simple connections with virtual networks in order to reduce resources costs in function of the applications consumption [13] . Allowing 5G to focus on IoT by offering reliable solutions for low broadband and low power applications differently from the current way which is a wide variety of additional networks such as Wi-Fi, LoRa, 3G, 4G, LTE, etc. It is expected that 5G will reach 40% of the world's population by 2024, which will make 5G the fastest globally implemented mobile communications generation due to IoT and smart vehicles applications. While 5G networks will be progressively implemented 3G and 4G networks will remain fully operational. As for costumers 5G implies that mobile internet access not only will offer higher speeds and higher data exchange rates but also connectivity on daily-

life use devices in the household appliances and vehicles. Samsung, Sony and Apple have started to advertise their newest mobile devices as “5G ready” claiming these will be fully compatible with 5G requirements and still offering interoperability with 4G and 3G when needed. While 5G networks will be progressively implemented 3G and 4G networks will remain fully operational. This will represent a challenge in terms of the frequency spectrum due to the massive implementation expected for IoT leading to explore a new frequency range going from 6 to 300 GHz leading to massive investment for development of new adaptive devices such as reconfigurable antennas, mm-wave. Also, in order to reach the desired latency of 1ms [18] 5G will potentially have to invest in optical fibre connections towards BTS, this is a great opportunity for researchers to develop versatile devices that adapt quickly to these requirements and technologies such as reconfigurable antennas, tunable devices capable to control their performances depending on external factors and also exploring novel trends.

1.3. Research opportunities for this project

It has been highlighted that adaptive devices are the clear trend of technology companies with a view to fulfil the requirements of the next generation of mobile communications. Multiband antennas with frequency agility are one of the most recurrent approaches found in industry and academia, nevertheless there is little work carried out in the field of multiband independently tunable multiband antennas. Frequency agility has been studied deeply in discrete printed antennas, nevertheless, the constant grow of the amounts of data being exchanged demands for many devices operating simultaneously which is the principle of spatial diversity schemes. Diversity has not been studied in frequency agile antennas, which highlights this gap as a good research opportunity to deliver innovative devices combining both technologies with a view to fulfil 5G requirements. However, the return of technologies that were established in the last century such as dielectric resonator antennas (DRA) represents an opportunity to carry out an investigation on novel materials in order to exploit the innovative properties of these and combine them with the theoretical principles of the antenna technologies.

Given this gap between novel materials and their combination with emerging and outstanding technologies it is considered that a further investigation is in order to close this gap and the industry and academia can be benefitted from the development of new technologies as a result of this research. In the past few years many substances with adaptive and innovative properties have been developed and are suitable candidates to be studied in an antenna system. Also, in terms of materials, the worrying extension of plastic use around the world is calling

for alternative and environment-friendly solutions in the manufacture of nowadays devices. This project is aiming to develop antennas constituted by a novel material with these features. Dielectric resonator antennas are generally made from plastics, glass or more commonly ceramics, requiring precise and expensive techniques of manufacture, consequently elevating the cost of the system in which the antenna is implemented. As a proposed solution, the use of bioplastics is planned to be investigated given these materials are derived from biological waste from plants, also known as biomass, this also is an environmental advantage due to biodegradation properties of bioplastics which are more rapidly degraded than common plastics, which increases the suitability for bio-sustainable solutions in future technological developments. Further to the advantages of using bioplastics, in innovative manufacture techniques, such as 3D-Printing, bioplastics are becoming a more common material. this could potentially reduce the costs and complexity of the fabrication of antennas. However, an appropriate study on the impact on the efficiency and accuracy of these materials compared to the conventional ones must be carried out.

As the established gaps in the knowledge of adaptive antennas have been discussed previously, in this thesis I propose to develop a set of antennas that fulfil the requirements of the research opportunities. In order to address the need of independently tunable antennas when introduced in a multi antenna system and to explore the operation of bioplastics as dielectric resonators I describe the development of these devices in the following objectives.

1.4. Objectives.

The objectives of this thesis are as follows:

1. Design, construct and fully measure a 1×2 Triple-slot MIMO antenna offering independently tunable frequency bands.

2. Design construct and fully measure a dielectric resonator antenna using that can offer a tunable frequency band.

3. Evaluate the compatibility of the achieved devices with the 5G mobile communications standards and requirements.

1.5. Outline.

In this thesis we present reconfigurable devices with potential applications in the next generation of mobile communications, the first part of this project presents a frequency reconfigurable antenna system constituted by two triple-slot antennas placed in the same board, which is therefore a 1x2 MIMO antenna providing diversity parameters fully compatible with the requirements for 5G. Secondly a frequency reconfigurable dielectric resonant antenna is presented operating at millimetre wave (mm wave) communications ranges. The outline is as follows:

This chapter presents an introduction, motivation of thesis and a brief overview of 5G standards, and objectives of the project.

Chapter II undergoes a review of the theoretical background of slot antennas and dielectric resonant antennas and a literature review of frequency reconfigurable antennas, reconfiguration mechanisms, independent frequency tuning antennas, state of the art dielectric resonant antennas.

Chapter III describes the process of simulation, manufacture, and measurements of three different 1×2 Triple-slot MIMO antenna prototypes.

Chapter IV analyses the MIMO metrics which determine the compatibility of the antenna discussed in Chapter III and the requirements for 5G standards.

Chapter V discusses the design, simulations, manufacture, and tests of a 3D printed rectangular dielectric resonant antenna that offers a tunable frequency band.

Chapter VI presents the conclusions of this thesis, foreseeable future work and possible applications of the antennas developed on this project.

CHAPTER 2. LITERATURE REVIEW AND THEORETICAL BACKGROUND

Reconfigurable antennas are capable of modify their operation by altering their structure through different means. Tuning mechanisms can be classified by the way the current distribution of an antenna is controlled, typically these changes area achieved by using electrical or mechanical alterations. Essentially, the properties of these materials are controlled to achieve a desire performance. The use of novel experimental materials is also being investigated for this purpose e.g. graphene where versatile new properties have been found and can be useful on the mobile communication research field investigated in academia and industry by mobile communication companies. As mentioned previously reconfiguration aims to control one or more properties of the antenna, this allows the following classification:

Frequency reconfigurable antennas: antennas capable of tune over an extended frequency range useful devices for agile radio.

Radiation pattern reconfigurable antennas: devices that control their radiation pattern over a given frequency, change their direction of radiation.

Polarization reconfigurable antennas: these antennas can switch among diverse polarization schemes.

There is another type of reconfigurable antennas termed **hybrid** that control different parameters simultaneously.

A wide review on frequency reconfigurable antennas will be discussed in this section. In this research review many publications have been analysed and a critic perspective has been carried out. Generally, reconfiguration mechanisms can be classified as discrete and continuous and then each of these has a subtype such as mechanic, ferromagnetic, electronic, etc.

In terms of pattern reconfiguration devices, the reviewed mechanisms are based on either mechanical or electrical changes often controlled by an external circuitry. However, mechanical changes in the antenna structure normally aim to modify the radiation pattern of the system order to reconfigure the current distribution e.g. in [6] the author presents a horn operating at 2.47 GHz that controls its structure in order to reconfigure its radiation pattern and achieving variations from 16.5 º to 58.7º. Similarly, mechanical pattern reconfigurability is

reached by controlling the stiffness of a reflector and controlling the gain of the beam achieving up to 32 dBi over C and Ku bands in satellite applications with a view to rearrange the coverage of certain areas around the globe [7].

2.1. Frequency reconfiguration methods.

This thesis aims for frequency reconfigurable antennas as they will offer a wide selection of frequency bands covered by a single device which is a desirable feature for novel devices. Therefore, this section will emphasize on this group of antennas. The redistribution of surface currents of reconfigurable antennas is achieved by using external control circuits, e.g. the research carried out by Prof. Peter Gardner et al. on microstrip patch antennas incorporating injection theory by using two-ported structures where the main one feeds the patch and the secondary port is used to match the primary port with the source, resulting in a smaller antenna with a wide tuning range and bandwidth [4]. Injection theory dictates that two RF amplifiers are feedback connected via a λ/4 waveguide, this theory comes from the Doherty amplifier, which is a technique to improve the performance and efficiency of an RF amplification [20]. This article introduces a new form of linear power amplifier for modulated radio-frequency waves. The circuit achieves efficiencies of 60 – 65% per cent independent of modulation are obtained by means of the combined action of varying load distribution among the valves and varying circuit impedance over the modulation cycle. The theory of operation is developed and detailed observations on the behaviour of valves in the new circuit are given in the article. The use of stabilized feedback in connection with this circuit is discussed and significant measurements on a laboratory model of a 50 kW transmitter are shown. This theory is applied by injecting current from an auxiliary source to the main amplifier into a rectangular patch antenna fed by two ports. By a manipulation of phase and amplitude of the signal between the two ports achieves a mechanism to tune the antenna. However, the antenna may be too big to fit in small mobile devices such as a mobile phone but more suitable to a base station or tablet.

Ultra-wideband antennas are also an alternative to a tunable radiator, the work of Sai-Wai Wong [21] uses a simple monopole with a modified ground plane which is a feeding line designed at 50 Ω. The main feature of this work is that four interconnected stubs have been added into the structure to achieve selectivity of the frequency bands desired, giving a filter-antenna with improved in band selectivity and notched-band performance. However, despite developing this low-cost antenna which can be reliably constructed, the dimensions and

especially the thickness and properties of the materials used are not practical for low cost production.

In terms of miniaturizing antenna elements active matching is a recurrent technique. Circuits that do not follow the Foster's reactance theorem, i.e. using active components to generate impedances equivalent to negative L or C are ideal to eliminate the physical limitations due to the geometry-based calculations and therefore magnitudes of antennas. Nevertheless, active components are required for such devices, e.g. Negative impedance converters (NIC) do not behave in a stable way at high frequencies due to this limitation despite the size reduction. However, a frequency tuning is achieved from 1 to 2 GHz in the device presented in [22]. Although, bandwidth and matching are improved using simultaneous injection matching which was also used on previously reviewed work. This miniaturization technique is suitable to improve the efficiency of UWB antennas. Small sizes are always a good feature for mobile communication devices, this can be achieved by using a double feeding technique and combined with a proximity feed line located between the ground plane and the patch [23].This method aims to achieve a bandwidth improvement of a circular patch antenna also using a two-ported structure and based on the injection theory manipulating the two incident signals and therefore creating a phase shift and amplitude coefficient.

2.1.1. PIN diodes.

PIN diodes are commonly used in reconfigurable antennas acting as switches and therefore controlling the electrical length of the antenna and covering multiple frequency bands, e.g. we find PIN diodes offering to control the electrical length of frequency ranges from 70 to 600 MHz in [21], moreover PIN diodes are used to switch current paths and therefore selecting operational modes from 4.6 GHz to 6 GHz in [24]. A novel microstrip circular disc monopole antenna with a reconfigurable 10 dB impedance bandwidth is proposed in this communication for cognitive radios (CRs). The antenna is fed by a microstrip line integrated with a band pass filter based on a three-line coupled resonator (TLCR). The reconfiguration of the filter enables the monopole antenna to operate at either a wideband state or a narrowband state by using a PIN diode. For the narrowband state, two varactor diodes are employed to change the antenna operating frequency from 3.9 to 4.82 GHz continuously, which is different from previous work using PIN diodes to realize a discrete tuning. Similar radiation patterns with low cross-polarization levels are achieved for the two operating states. Measured results on tuning range, radiation patterns, and realized gains are provided, which show good agreement with numerical simulations [25]. Overall PIN diodes can be very useful components

when aiming for reconfigurable antennas, nevertheless they are limited to only offer discrete tuning, different from other components that easily achieve gradient control of variables.

2.1.2. Varactor diodes.

Antennas using component-loaded structure like slots tuned by varactor diodes are widely used in reconfigurable antennas. A varactor diode is capable to progressively control a parameter given its capacitance varies when applying different voltage levels. Recent works achieved frequency ranges from 2 GHz to 4 GHz using a slot-ring structure loaded with varactor diodes [26]. However, future networks require independently tunable frequency bands suggesting a single device will cover several services simultaneously as requested for novel devices in 5G and currently used in 4G [27]. Independent tuning is present in a dual-band antenna using single-layered rings offering two independently tunable frequency bands (3.2 GHz - 3.7 GHz and 4.3 GHz - 5.4 GHz) controlled by varactor diodes and biasing circuitry in [28], in [29] varactors on high impedance surfaces as ground planes offer independently tunable frequency bands from 0.926 GHz to 2.72 GHz and from 0.905 to 2.76 GHz. In previous work a triple-band antenna has provided an independent tuning range from three slots loaded with varactors [30] this structure is shown in Fig. 1.

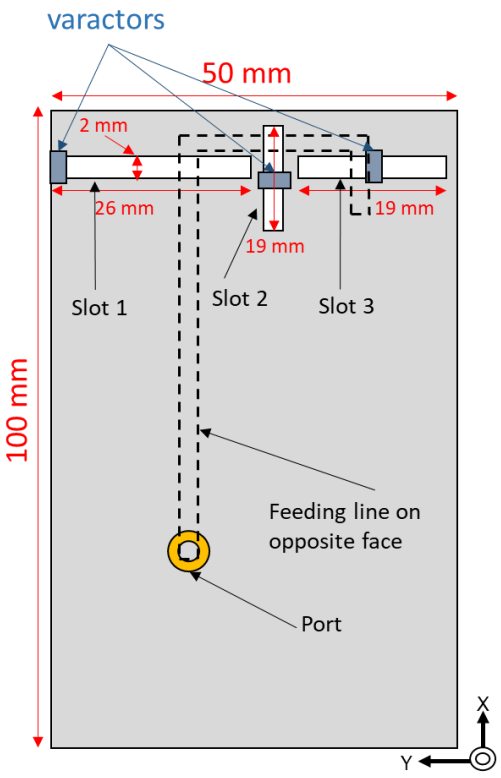

Fig. 1 Independently tunable varactor-loaded triple slot antenna.

The tunable frequency range was 0.6 GHz – 1.12 GHz for slot 1, 1.04 GHz – 2.47 GHz for slot 2 and 1.89 GHz – 2.70 GHz for slot 3. Having multiple antennas operating simultaneously is a technique used in MIMO systems in which several devices send the same data [31] the simultaneous operation of multiple resonators calls for a study to analyse the mutual effects as well as take advantage of multipath, MIMO techniques have been used previously in the LTE and 4G providing better efficiency, energy performance and coverage than single antenna systems and proved to be useful resources in order to ensure continuous connectivity [14].

2.1.3. Liquid crystals.

Adaption of some of the latest cutting-edge devices is based on the properties of the manufacture materials. Innovative features such as changing the dielectric constant or relative permittivity ε_r of a material has many advantages that have been implemented in mobile communications devices. These materials are particularly present in substrates over which an antenna is printed or in the antenna itself. The capacity of these materials to control their dielectric constant will alter the radiation performance of an antenna, and I consider that given the constant grow in the use of these materials it is appropriate to explore new possibilities for communications equipment. The most common examples of reconfigurability by altering properties are ferromagnetic, ferroelectric materials and liquid crystals used in tunable antennas as their permittivity changes when an external electrostatic field is applied.

Frequency reconfigurability is achieved in these materials by altering the material properties using an external incident field to control the radiation of the antenna. The more commonly used are the liquid crystals, applied normally inside a substrate modifying its properties using DC voltages and therefore controlling the frequency operation range of the system, we can see in some works a decent tuning and a wide frequency range e.g. obtaining a 4% tuning range in [32] This system is shown in Fig. 2. The use similar substances such as aerogels has been observed capable to control the frequency range of a system and also reducing the size of the whole antenna system and achieving frequency ranges from 1.6 GHz to 4 GHz [33] A typical application of liquid crystal is as a substrate of a patch antenna in [34]. Moreover, as a substrate of an array of patches or as known in these cases “reflectarray”. This combination achieves its tunability using a series of voltage lines applied to the liquid crystal substrate and provoking different phases for the patch array which controls the resonances obtained by this one, also the beam radiated by this array is incident into a waveguide horn which conduces to a feeding line [35].

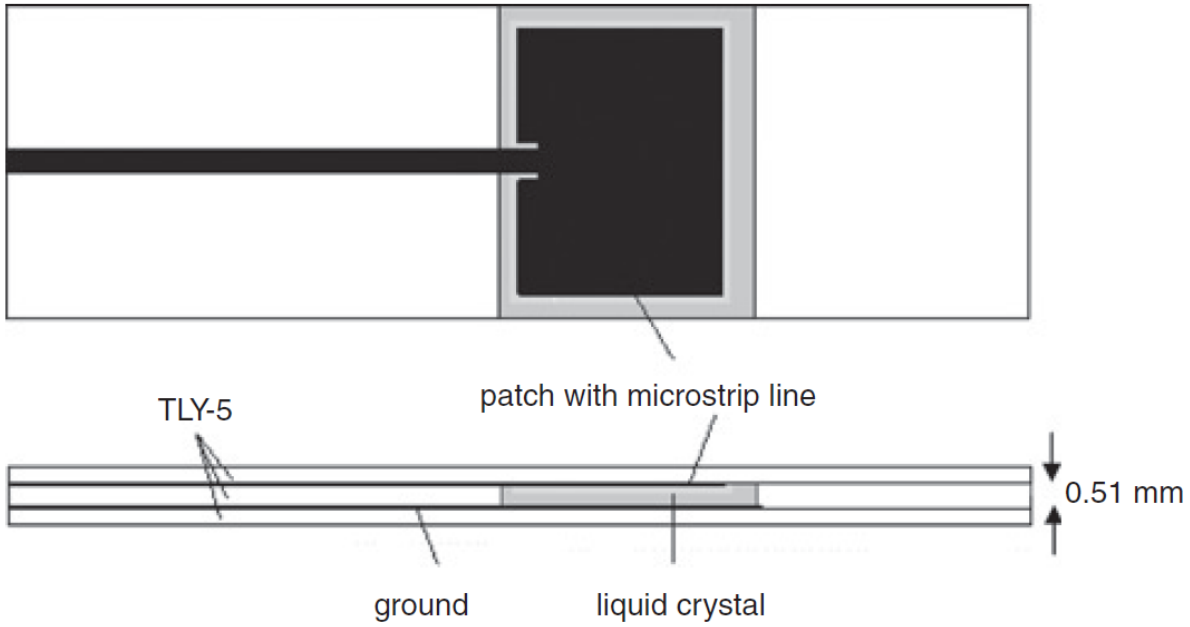

Fig. 2 Liquid crystal substrate reconfigurable antenna [32].

Other approaches can be a simple patch fed by a microstrip line over a LC substrate, which is electronically tuned also using DC bias voltages [36] similar to liquid crystal substrates, there is also the aerogel approach which is a polymer suitable for RF applications [37] and likewise, is biased using DC bias voltage lines but also tuned by electrostatic external fields, the advantage of this antenna is an alternative using bio polymers to reduce the biological impact on its fabrication. Even though liquid crystal-based structures can offer a novel way to achieve tunability, they are expensive and difficult to manipulate without the appropriate security measures given they require health and safety protocols to implement and combine this substance with communications equipment. Also, in order to achieve a rearrangement in the liquid crystals internal structure very high voltages are required which must be provided by complex power sources. Furthermore, liquid crystals can only provide a very reduced tuning range. This conclusively highlights this substance as a marginally suitable candidate for tuning purposes in a reconfigurable antenna due to the limitations above described. Despite that liquid crystals are innovative materials that have been successfully implemented in reconfigurable antennas and microwave engineering applications, they are not flexible in the frequency range and are expensive, which are significant disadvantages in the search for suitable tunable substances. Nevertheless, the established precedent of reviewed works where electronically tunable substances are the working principle of reconfigurable antennas leads to further review of tunable materials.

2.1.4. Graphene.

One of the most innovative materials present in multiple research fields nowadays is graphene. This material is progressively more used in different disciplines offering extraordinary performances and outstanding results, particularly in manufacture, medicine and most recently in water filtration. The graphene theory was published on the 40's and its atomic structure was synthesized for the first time ever in 2004 by scientists from the University of Manchester, shortly after, multiple studies were carried out in order to assess its properties and their potential applications in different research fields. Graphene consists in graphite cells exfoliating atomic carbon sheets, achieving an internal structure capable to rearrange in presence of external factors. This allows graphene to offer a resistance higher than the steel but with an much lighter weight changing in presence of thermal and electric sources [38] which suggests that its internal structure can also be controlled by electric fields or signals. Consequently, graphene can be integrated in electronic systems and potentially in microwave, RF and electromagnetic applications, more precisely mobile communications. Companies such as Samsung, Huawei, and Apple etc. are recently having difficulties with their energy storage in their battery cells, including their most novel releases, graphene battery cells are being investigated for these purposes. Further in communications engineering, there has been some development in tunable antennas based on graphene structures. The work of M.F. Craciun, S. Russo, M. Yamamoto and S. Tarucha about the tunability of graphene [39] describes the ability of this material to achieve frequency reconfiguration in presence of an adjacent electric field, specifically a DC biasing voltage line. This device incorporates graphene and SiO_2 merged in thin film layers of 300 nm combined with gold as a substrate. A tunable slot of graphene and SiO_2 sits in the middle of a gold layer, the slot is biased by a dc voltage aiming for frequency reconfiguration. As the graphene-SiO_2 slot rearranges its internal structure with different voltages so does the reflection coefficient, hence achieving a frequency range of 8.8 – 11.4 GHz varying the DC voltage 0 – 200 V.

Overall, graphene-based frequency reconfiguration mechanisms for antennas are achievable through the incorporation of DC voltage lines that injecting an electric field that rearranges the internal structure of graphene. Nevertheless, the implementation of these devices imply the use of expensive equipment and materials as well as high voltages, although, the use of derived substances such as graphene oxide suggests possibilities that have not been studied yet and could be suitable for the work developed in this thesis and in future research development.

2.2. Slot Antennas.

A recurrent kind of antenna often used in adaptive and innovative communications equipment are aperture antennas, which are discrete and easy to fabricate and to control. Slot antennas belong to the aperture antennas family which are compact, discrete resonators, easy to manufacture and low-cost devices. A slot antenna is an aperture in a conductive surface and typically fed by a transmission line, these two layers are separated by a dielectric substrate. Fig. 3 shows in (a) the perspective view (b) the top view of a typical slot antenna layout with a microstrip feed line.

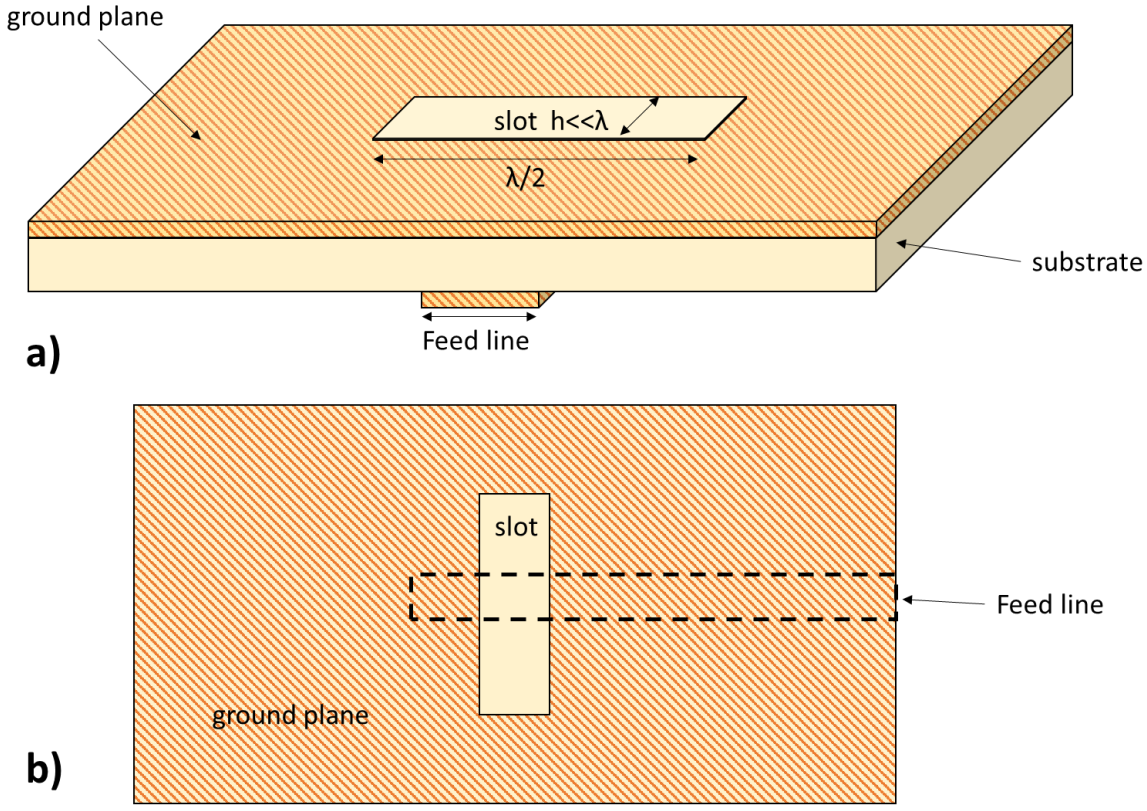

Fig. 3 Perspective views of a slot antenna.

The radiation of a slot antenna is based on the electric field associated to the voltage adding up in phase. As the slot is fed, the voltage distribution from top to bottom in the slot while the current cancels out, contrary to the working principle of dipole antennas. The geometrical dimensions of slots are stablished by the wavelength corresponding to the operating frequency they have been designed for, with height $h << \lambda$ and length $l = \lambda/2$. The position of the feed in a slot antenna impacts on the behaviour of the aperture. If the feed is located in the centre of the slot then the input impedance will reach its maximum level, parallelly, the impedance will be in its lowest levels once the slot is fed in any of the edges. However, if the feed divides

unequally the antenna length the section smaller than λ/4, it will have inductive effects, while the larger section will have capacitive behaviour in addition to the considered radiation resistance in the equivalent circuit of an antenna. So that when the capacitance and inductance cancel each other out they allow the radiation with the voltage adding up in phase [40]. Fig. 4 shows the current and voltage distribution in a slot antenna.

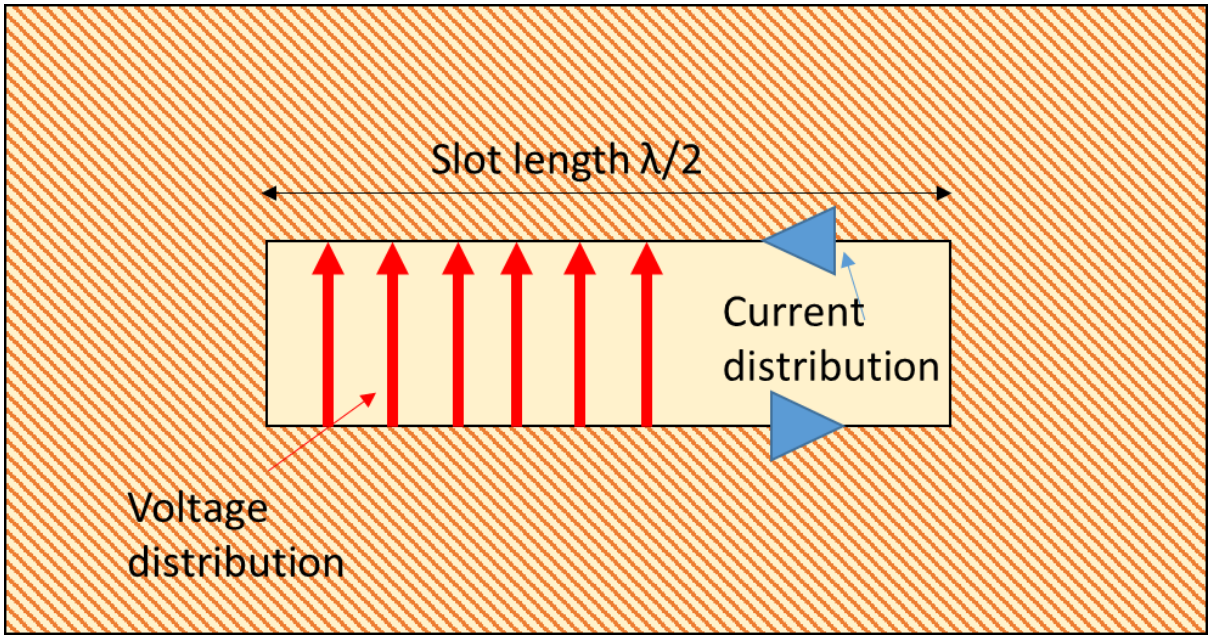

Fig. 4 Voltage and current distribution in a slot antenna.

Slot antennas are easily manufactured; they can be basically carved from any printed circuit board which reduces costs and optimises its integration within more complex systems. Nevertheless, the operation features are limited as they offer linear and circular polarisation offered by cross-slots as well as omnidirectional radiation patterns as well as. These limitations can be overturned by short-circuiting the slot using an adaptive load able to generate a stationary wave through current variations and therefore producing an optimal radiation efficiency for the antenna [41]. Similar to patch antennas, slot antennas are composed by two conductive layers separated by a dielectric substrate, nevertheless the radiation of these antennas occur on cavities in the ground plane which are named slots which are fed by on the opposite face to the ground plane which will correspond to the second conductive layer, normally the slots are fed by a microstrip feeding line, nevertheless other less common feeding methods are used [42]. These antennas have a very wide range of application on frequencies from 300 MHz to 24 GHz, this means they can operate with TE modes depending on the length of the slots.

2.2.1. Input impedance.

As briefly described previously, the input impedance of a slot antenna depends on the location of the feed line with a very high input impedance achieved when the feed line is in the centre of the slot and a very low if the antenna is fed in the edge, moving the feed away from the edge but not too close to the centre will reach the optimal input impedance which is near 50 Ω. Furthermore, the impedance of the slot antenna Z_s is related to the impedance of its complementary structure Z_c. This is dictated by the Babinet's/Booker's principle, that establishes the duality of properties between a dipole antenna and a slot antenna. Considering a dipole antenna of length L = λ/2 and its complementary structure being an air gap with the same length but surrounded by metal. Hence, their electric field associated to current and voltage respectively will provide a radiation pattern in the same direction for both structures. Moreover, the impedances Z_s and Z_c will be related to the intrinsic impedance in the free space (η=377 Ω) as described in equation (1) [43].

$$Z_s Z_c = \frac{\eta^2}{4} \tag{1}$$

Also, the feeding line will provide a normalised impedance which normally is 50 Ω which will be an essential parameter to determine its width. Fig. 5 illustrates the duality principle of Babinet as well as the E-field vectors that allow the radiation in each structure.

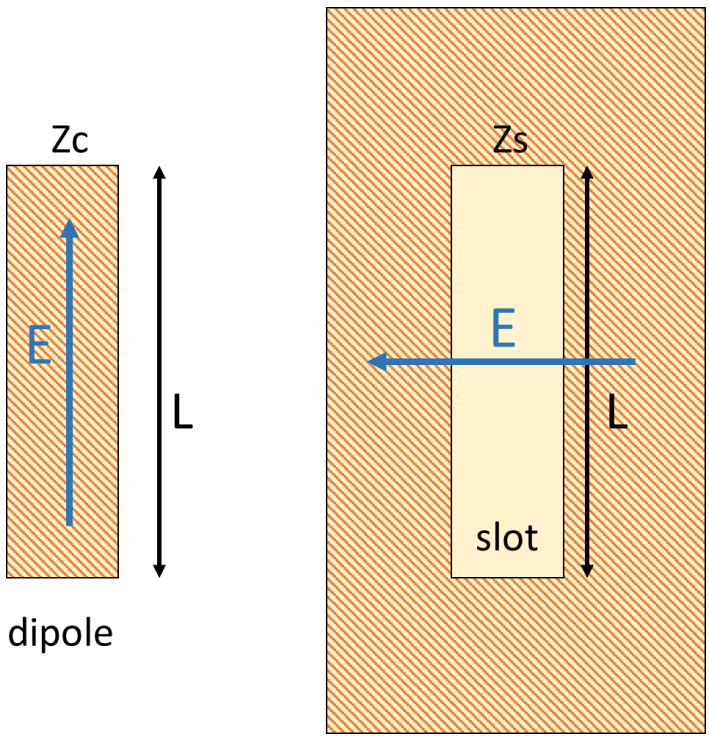

Fig. 5 Duality correspondence of Babinet's principle.

2.2.2. Radiation pattern.

Slot antennas show normally omnidirectional patterns given a cavity behaves as dipole and radiates rather in all directions. As the electric field associated to the In order to describe radiation features of an antenna it is only required to analyse the tangential components of both E and H fields, for this purpose a spherical coordinates system has to be defined and is presented in 6 below:

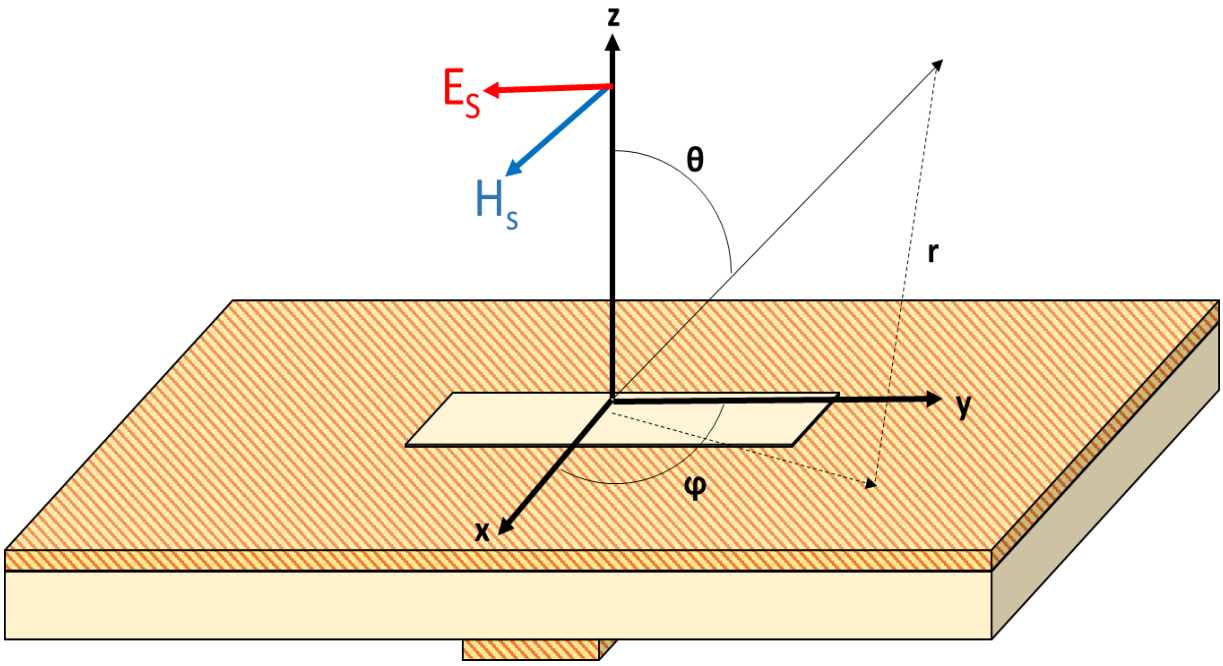

Fig. 6 Direction of E and H field tangential vectors in a slot antenna.

As mentioned previously, the duality described by the Babinet's principle relates the radiated fields of a dipole antenna with those of a slot antenna as it considers a slot antenna of length L as the complementary structure of a dipole antenna of length L. In both cases the direction of propagation remains the same, however the tangential components have opposite directions, which also changes the polarisation from the dipole to the slot. The expressions for the tangential components for the electric and magnetic fields follow the Babinet's/Booker's principle and are given by equations (2) and (3):

$$H_\theta = \frac{E_\theta}{\eta^2} \tag{2}$$

$$E_\theta = E_0[\sin\theta] \tag{3}$$

2.2.3. Polarization.

The polarization of a slot antenna is normally linear, in these antennas, polarization depends on the position and geometry of the slots depending i.e. horizontal and vertical; similar to patch antennas these antennas are linearly polarized given E field only varies in one direction. This feature is also exploitable to achieve a reconfiguration mechanism.

2.2.4. Feed methods and analysis.

As a slot antenna is basically a resonant cavity, one of the most common methods to analyse it is the Babinet's/Booker's Principle which considers a slot antenna as a cavity in the surface of an ideal conducting plane [42], [43]. The most common method to feed the cavity is via a microstrip feed line which normally is placed near the centre as this splits the slot into equivalent inductances and capacitances as mentioned previously in section 2.2.1. another recurrent method is a coaxial feed which reduces the discretion of the antenna. In Fig. 7. a cross-section of an antenna fed by a microstrip transmission line is presented, specifying the width of the line and the length of the slot. The feeding method for slot antennas is often a microstrip transmission line which gets a uniform distribution of current flow [44]. Given there is a voltage moving on the edges of the slot there is axiomatically a current flow as well, this is what causes the radiation of the slot. In real practice there is no such thing as ideal conductive planes. Given this flexibility, slot antennas are easily carved in printed circuit boards, nevertheless, some of these antennas might have been unexpected irregularities on a ground plane of a printed antenna and created unexpected effect on their performances.

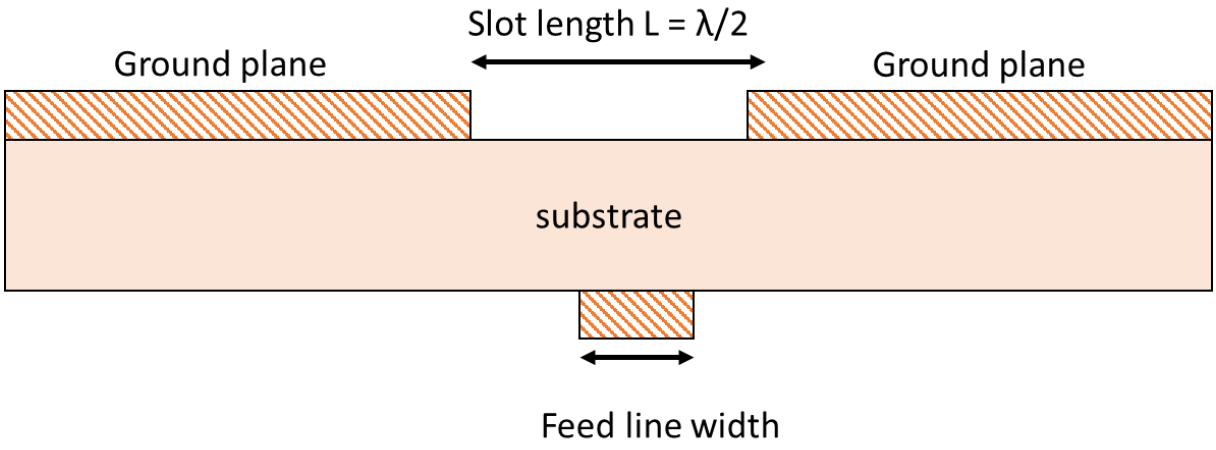

Fig. 7 Cross section of a slot antenna fed by a microstrip transmission line.

2.3. Frequency reconfigurable slot antennas.

We have reviewed numerous systems capable to alter their structure and properties in order to achieve a desired performance in the previous sections as well as the many advantages that aperture antennas, specifically slot antennas can offer in terms of versatility, discretion and low cost implementation. In this section we will discuss reviewed works in which slot antennas are capable of reconfigure their frequency operative modes. We analysed devices having tunable elements such as strips which change their length and therefore modify their resonant frequencies achieving useful frequencies for Wi-Fi applications at 2.4 GHz and 5 GHz bands, reaching bandwidths of nearly 100 MHz for 2.4 GHz band and 1550 MHz for the 5 GHz band [45]. Moreover, we observed reconfigurable slots placed in ground planes and controlled by capacitors covering frequencies useful for LTE and GSM when the capacitor varies, hence covering simultaneously two services [46]. Slot-rings are also widely used for reconfigurable devices as they can be loaded with components such as PIN diodes as reviewed in section 2.1.1 we find in [47] a slot-ring antenna operating at two frequency bands (1.76 GHz and 5.71 GHz) using PIN diodes switching states to activate one of the two operating bands, offering high efficiencies and decent gains up to 4.2 dBi. PIN diodes have proved to be versatile elements very useful for reconfiguration mechanisms which can be used to select six different states and therefore selecting nine different resonant frequencies covering a range from 2.7 GHz up to 9.5 GHz [48]. A folded slot antenna that switches two modes was reviewed and is shown in Fig. 8 depending on three diodes altering the length of the slot. In (a) PIN diodes are in ON state, and a current flow is occurring in the edges of the slot, whereas in (b) PIN diodes are in OFF state and current gets redistributed into the internal slot. This device achieves frequencies useful for WLAN at around 5.25 GHz, WiMAX at up to 3.69 GHz and Bluetooth and Wi-Fi at up to 2.48 GHz [49]. A similar structure can be controlled by a bias network in order to switch the length of slots covering frequencies from 500 MHz and up to 3.6 GHz [50]. Slot antennas offer numerous possibilities of applications when used as reconfigurable devices, nevertheless there is a need of versatile elements that can control a desired parameter such as frequency which leads to the next section.

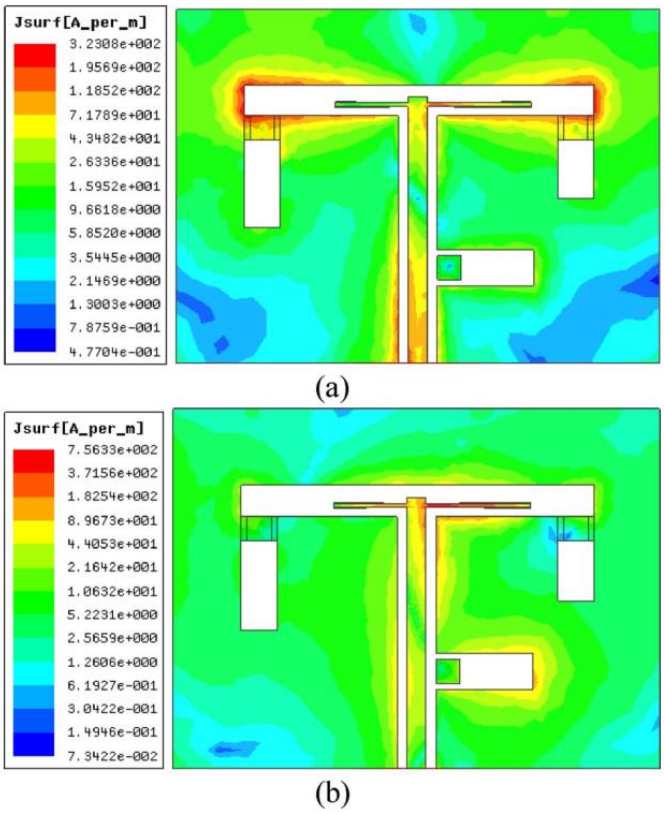

Fig. 8 Operating modes of reconfigurable slot antenna controlled by PIN diodes [49].

2.3.1. Varactor-loaded slot antennas.

While reviewing different techniques to achieve parametrial reconfiguration for aperture antennas a recurrent approach is the incorporation of active components in the aperture cavity. Components load the slot and control its resonant frequency by gradually varying their characteristic properties, in these particular cases, using varactor diodes. [24] Mainly, for varactor-loaded the reconfiguration is carried out in frequency, controlling the internal capacitance of varactor diodes creates an effect of frequency shifting. A special emphasis on the efficiency of these loaded structures has been carried out in [51], this is a study that has corroborated the suitability of varactor loaded slot antennas reviewing antennas with efficiencies up to 60%. Different shapes of slots have proved to adapt well to the incorporation of varactors, this is the case of slot-ring antennas loaded with varactor diodes that vary their internal capacitance when applying different DC voltages to it which is the case of [26] where varactors are used in a slot-ring structure and offer a frequency tuning range of 1 – 4 GHz. This device is shown in Fig. 9, where switches and diodes are operating to achieve the reconfiguration in frequency.

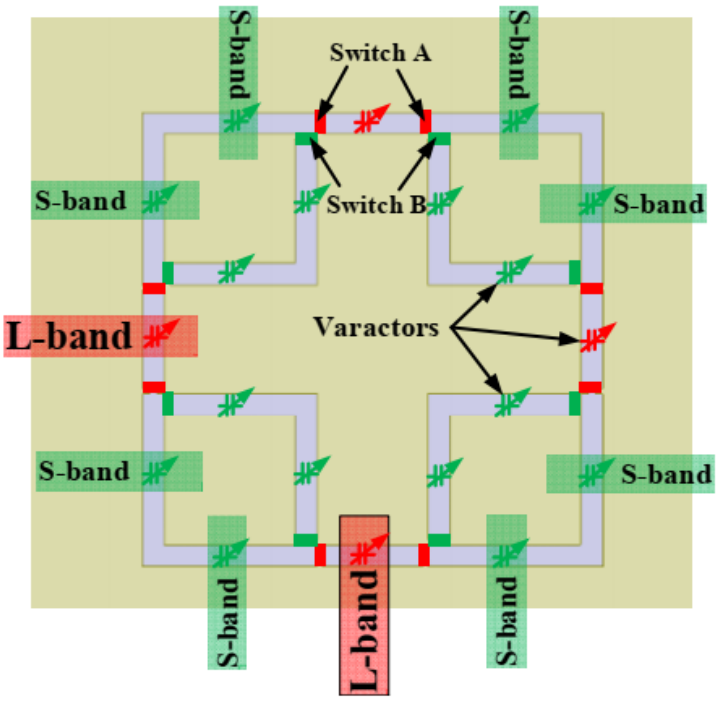

Fig. 9 *Varactor-loaded reconfigurable slot-ring antenna [26].*

In addition to loaded slot loops, slot lines offering frequency agility have been reviewed as well, however, the trend in these kind of antennas is the addition of LC low-pass circuitry including DC block capacitor and RF choke inductors in order to avoid external interferences, the device reviewed in [52] achieves frequencies from 2.34 GHz and up to 4 GHz and incorporates a LC network acting as shield to external RF interferences which does not have a negative effect on the performance of the system. Manufacture of components using thin-film deposition techniques such as sputtering is an innovative approach in the search of incorporating more discrete elements in an aperture antenna. Slot lines loaded with thin film printed varactor diodes is a cutting-edge approach and proved to be effective with similar results to antennas that have incorporated regular varactors. In [53] a comparison of a slot line with thin-film varactors and another with regular varactors has been carried out. In terms of frequency response, similar results have been obtained for both cases achieving frequencies from 5.8 GHz to 6.1 GHz with a maximum value of 3V applied to the thin-film varactors. Ultra-wideband slot antennas have been loaded with varactors in reviewed articles offering an appropriate frequency agility. UWB slot antennas are often used for cognitive radio applications, which is the cased presented in [54], a varactor loaded-slot resonator integrated in the same substrate than an elliptical monopole proved to offer a tuning range from 5 – 6 GHz when varying an input voltage to the varactor from 0 – 5V. As an additional feature, varactor

diodes not only achieve frequency reconfigurability but also manage to control the polarisation of an antenna. This is the case of the device discussed in [55] which switches from linear (right and left-handed), circular and elliptical polarisations using a reconfigurable feeding circuit composed by two varactor diodes and two inductors selecting different transmission lines when varying its input voltage from 0 – 30V and achieving frequencies from 1 – 1.9 GHz.

The versatile performance of devices tuned by varactors has leaded to the development of adaptive systems that allow simultaneous frequency agility for several apertures loaded with varactors, however, operating at multiple bands means the presence of undesired interferences might impact on the performance of the system. The addition of LC filtering circuits has been reviewed in single antennas, however, a multiband antenna has provided an independent tuning range in slots loaded with varactors in [30]. Three independently tunable frequency bands 0.6 –1.1GHz, 1.0 – 2.5 GHz, and 1.9 – 2.7 GHz when varying the voltages into the varactor 4.6 – 30V, 3V – 17.4V and 7.3 – 25.5V respectively, this work is highlighted as a potential candidate for MIMO applications as it introduces multiple antennas operating simultaneously.

2.3.2. MIMO frequency reconfigurable slot antennas.

In the currently developing mobile communication generation 5G, large amounts of data are expected to be exchanged between devices and a recurrent technique to achieve this using multiple antennas to transmit and receive the same information. The acronym MIMO stands for multiple input – multiple output and refers to systems with numerous antennas used for transmission and reception, this is called a diversity or MIMO scheme introduced in an antenna system [14]. Slot antennas have been reviewed introducing a MIMO scheme and offering frequency reconfiguration, multiple slot antennas can coexist on the same board and offer a frequency range from 1.6 – 2.48 GHz for LTE, WIFI and WIMAX applications [56]. Miniaturised antennas are the most recurrent approach for reconfigurable MIMO antennas. This is the case of a double-slot MIMO antenna presented in [57] this antenna is printed over a Rodgers RO4350 substrate with a relative permittivity of $\varepsilon_r = 3.48$, both antennas are loaded with varactors and achieve frequency ranges of 0.665 – 1.13 GHz, 1.415 – 2.005 GHz, 2.42 - 3.09 GHz and 3.18-3.89 GHz when varying the input voltage of the varactors from 0 – 15 V. Also, a 4-slot antenna system tuned by varactors is discussed in [58] covering three frequency bands as follows: 1.7 – 2.28 GHz, 2.5 – 2.85 GHz and 2.9 – 3.1 GHz. This article introduces the calculation of envelope correlation coefficient (ECC) which is a parameter that determines the low interaction between the multiple number of antennas in a MIMO scheme proving that

ECC < 0.5 which is the optimal condition for a number of antennas operating simultaneously. Schematic views of this system are shown in Fig. 10 (a) bottom side, (b) top side, (c) bottom side of single antenna element and (d) top side single antenna element.

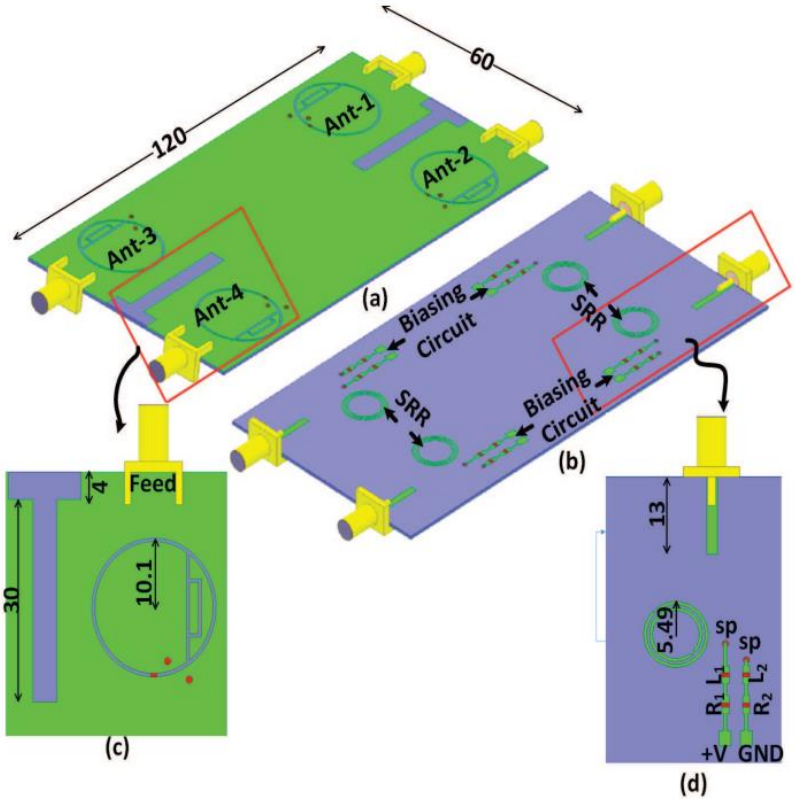

Fig. 10 Views of antenna system presented in [58]by Hussain, Khan and Sharawi.

Further on reconfigurable MIMO slot antennas, varactors can act similarly to PIN diodes and select states. The system discussed in [59] incorporates 6 varactor diodes on one side of the slot and select 6 different operating modes covering a tuning range from 1.8 GHz to 2.45 GHz, this article includes a MIMO performance metrics study as well. Dual-band slot antennas could be considered a MIMO system, in [60], varactor diodes are loading a dual-slot antenna covering two frequency bands 1.6 – 1.8 GHz and 2.2 – 3.1 GHz however they do not introduce the MIMO metrics analysis.

As a conclusion for reviewed articles in frequency reconfigurable slot antennas, many of the discussed systems offer attractive properties for agile and versatile performances which are required for the next mobile communication generation standards, nevertheless it will be desirable to merge many of these properties into a single device. For instance, the reviewed independently tunable devices could introduce a MIMO scheme and incorporate the correspondent metrics in order to prove their compatibility with 5G standards.

2.4. Dielectric Resonator Antennas.

Given the increasing amount of data that is exchanged among devices nowadays it is imperative to explore higher frequencies over a range that is not fully exploited. Although slot antennas offer multiple applications, versatile solutions and are used on high frequencies due to the operability of these antennas on frequencies from 300 MHz to 24 GHz they present some disadvantages. Metallic resonators have large conduction losses when operating at high frequencies which lowers the expected performance and lead to poor radiation efficiencies. Therefore, this requires an alternative solution to avoid these losses. When using dielectric resonators these problems are significantly reduced. DRAs (standing for Dielectric Resonator Antennas) are being under further investigation and development as they can achieve optimal performances at high frequencies if they are excited properly. Due to the experimental nature of the materials used in these antennas and of course because the versatility of devices leading to unexpected performances the simulation process is a necessary part of the conception of a reconfigurable antenna system for this Thesis. Full wave electromagnetic simulation software is essential to find an optimal tuning mechanism to provide a solution for a reconfigurable antenna system.

Dielectric resonant antennas manage to radiate when excited properly i.e. a feeding technique that secures the injection of an RF signal into the DRA walls. Originally DRAs were applied fundamentally in microwave circuits such as filters, oscillators, etc. where the resonator was made out of a ceramic material with high permittivity or dielectric constant ε_r normally higher than 20 which leaded these elements to be used as energy storage instead of radiate it by encasing them in order to prevent radiation losses. Nevertheless, this material's capacity to radiate was discovered in 1938 and published in some works [61] describing in detail that dielectric resonators do not present conductive losses at high frequencies, this is of course a contrasting and desirable characteristic of these materials as metallic antennas suffer from high conductive losses at high frequencies and therefore experience due to this effects very low radiation efficiencies. The only observed losses on dielectric resonators are due to the microscopic imperfections of the material itself however in practice some of these imperfections can be negligible. Dielectric resonators operate by following the principle of a cavity resonator which is a hollow conductor, normally closed, that allows the reflection of electromagnetic waves within its inner walls, resonant cavities are widely used in microwave applications as the reflections lead to high frequencies [62].

2.4.1. Main advantages and characteristics of DRAs.

5G technologies tend to increase data exchange rates and therefore research is required to explore the unlicensed and recently released high frequencies bands >50 GHz. This is where the high operation frequencies achieved by dielectric resonators can have potential applications. DRAs have significant advantages when compared to conventional metallic antennas. Sizes of DRAs can be substantially reduced due to the proportionality to the wavelength λ_o they work at with $\lambda_o = \frac{c}{f_o}$ where f_o corresponds to the frequency of operation of the dielectric resonator. Namely DRA size $\propto \frac{\lambda_o}{\sqrt{\varepsilon_r}}$ different from metallic antennas that are sized proportionally to λ_o only [63]. Furthermore, and due to the minimal conductive losses at high frequencies given the dielectric nature of the material of the resonator, this increases the radiation efficiency and makes them optimal for high frequency applications, estimating a range from 20 GHz to 300 GHz [64]. The resonant frequency of a DRA depends also on the permittivity of the material used, typically for these antennas the more commonly used materials are ceramics with a high permittivity and therefore high Q factor [65]. However not only ceramics are applied as resonators, we can observe some plastics and glasses in certain works offering decent results, reaching frequencies above 40 GHz and high radiation efficiencies, similar to conventional ceramic resonators [66], [67].

DRAs base their propagation principle in supporting certain modes of electromagnetic radiation. EM waves propagate normally in a medium such as air, water, etc. with E and H field component's perpendicular to each other and transverse to the direction of propagation, this is known as Transverse Electric and Magnetic mode (TEM mode). Nevertheless, in some cases, either electric or magnetic field are transverse to the direction of propagation and the remaining component is normal to the direction of propagation. i.e. for the transverse electric mode (TE mode) the electric field is transverse to the direction of the propagation of waves and the magnetic field is normal to the direction of propagation. Parallelly, for the transverse magnetic (TM mode) the magnetic field is transverse to the direction of propagation and the electric field is normal to the direction of propagation. TE and TM modes are only supported by certain structures, such as waveguides. The inner walls of a waveguide act as reflective surfaces and the propagation occurs in a single direction reducing capacitive losses. This is also true for a dielectric resonator antenna which can be analysed as a waveguide constituted by a dielectric material in which the waves bounce back and forth. In Fig. 11 (a) TEM, (b) TE and (c) TM modes in a waveguide are presented.

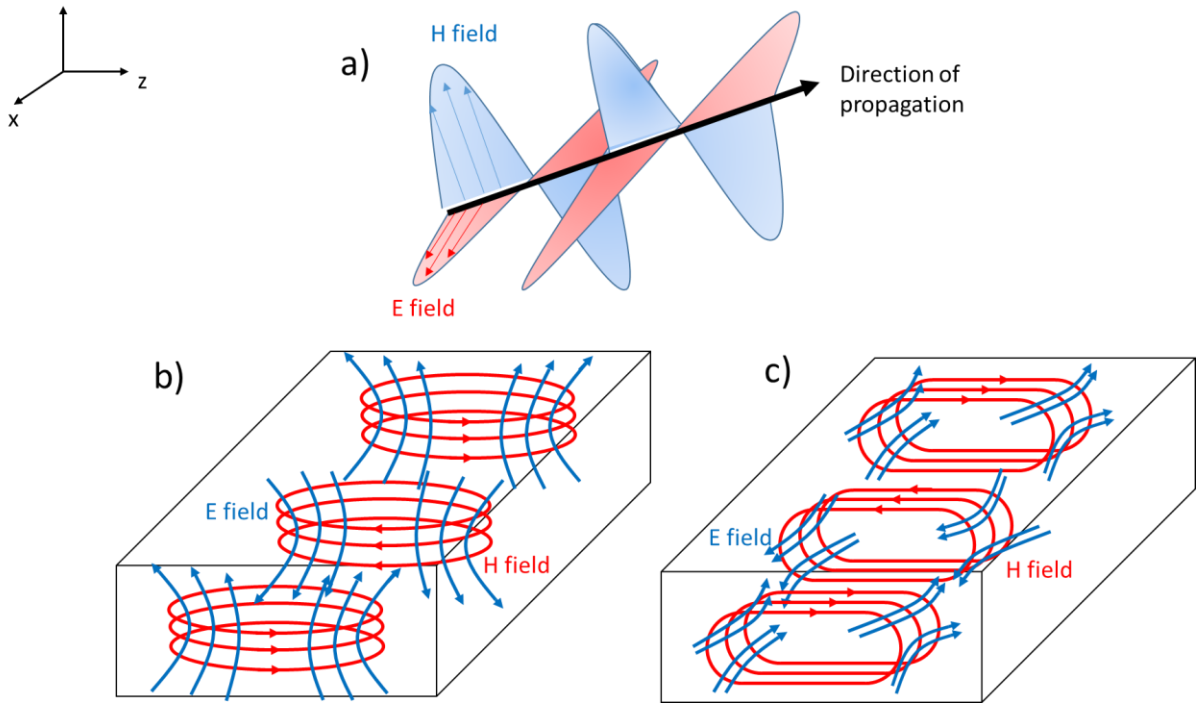

Fig. 11 Transverse wave propagation modes.

2.4.2. Geometrical variants of DRAs.

Dielectric resonant antennas can have numerous shapes and materials, depending on the desired application. Fig. 12 illustrates some of the most typical forms of dielectric antennas which can be summarised in three main groups: cylindrical, hemispherical, and rectangular. These will be discussed in detail in this section as well as their respective design equations.

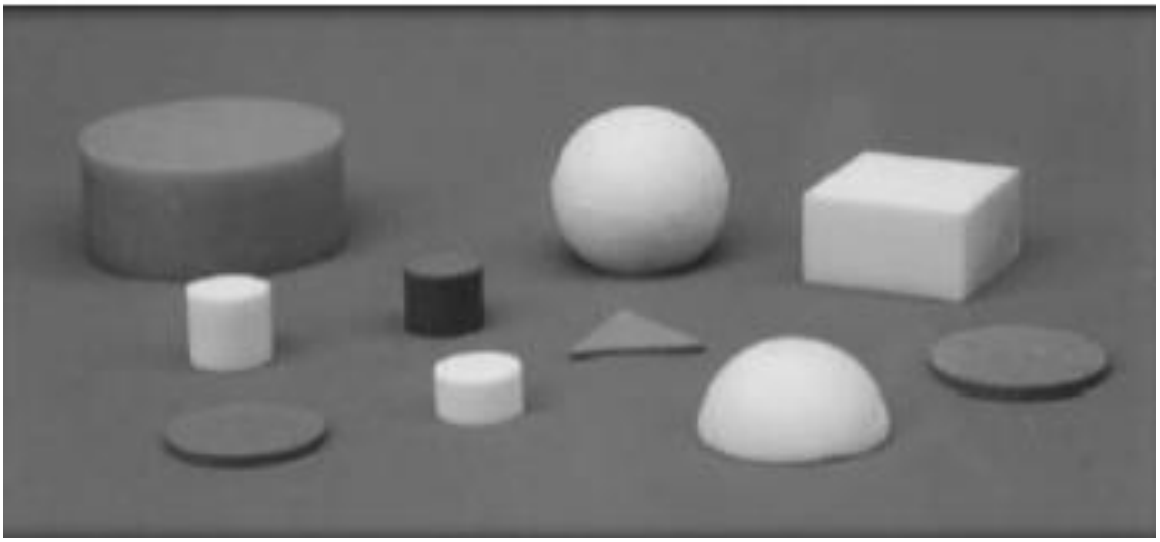

Fig. 12 Variety of shapes of dielectric resonators [63].

Cylindrical dielectric resonators. They are the simplest shape of DRAs as it is only required to precise a radius *r* and a height *h* to dimension the solid. In addition to this, a value for the relative permittivity corresponding to the material chosen for the DRA is required as well. Generally, CDRAs are sized by a radius – height ratio as follows: $0.5 < r/h < 4$. Their design equations are based on the resonant transverse modes supported by the resonator as discussed in section 2.4.1 with *n*, *p* and *m* as the horizontal, vertical and normal orders of the patterns, the respective permittivity ε_r and permeability μ_r of the material, *c as* the light speed in vacuum and the roots of the Bessel functions X_{np} and X'_{np} that are fixed values that can be selected depending on the desired order. Equations (4) and (5) determine the supported modes and are as follows: [65]:

$$f_{TE_{npm}} = \frac{c}{2\pi\sqrt{\varepsilon_r \mu_r}} \sqrt{\left(\frac{X_{np}}{r}\right)^2 + \left(\frac{(2m+1)\pi}{2h}\right)^2} \tag{4}$$

$$f_{TM_{npm}} = \frac{c}{2\pi\sqrt{\varepsilon_r \mu_r}} \sqrt{\left(\frac{X'_{np}}{r}\right)^2 + \left(\frac{(2m+1)\pi}{2h}\right)^2} \tag{5}$$

The Bessel functions of the first kind X_{np} and X'_{np} in equations (4) and (5) are given by their corresponding *n* and *p* values which are the roots of their first-order derivative [65], [68]. the geometry of CDRAs is normally represented in a system of cylindrical coordinates as observed in Fig. 13. These are industrially the easiest DRAs to manufacture.

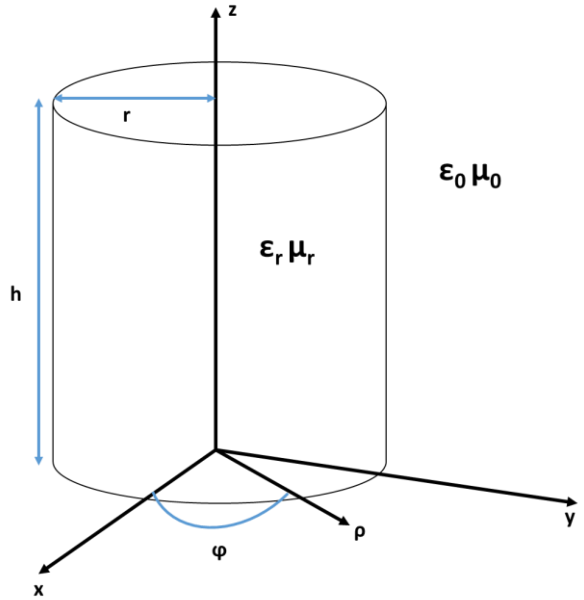

Fig. 13 Cylindrical dielectric resonator and its dimensions.

Hemispherical dielectric resonators. These DRAs consist on a semi-sphere of a dielectric material with relative permittivity ε_r and a radius a and also placed over a conductive ground plane. Hemispherical DRAs can be analysed by using the image theory in order to compare this structure with an isolated full sphere sharing the exact same dimensions. These resonators support TE and TM modes having TE_{111} modes as their fundamental operational ones. Feeding methods of hemispherical dielectric resonators are mainly feeding probes, nevertheless, cross-shaped slots are staring to emerge as recurrent alternatives [65]. The typical DRA sitting on a conductive ground plane is presented in Fig. 14. The incorporation of air gaps in hemispherical DRAs with a view to improve the antenna bandwidth is also a recurrent technique described in [69] having the -3dB impedance bandwidth substantially enhanced as a result.

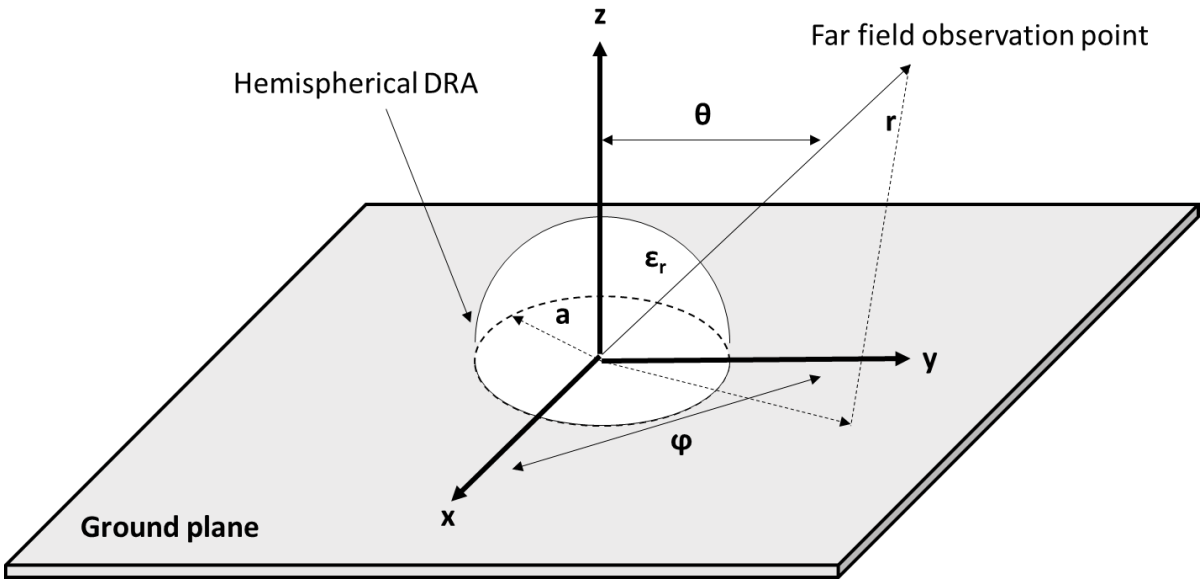

Fig. 14 Hemispherical dielectric resonator, dimensions and coordinates system.

Rectangular dielectric resonators are one of the most commonly used DRAs and offer practical advantages compared to other shapes of resonators. For instance, in rectangular DRAs frequency modes cannot be hybridised, which means two different configurations of the electromagnetic field at the same frequency cannot coexist. Hybrid modes are supported in hemispherical structures which increases the cross polarisation levels and reduces their performance which is a highlight of rectangular dielectric resonators as hybrid modes are not supported on these shapes [70]. In order to obtain a desired resonant frequency two independent ratios of parameters can be adjusted in terms of dimensions: height-length and width-length. Rectangular DRAs are more flexible in terms of controlling their bandwidth,

however their analysis becomes more complex due to the edges of the structure. The dimensions of rectangular DRAs are width *w* length *l* and height *h* which are independent from each other and assuming a relative permittivity ε_r. Their design depends on the analysis of the structure carried out by the waveguide model [71] when the DRA is placed over a conductive ground plane similar to the previously reviewed shapes. Following the waveguide model, the resonant frequency for the fundamental TE_{111} mode is obtained by equation (6) [72].

$$f_o = \frac{c}{2\pi\sqrt{\varepsilon_r}}\sqrt{{k_x}^2 + {k_y}^2 + {k_z}^2} \tag{6}$$

$$\text{Where } k_x = \frac{\pi}{w}, k_z = \frac{\pi}{2h}$$

$$\text{And } l = \frac{2}{k_y}\tanh\left(\frac{k_{y0}}{k_y}\right),\ k_{y0} = \sqrt{{k_x}^2 + {k_z}^2}$$

These expressions determine the geometrical dimensions of the rectangular DRA leading to the conception of a structure like the one shown in Fig. 15. Typically, a RDRA is sitting on top of a conductive ground plane acting as reflective surface. In terms of feeding methods for rectangular resonators the most commonly used is an aperture in which the DRA will be placed over it, although direct feeding probes are also a recurrent technique.

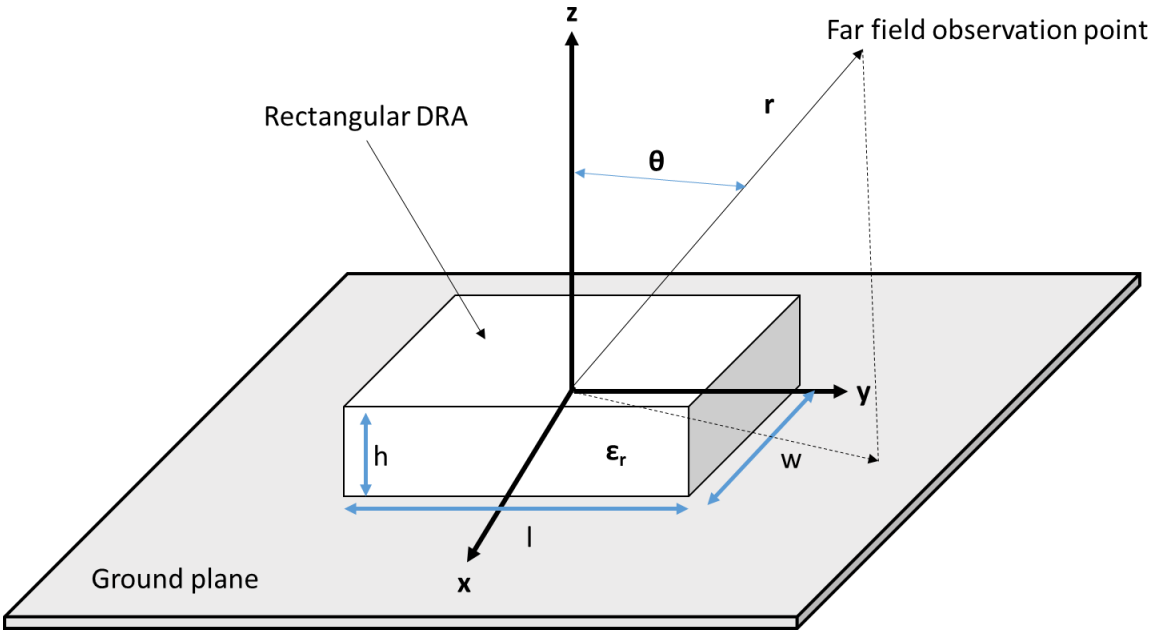

Fig. 15 Rectangular dielectric resonator with its dimensions and coordinates system.

2.4.3. Radiation resistance and intensity.

In a transmission scheme the antenna and the transmitting system must adapt with a view to reach a maximum power transfer. Usually the transmitter is away from the antenna and is connected through a transmission line or waveguide. The input impedance of an antenna Z_e can be defined by voltage-current ratio in a phase notation, if Z_e does not present a reactive part to a frequency then that antenna is resonant. There are significant power losses due to radiation which are directly related to a radiation resistance R_r. Hence the total delivered power equals to the addition of the radiated power plus the losses, in other words $P = I^2 \times R_r + I^2 \times 2R_\Omega$ delivered where I stands for the current that circulates the antenna and R_Ω is the losses resistance. The input impedance of an antenna is an essential parameter that establishes the voltage conditions required to obtain certain levels of current once applied to the antenna and consequently a desired radiated power. If the reactive part of an antenna is too high then high voltages have to be applied in order to obtain decent currents, on the other hand if the radiation resistance is too low then high current levels are needed to achieve a significant radiated power [43], [63].

Given the losses of an antenna causes the radiated power to be far from the total delivered power by the resonator, its efficiency η_l can be determined expecting very reduced losses for DRAs and establishing it as follows: $\eta_l = P\ radiated / P\ delivered = R_r + R_\Omega$. Derived of this, radiation intensity is a useful parameter that determines for an antenna the capacity to radiate towards a given direction. In order to define a reference space for an antenna a spherical system of coordinates is commonly used. Specifying unit vectors $\hat{r}$, θ, ϕ and using angles θ, ϕ forming an orthogonal base and the radiation direction is determined by the intersection of a sphere with radius r and a cone with an angle θ and a semi-plane passing by z axis. DRAs tend to typically radiate towards this axis too with the highest intensity as seen in Fig. 16.

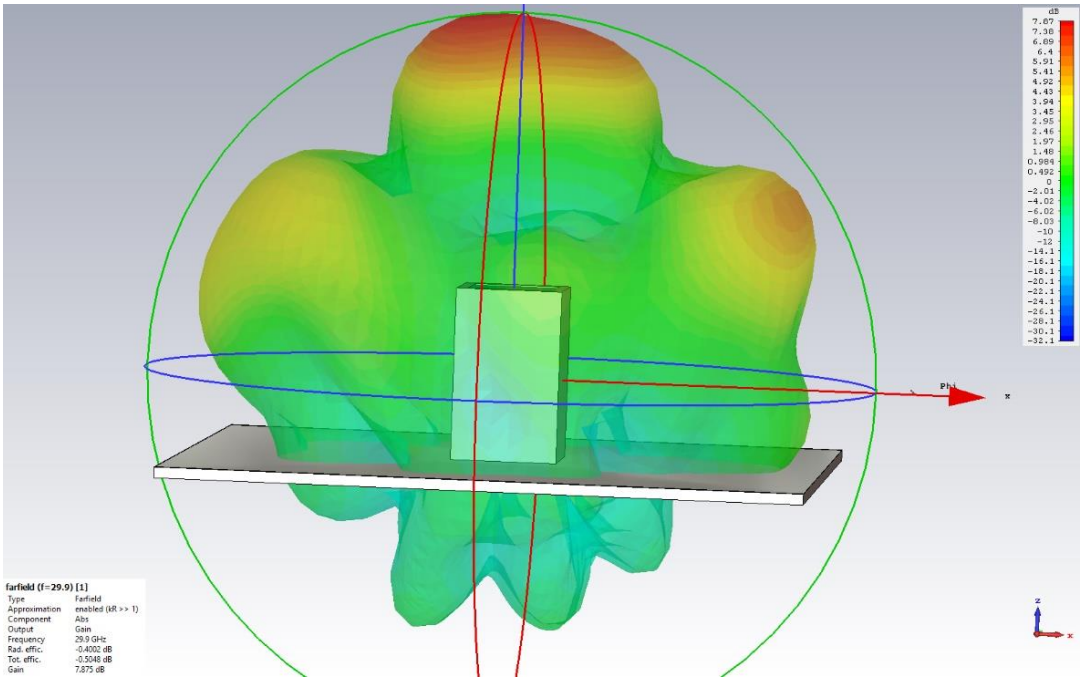

Fig. 16 Simulated 3D radiation pattern for a DRA.

2.4.4. Bandwidth.

Due to the finite geometry of every antenna they are encased to operate within a delimited frequency range, this is known as bandwidth BW which can be described as $BW = fmax - fmin$ with a central frequency fo. Bandwidth will be determined by the system the antenna is applied in. This will also have repercussions to the directivity, polarization, beam width and of course the magnitude of main and secondary lobes etc. A typical bandwidth for DRAs is expected around 10% for optimal performance in order to get the best antenna impedances, reflection coefficients and VSWR possible. Bandwidth is inversely proportional to directivity of the antenna.

2.4.5. Directivity and gain.

This parameter is defined as the ratio between radiated power and power density at a given direction at a given distance towards an isotropic antenna radiating at the same power. The general expression for directivity is given by $D\ (\theta, \phi) = P_r\ (4\pi r^2 / \rho\ (\theta, \phi))$ if an angular direction is not specified then it is assumed that the calculated directivity is the maximum value $D = P_r\ (4\pi r^2 / \rho_{max})$. Directivity is related to the gain expression $G = D\ (\theta, \phi) \times$ eff where eff is the antenna efficiency ($eff = P_r/P_{input}$). Typical values of gain and directivity are around 10 dBi and above as they are expected to be very directional antennas radiating with high intensity towards z axis [63], [64] as discussed in section 2.3.4.

2.4.6. Feed methods.

As mentioned in previous sections, the most recurred methods to feed a dielectric resonator are the aperture feeding where we can generally find two shapes, a rectangular slot and a cross-shaped slots which are most commonly used in hemispherical DRAs. In order to make the slot resonate a microstrip line is placed beneath the slot, creating a 3-layer structure for the feeding network [63], [65], [73] this is presented in Fig. 17. The dielectric resonator will be sitting on top of the slot and therefore create coupling between both elements hence creating resonant modes for the DRA. Microstrip lines can also be placed directly on the dielectric resonator however this will bring metallic loses to the structures [74].

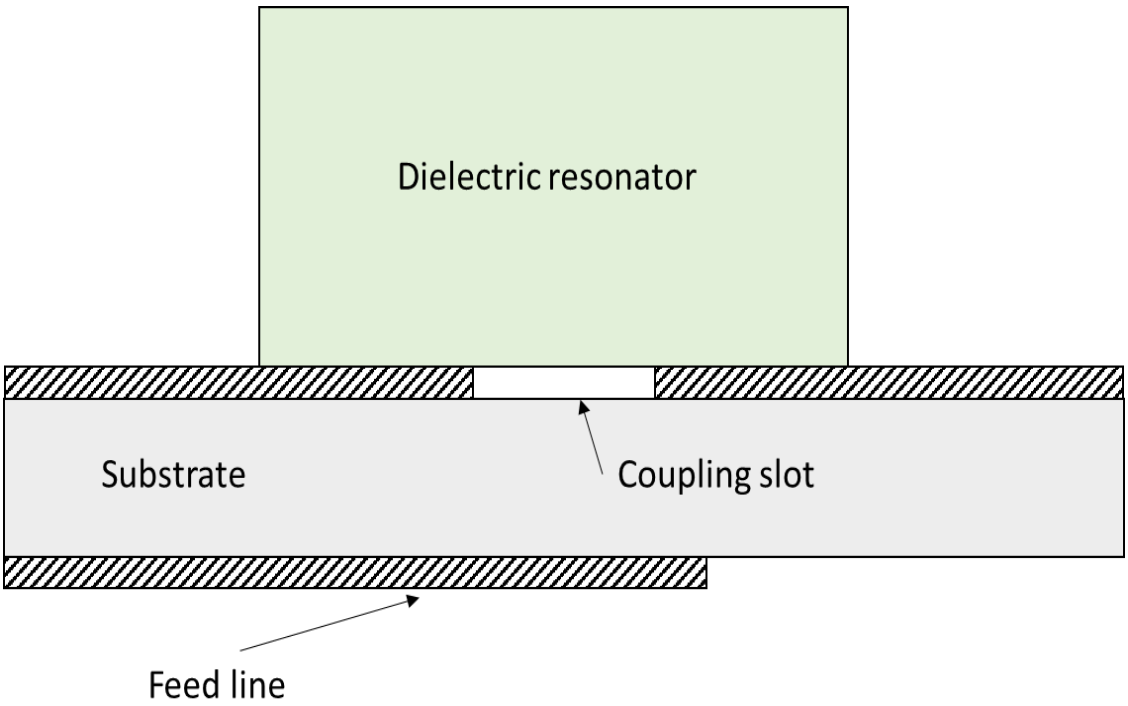

Fig. 17 Rectangular DRA fed by a coupling slot.

The second method is a probe which can be placed in different locations and still manage to feed the DRA. Similar to the microstrip lines they can be placed through a dielectric substrate and a ground plane of the same dimensions. Probes can go through the DRA and bring the input signals directly inside the dielectric resonator walls, nevertheless the metallic part of the probes will increase the losses and will reduce the performance pf the DRA [75]. Fig. 18 presents different locations of the probe in the structure depending on the dimensions of the dielectric resonator, typically probes are placed in the centre of the DRA but they can also be located at l/2, w/2 on an edge of the resonator walls etc. [75].

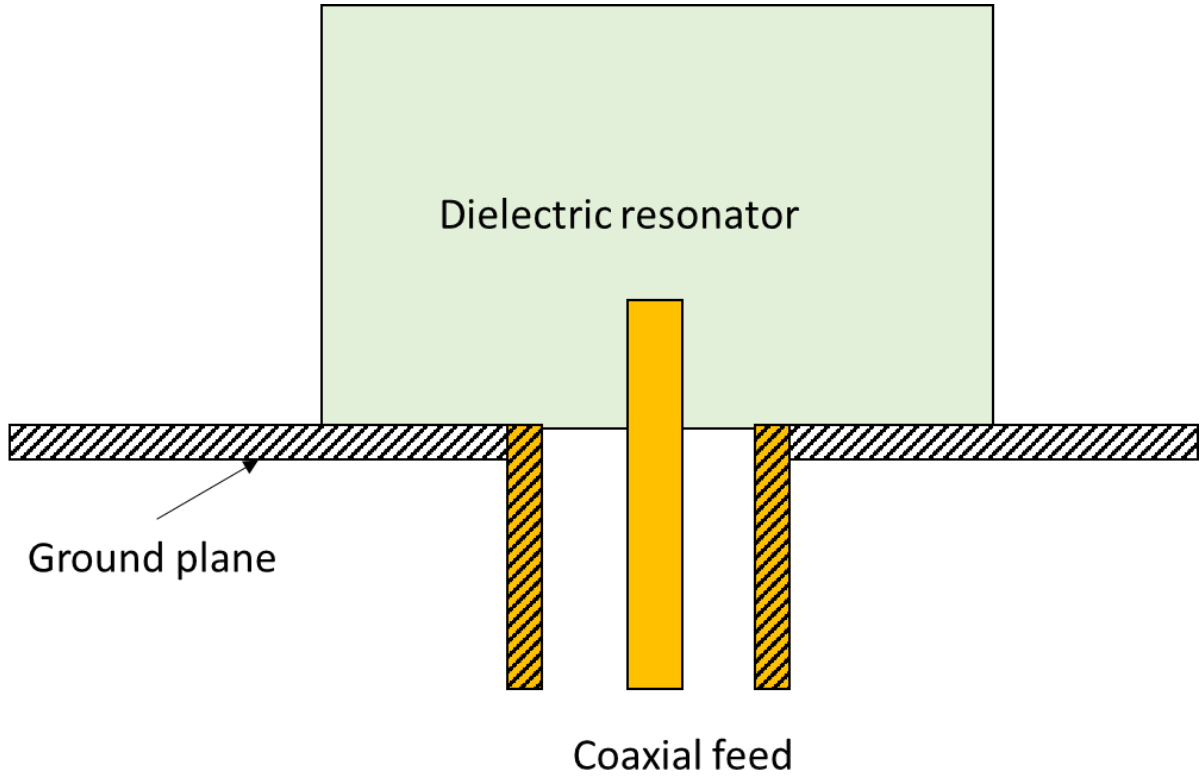

Fig. 18 Dielectric resonator fed by a coaxial probe.

Less commonly, dielectric antennas are fed by coplanar waveguides (CPW) where the apertures are located on the ground plane and printed over the dielectric substrate. One can sit a dielectric resonator on top of the CPW and have decent results, however they present a reduced directivity as the cavities on the ground plane need to avoid unexpected resonators [76]. Fig. 19 presents these structures.

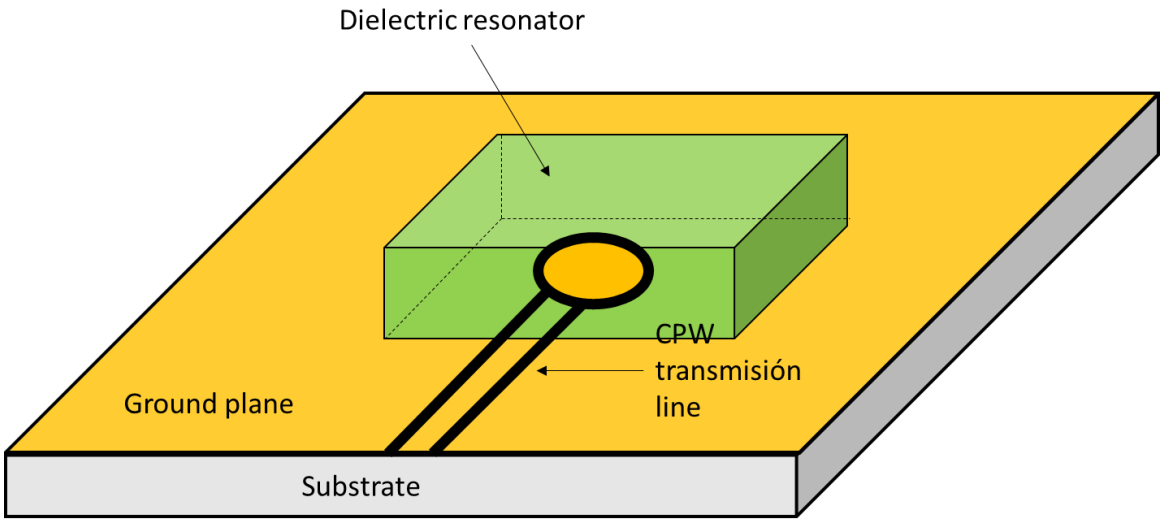

Fig. 19 DRA fed by a coplanar waveguide.

2.4.7. Dielectric waveguide model analysis.

Dielectric resonators can be analysed as waveguides, which are hollow metallic cavities that allow electromagnetic waves to be transmitted between two points in a confined medium. Waveguides are used at microwave frequencies which are commonly from 300 MHz and up to 300 GHz. They are an alternative solution for transmission lines, especially when used in high power applications [77].

Ideally a dielectric resonator presents no conductive losses, hence they can be analysed as lossless waveguides [78]. There is an infinite number of electromagnetic waves that can be propagated through a waveguide and they are known as modes. If a DRA is considered as an ideal (lossless) waveguide with negligible conductivity, permeability μ_0 and permittivity ε_0 and placed over an orthogonal coordinates system with the waveguide going lengthwise over the $\hat{\boldsymbol{z}}$ axis as the direction of propagation with a surface S and contour C of the cross-section of the waveguide [79]. The electric and magnetic fields supported by the guide have the following expressions (7) and (8) :

$$\boldsymbol{E}(r,t) = Re\left[\tilde{\boldsymbol{E}}(r)e^{j\omega t}\right] = Re\left[e_t(x,y) + e_z(x,y)\hat{\boldsymbol{z}}\right)e^{j(\omega t-\beta z)}\right] \quad (7)$$

$$\boldsymbol{H}(r,t) = Re\left[\tilde{\boldsymbol{H}}(r)e^{j\omega t}\right] = Re\left[h_t(x,y) + h_z(x,y)\hat{\boldsymbol{z}}\right)e^{j(\omega t-\beta z)}\right] \quad (8)$$

Where $\tilde{\boldsymbol{E}}(r)$ and $\tilde{\boldsymbol{H}}(r)$ are the phasors related to **E**(r, t) and **H**(r, t). Inside the waveguide **E** and **H** must satisfy the wave equations (9) and (10) which are as follows:

$$\nabla^2\boldsymbol{E} - \mu_0\varepsilon_0\frac{\partial^2\boldsymbol{E}}{\partial t^2} = 0 \quad (9)$$

$$\nabla^2\boldsymbol{H} - \mu_0\varepsilon_0\frac{\partial^2\boldsymbol{H}}{\partial t^2} = 0 \quad (10)$$

Also, a unit vector normal to the waveguide walls must be considered $\boldsymbol{n}]_C = \hat{\boldsymbol{z}} \times \boldsymbol{\tau}$ where $\boldsymbol{\tau}$ is a unit vector tangent to the contour C of the waveguide cross-section. Hence **E** and **H** have the following contour conditions established by equations (11) and (12) as follows:

$$\boldsymbol{E}\cdot\boldsymbol{\tau}]_C = 0 \quad (11)$$

$$\boldsymbol{H}\cdot\boldsymbol{\tau}]_C = 0 \quad (12)$$

These contour conditions have been established due to the fact that the waveguide is assumed to be lossless.

For instance, customising wave equations (9) and (10) for z component and considering the electric and magnetic fields supported by the waveguide given by equations (7) and (8) in the resultant equation we concluded that e_z and h_z ought to satisfy the following differential equations (13) and (14) :

$$\nabla_t^2 e_z + (k_0^2 - \beta^2) e_z = 0 \tag{13}$$

$$\nabla_t^2 h_z + (k_0^2 - \beta^2) h_z = 0 \tag{14}$$

Where $\nabla_t = \nabla - \frac{\partial}{\partial z}\hat{z}$ and $k_0 = \omega\sqrt{\varepsilon_0\mu_0} = \frac{\omega}{c}$ which is the number of plane waves out of a traveling wave through the confined medium. On the other hand, introducing (7) and (8) into the Maxwell equations for **E** and **H** rotational, conclusively, e_t and h_t ought to satisfy the following differential equations (15) and (16) :

$$e_t = \frac{1}{k_0^2 - \beta^2}[j\omega\mu_0 \hat{\boldsymbol{z}} \times \nabla_t h_z - j\beta\nabla_t e_z] \tag{15}$$

$$h_t = \frac{1}{k_0^2 - \beta^2}[j\omega\varepsilon_0 \hat{\boldsymbol{z}} \times \nabla_t e_z + j\beta\nabla_t h_z] \tag{16}$$

Considering these two equations (15) and (16) we can prove that in order to satisfy the contour conditions given by equations (11) and (12) it is required that the following conditions described by equations (17) and (18) are fulfilled.

$$e_z]_C = 0 \tag{17}$$

$$n \cdot \nabla_t h_z]_C = \frac{\partial h_z}{\partial n}\Big]_C = 0 \tag{18}$$

Hence, in order to calculate the modes supported by a waveguide it is need that equations (13) and (14) are customised under the contour conditions (17) and (18). Once ez and hz are calculated et and ht can be obtained as well as the cross-section components of **E** and **H** using equations (15) and (16) [80].

2.4.8. Transverse electric and magnetic modes.

As electric and magnetic fields travel perpendicular to each other and transverse the direction of travel we can classify the propagation modes supported as transverse electric modes (TE modes) and transverse magnetic modes (TM modes) as briefly discussed in section 2.4.1 [78], [81].

TE modes also known as H waves happen when the electric field is transverse to the direction of propagation while the magnetic field is normal to the direction of propagation. For these modes the contour condition $e_z = 0$. In order to calculate these modes, we solve in S the bi-dimensional Sturm-Liouville boundary problem [82] in equation (19) as follows:

$$\nabla_t^2 h_z + k_c^2 h_z = 0 \; ; \; \frac{\partial h_z}{\partial n}\Big]_C = 0 \tag{19}$$

This contains a finite number of auto-functions h_z and auto-values $k_c^2 = k_0^2 - \beta^2$. For TE modes, e_t and h_t are calculated by equations (20) and (21) derived from (15) and (16) .

$$\boldsymbol{e}_t = \frac{j\omega\mu_0}{k_0^2 - \beta^2}\hat{\boldsymbol{z}} \times \nabla_t h_z \tag{20}$$

$$\boldsymbol{h}_t = -\frac{j\beta}{k_0^2 - \beta^2}\nabla_t h_z \tag{21}$$

TM modes or E waves have opposite characteristics to the ones of TE modes, magnetic field is transverse to the direction of propagation while the electric field is normal to the direction of propagation, nevertheless similar to TE modes, the contour condition is $e_z = 0$ and also the Sturm-Liouville boundary problem is required to obtain the modes in equations (22) and (23) as follows:

$$\boldsymbol{e}_t = -\frac{j\beta}{k_0^2 - \beta^2}\nabla_t e_z \tag{22}$$

$$\boldsymbol{h}_t = -\frac{j\omega\varepsilon_0}{k_0^2 - \beta^2}\hat{\boldsymbol{z}} \times \nabla_t h_z \tag{23}$$

With these equations, a prediction of the modes supported by a dielectric waveguide can be accurately carried out. The mathematical determination of the supported modes in a waveguide derive the expressions of the design equations for each of the geometrical variants for dielectric resonant antennas as reviewed previously, these are complex equations involving the essential parameters of DRAs such as the relative permittivity of the selected material and the resonant frequency for the antenna. Approximation equations have also been derived from the described expressions and offer expressions with reduced complexity to obtain approximations of the geometric dimensions of a DRA studied in question. Often these approximations equations have as a result geometric dimensions that might differ from the mode equations but are used as a starting point that can be refined by simulation of prototypes which is an essential step of the conception of a DRA.

2.5. Frequency reconfigurable dielectric resonant antennas.

The versatility offered by dielectric resonator antennas highlight them as excellent alternative solutions to tunable devices in order to offer a multiple range of services simultaneously and with a view to reduce the size of devices as well as optimise the energy performance. The methods used to achieve frequency reconfigurability for dielectric resonators depend on switching from a set of dielectric resonators, choose from different modes using different paths or changing the dielectric constant of dielectric resonators.

Numerous dielectric resonators have been used to achieve a wide frequency range when selecting them using electronic switching. 4 dielectric resonators, each with different dimensions, achieve a frequency range of 1.60 – 2.71 GHz, each resonator holds a relative permittivity $\varepsilon_r = 10$, a set of PIN diodes selects one or multiple dielectric resonators in order to operate simultaneously [83]. Wideband dielectric resonators are also tuned by switching between two bands using a switch to select from an ON and an OFF state, selecting the operating mode of 4.12 GHz and 8.85 GHz respectively, the switch creates a wideband mode by connecting the feed line to create this wideband mode offering impedance bandwidths of 49% and 25% [84]. Coplanar waveguides used as feedlines have used also to feed dielectric resonators, this association have proved to be able to achieve tuning when varying the dielectric constant of the dielectric resonator by selecting a combination of states using two PIN diodes hence selecting feed line paths achieving tuning at three different frequency bands between 3.45 and 6.77 GHz and a maximum impedance bandwidth of 16%, [85] this system is presented in Fig. 20.

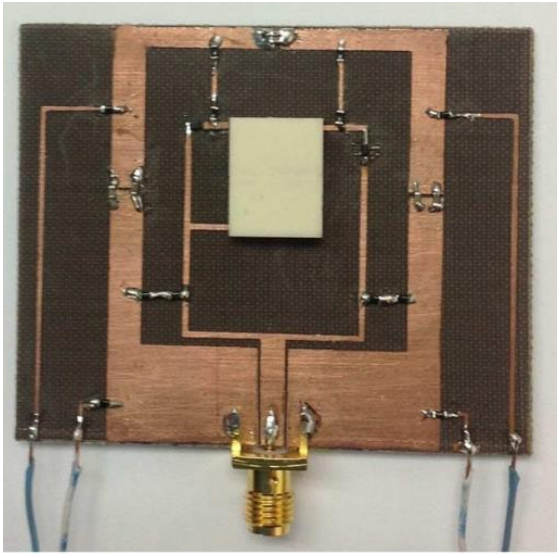

Fig. 20 Reconfigurable DRA fed by a CPW and tuned by PIN diodes [85].

Moreover, on PIN diodes used to select states a U-shaped dielectric resonator antenna sitting over a ground plane can operate in three different modes when a switch selects between an on and an OFF state, when activated, the reflection coefficient and bandwidth are substantially improved, covering a frequency range of 7.5-14.5 GHz depending on the three combinations depending on the switches states OFF-OFF, OFF-ON, ON-OFF providing three bandwidths 32.5%, 25% and 87.25% respectively [86]. Cylindrical dielectric resonators are not very commonly used despite they have a simple design, nevertheless we reviewed a reconfigurable cylindrical DRA or CDRA fed by a couple aperture, this device achieves its reconfiguration using two diodes and selecting states, selecting the operative modes for Wi-Fi (when D1 on and D2 off) and WiMAX (when D1 off and D2 on) covering a frequency range of 3.29 – 5.5 GHz [87]. Parasitic elements such as small metallic strips can be introduced in a DRA in order to achieve its reconfigurability, conical DRAs are less commonly used but offer a versatile shape offering versatile applications space wise, in reviewed works switches have also been used to select from different states in which they control the length of the parasitic metallic elements in order to create a reflective effect and achieving three different modes which are two unidirectional and one bidirectional modes and offering a frequency cover range of 8.96 – 10.51 GHz. [88].

2.6. Conclusions for Chapter 2.

In conclusion for this chapter 2, the reviewed reconfigurable antennas both slot and DRAs offer adaptive performance with a view to fulfil the demanding and rapidly changing requirements for 5G. Discrete antennas are now implemented in mobile communication equipment offering frequency agility, operation in multiple frequency bands simultaneously and often present miniaturisation as well as reconfiguration either in frequency or pattern. The use of components such as PIN diodes and varactor diodes which allow the electronic control of the operation of the system. Moreover, multiple antennas working simultaneously in the same system is a recurrence in the current approaches developed in industry and academia. Appropriate calculations determine the suitability of a diversity scheme introduced in a communication system have been carried out in most of the reviewed articles. For the reviewed dielectric resonator antennas an appropriate range of frequencies covering a number of existing services a such as Wi-Fi, WiMAX, Bluetooth, and mm-wave applications have been reviewed. In terms of frequency agile DRAs the fewer works present in industry and academia are based in mechanisms that select from different DRAs to cover a chosen service or the combination of certain blocks operating simultaneously.

Despite the incursion of novel antennas implemented in communication systems there are many aspects that are not addressed and could be beneficial for further investigation and for the development of equipment that can fill the gaps as well as offer the desired adaptive performance. The slot antennas reviewed often presented a gradual control of its frequency response when incorporating varactor diodes and Multiband slot antennas have been reviewed offering simultaneous frequency agility without altering the rest of the unchanged resonators. However, the frequency reconfiguration could be benefited from adding more antennas in the same system and studying its effect through the appropriate calculations such as the diversity parameters reviewed in MIMO antennas. Therefore, in order to address this lack of multiple independently reconfigurable devices and their respective diversity study, I propose the development of a MIMO independently tunable antenna as discussed in the objectives of this Thesis.

Finally, concerning the reviewed articles presenting innovative dielectric resonator antennas in their reconfigurable forms often present a selection system based in electronic switching. Reconfigurable DRAs basically depend on additional circuitry to reconfigure their operating modes which introduces more metallic structures and consequently more metallic losses could be introduced at mm-wave frequencies. Due to the absence of dielectric resonant antennas offering reconfiguration through less invasive mechanisms and incorporating the use of novel materials and substances such as the reviewed in this chapter, the proposal of developing a tunable DRA using innovative materials with adaptive and controllable properties.

CHAPTER 3. SIMULATIONS, MANUFACTURE AND MEASUREMENTS OF INDEPENDENTLY TUNABLE TRIPLE-SLOT 1×2 MIMO ANTENNAS

Three different reconfigurable MIMO antennas are presented in this chapter. Three different printed circuit boards consisting of a 1×2 array of three varactor-loaded slots controlled by DC voltage biasing lines. Each unit board has different positions of the elements, specifically for the second array of three slots in the system. However, each triple-slot antenna offers three independently tunable frequency bands which potentially highlights these innovative devices as 1×2 MIMO antennas which with the correspondent metrics could be analysed to be compatible for use in future 5G applications.

3.1. Design process for a 1×2 triple-slotted antenna.

The Communications group of the Electronic and Electrical Engineering department of the University of Sheffield have developed a frequency agile antenna offering three independently tunable slots for cognitive radio applications [30]. This device is constituted by three slots on a copper ground plane printed over a FR-4 substrate measuring 100 × 50 mm ×1.6 mm with a relative permittivity of ε_r = 4.3. Two of the slots are horizontally orientated and parallel to the **x** axis separated by 4 mm and 6 mm away from the top edge of the board. The third slot is vertically orientated, parallel to **y** axis and separated by 2 mm form the top edge of the board. Each of the three slots is fed by a single microstrip line. The slots are in the top edge of the ground plane and distributed as shown in Fig. 19 (a) and the feed line view in Fig. 19 (b). this is a relatively reduced size for a tunable antenna, making it a compact solution for versatile applications. In terms of the performance of this antenna we find a very useful yet not explored feature of independent tuning. It is known that length of slots is geometrically described by $\lambda = \frac{c}{f}$ and hence the length of slot is $L = \frac{\lambda}{2}$.

It is considered that once a load is placed on a slot antenna, we can consider it as a transmission line, dividing the impedance of the slot into Z_1 and Z_2 corresponding to the proportional impedances depending on the position of the load. Fig. 21 shows the transmission line model of a loaded slot where the division of Z_0 into Z_1 and Z_2 with the following condition $Z_1 + Z_2 = 0$ to be fulfilled.

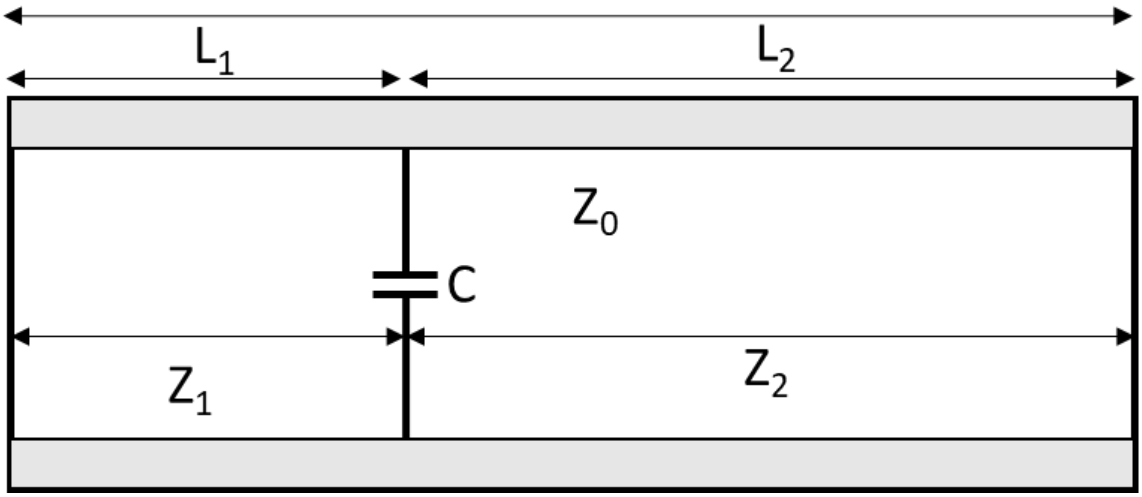

Fig. 21 Transmission line model of capacitive-loaded slot.

Once the input impedance is being split into Z_1 and Z_2 and can be calculated using the following expressions (24) – (26).

$$Z_1 = \frac{jZ_0 \tan(\theta-\theta_1)}{1-\omega C Z_0 \tan(\theta-\theta_1)} \quad (24)$$

$$Z_2 = -jZ_0 \cot(\theta_1) \quad (25)$$

$$\theta = \beta(\omega)L, \theta_1 = \beta(\omega)L_1 \quad (26)$$

Where Z_0 is the slot antenna impedance, ω is the angular frequency corresponding to $\omega = 2\pi f$, L is the total slot length, β(ω) is the propagation constant, C is the capacitance value of the varactor, this capacitor position splits the impedance of the slot in two partitions of lengths L_1 and L_2 to the left and to the right of the varactor respectively. The slot line frequency is therefore related to the width of slot, thickness of the substrate, and relative permittivity ε_r of the substrate. The resonance condition can be expressed as shown in equation (27), using equations (24) – (37).

$$\tan(\theta-\theta_1) - \cot(\theta_1) + wCZ_0 \tan(\theta-\theta_1)\cot(\theta_1) = 0 \quad (27)$$

Equation (27) shows that the resonant frequency of the slot antenna depends on the capacitance value C and position L_1. Therefore, the frequency tuning is achievable by controlling these parameters and specifically C which can electronically tuned using a DC biasing circuit. The slot antenna offers three frequency bands, each of them independent of each other, which means, if a band is tuned, the remaining bands will stay unaltered. This antenna achieved frequency reconfiguration using the reviewed technique of loading slot lines with tunable capacitors. The capacitors loading the slots are positioned in the left edge of the board for slot

1 and in the middle of the slots 2 and 3. The varactor diodes were controlled by a DC bias circuitry composed by the variable capacitors themselves, DC block capacitors and RF choke inductors in order to avoid external interferences that can reduce the optimal levels of performance. The input voltage for this biasing circuitry varied from 3.0 V and up to 30 V and achieved to tune the capacitors from 4.0 pf and up to 0.5 pF respectively, this device achieved a tunable frequency range of 0.6 GHz – 1.12 GHz for slot 1, 1.04 GHz – 2.47 GHz for slot 2 and 1.89 GHz – 2.70 GHz for slot 3. Tunable capacitors C1, C2 and C3 were placed in their correspondent slots as showed in Fig. 22 (a) for the slots view and Fig. 22 (b) for the feed line view.

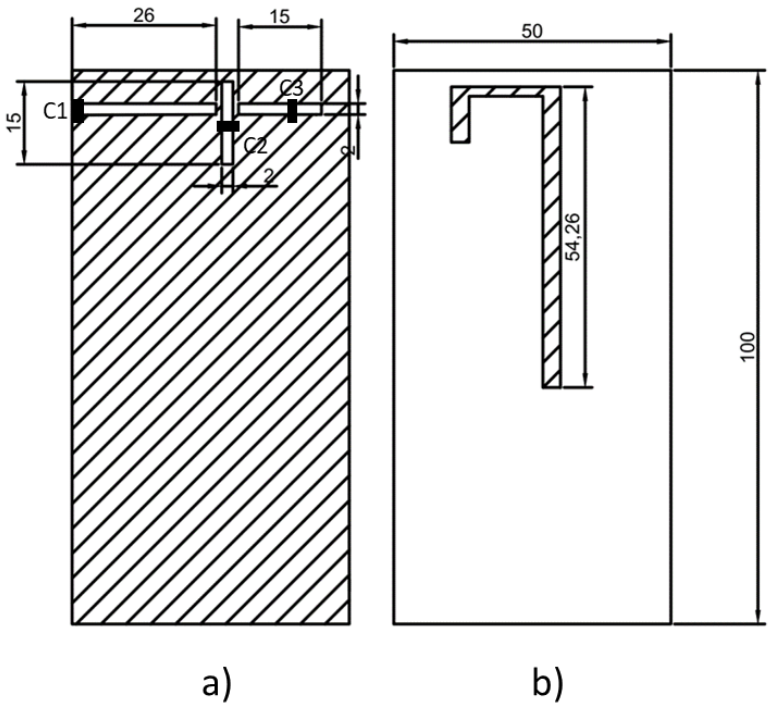

Fig. 22 front and back views from the prototype [30].

In addition to frequency agility achieved by tunable capacitors, this antenna offers omnidirectional patterns and optimal operational metrics. The highlighted features of this work are the frequency agility and the independent tuning of each capacitor-loaded slot. Fig. 23 shows the measured reflection coefficients for this antenna when a band is tuned and the remaining two are without change. This device offers a frequency range of 0.6 GHz – 1.12 GHz for slot 1, 1.04 GHz – 2.47 GHz for slot 2 and 1.89 GHz – 2.70 GHz for slot 3 when different voltages are applied to the tuning capacitors. In the same work, it was discussed the use of digitally tunable capacitors (DTCs) instead of the variable capacitors C1 – C3. The incorporation of DTCs represented a significant improvement of gain when compared to the

triple-slot antenna using varactors. However, the tuning achieved remained independent for each frequency band and the frequency cover ranged was similar.

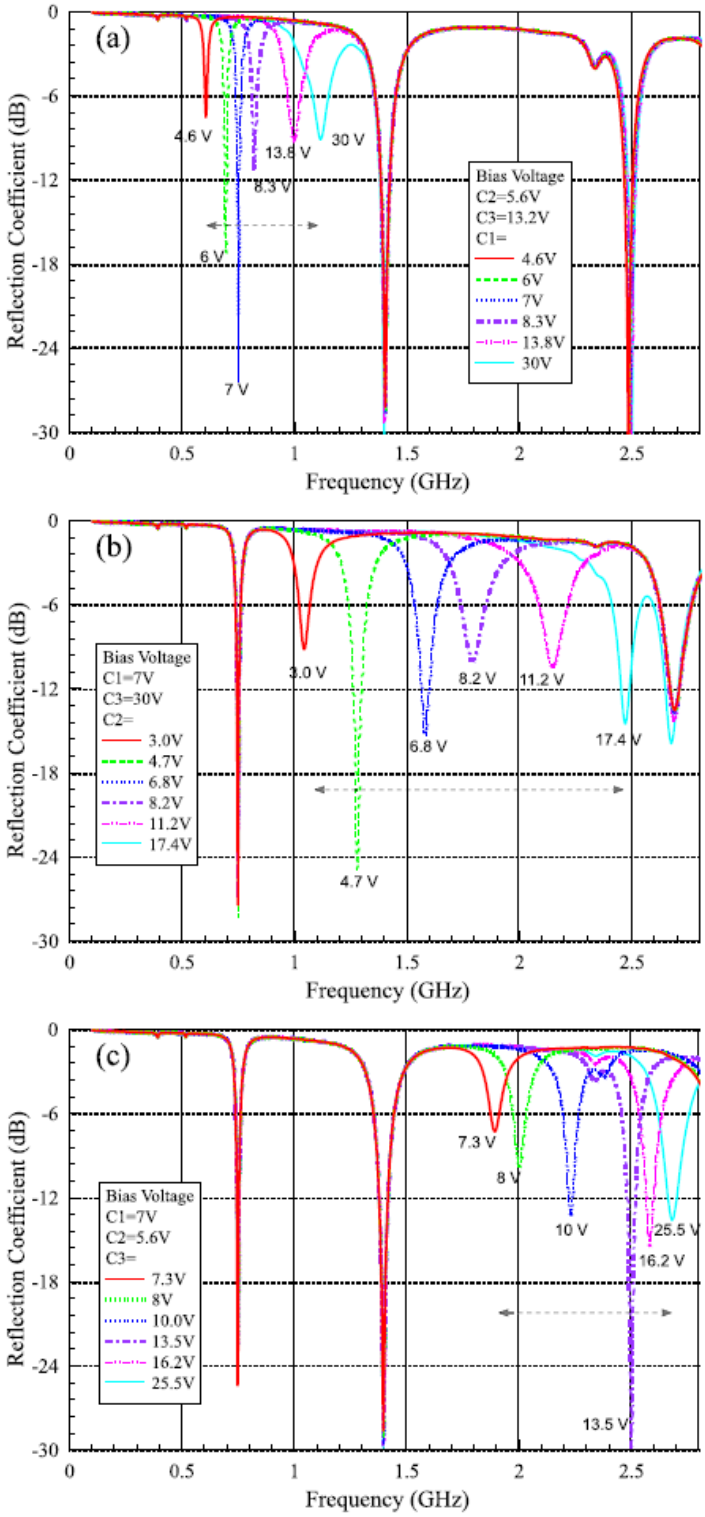

Fig. 23 Tuning ranges for the three independently tunable slots in the antenna [30].

In this approach, the work discussed in this chapter describes three different 1×2 MIMO antennas following the original model [30]. We have duplicated the triple slot antenna and placed it in the same board in such a way that we have a 1×2 triple slot antenna each offering the same independently tunable features. The aim of these experiments is to demonstrate that the independent tunability of multiple elements in the same board can be achieved by similar structures coexisting in the same board as well as an appropriate assessment of the mutual coupling between the antennas in each board. Specifically speaking, two triple-slot antennas can achieve independent tuning and not only achieve independent tuning among their slots but also between both arrays in the same board regardless of their position in the antenna geometry.

3.1.1. Addition of a second antenna in the PCB.

It has been demonstrated that a set of slot antennas that control their frequency tuning range using a DC circuitry network achieved independent tuning [30]. The main objective of this chapter is to demonstrate that not only a single triple-slot reconfigurable antenna can achieve independent tuning for each slot but also a double array of slots can still offer independent reconfiguration from one antenna to the other. The original antenna has been duplicated and placed over a PCB board measuring 100 × 50 mm ×1.6 mm. In order to explore different positions of multiple antennas coexisting in the same board we propose the following prototypes naming them MIMO 1, 2 and 3. As they will be later analysed for MIMO metrics in chapter 4 given they can be considered 1×2 MIMO triple-slot antennas. These three prototypes are superficially described in Fig. 24 (a) for MIMO 1, Fig. 24 (b) for MIMO 2 and Fig. 24 (c) for MIMO 3 each of them indicating Antennas 1 and 2.

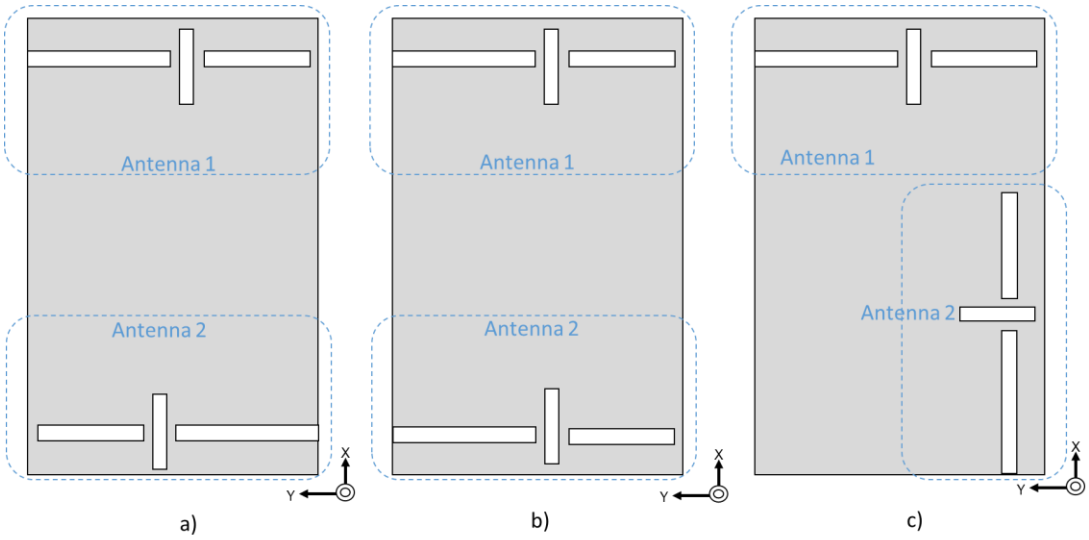

Fig. 24 Antenna distributions in PCB for each prototype.

3.1.2. Prototype MIMO 1.

Firstly, for prototype number one, the original antenna is kept on top of the board, keeping the same dimensions for slots 1, 2 and 3, fed by a single microstrip transmission line. An identical set of elements is then located at the bottom of the board; however, this array is reversed symmetrical to X axis. Slots 1 and 3 keep their dimensions corresponding to the original design, 26 mm × 2mm and 15 mm × 2 mm respectively, which are the horizontally oriented slots. Slot 2 is vertically oriented measuring 15 mm × 2mm and separated 3 mm from the top edge of the board. Slots in second antenna will hence have the same dimension as Slots 1 – 3 but will be named as Slot 1a, Slot 2 a and Slot 3a. Fig. 25 (a) shows the slot view of this prototype whereas Fig. 25 (b) presents the feed lines view.

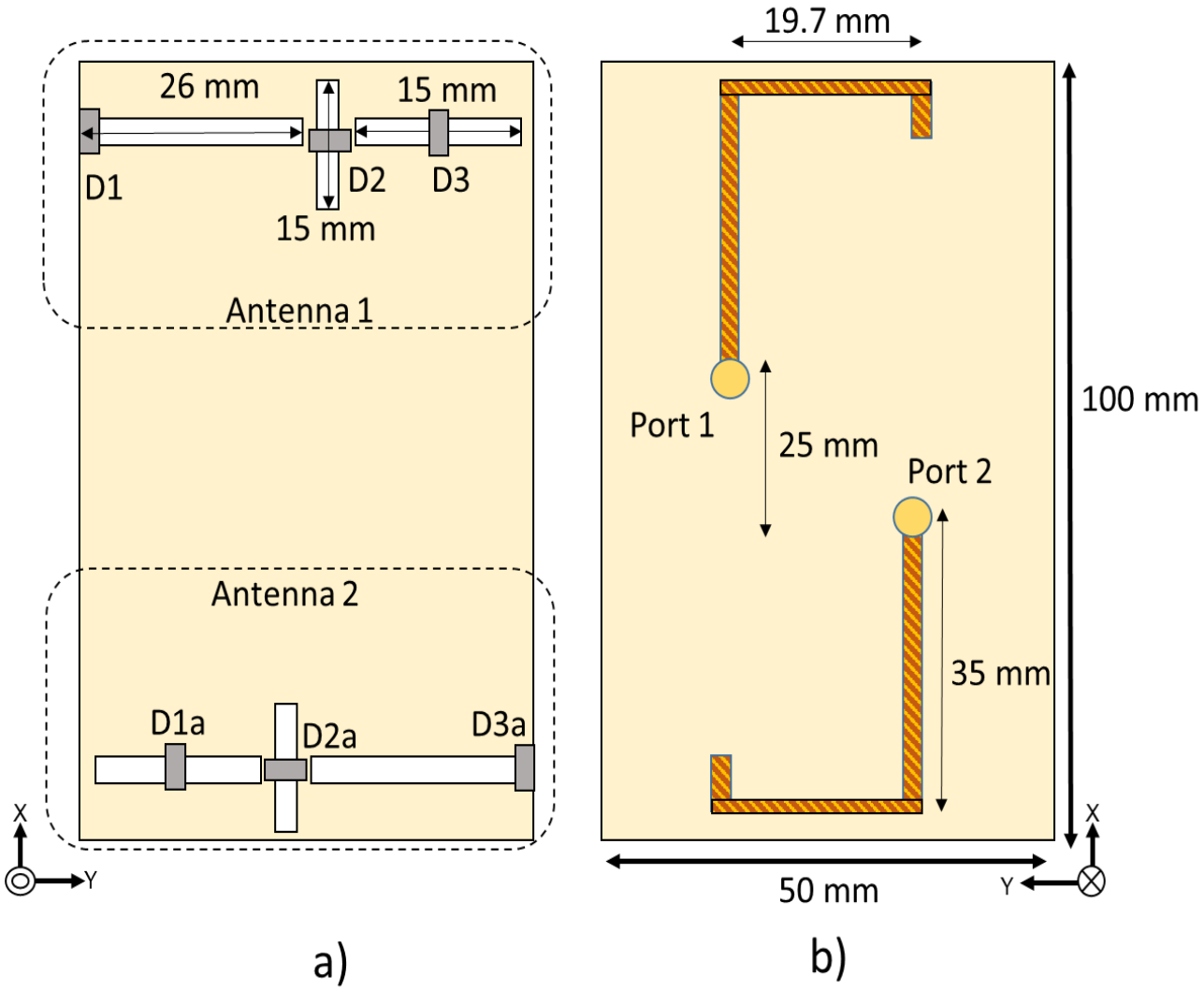

Fig. 25 Views of design of MIMO 1.

3.1.3. Prototype MIMO 2.

Secondly, the next prototype has also an antenna on top and another one at the bottom, however, Antenna 2 in this board is mirrored symmetrically to the top antenna, and so are Slots 1a – 3a. Which is different from MIMO 1 where Antenna 2 is reversed. This board is named MIMO 2 and is shown in Fig. 26 (a) for its ground plane view and in Fig. 26 (b) for its feed lines views.

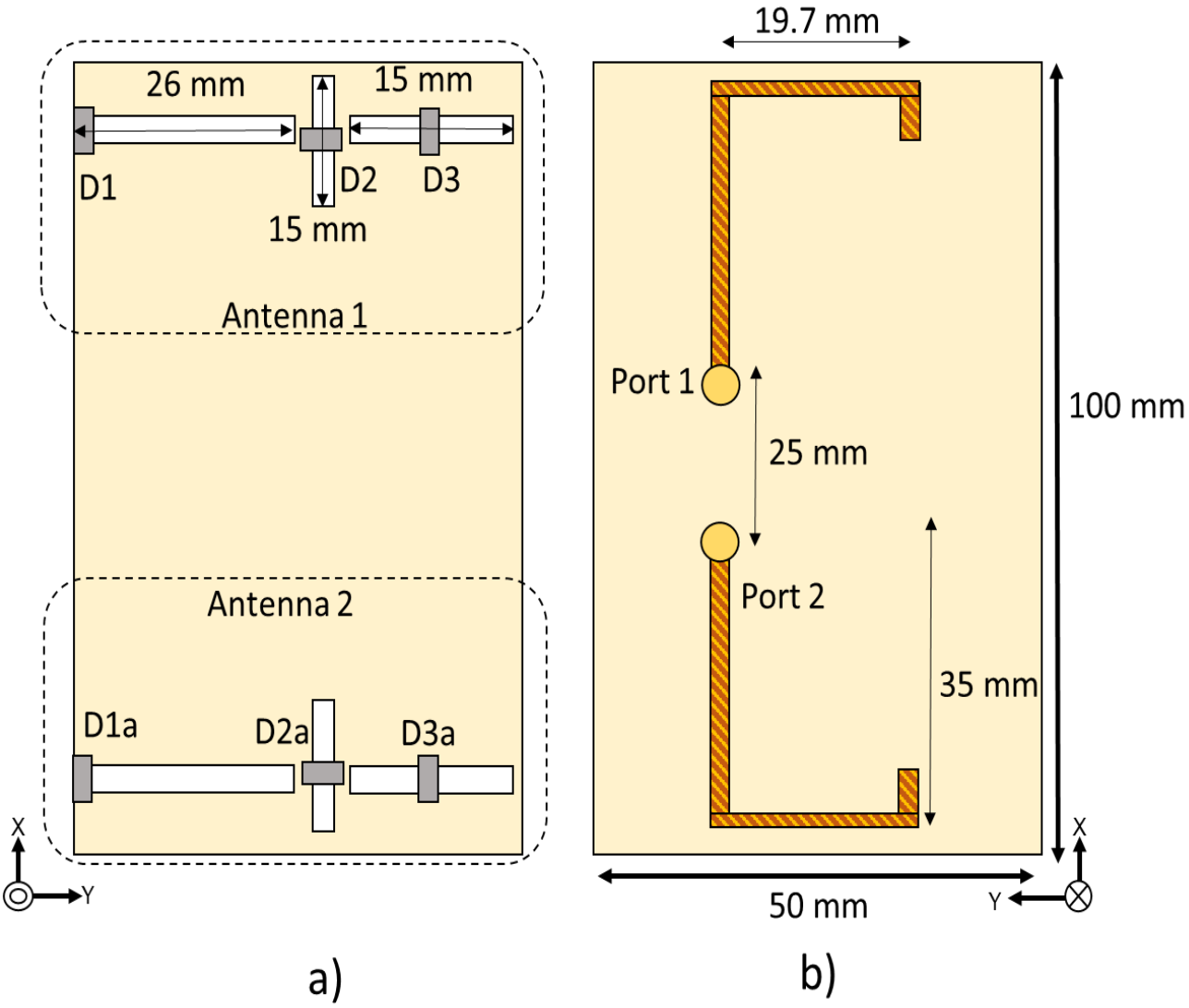

Fig. 26 Views of design of MIMO 2.

3.1.4. Prototype MIMO 3.

Finally, the third board, always keeping the original antenna (Antenna 1) on top, holds the Antenna 2 on the right side of the board but rotating 90° clockwise both slots and feed line. keeping a gap between the vertically oriented (in this case horizontally oriented after rotation) and the right edge of the board of 2 mm. This prototype explores the lateral positions of the triple-slot antenna and we will study the performance of two of these arrays coexisting in the same board and polarised differently. Sequentially, this third prototype is named MIMO 3. Fig. 27 (a) presents its ground plane views whereas Fig. 27 (b) shows the feed lines views.

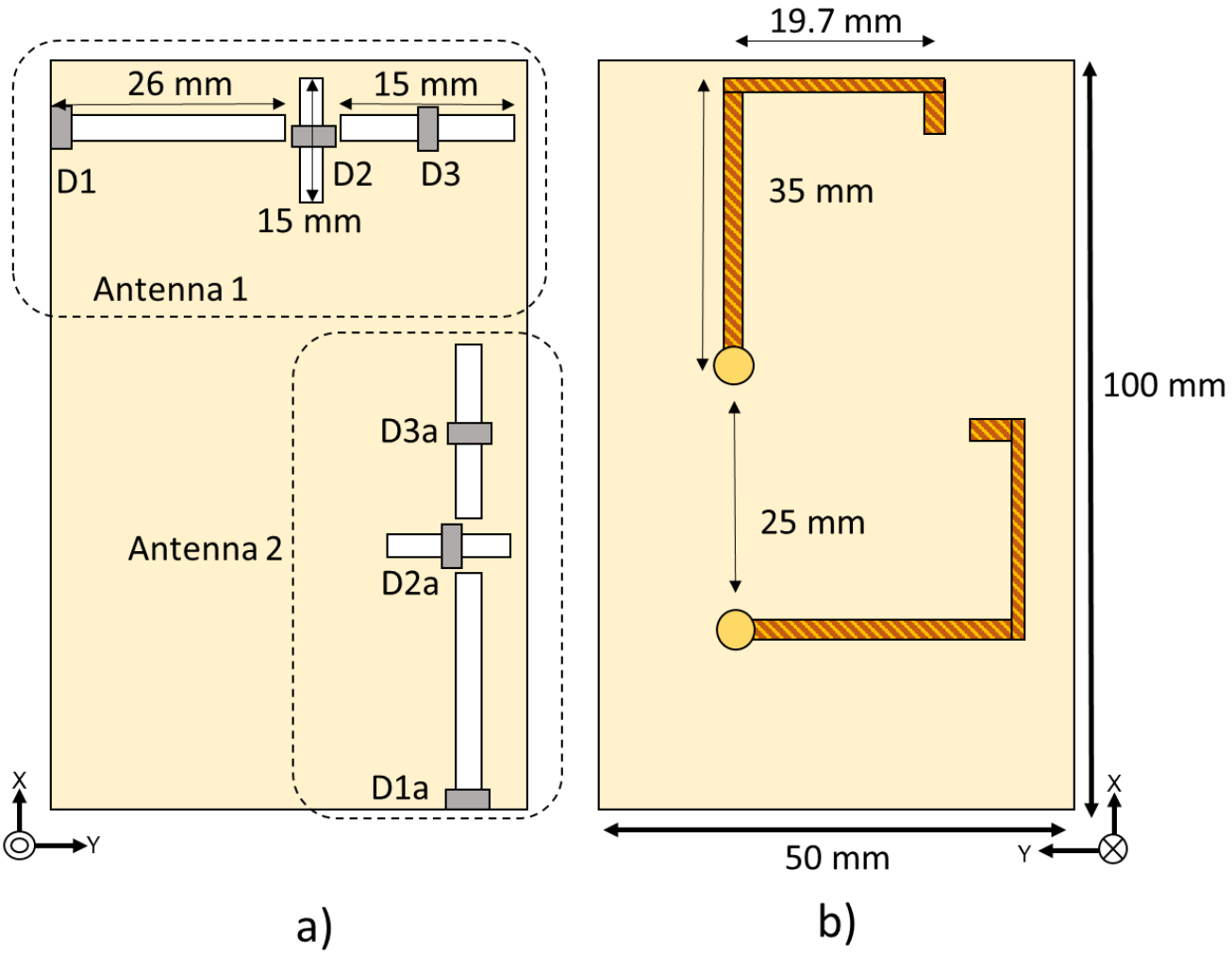

Fig. 27 Views of design of MIMO 3.

The separation between the feed lines for the three prototypes aim to achieve an appropriate isolation, near 25-30 dB which must be corroborated by simulation and eventually measurements.

3.2. Simulation methodology.

An essential step in the design process of a reconfigurable antenna are the simulations of the prototypes designed in order to optimise it before proceeding to manufacture and therefore avoid unexpected fabrication costs and waste of resources. For our simulations the software package used to perform the correspondent simulations was CST Microwave Studio which is a very useful software that calculates accurately the resonant frequencies of structures, as well as radiation patterns, efficiencies and surface current distributions. We began the simulation process by reproducing the antenna system from [30] starting with a FR-4 substrate measuring 100 × 50 ×1.6 mm, then using a copper ground plane over the substrate and creating both sets of slots Antennas 1 and 2 in their respective positions as described in section 3.1. also, the feed lines were created over the opposite faces of the boards and then a model for each board MIMO 1 – 3 has been created. Fig. 28 (a) shows the model created in CST for MIMO 2 with its correspondent dimensions in its feed line view and Fig. 28 (b) shows the slots distributions.

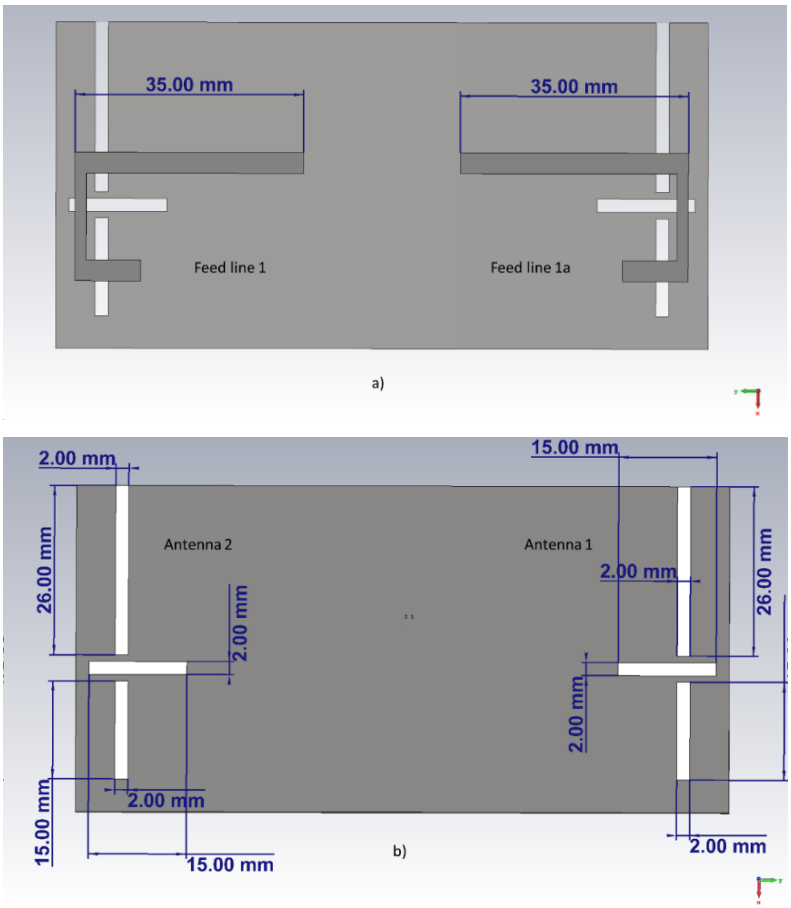

Fig. 28 Views of model created for MIMO 2 prototype in CST Microwave Studio.

3.2.1. Model of DC biasing circuitry components.

Furthermore, in simulation, an accurate model to allocate the components of the DC biasing circuitry that will control the varactor diodes had to be designed. The slots original structure will be therefore slightly modified in order to fit the components the slots biasing circuity and varactor diodes.

After reviewing many options, the varactor Infineon BB833 was selected to be incorporated in the slots. This varactor diode offers a capacitance range from 0.5 pF to 10 pF when varying the input voltage from 30 V to 0 V respectively which is an appropriate range to explore. In order to control the input voltage in the varactors without being affected from external distortions from undesired RF signals a DC biasing network containing inductors acting as RF chokes has been implemented. Inductors allow only the DC pass and will block every other signal, including external high frequencies. Fixed capacitors used as DC blocks and of course the DC voltage source applied to the varactor diodes. This biasing network is shown in Fig. 29.

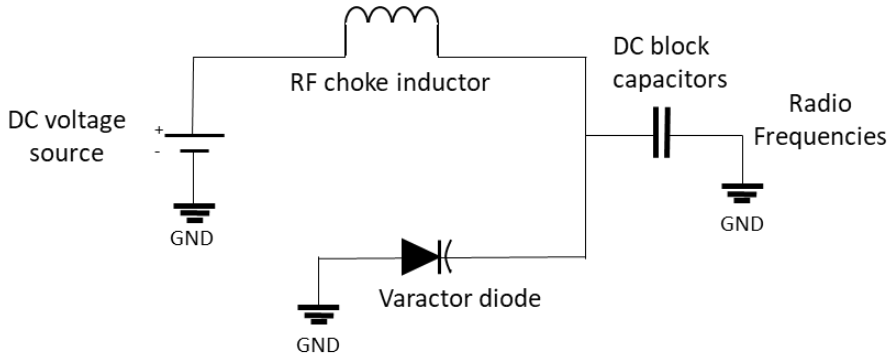

Fig. 29 Electronic diagram of DC biasing network to control varactor diodes.

This biasing network and its components will be allocated within each slot structure. A metallic pad was created to be the feeding point of the DC voltage that will control the varactors. This pad was separated by a gap of 2 mm in order to isolate it from the ground plane, acting as the connection node of the varactor diode which then will be connected to the ground plane and the DC block capacitors. Then in the opposite face of the board, near the feed lines, another pad will be allocated along with a metallic bias connecting it with the one in the ground plane. This second pad will be connected to the RF choke inductor and this last one to the DC voltage line. This distribution was carried out for each slot.

Fig. 30 (a) shows the ground plane view of this connection and Fig. 30 (b) the feed line view of the slot structure including the DC bias network components.

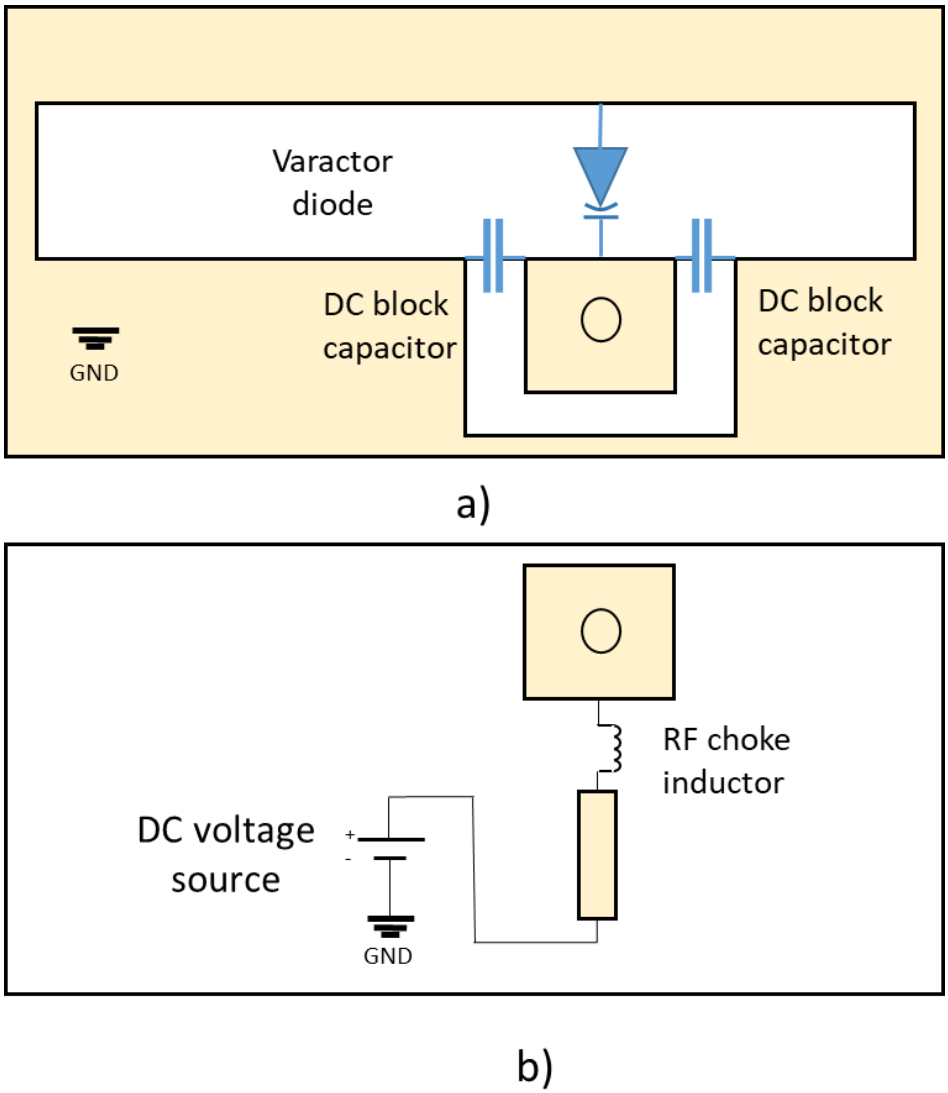

Fig. 30 Schematic allocation of components of DC biasing network.

In order to properly dimension the components of this network and place them on the board it was imperative to calculate the proper values for RF choke inductors and DC block capacitors including the packages dimensions. Referring to the reactance expressions, X is a magnitude that describes the opposition of capacitive and inductive loads face to electric current and depends on the frequency of the signal. Reactance is given by the expression $X = X_L - X_c$ where X_L is the inductive reactance and X_C is the capacitive reactance given by $X_L = 2\pi f L$ and $X_C = \frac{1}{2\pi f C}$ respectively, with L and C as the inductance and capacitance values.

Based on the frequency ranges obtained in the original work one can consider the peak values for each band 1.12 GHz for band 1, 2.47 GHz for band 2 and 2.70 GHz for band 3 and in order to determine the values for L and C in the biasing network. In practice, when working in high frequencies one aims for high values of inductive reactance and low ones of capacitive reactance. After reviewing commercial values for inductors and capacitors in the market the selected values were for RF choke inductors L = 560 nH and DC block capacitors C = 380 pF and corroborated them using the reactance expressions as follows:

X_c values < 1 Ω:

Band 1 f_{max} value 1.12 GHz, C = 300 pF, $X_C = \frac{1}{2\pi fC} = \frac{1}{2\pi(1.12\ GHz)(380\ pF)} = 0.473\ \Omega$

Band 2 f_{max} value 2.47 GHz, C = 300 pF, $X_C = \frac{1}{2\pi fC} = \frac{1}{2\pi(2.47\ GHz)(380\ pF)} = 0.214\ \Omega$

Band 3 f_{max} value 2.70 GHz, C = 300 pF, $X_C = \frac{1}{2\pi fC} = \frac{1}{2\pi(2.70\ GHz)(380\ pF)} = 0.196\ \Omega$

X_L values > 1 KΩ:

Band 1 f_{max} value 1.12 GHz, L = 500 nH, $X_L = 2\pi fL = 2\pi(1.12\ GHz)(560nH) = 3518.58\ \Omega$

Band 2 f_{max} value 2.47 GHz, L = 500 nH, $X_L = 2\pi fL = 2\pi(2.47\ GHz)(560nH) = 7759.73\ \Omega$

Band 3 f_{max} value 2.70 GHz, L = 500 nH, $X_L = 2\pi fL = 2\pi(2.70\ GHz)(560nH) = 8482.30\ \Omega$

As the calculations proved, the chosen values for L and C achieved low reactance values in the order of < 1 Ω for X_c and high reactance values in the order of > 1 KΩ for X_L.

Once the value of components had been determined we allocated the space they would occupy in the board and distributed them by knowing their dimensions. Varactor diodes BB833 are available in package SOD-323 measuring 1.7 mm × 1.25 mm and two terminals of 0.8 mm × 0.6 mm covering a total are of 2.5 mm × 1.25 mm. DC block capacitors and RF choke inductors are both available in package 0603 measuring 1.6 mm × 0.8 mm. In order to fully assess the effects of the components in this biasing network the corresponding self-resonance frequency (SRF) must be considered as well. This SRF is the frequency associated to the internal and parasitic inductances and capacitance of their respective components. Every component can be considered as a LC equivalent circuit, the corresponding value for this is given by $SRF = \frac{1}{2\pi\sqrt{LC}}$. Although the values for RF chokes and blocking capacitors has been superficially calculated without including the effect of SRFs for each component, an

appropriate assessment for this must be carried out in future work derived from this precedent. The footprint of these components was included in the CST models with their corresponding dimensions. Fig. 31 (a) shows the ground plane view and Fig. 31 (b) the dimensions of the gaps created in both faces and the DC voltage feeding lines for each slot structure. The biasing metallic element connects both pads, each pad has a perforation of 0.8 mm of diameter. The footprint of components was achieved as vacuum blocks with the dimensions of components were placed on the CST model.

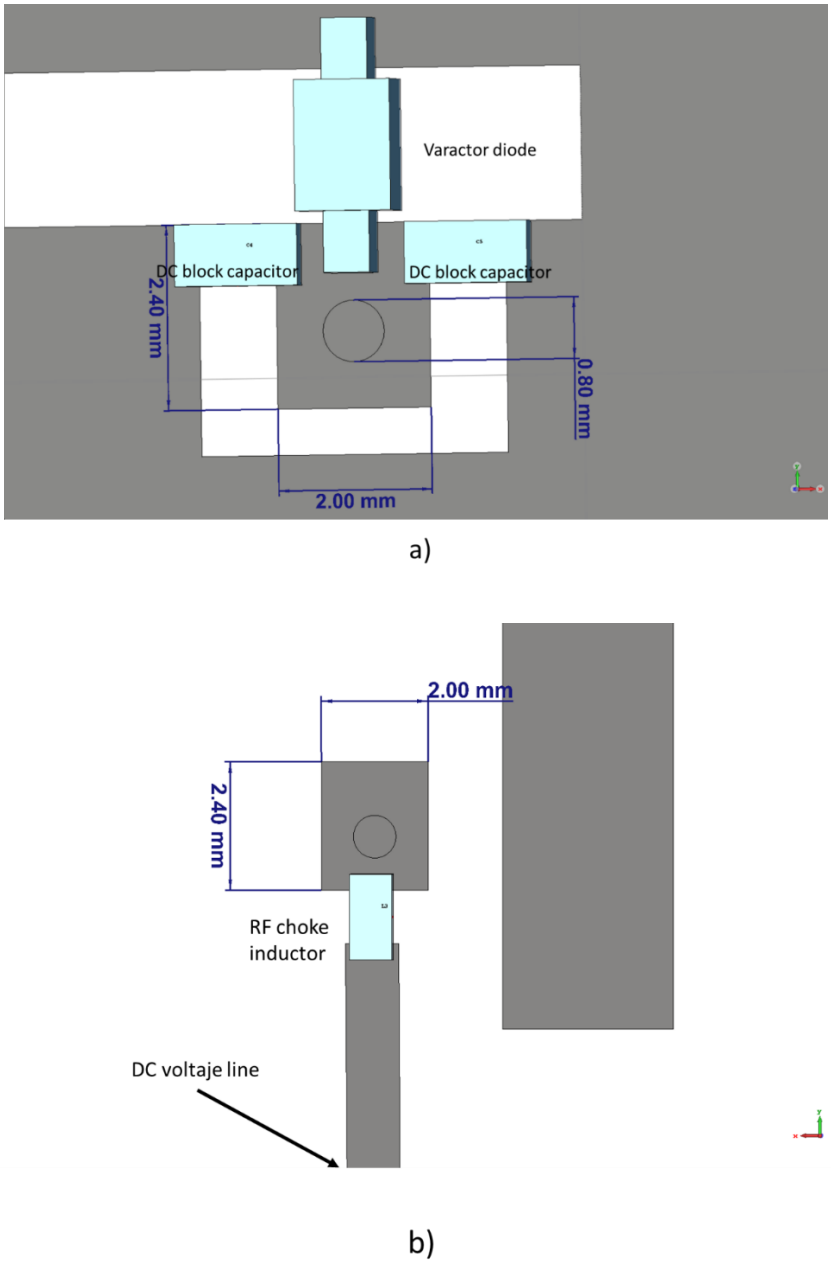

Fig. 31 Detailed views of components, gaps and pads created on the simulated model.

The varactor diodes, DC block capacitors and RF choke inductors were modelled as RLC lumped elements with their respective properties and values. Internal inductance and resistance were replicated for the varactor diode after consulting the Infineon BB833 datasheet. While capacitors and inductors were just assigned their corresponding value.

Two methods to model the components were carried out as the CST software suite offers to create point to point and edge to edge lumped RLC elements. Firstly, the method of point to point lumped RLC components was assessed in the simulator. For this method only two points of the geometrical space are required, they are easy to create, faster to analyse but less accurate in terms of results as it provides a superficial estimation of the magnitude simulated from one point to other in the antenna geometry. Fig. 32 shows the allocation of the elements for both faces of the board.

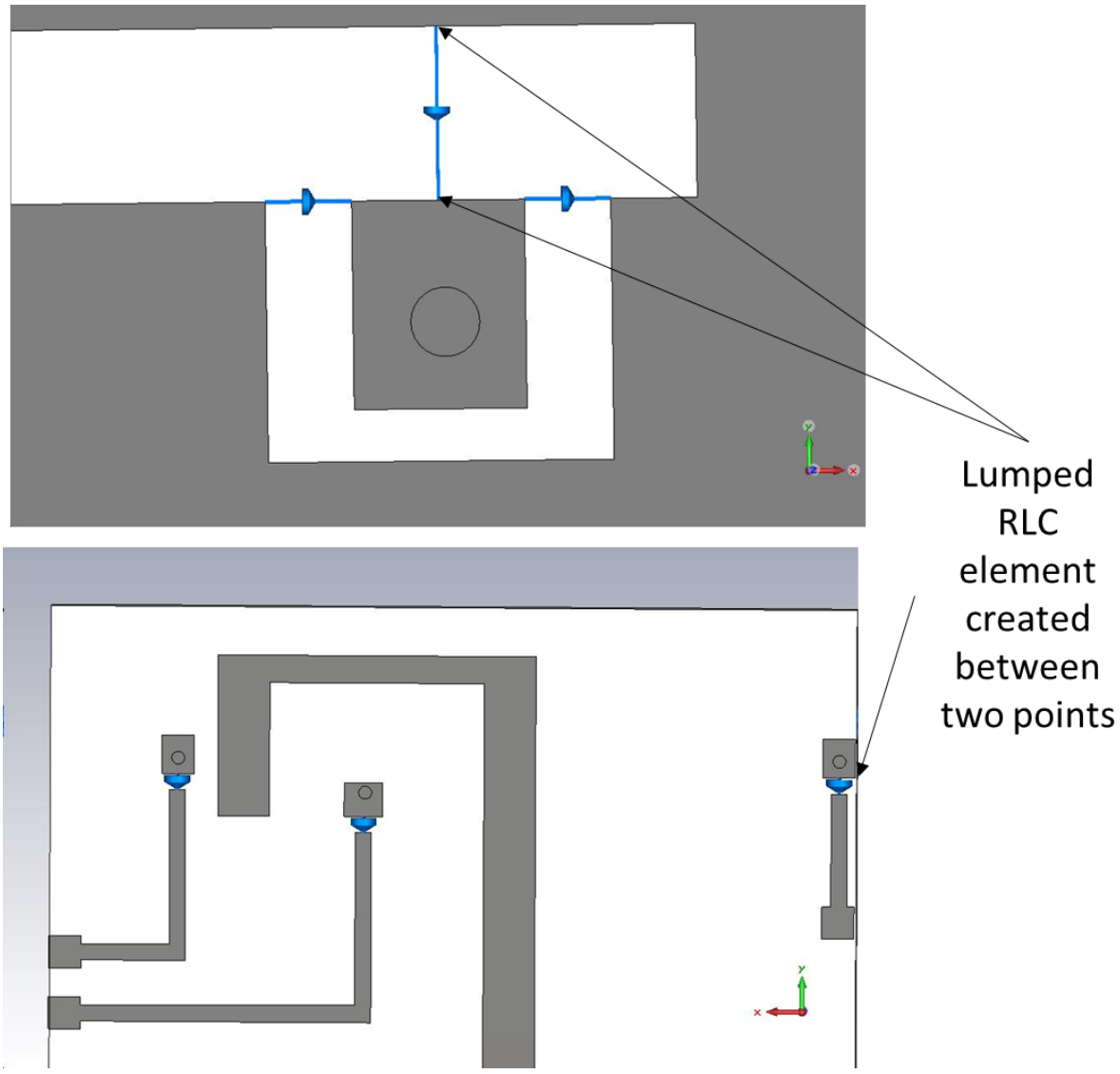

Fig. 32 Modelling of point to point lumped components in simulator.

On the other hand, the creation of edge to edge components required a physical model of the real components in the boards, for this purpose, the vacuum blocks created for the component's footprint holding the real dimensions were used to develop the lumped elements. This method creates more precise lumped RLC elements that are more accurate. Fig. 33 shows the creation of edge to edge lumped elements.

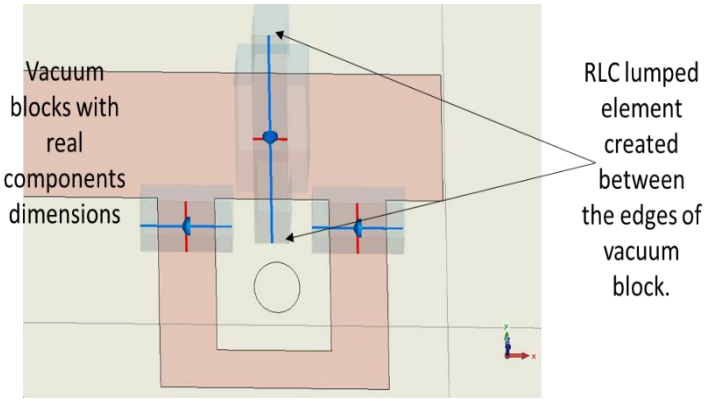

Fig. 33 Modelling of edge to edge lumped components in simulator.

After many tests were carried out and as expected, the use of edge to edge lumped elements offers a more efficient and precise model of components, closer to the real-life components. In the simulated results in next section we will therefore discuss the results of the models holding edge to edge components. Finally, and as a summary, we will show the models for each prototype with their corresponding components and additional pads and lines in Fig. 34 (a) (b) and (c) for feed line views and (d), (e) and (f) for the ground plane views.

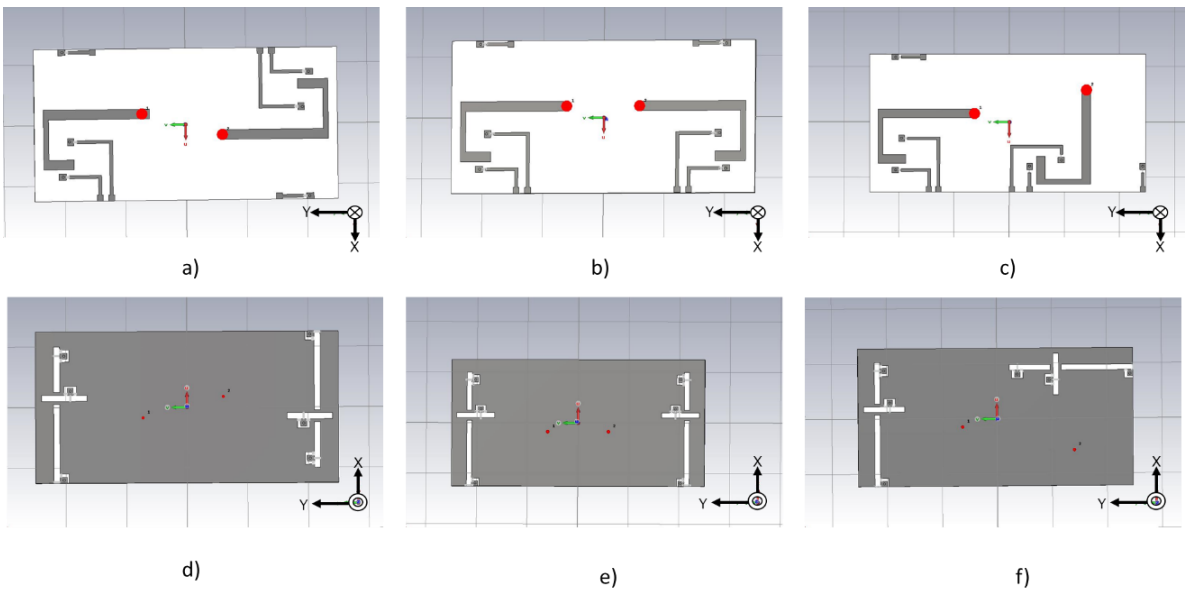

Fig. 34 Views of feed lines and ground planes of the simulated prototypes.

3.2.2. Simulated S-Parameters.

After successfully model in simulation the designed prototypes the analysis of reflection coefficients for each antenna for each board was carried out. Full wave simulation offers to obtain an estimation of the near field effects on the elements of the boards as well as an estimation of the isolation and ways to improve it. It was expected to benefit from three different frequency bands in each triple-slotted antenna which will be independent from each other. With the addition of the second antenna we aim to prove our hypothesis which is that two sets of slots will still offer independent tuning and will not affect the unchanged bands when tuning one. Essential metrics to evaluate the performance of an antenna are the scattering parameters or S-Parameters. These useful metrics aid antenna analyses in order to study its performance in the frequency domain. Overall, scattering parameters provide a complete analysis of a multi- port electrical network. As our prototypes MIMO 1, 2 and 3 are boards with two ports each feeding their respective antenna we will carry out an S-Parameters analysis of the boards where we will be focusing on the reflection coefficients for antenna 1 and 2. Mutual couplings have also been obtained for each board but will not be presented in this chapter as they will be part of an essential analysis in chapter 4. Nevertheless, the complete analysis of a two-ported network was carried out for the presented prototypes of double triple-slotted antennas.

The simulator CST offers the possibility to calculate the S-Parameters which describe the resonant frequencies of the antennas, as they are two evaluated antennas in each board, we will evaluate the simulated S_{11} parameters corresponding to Antenna 1 for each board and S_{22} for Antenna 2 in each prototype. Given the presence of Antennas 1 and 2 in each board it was imperative to evaluate the mutual coupling as well as it is an essential part of scattering parameters analysis in order to evaluate the interaction between antennas in a multi-antenna system. However, for this section we will only present the simulated reflection coefficients corresponding to antenna 1 and 2 in each board. Nevertheless, we also simulated S_{12} and S_{21} parameters, also known as reception and transmission coefficients, in order to evaluate the effect between antennas which will be a deeper analysis in the next chapter.

Given the frequency for each resonant slot can be tunable by gradually control the capacitive load in each cavity, we will proceed in a similar way to achieve a frequency reconfiguration for each slot as explained in the design process of the prototypes discussed in previous section 3.1. Hence, in order to control the resonant frequencies, we varied the

capacitance of the varactor diodes in the simulator by carrying out a parameter sweep with different values for each varactor diode. We have simulated different values for each varactor tuning a different band, naming varactors D1, D2 and D3 tuning its corresponding band. The capacitance of each varactor was varied in order to control the resonant frequency of the slot that is loading. By consulting the documentation of varactor Infineon BB833 the estimated capacitance values that will control different resonant frequencies for each slot were obtained. For Band 1 the capacitances varied from 4.0 pF to 0.5 pF expecting to achieve frequencies up to 1.1 GHz. For Band 2 values were varied from 4.0 pF to 1.0 pF aiming for values up to 2.4 GHz. Finally, for Band 3 these varied from 1.5 pF to 0.5 pF corresponding to the non-linear region of the varactor characterisation curve. Table 1 presents the values used for each varactor in each Antenna.

Band 1, capacitance of D1	Band 2, capacitance of D2	Band 3, capacitance of D3
4.0 pF	4.0 pF	1.5 pF
3.5 pF	3.5 pF	1.0 pF
3.0 pF	3.0 pF	0.7 pF
2.5 pF	2.5 pF	0.6 pF
2.0 pF	2.0 pF	0.5 pF
1.5 pF	1.7 pF	
1.0 pF	1.5 pF	
0.5 pF	1.0 pF	

Table 1 Simulated capacitance values for D1, D2 and D3 in each triple-slotted antenna.

After establishing the capacitance values for each slot, the simulated reflection coefficients will be analysed next for each prototype. Overall, simulated results showed an independent tuning range for three frequency bands, which are as follows:

- Band 1 for the three prototypes achieved frequencies from 0.6 to 1.3 GHz.
- Band 2 presented in each case frequency ranges of 1.2 – 2.3 GHz.
- Band 3 showed a range from 1.6 – 2.8 GHz for the three boards.

The analysis of the obtained results for each antenna for each board is presented next in order to demonstrate the independent tuning for each frequency band. In Fig. 35 the simulated S_{11} parameters corresponding to Antenna 1 in boards (a) MIMO 1, (b) MIMO 2 and (c) MIMO 3. We can observe for each case an independent tuning of Band 1 and Bands 2 and 3 unchanged when different capacitances for D1 are varied from 4.0 – 0.5 pF.

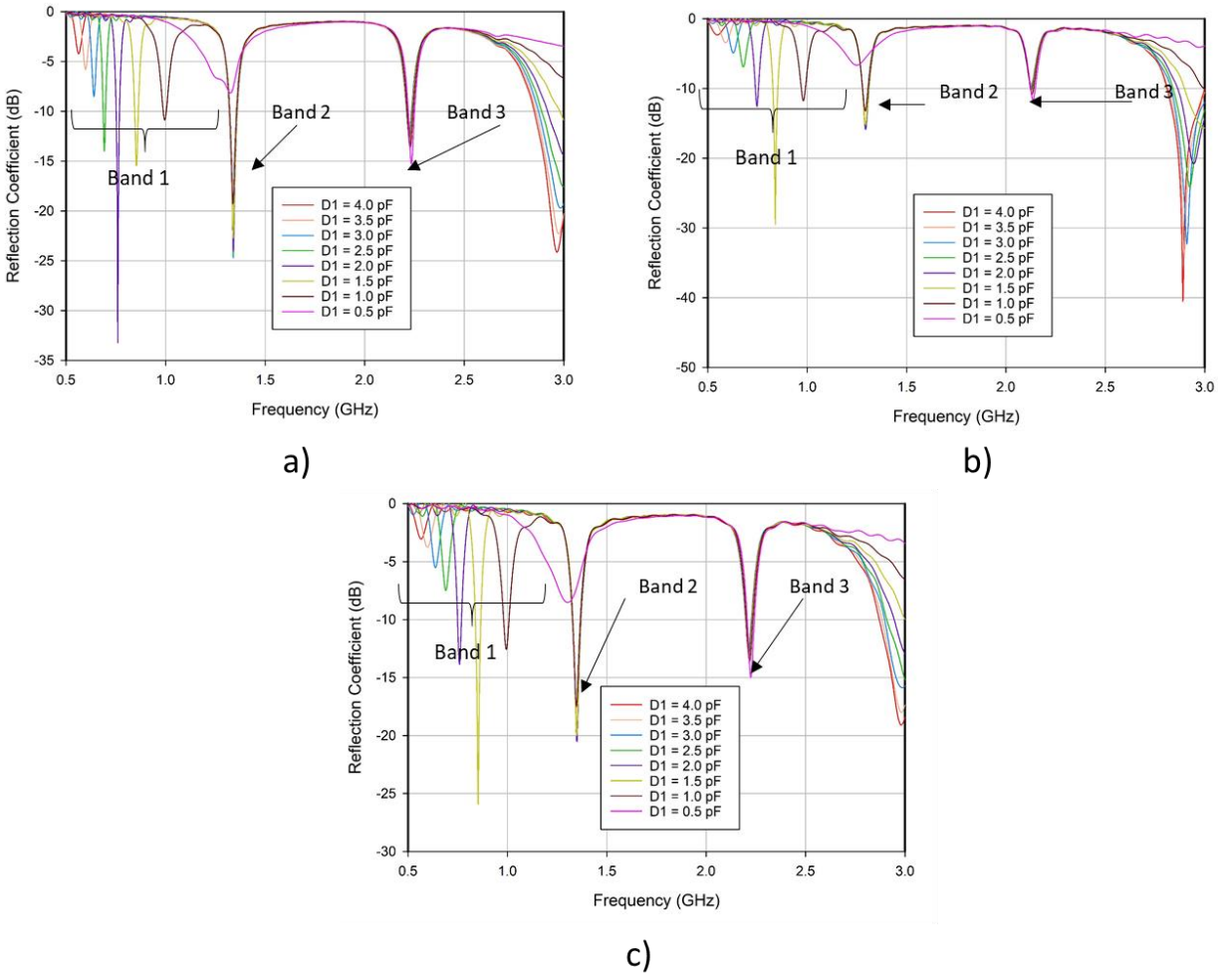

Fig. 35 Simulated S_{11} parameters for Antenna 1 in MIMO 1, 2 and 3 tuning Band 1.

Furthermore, for Band 1 the S_{22} Parameters will be presented next, corresponding to the simulated reflection coefficient for Antennas 2 for each board. Fig. 36 shows the simulated S_{22} parameters for Antenna 2 in (a) MIMO 1, (b) MIMO 2 and (c) MIMO 3 respectively. We can see similar results to the ones presented in Fig. 35 which demonstrates the independence not only from slot to slot but also antenna to antenna in simulation. Similar to the simulated reflection coefficients for Antenna 1, we varied capacitance values for D1 from 4.0 – 0.5 pF and similar frequency ranges have been obtained compared to those obtained for Antenna 1 for each board.

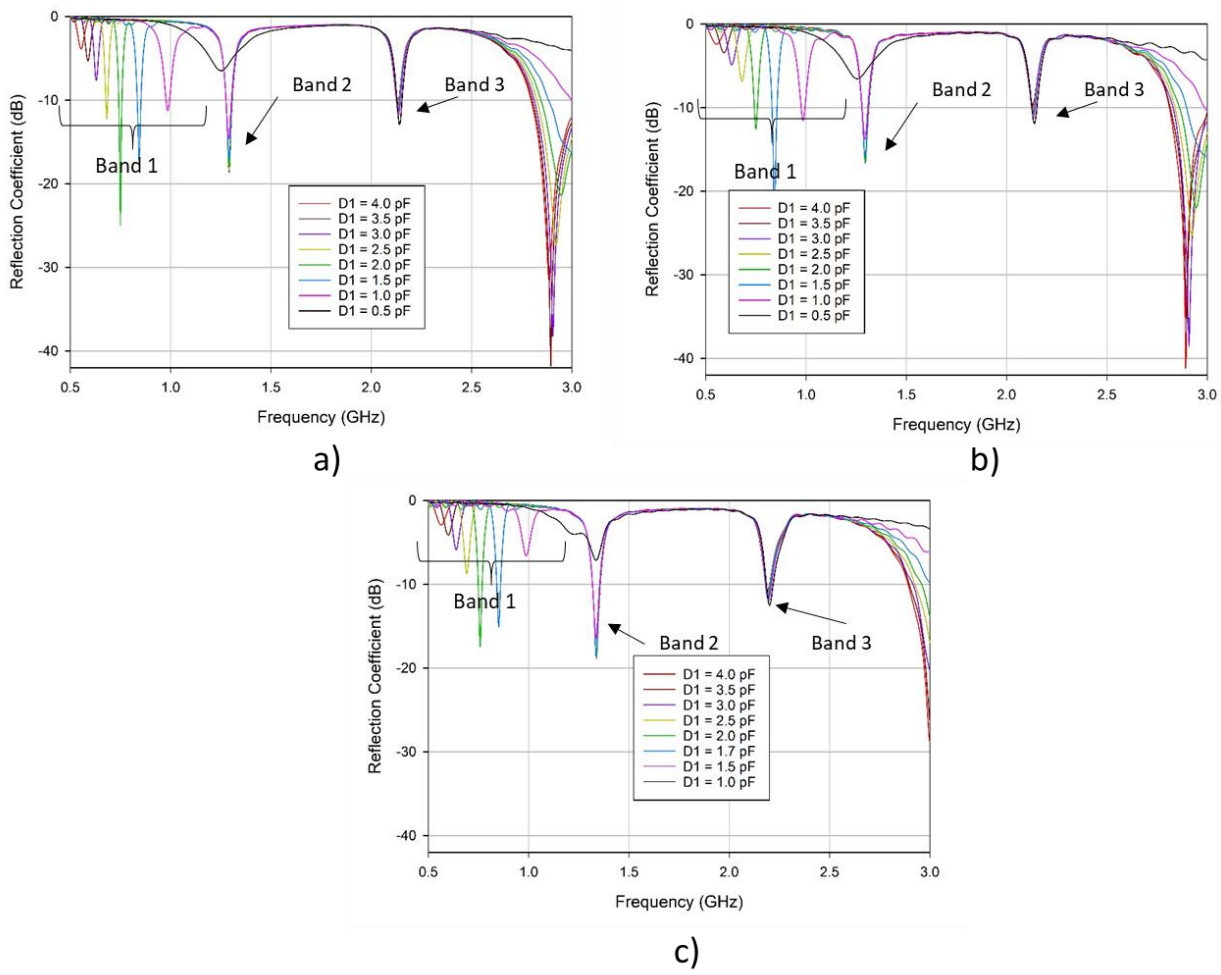

Fig. 36 Simulated S_{22} Parameters for Antenna 2 in MIMO 1, 2 and 3 tuning Band 1.

As an additional assessment of the simulated S-Parameters, in Fig. 37 the S_{11} parameters corresponding to Antenna 1 are presented while the S_{22} parameters for Antenna 2 is being tuned. The reflection coefficient for Antenna 1 remained fixed when Antenna 2 was tuned. This demonstrates in simulation that there is no coupling effect between the antennas in the board.

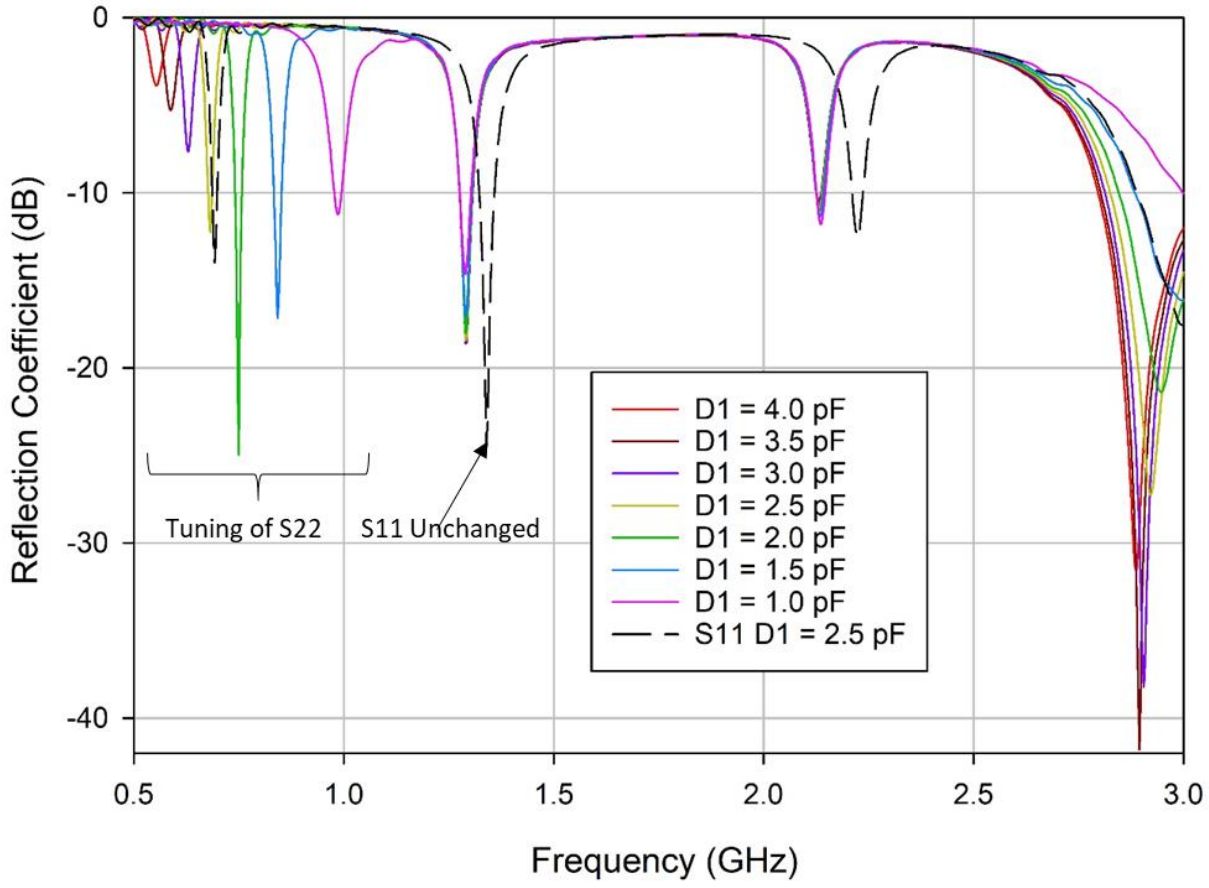

Fig. 37 Absence of coupling effect between antennas 1 and 2 in the board.

For Bands 2 in each case, the procedure carried out was similar to Fig. 35 and Fig. 36 according the capacitance variation for varactors D2 described in Table 1. In each case observed a frequency ranges of 1.2 – 2.3 GHz when varying the capacitance of D1 from 4.0 – 1.0 pF. A clear smooth transition for each resonant frequency of this range is observed. The remaining bands (Band 1 and Band 3) are unaltered for each resonant frequency of Band 2 which, again, proves that independent tuning for each prototype is achievable. Fig. 38 presents the simulated S11 parameters corresponding to the reflection coefficients for Antenna 1 when tuning D2 for (a) MIMO 1, (b) MIMO 2 and (c) MIMO 3.

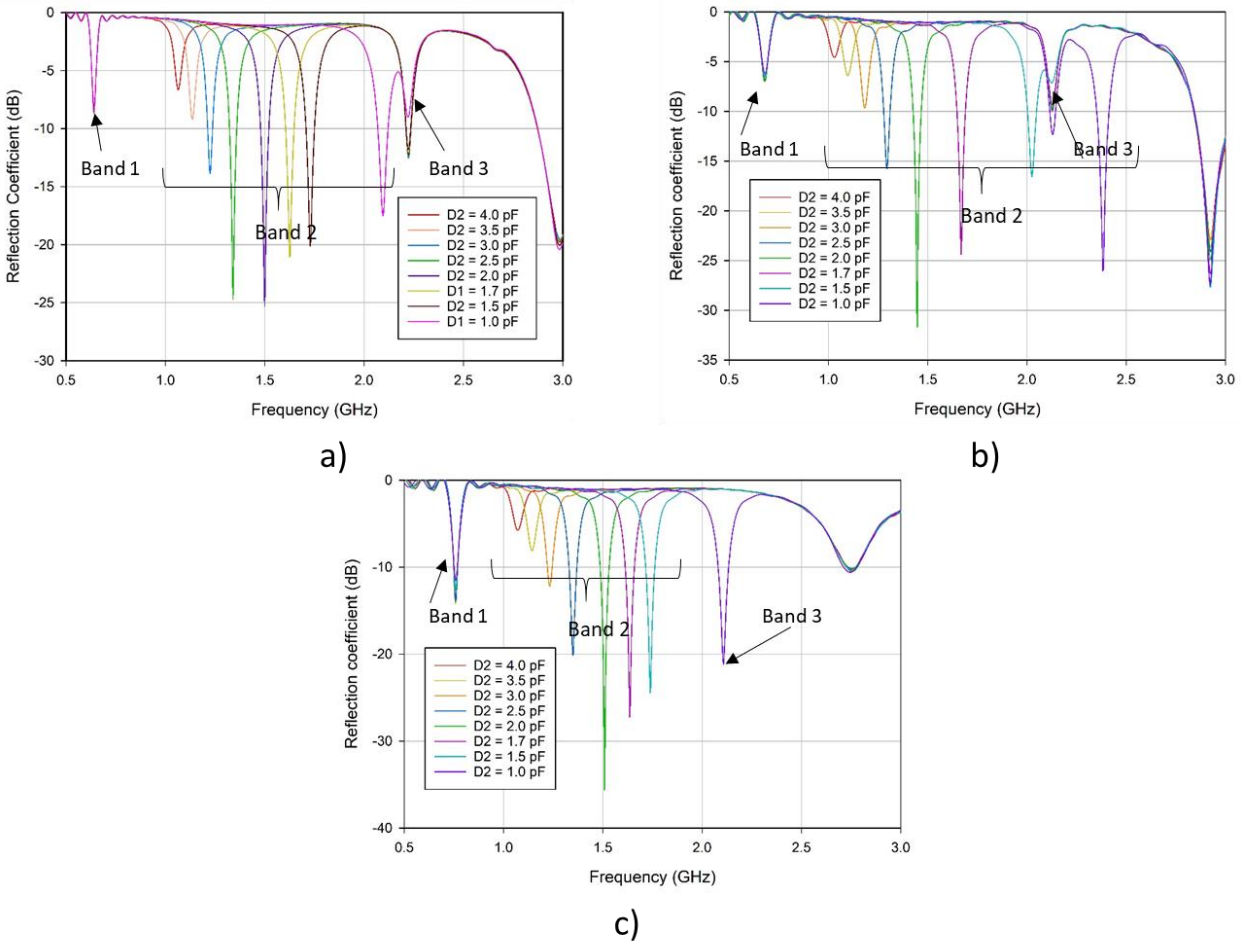

Fig. 38 Simulated S_{11} Parameters for MIMO 1, 2 and 3 tuning Band 2.

Antenna 2 in each board presents similar results to Antenna 1 when tuning Band 2 as well. Band 1 and Band 3 remain unchanged when the capacitance values for D2 have been gradually controlled. Therefore, independent tuning is also achieved for both antennas in each board when tuning D2. In Fig. 39 the simulated S_{22} parameters are presented corresponding to the reflection coefficient for Antenna 2 in (a) MIMO 1, (b) MIMO 2 and (c) MIMO 3 where multiple resonant frequencies are observed for Band 2 whilst Bands 1 and 3 remain unaltered.

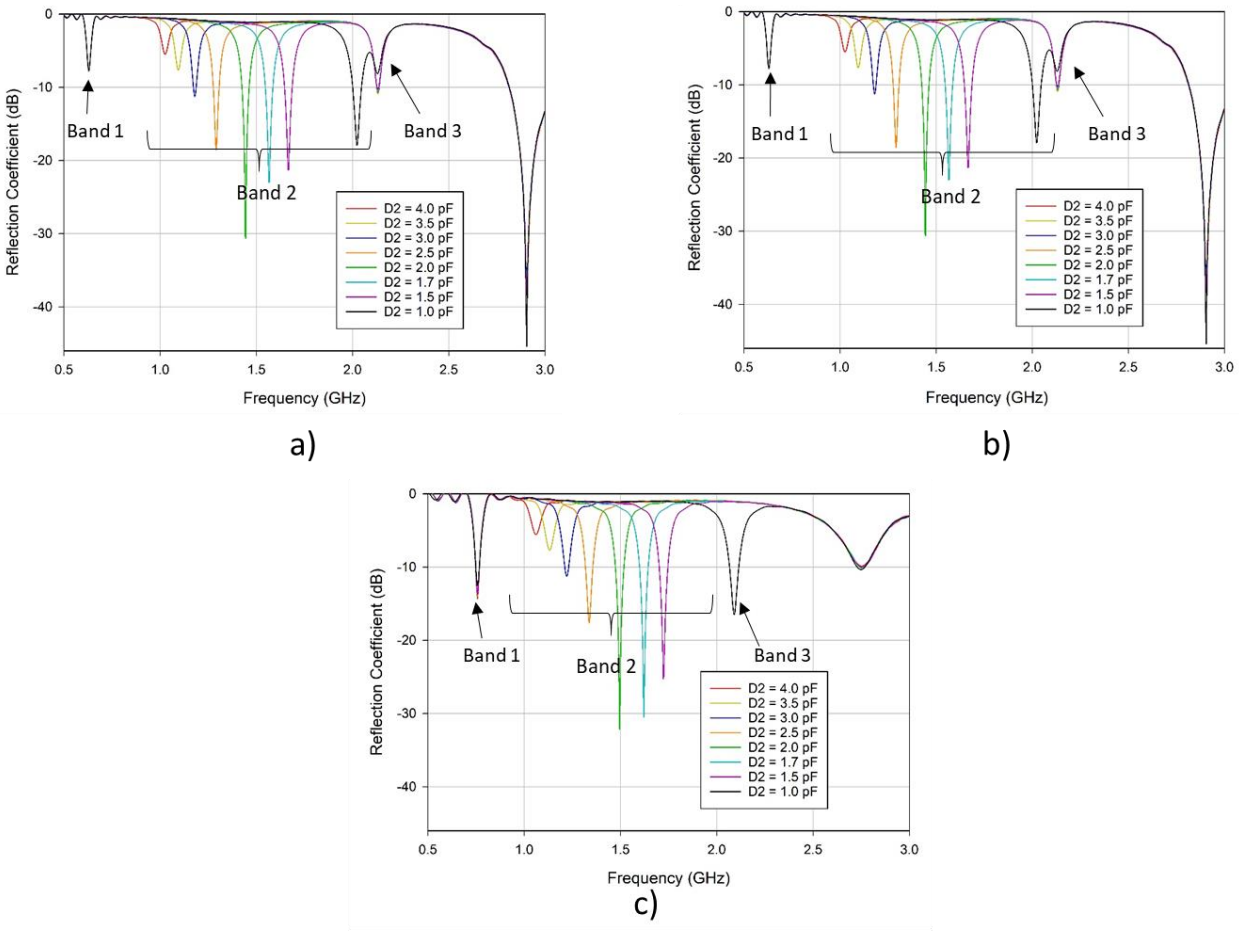

Fig. 39 Simulated S_{22} Parameters for MIMO 1, 2 and 3 tuning Band 2.

Then for Band 3 a slight variation for the capacitances for D3 given at frequencies higher than 2.5 GHz Slot 3 will be much more sensitive for low capacitances than for high capacitances. The capacitance values for D3 varied from 1.5 – 0.5 pF as described in Table 1. For values higher than 1.5 pF the resonant frequencies had very weak matching and are negligible. Overall, for Band 3 the achieved frequency ranges were 1.6 – 2.8 GHz in the simulated models. For Antenna 1 in Fig. 40 the S_{11} parameters are presented corresponding to the simulated reflection coefficients Antenna 1 for (a) MIMO 1, (b) MIMO 2 and (c) MIMO 3 when tuning Band 3 and Band 1 and Band 2 have remained unchanged.

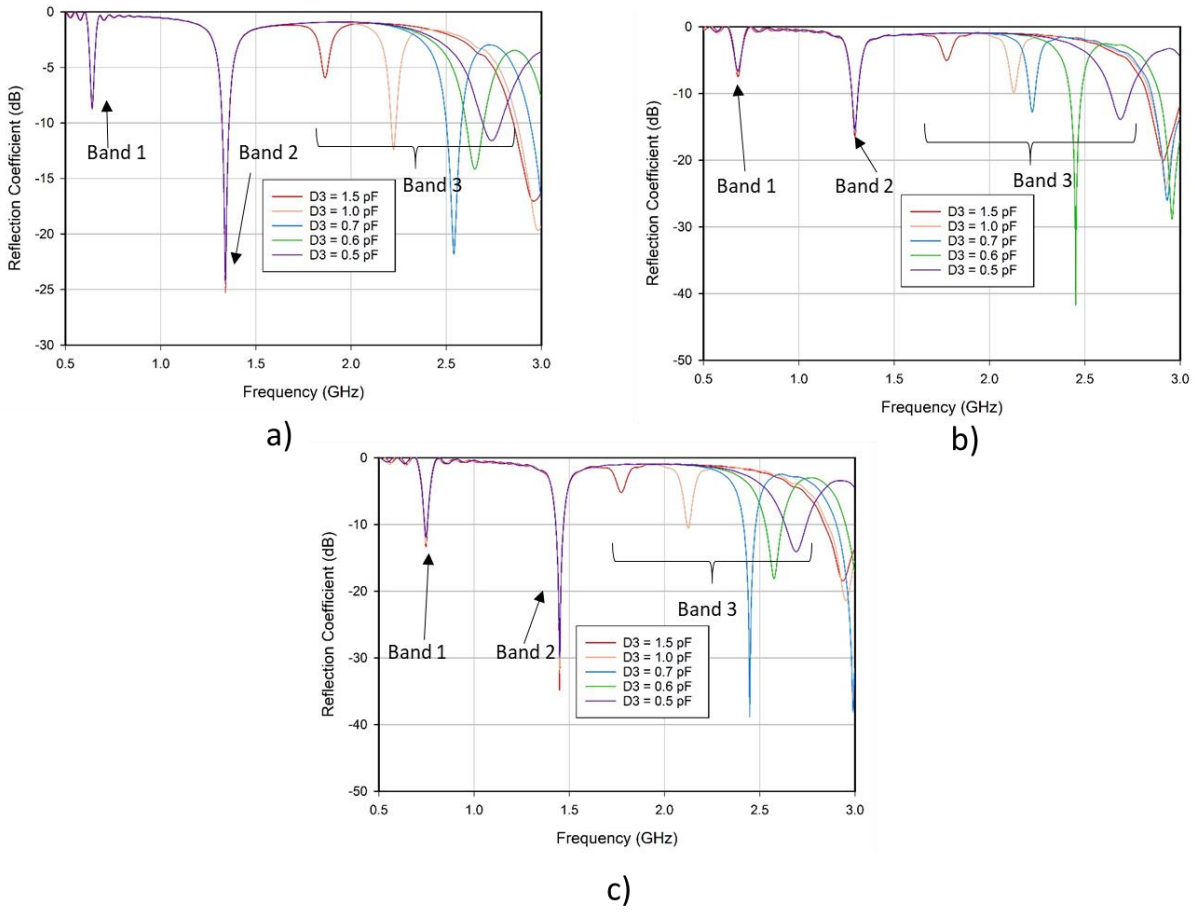

Fig. 40 Simulated S_{11} Parameters for MIMO 1, 2 and 3 tuning Band 3.

Finally, for Band 3, for Antenna 2 in each board, similar results were obtained to those presented in Fig. 40. Band 3 was tuned from 1.6 – 2.8 GHz whilst Bands 1 and 3 remain unaltered. In Fig. 41 we observe the simulated S_{22} parameters corresponding the reflection coefficients for Antenna 2 in (a) MIMO 1, (b) MIMO 2 and (c) MIMO 3.

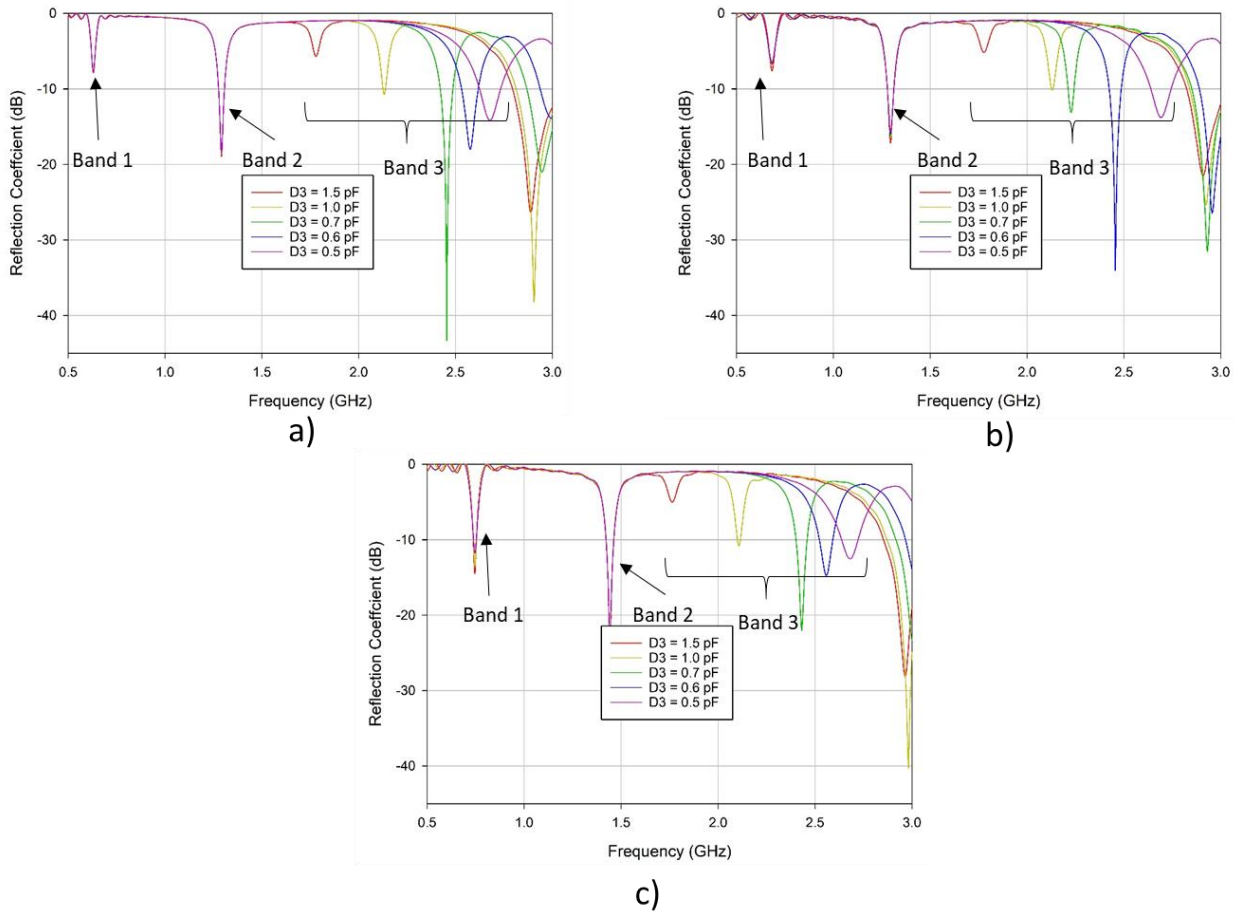

Fig. 41 Simulated S_{22} Parameters for MIMO 1, 2 and 3 tuning Band 3.

Overall, three independently tunable frequency bands are offered for each board, for each antenna. When a band tuned in question is being controlled via the capacitance of the varactor diode loading the respective slot, the remaining bands are not altered. For band 1 and 2 a linear tuning was observed whilst for Band 3 the variation was smaller given the at higher frequencies components behave differently. Conclusively, in simulation, independent frequency ranges for each prototype in each of their antennas were obtained, proving the independent tuning can be achieved by multiple antennas operating in the same boards and will not be affected by each other due to the coupling effects.

3.2.3. Simulated surface current distributions.

Furthermore, in CST Microwave Studio software we have useful tools to analyse the mutual effect among multiple antennas. With a view to achieve reconfiguration in an antenna system one can alter the current distribution on its structure. CST Microwave studio offers a surface current analysis that have helped the analysis of the MIMO prototypes in order to determine the independent operability of each antenna in each board.

The simulation of the surface current distributions for each board were carried out, for each antenna at a given resonant frequency in each of the independently tunable bands. comparisons were also carried out for Antenna 1 and 2 in each board analysing the surface current of the prototype at the same resonant frequency for each antenna. Similar to the comparisons discussed in the analysis of the simulated reflection coefficients in section 3.2.2, a comparison will be presented for each board at a given frequency presenting both antennas operating in the board and showing the effect of the resonant slot in question on the remaining slots when they remain idle.

In Fig. 42 – Fig. 59 the surface current analysis for MIMO 1, MIMO 2 and MIMO 3 are presented. In each figure, a comparison between (a) Antenna 1 and (b) Antenna 2, respectively. In each case, the slot radiating for Antenna 1 behaves similarly to its symmetrical copy at Antenna 2, this is described by arrows coloured in tones of red for the highest current distribution and blue for the lowest. For Band 1, Slot 1 and Slot 1a radiate both at similar frequencies working at 0.70 GHz, 0.68 GHz, and 0.71 GHz , respectively as observed in Fig. 42, Fig. 45 and Fig. 48 , however, a negligible intensity of radiation is observed on the idle slot when the other one radiates as described in arrows coloured in tones of red for the highest current distribution. For frequencies at Band 2, presented in Fig. 43, Fig. 46 and Fig. 49, a similar comparison was carried out at 1.42 GHz, 1.44 GHz and 1.38 GHz respectively, where no effect on the non-radiating Slot 2 and Slot 2a is observed in each case when their corresponding symmetrical replica is radiating. Finally in Fig. 44, Fig. 47 and Fig. 50 Slots 3 and 3a operating at 2.52 GHz, 2.60 GHz and 2.54 GHz, respectively, are presented and the remaining duplicate of Slot 3 and Slot 3a present negligible effects on its edges.

Overall, when slots are operating simultaneously in the same board, little mutual coupling is observed by analysing the surface current plots. This shows that the antennas are not affecting each other after the analysis of the previous figures.

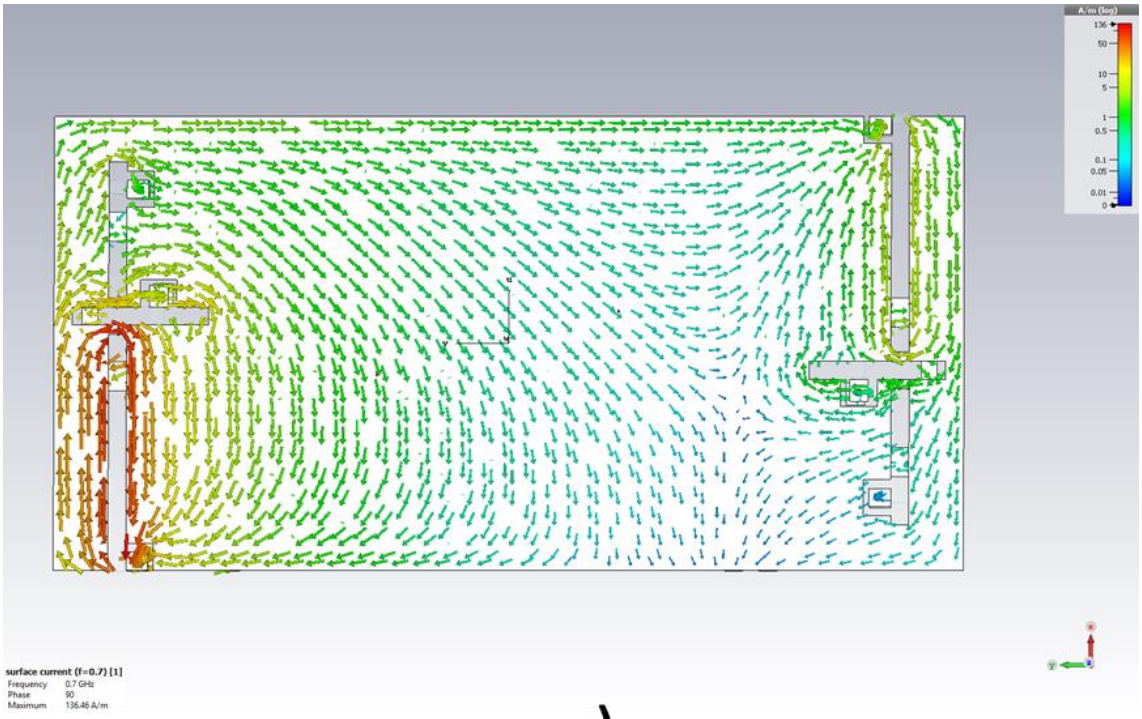

a)

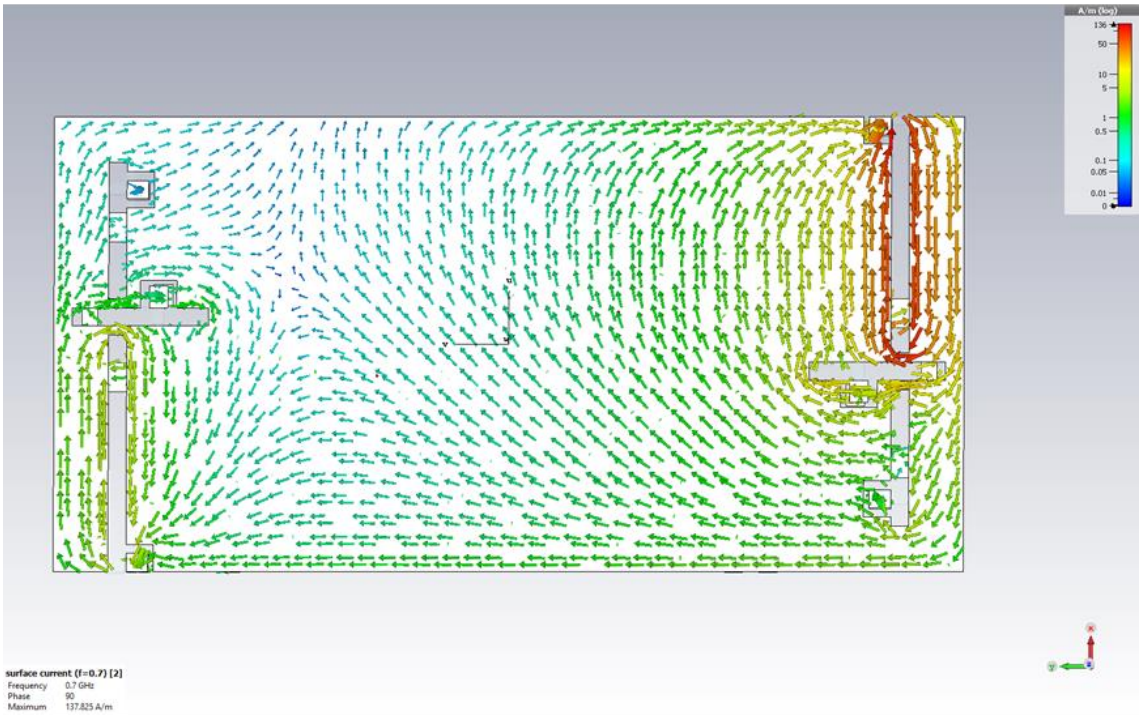

b)

Fig. 42 Simulated surface current distributions for Antennas 1 and 2 for MIMO 1 at 0.7 GHz.

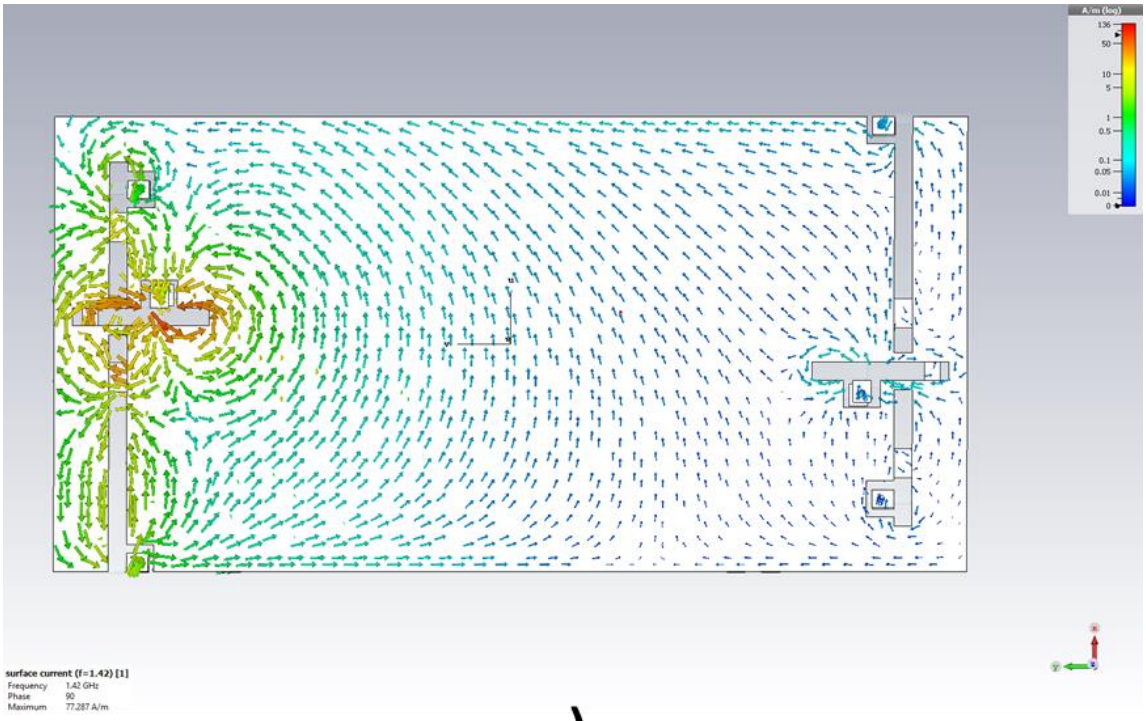

a)

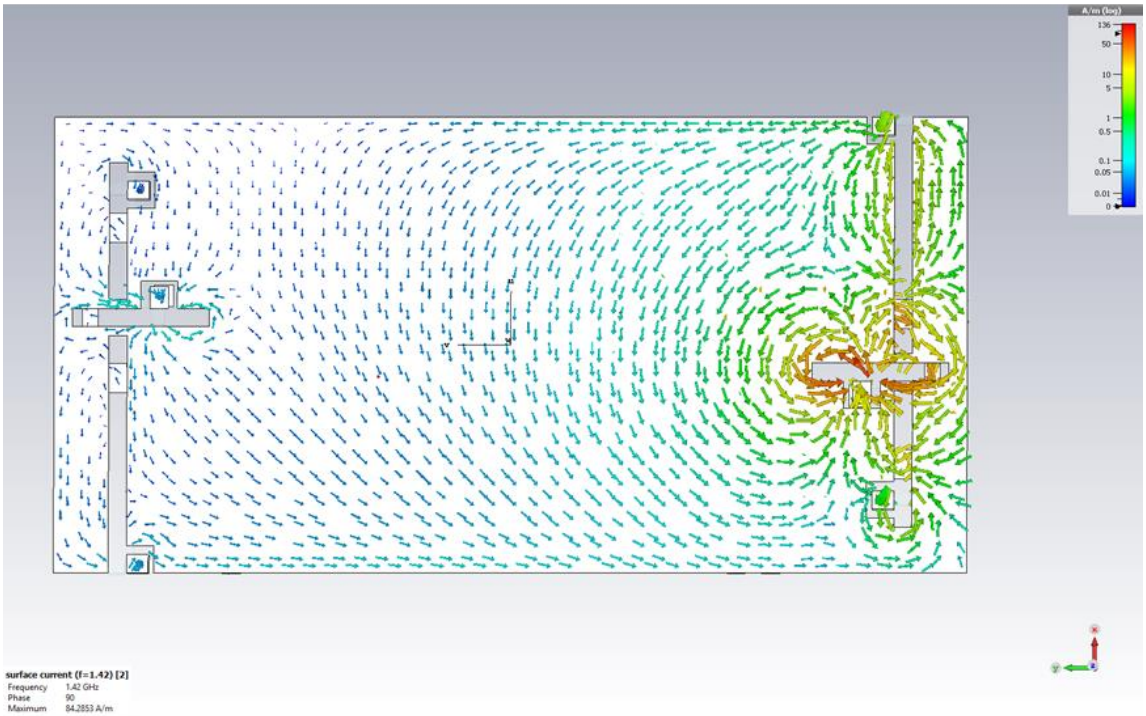

b)

Fig. 43 Simulated surface current distributions for Antennas 1 and 2 for MIMO 1 at 1.42 GHz.

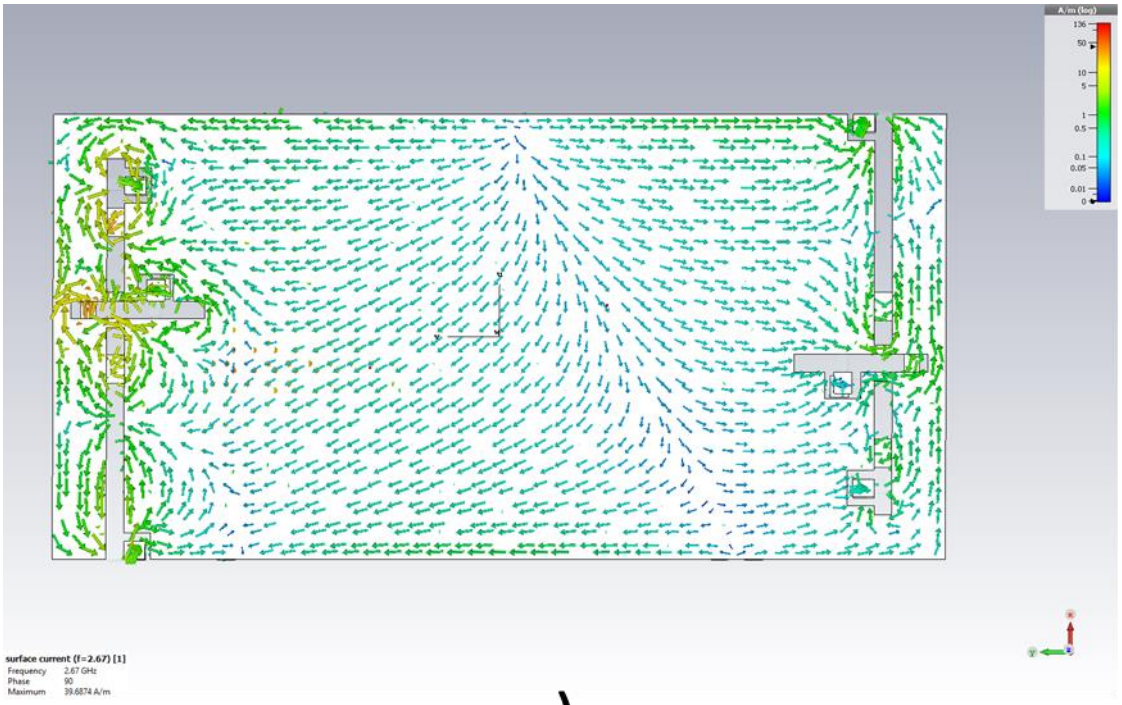

a)

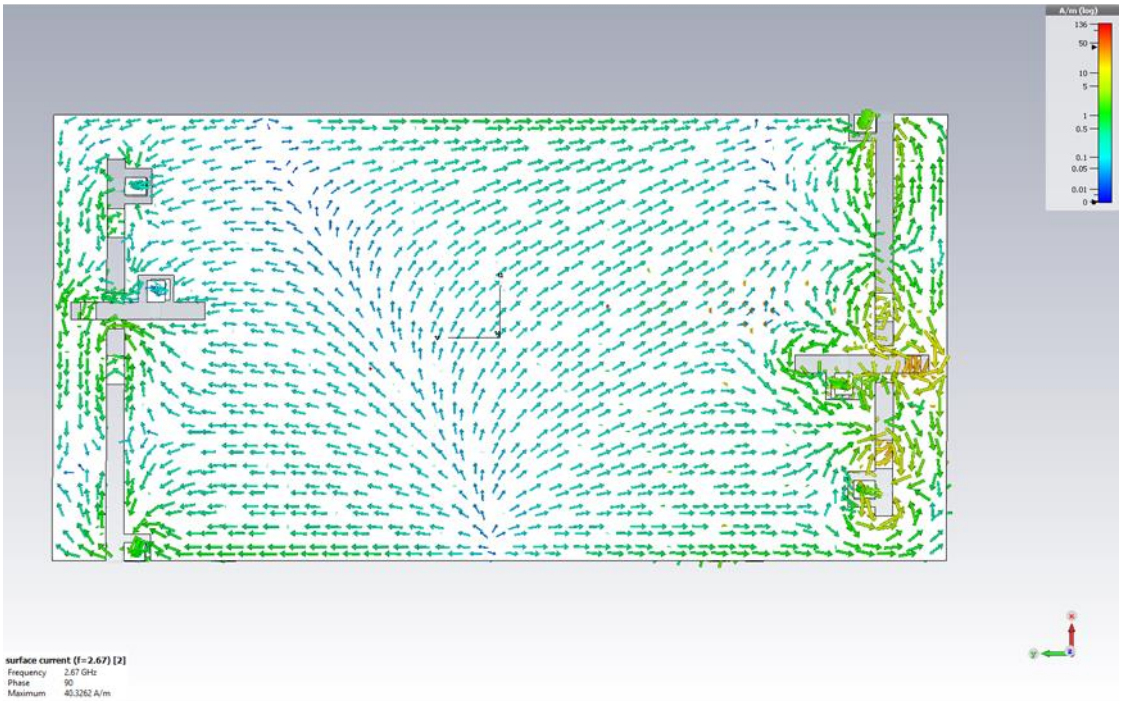

b)

Fig. 44 Simulated surface current distributions for Antennas 1 and 2 for MIMO 1 at 2.67 GHz.

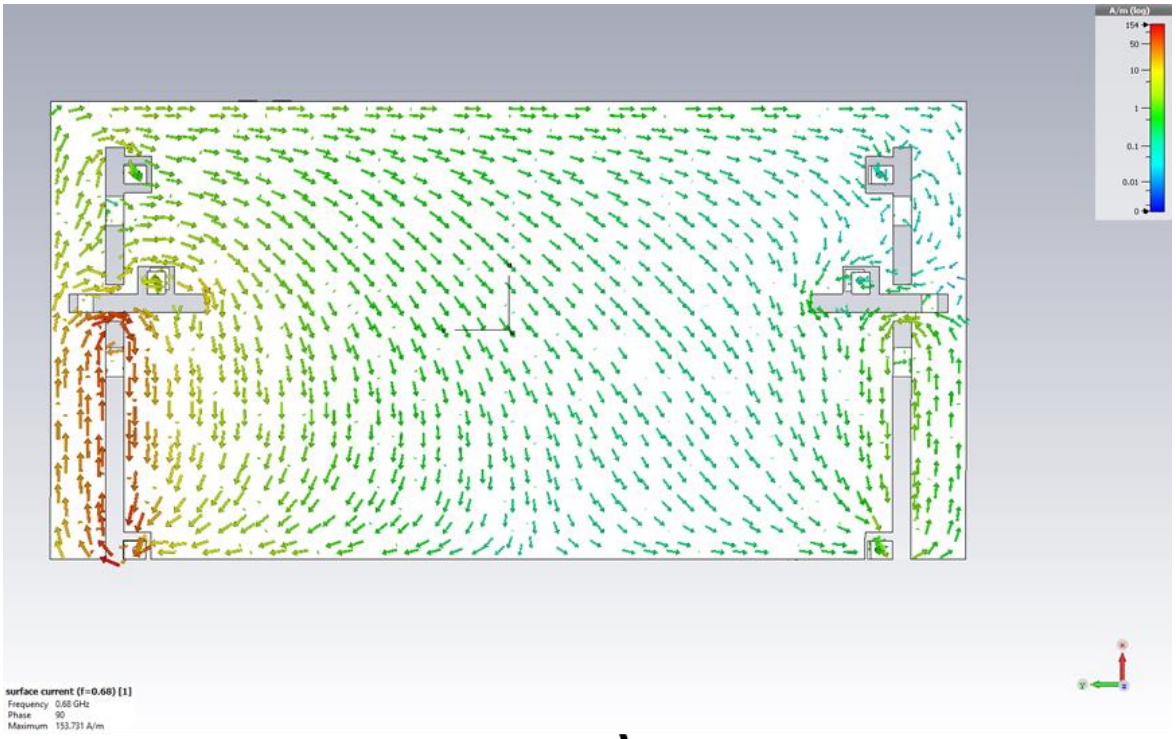

a)

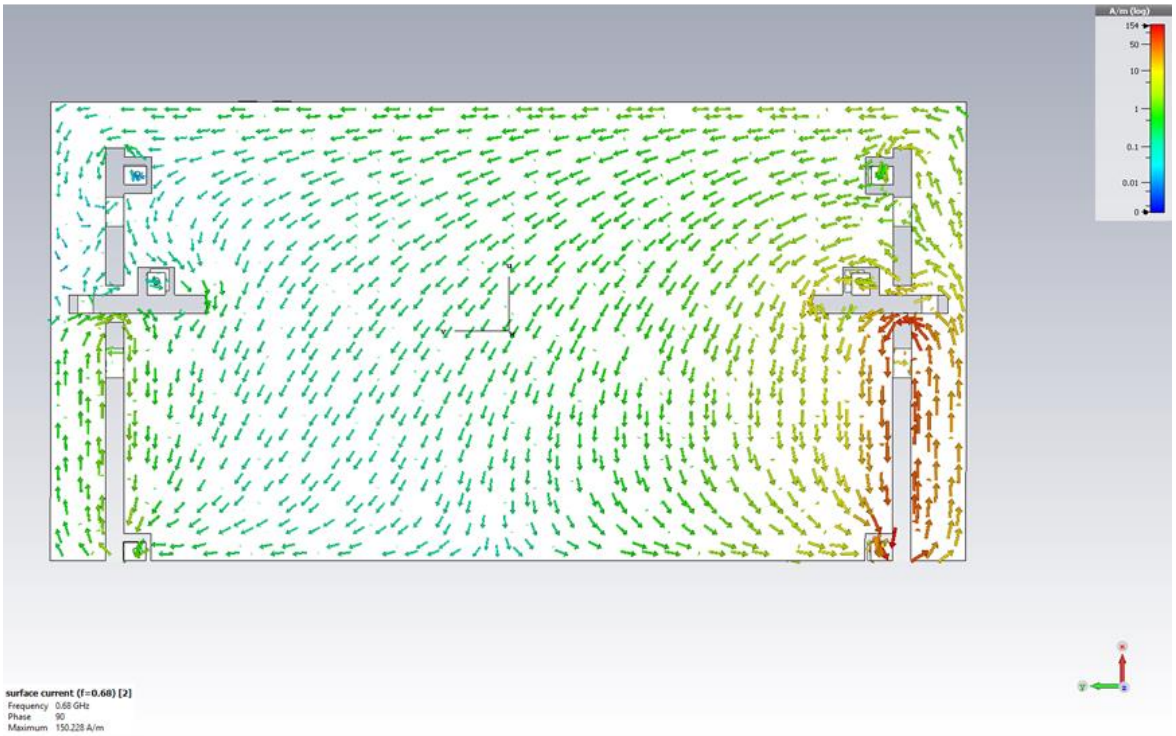

b)

Fig. 45 Simulated surface current distributions for Antennas 1 and 2 for MIMO 2 at 0.68 GHz.

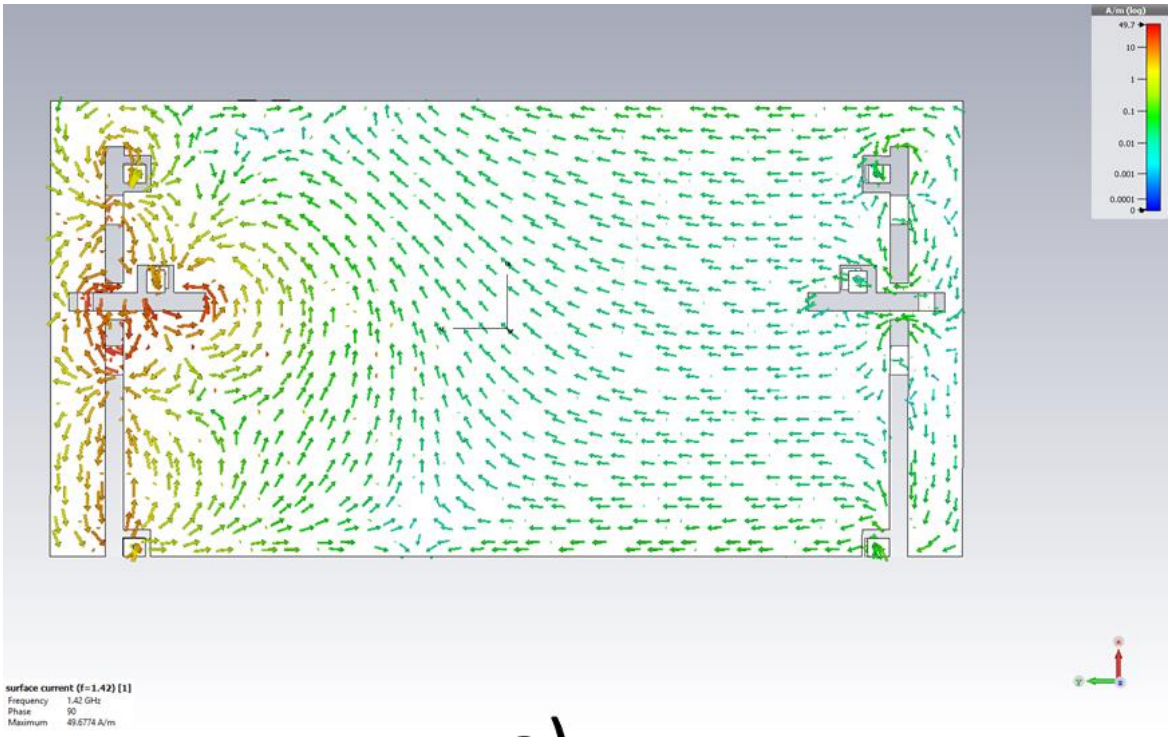

a)

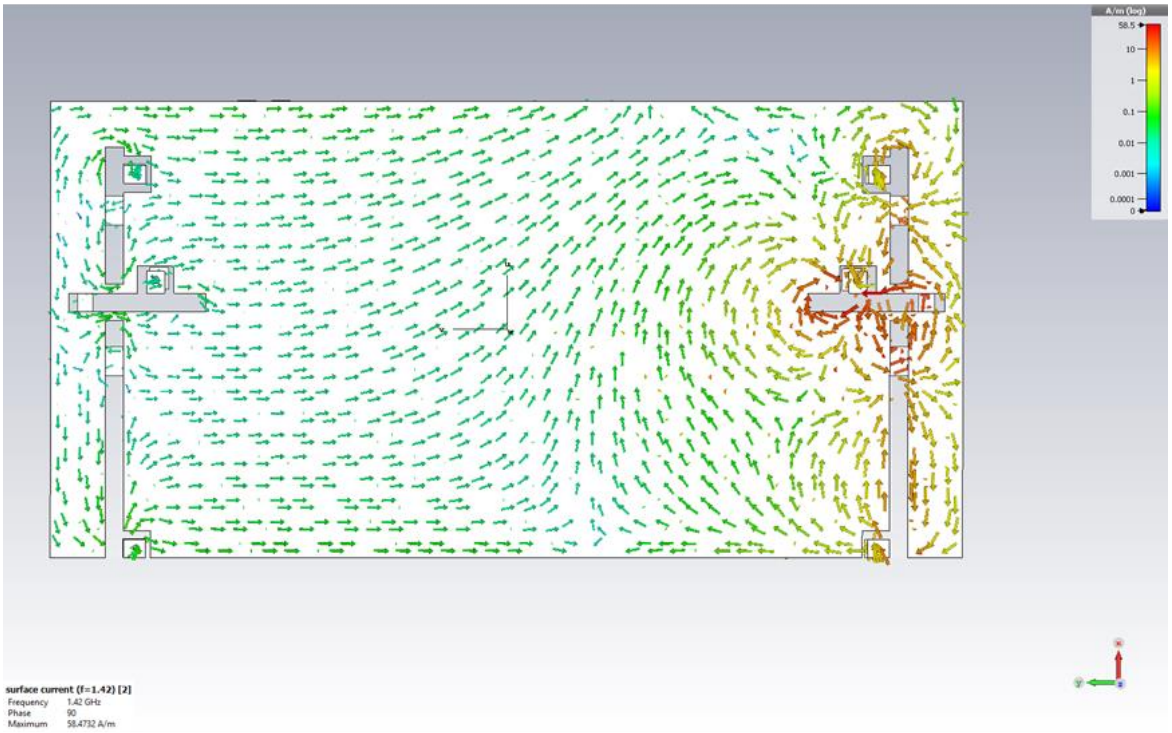

b)

Fig. 46 Simulated surface current distributions for Antennas 1 and 2 for MIMO 2 at 1.42 GHz.

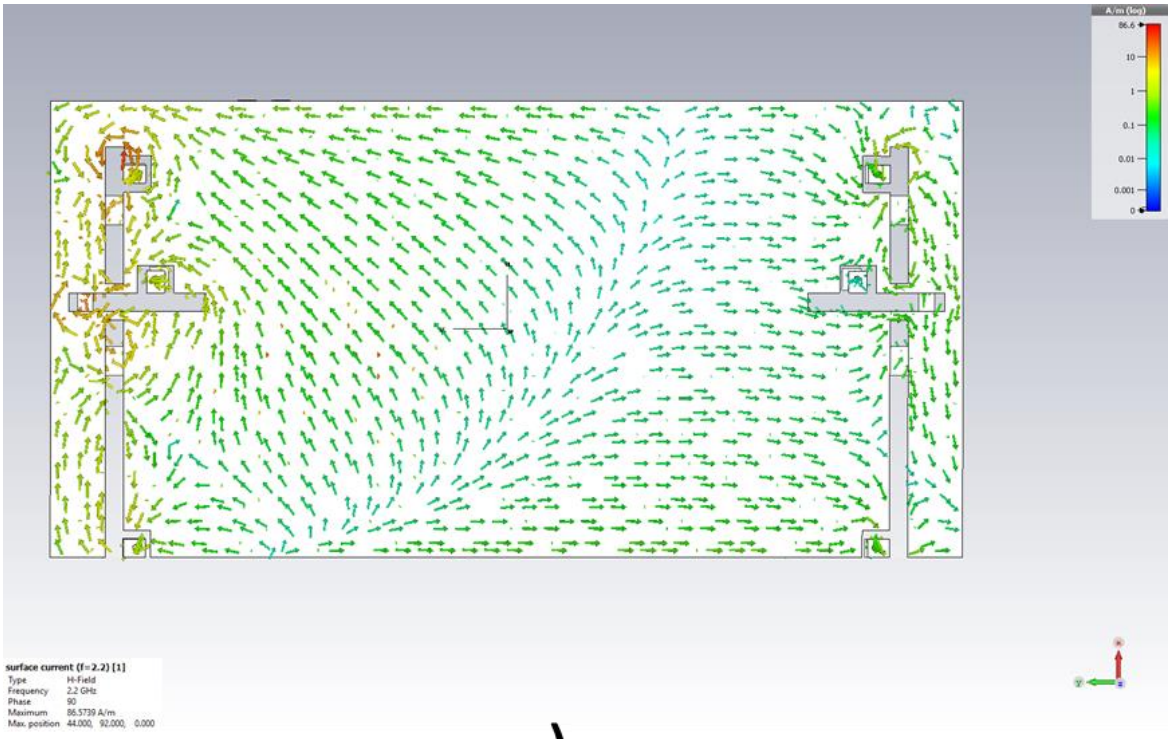

a)

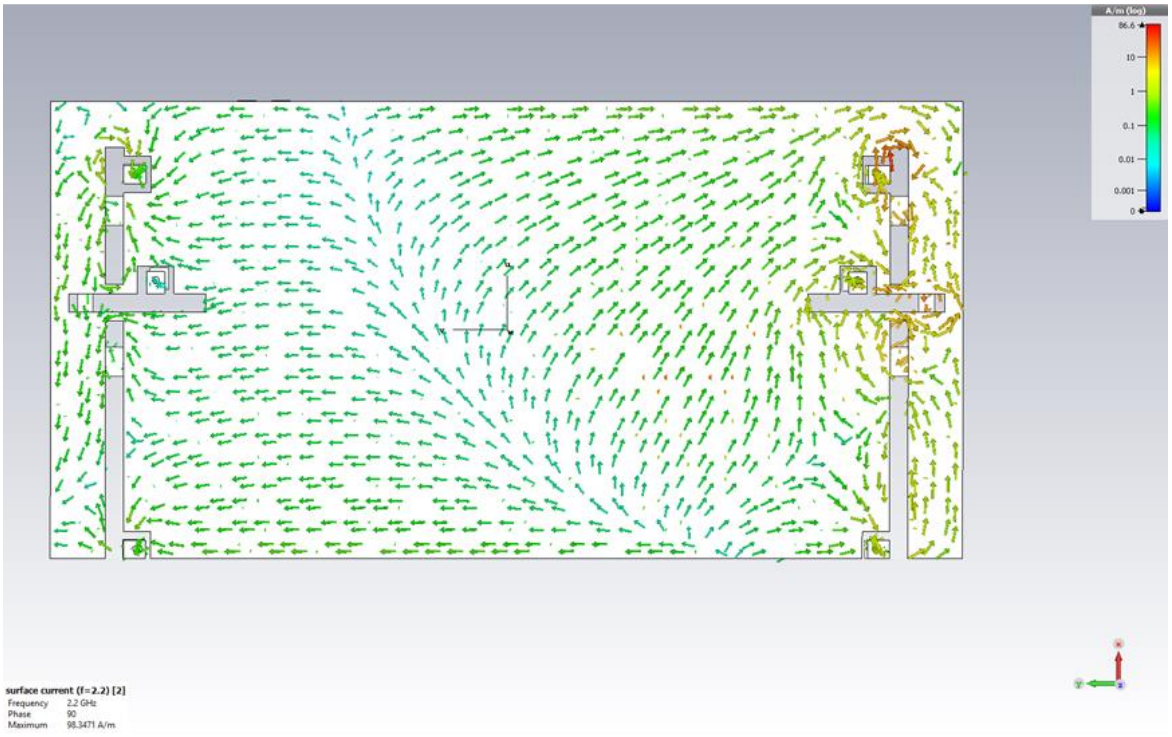

b)

Fig. 47 Simulated surface current distributions for Antennas 1 and 2 for MIMO 2 at 2.2 GHz.

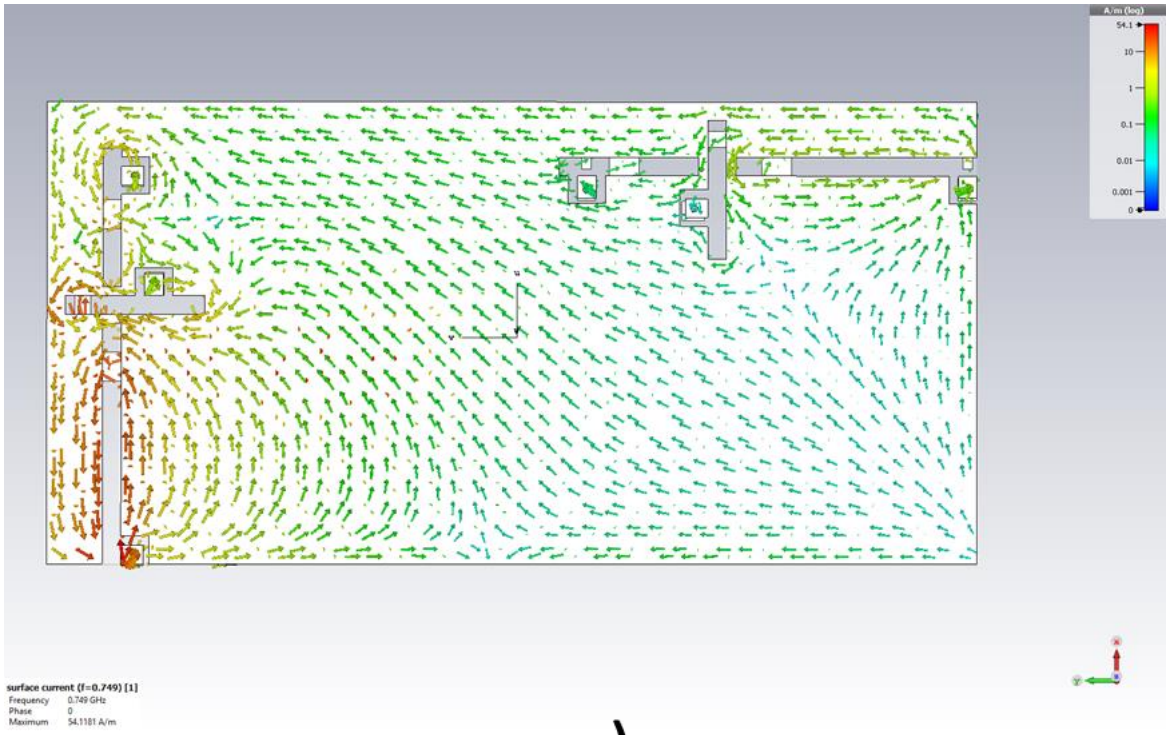

a)

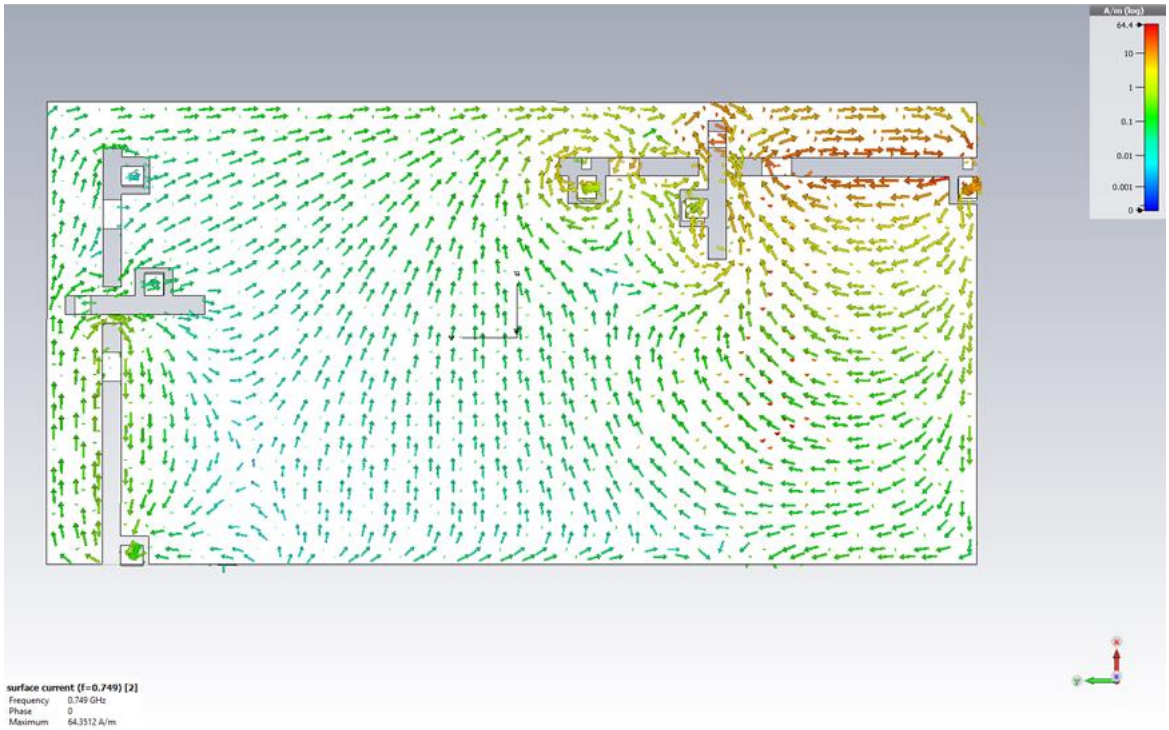

b)

Fig. 48 Simulated surface current distributions for Antennas 1 and 2 for MIMO 3 at 0.7 GHz.

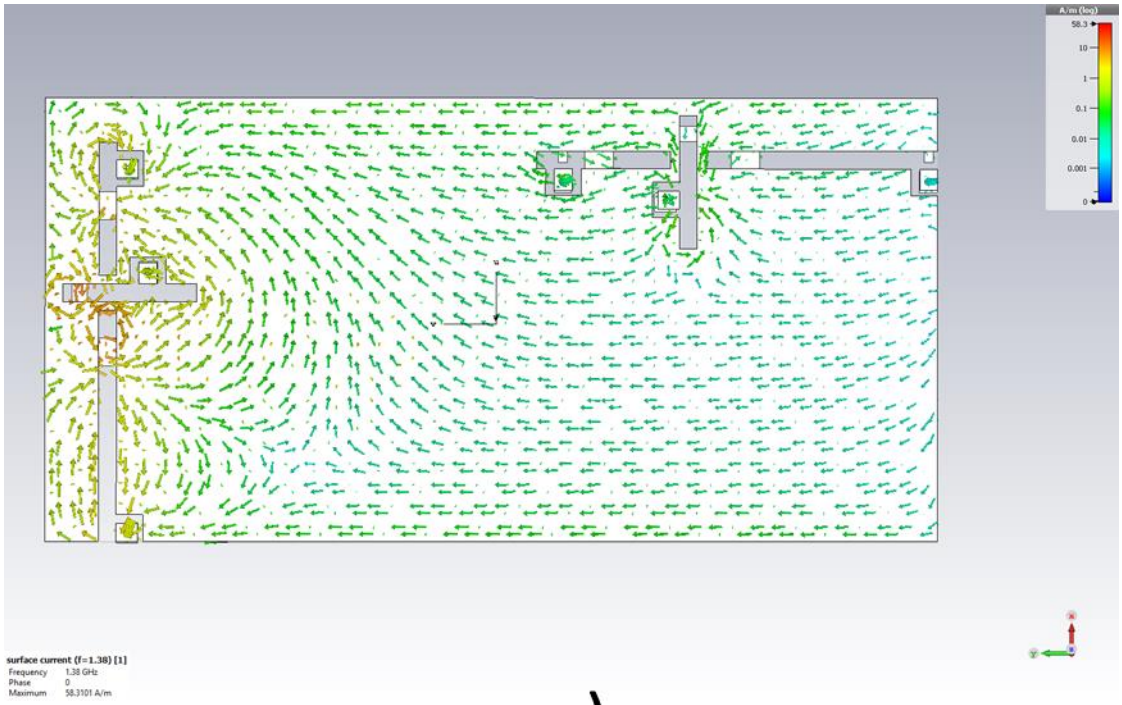

a)

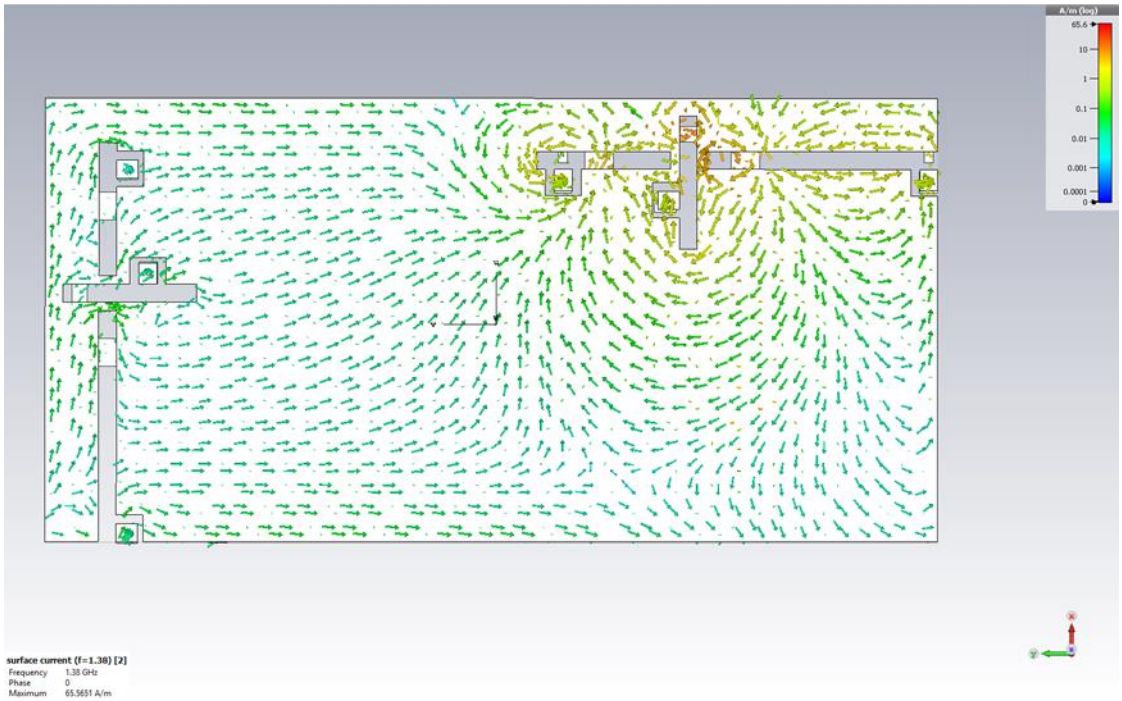

b)

Fig. 49 Simulated surface current distributions for Antennas 1 and 2 for MIMO 3 at 1.38 GHz.

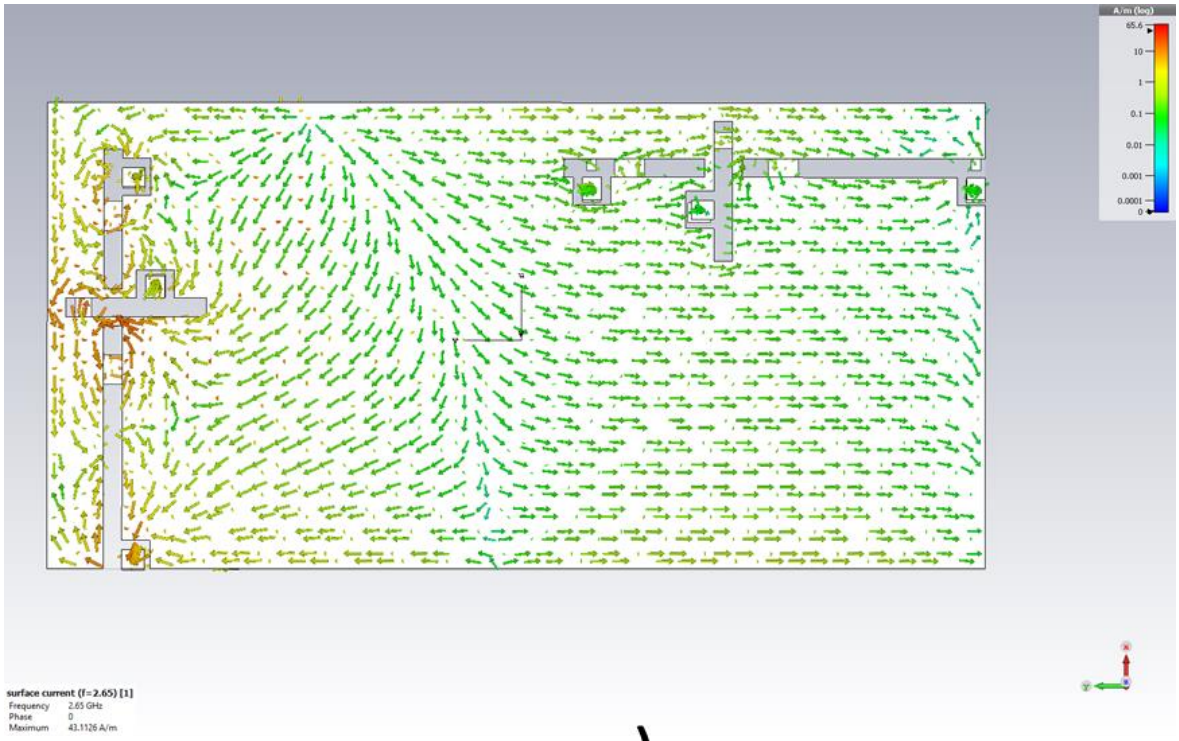

a)

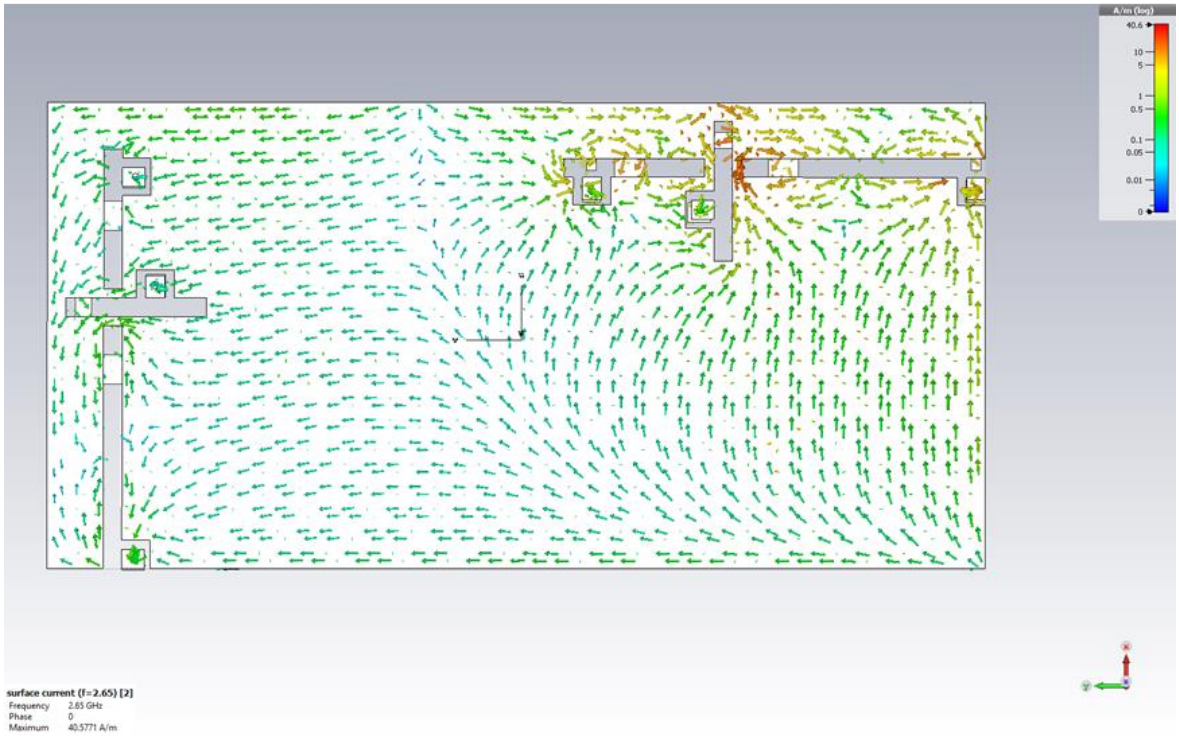

b)

Fig. 50 Simulated surface current distributions for Antennas 1 and 2 for MIMO 3 at 2.65 GHz.

3.2.3.1. Simulated radiation patterns.

Radiation patterns have been also calculated by the CST simulator with different results for each frequency. The software package offers to calculate these useful diagrams in order to have an estimation on the radiated energy from the antenna in question. CST is capable to display radiation patterns in polar, Cartesian and 3D forms. the analysis of the polar and 3D patterns for each board, for each antenna at a given frequency in each frequency band (Band 1, 2 and 3) was carried out. Similar to the analysis carried out in sections 3.2.2 and 3.2.3, the simulated patterns for each antenna, for each board are discussed.

The calculations offered by CST software refer to farfields, which is the pattern that the antenna describes at long distances which are generally measured for every antenna as a standard procedure. Farfield is defined as a distance $2D/\lambda$ where D is the antenna diameter and λ the wavelength. Farfield also refers to the second half of the antenna transmission cycle, similar to the operative principle of an inductor where first stores and then releases energy, in the second half of this cycle, the antenna releases its energy and that area covered by this emission is denominated as farfield.

For each board we measured a given frequency for each band analysing both Antenna 1 and Antenna 2 in each case in order to study the pattern coverage which also leads to study diversity parameters which will be discussed later in this work. The frequencies studied in each case have been as follows: for Band 1 in the order of 0.7 GHz, for Band 2 in the order of 1.4 GHz and for Band in the order of 2.5 GHz, all of these with slight variations depending on their corresponding resonant frequencies for each board.

In the next set of figures, a comparison will be presented for the three boards and for each antenna when working at the same frequency, showing the area coverage offered by the slot working in question. The figures show 3D and polar patterns for each board for each antenna, having phi = 90^{o} for the polar plots, corresponding to YZ planes. Only the patterns for YZ planes will be presented for illustration purposes only.

In Fig. 51 the simulated 3D and polar pattern for MIMO 1 are presented. the slot is resonating at 0.70 GHz corresponding to a frequency obtained for Band 1 (a) for Antenna 1 and (b) for Antenna 2. Similar shapes are observed in the pattern but different positions from one antenna to the other. Slot 1 in each antenna radiate in a rather omnidirectional pattern.

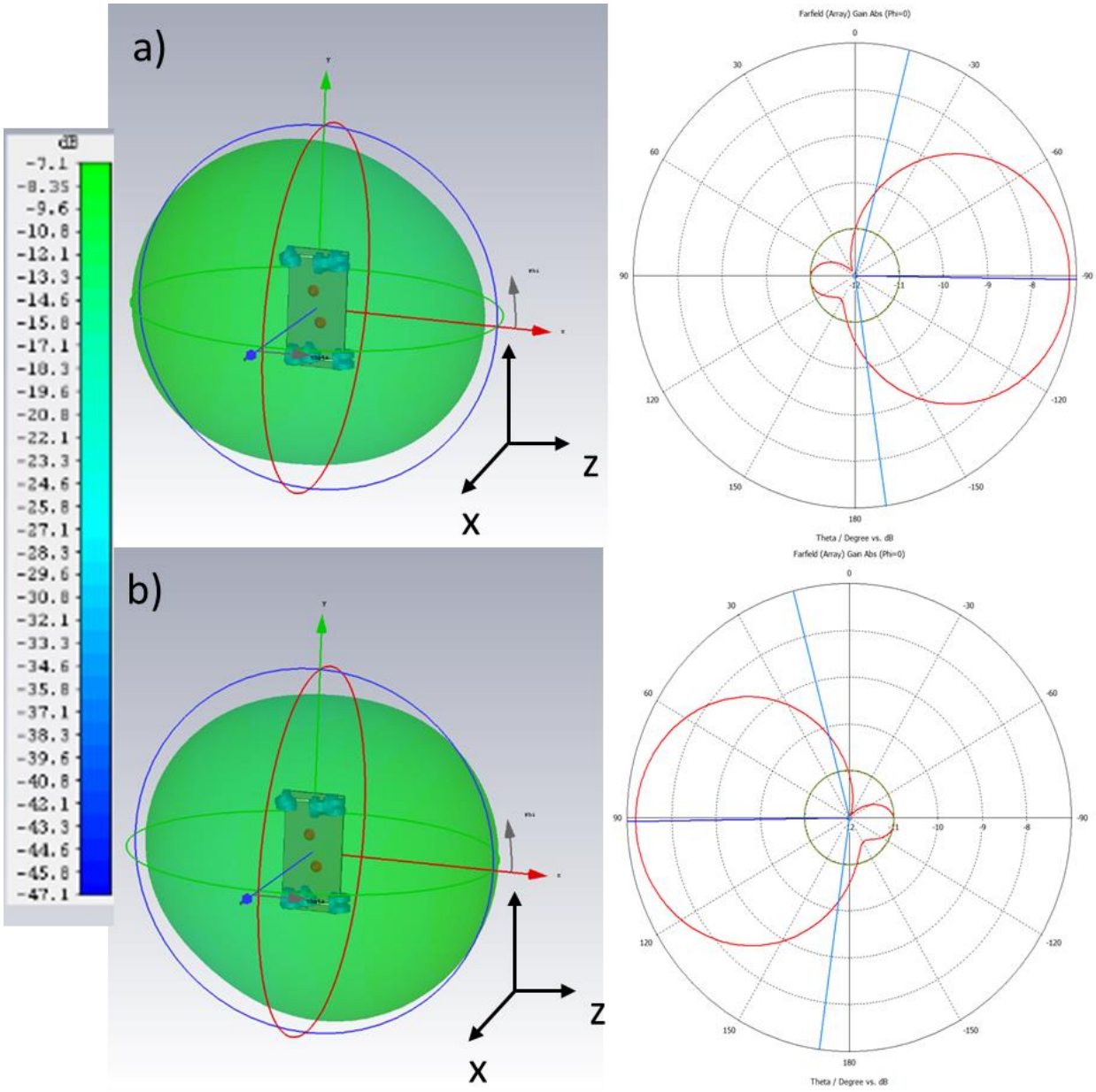

Fig. 51 Simulated 3D and polar radiation patterns for MIMO 1 at 0.7 GHz.

In Fig. 52 the simulated 3D and polar radiation patterns for MIMO 2 are presented when their Slots 1 are resonating at 0.68 GHz (a) for Antenna 1 and (b) for Antenna 2. Shapes for both patterns radiated for Antenna 1 and Antenna 2 are similar but have opposite positions.

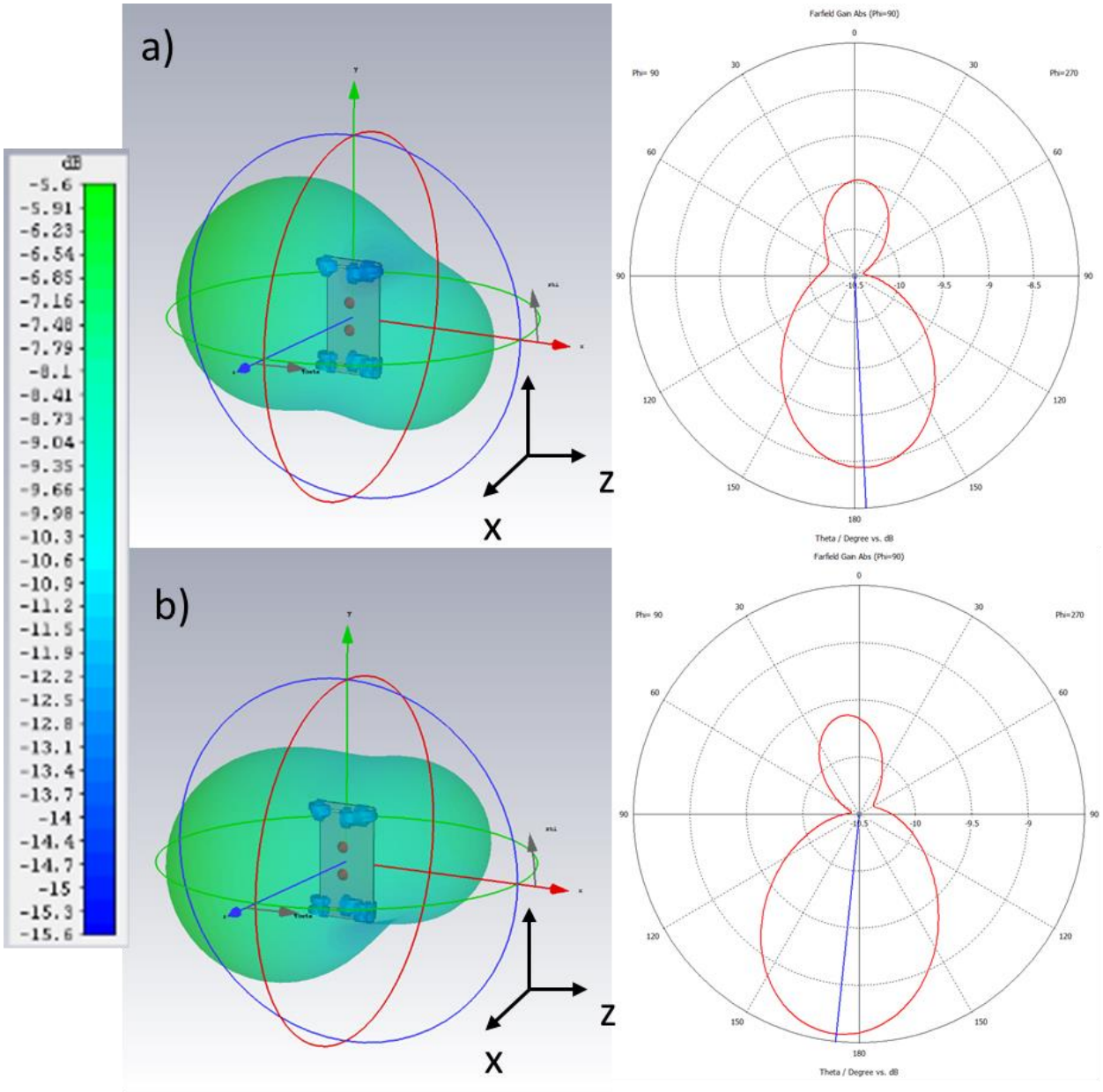

Fig. 52 Simulated 3D and polar radiation patterns for MIMO 2 at 0.68 GHz.

Then in Fig. 53 the simulated 3D and polar radiation patterns for MIMO 3 are presented, corresponding to their Slots 1 resonating at 0.749 GHz (a) for Antenna 1 and (b) for Antenna 2. Resembling shapes but flipping positions are observed for Antenna 1 and Antenna 2.

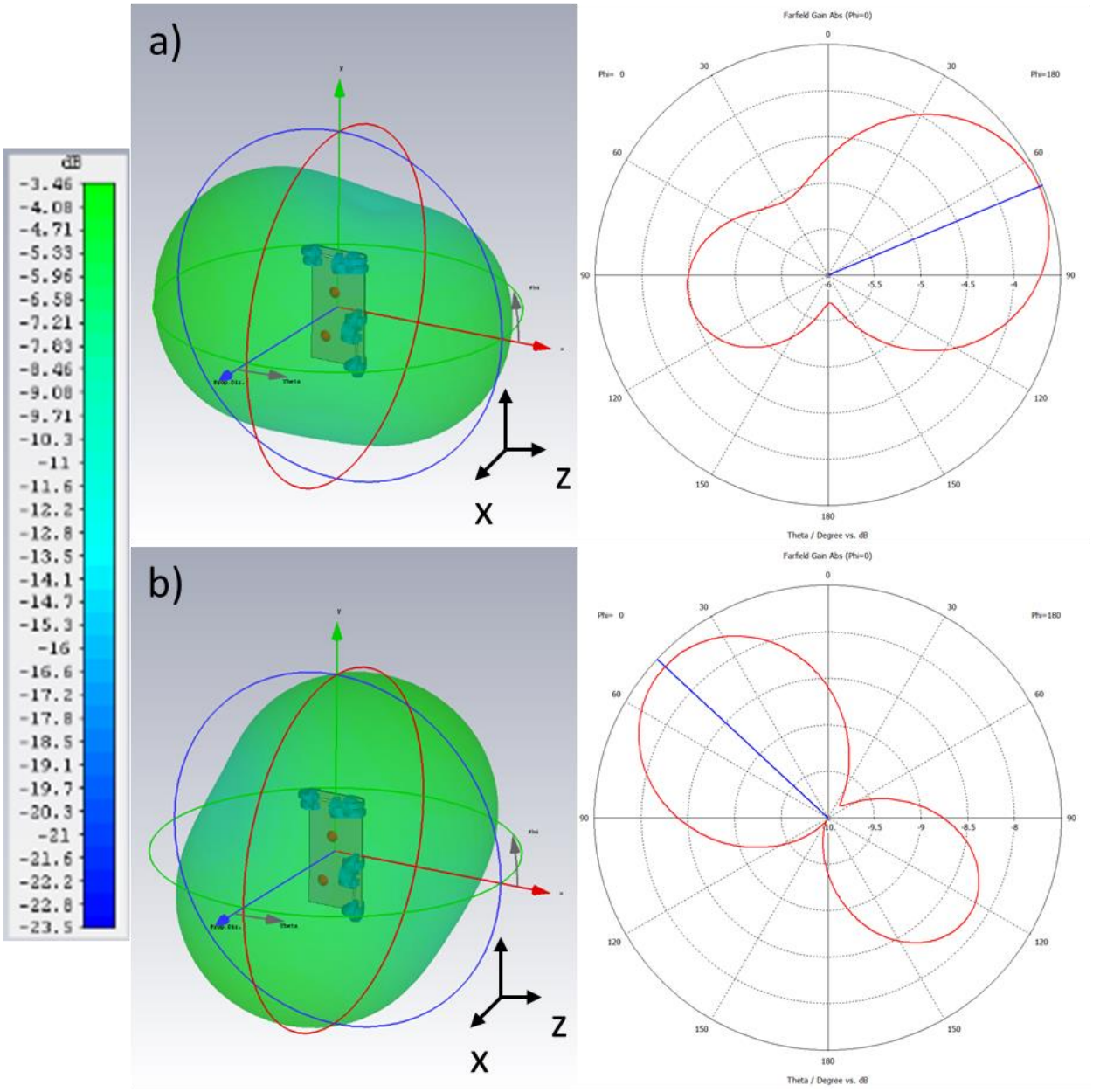

Fig. 53 Simulated 3D and polar radiation patterns for MIMO 3 at 0.749 GHz.

Fig. 54 shows the simulated 3D and polar radiation patterns for MIMO 1 when their Slots 2 are operating at 1.42 GHz (a) for Antenna 1 and (b) for Antenna 2. This resonant frequency corresponds to Band 2. We observed, like in the previous comparisons, similar shapes but opposite positions for Antenna 1 and Antenna 2.

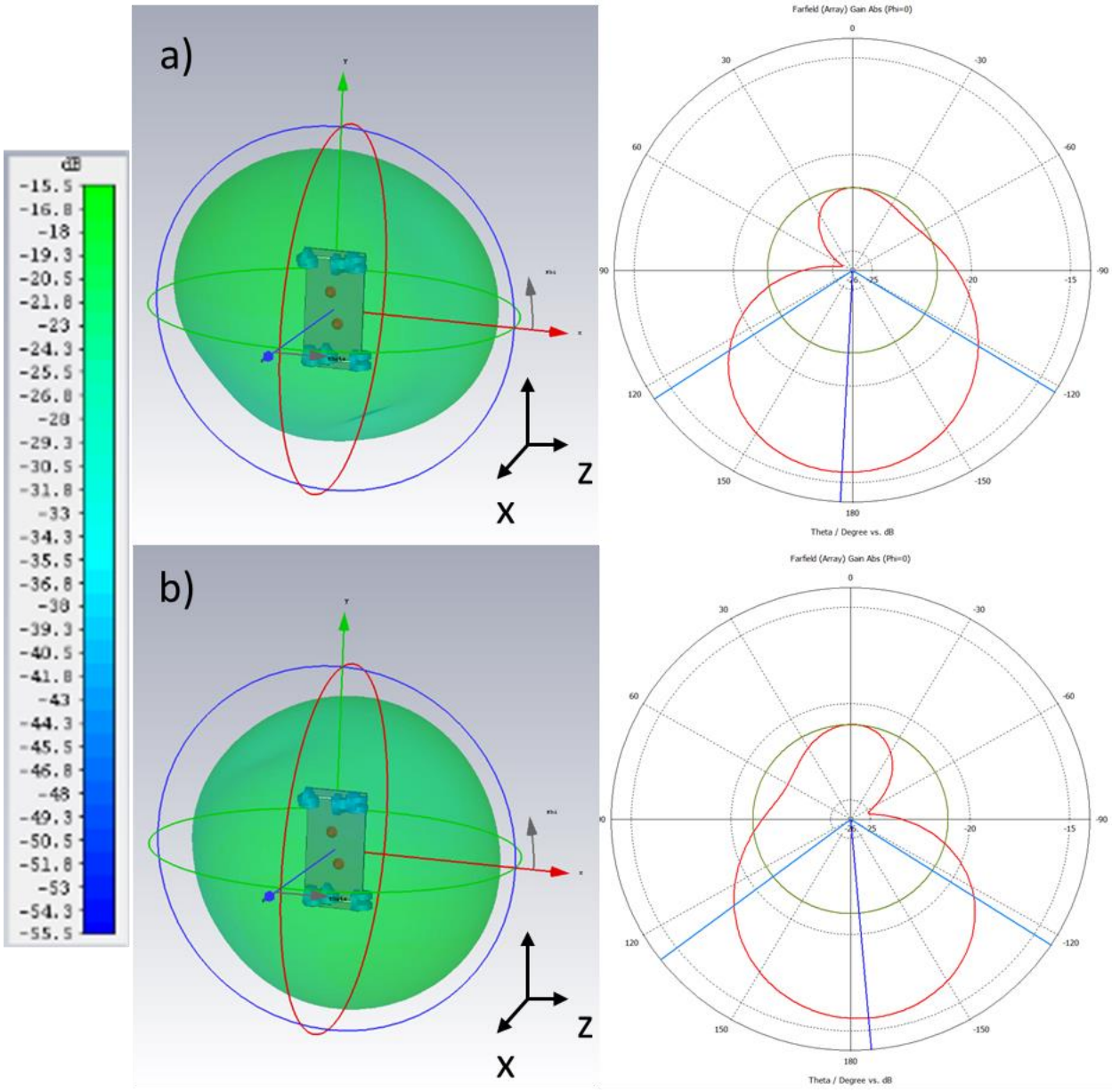

Fig. 54 Simulated 3D and polar radiation patterns for MIMO 1 at 1.42 GHz.

In Fig. 55 the simulated 3D and polar radiation patterns for MIMO 2 are shown when their Slots 2 resonate at 1.42 GHz which corresponds to Band 2 we observe the simulated patterns for (a) Antenna 1 and (b) Antenna 2. We can see similar shapes with different positions when comparing Antenna 1 and Antenna 2.

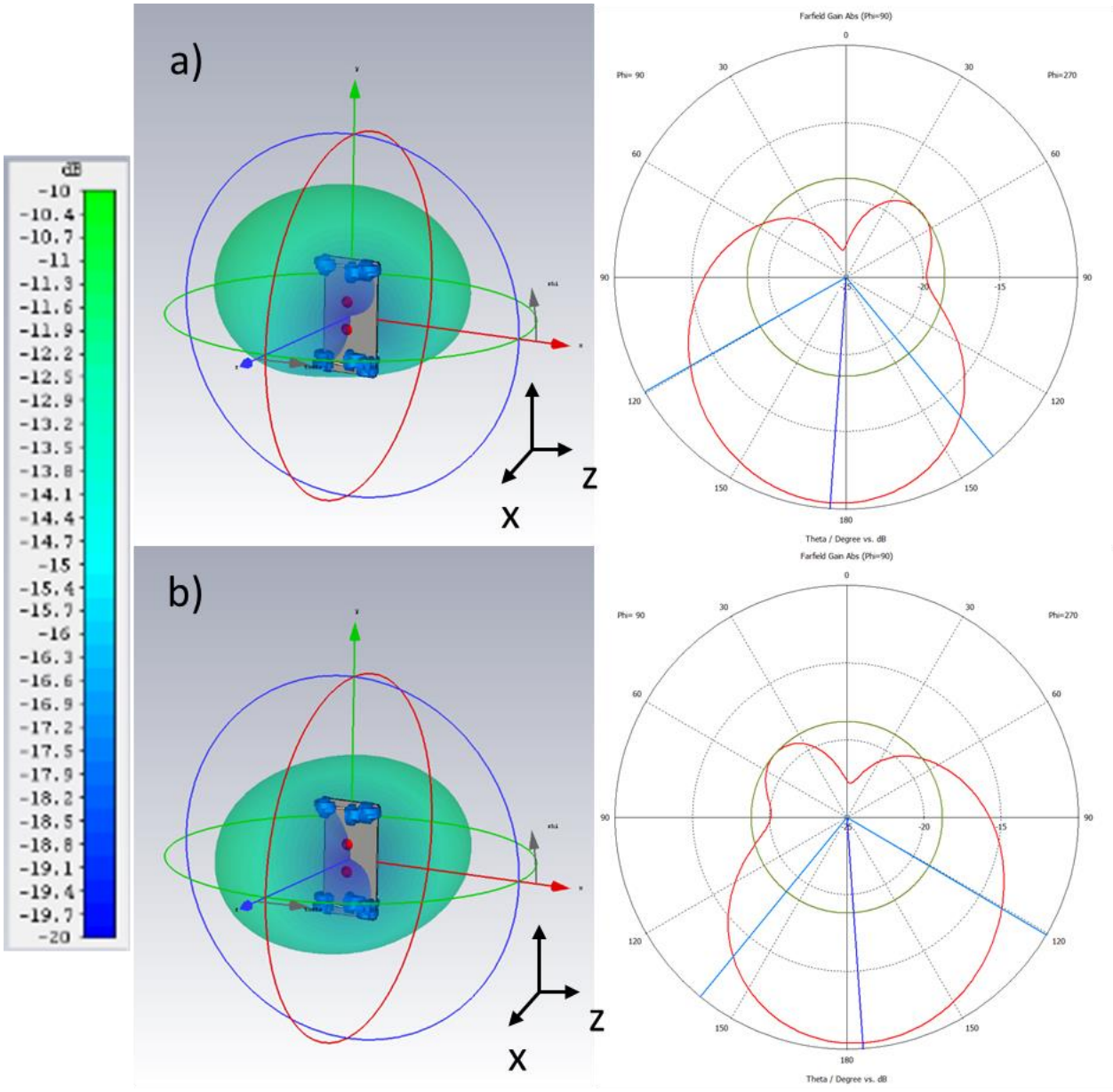

Fig. 55 Simulated 3D and polar radiation patterns for MIMO 2 at 1.42 GHz.

For the MIMO 3 prototype, in Fig. 55 the simulated 3D and polar radiation patterns are presented when their Slots 2 operating at 1.38 GHz, a resonant frequency in Band 2. Analysing the simulated patterns for (a) Antenna 1 and (b) Antenna 2 observing rather omnidirectional patterns with similar shapes but flipping positions between Antenna 1 and Antenna 2.

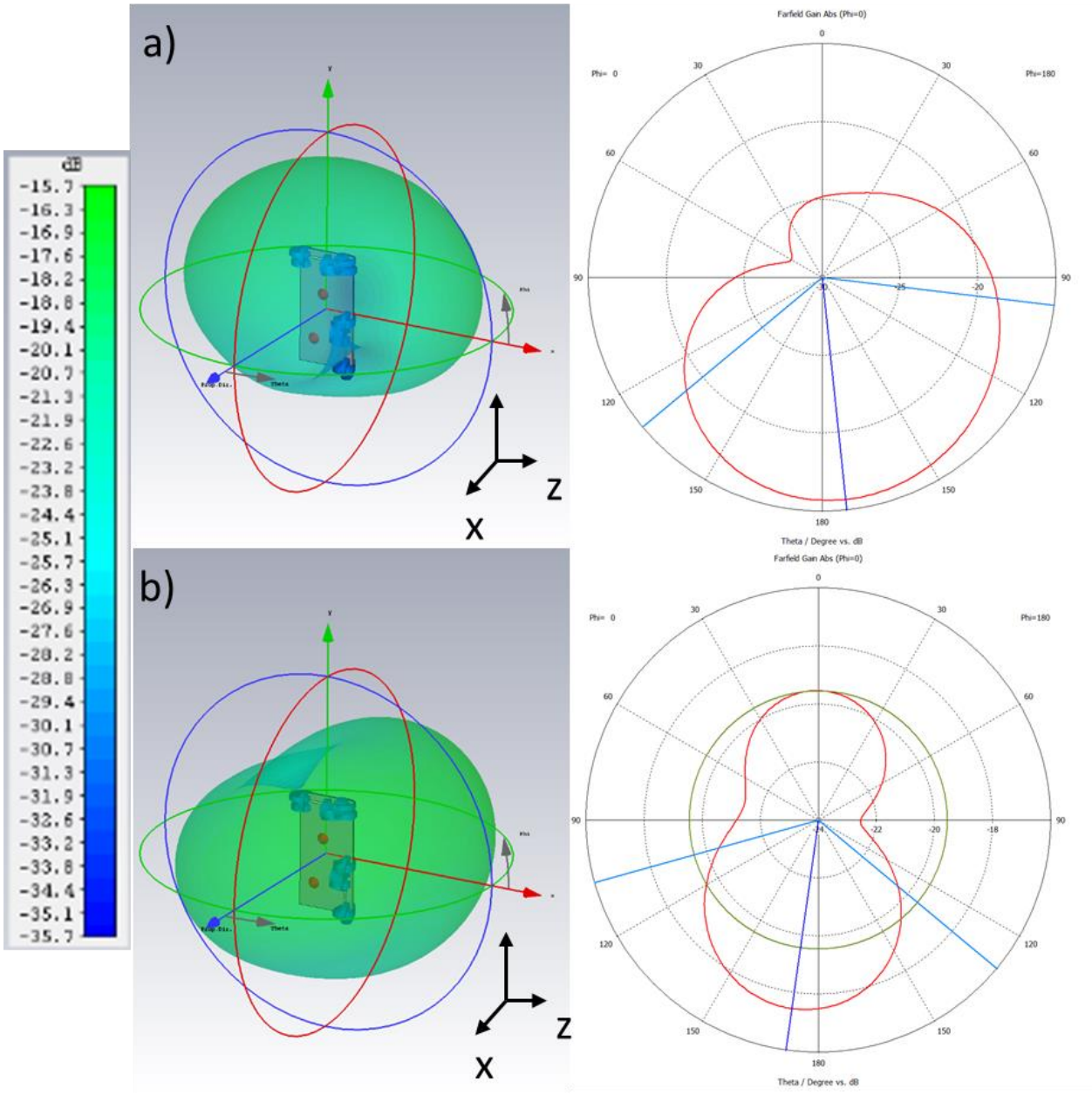

Fig. 56 Simulated 3D and polar radiation patterns for MIMO 3 at 1.38 GHz.

Now for frequencies in Band 3, in Fig. 57 the simulated 3D and polar radiation patterns are presented when their Slots 3 operating at 2.52 GHz. For (a) Antenna 1 and (b) Antenna 2 omnidirectional coverages are observed with opposite positions in Antenna 1 and Antenna 2.

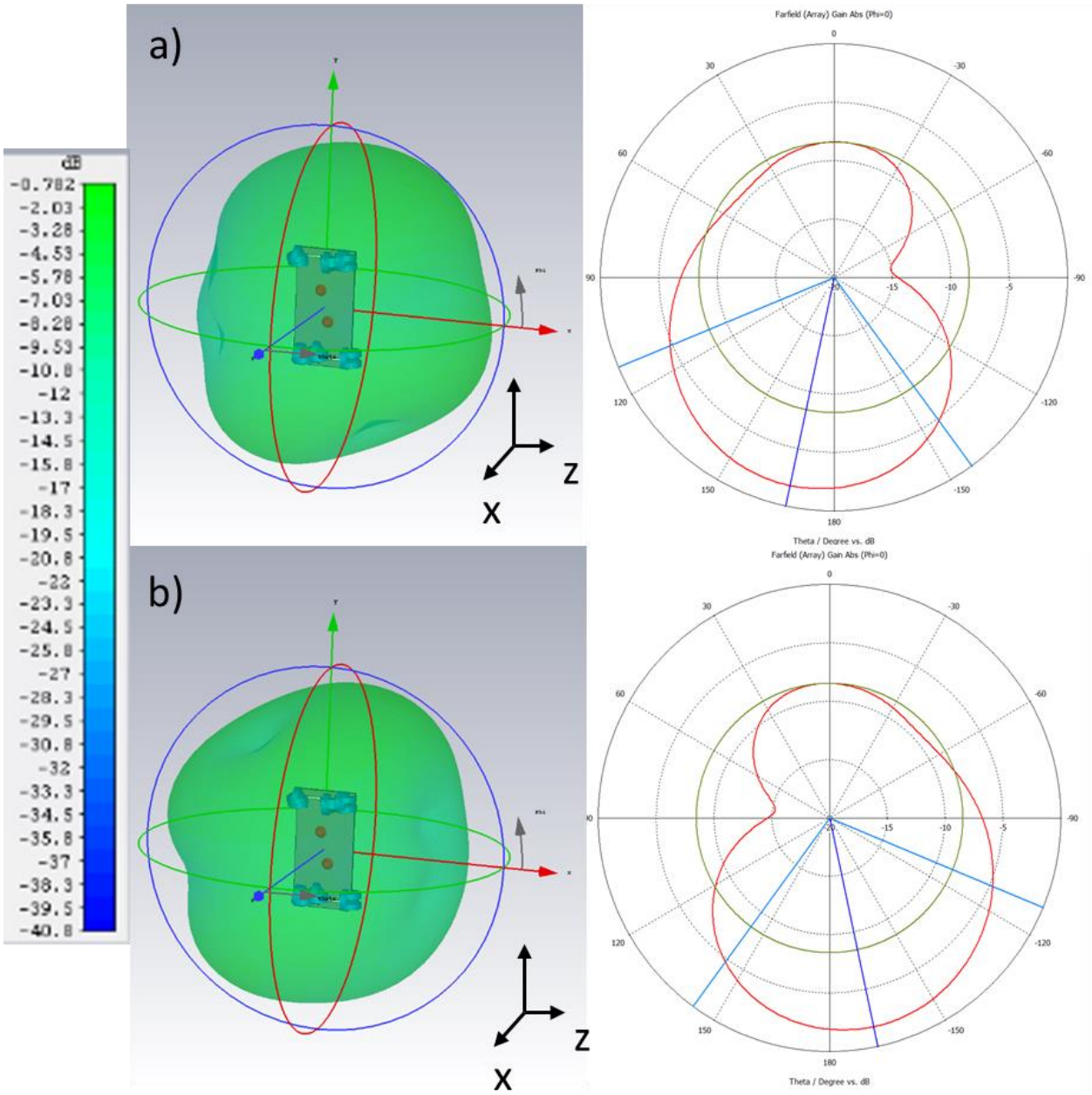

Fig. 57 Simulated 3D and polar radiation patterns for MIMO 1 at 2.52 GHz.

Then in Fig. 58 the simulated 3D and polar radiation patterns for MIMO 2 are shown when their Slots 3 resonate at 2.2 GHz. The shapes of the patterns are irregular but similar from (a) Antenna 1 to (b) Antenna 2 with different positions.

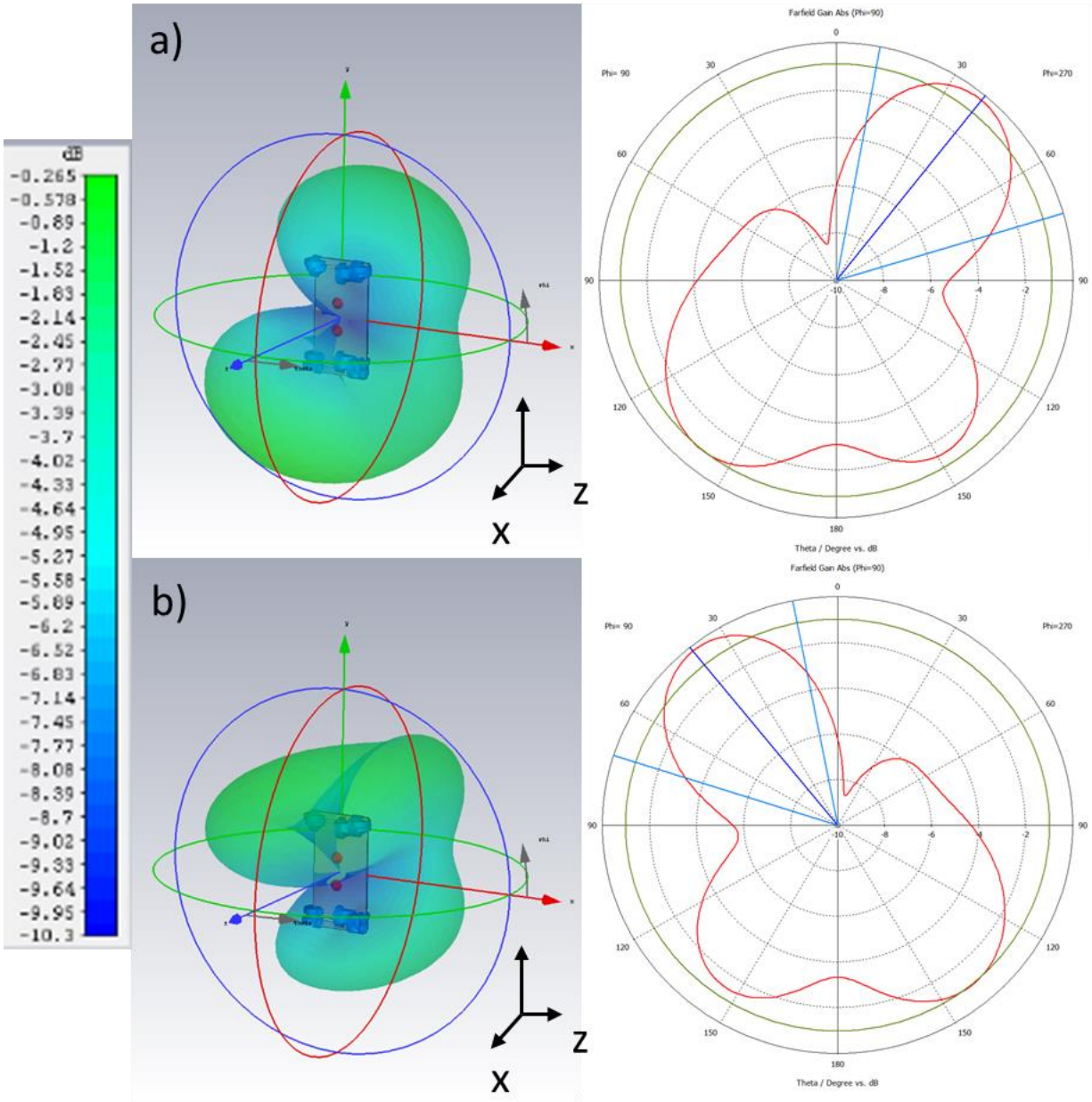

Fig. 58 Simulated 3D and polar radiation patterns for MIMO 2 at 2.2 GHz.

Finally in Fig. 59, the simulated 3D and polar radiation patterns for MIMO 3 are shown when their Slots 3 resonate at 2.65 GHz. The shapes of the patterns are resembling from (a) Antenna 1 to (b) Antenna 2 with opposite positions.

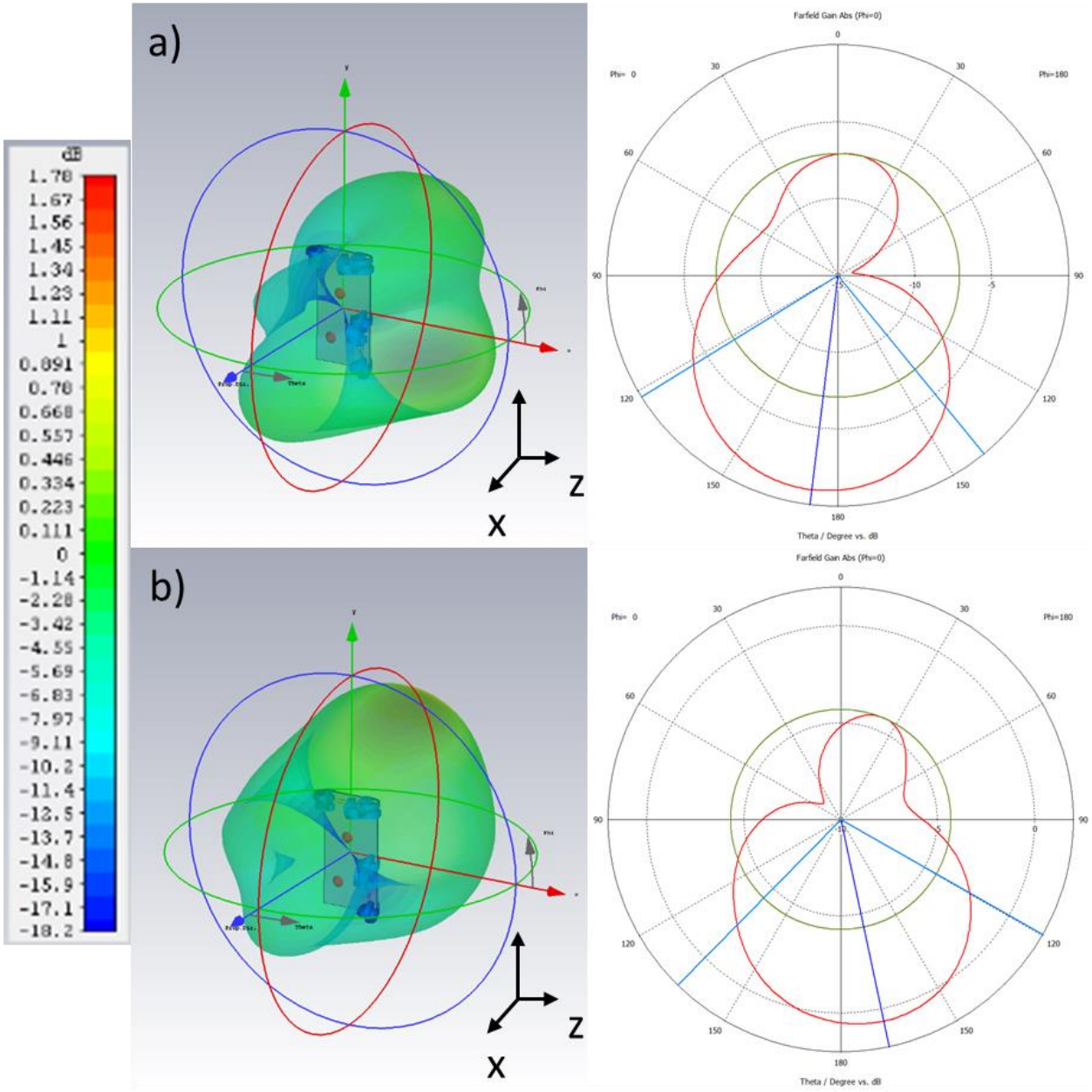

Fig. 59 Simulated 3D and polar radiation patterns for MIMO 3 at 2.65 GHz.

Overall, it has been observed for each comparison similar shapes but opposite positions as in each board the location of the slots are designed to be offering multiple areas covered by the reiterative amount of data by the same device.

The following recapitulative Table 2 Summary of simulated metrics for radiation patterns. summarises the essential metrics for the simulated radiation patterns including gain, angular width (3dB) and angle of peak gain.

Freq 1 (0.7, 0.68, 0.74 GHz)	Gain (dB)	Angular width (3dB)	Angle of peak gain (deg.)
MIMO 1 Antenna 1	-7.16 dBi	157.3º	-91º
MIMO 1 Antenna 2	-7.2 dBi	157.6º	90º
MIMO 2 Antenna 1	-8.44 dBi	143.2º	177º
MIMO 2 Antenna 2	-8.57 dBi	142.9º	174º
MIMO 3 Antenna 1	-3.54 dBi	138.1º	67º
MIMO 2 Antenna 2	-7.62 dBi	137.3º	47º
Freq 2 (1.4, 1.42, 1.38 GHz)	Gain (dB)	Angular width (3dB)	Angle of peak gain (deg.)
MIMO 1 Antenna 1	-15.6 dBi	114.5º	177º
MIMO 1 Antenna 2	-15.7 dBi	109.7º	175º
MIMO 2 Antenna 1	-10.4 dBi	99.9º	176º
MIMO 2 Antenna 2	-10.4 dBi	98.9º	176º
MIMO 3 Antenna 1	-15.7 dBi	133.5º	174º
MIMO 2 Antenna 2	-17.5 dBi	124.6º	172º
Freq 3 (2.52, 2.2, 2.65 GHz)	Gain (dB)	Angular width (3dB)	Angle of peak gain (deg.)
MIMO 1 Antenna 1	-1.82 dBi	103.7º	168º
MIMO 1 Antenna 2	-1.77 dBi	103.8º	168º
MIMO 2 Antenna 1	-0.26 dBi	62.9º	39º
MIMO 2 Antenna 2	-0.21 dBi	61.2º	39º
MIMO 3 Antenna 1	-0.99 dBi	97.6º	173º
MIMO 2 Antenna 2	0.62 dBi	104.8º	168º

Table 2 Summary of simulated metrics for radiation patterns.

3.3. Manufacture and measured results.

Once the simulated models were fully analysed and proved to be operating as expected we then proceeded to fabricate the modelled prototypes and measure their performance in order to corroborate the results obtained in simulations. Using the exact same dimensions previously calculated in the design process and exporting 2D Gerber model files from CST microwave studio in order to describe the layers from each PCB. These files were then sent to a manufacturer with a view to order the circuit boards only. Then, once the boards were received, I manually soldered the components on the boards very carefully, as well as cables that will be used as the DC voltage biasing lines later in measurements. The fabrication and measurement procedures will be discussed in this section.

3.3.1. Fabrication of prototypes

As briefly described previously, the boards were manufactured through industrial and customised procedures. The construction of the printed circuit boards for each prototype was carried out by an specialised company, but the soldering of components, as well as the DC voltage lines were manually elaborated. The components used were Infineon varactor diodes BB833 as the tuning components, 560 nH SMD inductors acting as RF chokes, SMD 680 pF capacitors acting as DC block elements, nº 22 cables as DC bias lines to control the tuning with different colour, a ground cable black coloured and SMA connectors as feeding ports. However, the fact of using DC biasing lines might introduce interferences or undesired effects due to the current flowing through these cables and consequently EM radiation.

In order to remove the antenna effects caused by the cables that control the varactors a shielding was implemented. The shielding was provided by an RFI and EMI shielding tape wrapping up the set of cables that control thee varactors and might add external interferences. Using a shielding tap reduces considerably the external signals emitted by components, such as self-resonance frequencies or in this case antenna effects from the cables. Shielding tape contains the undesired signals produced by the components wrapped by it and protect the surrounding elements from the PCB.

As the finished product, in Fig. 60 a detailed and zoomed view of the elements described and their locations are presented. This is the fabricated prototype MIMO 1 in their (a) feed line view and (b) ground plane view with their respective dimensions and positions.

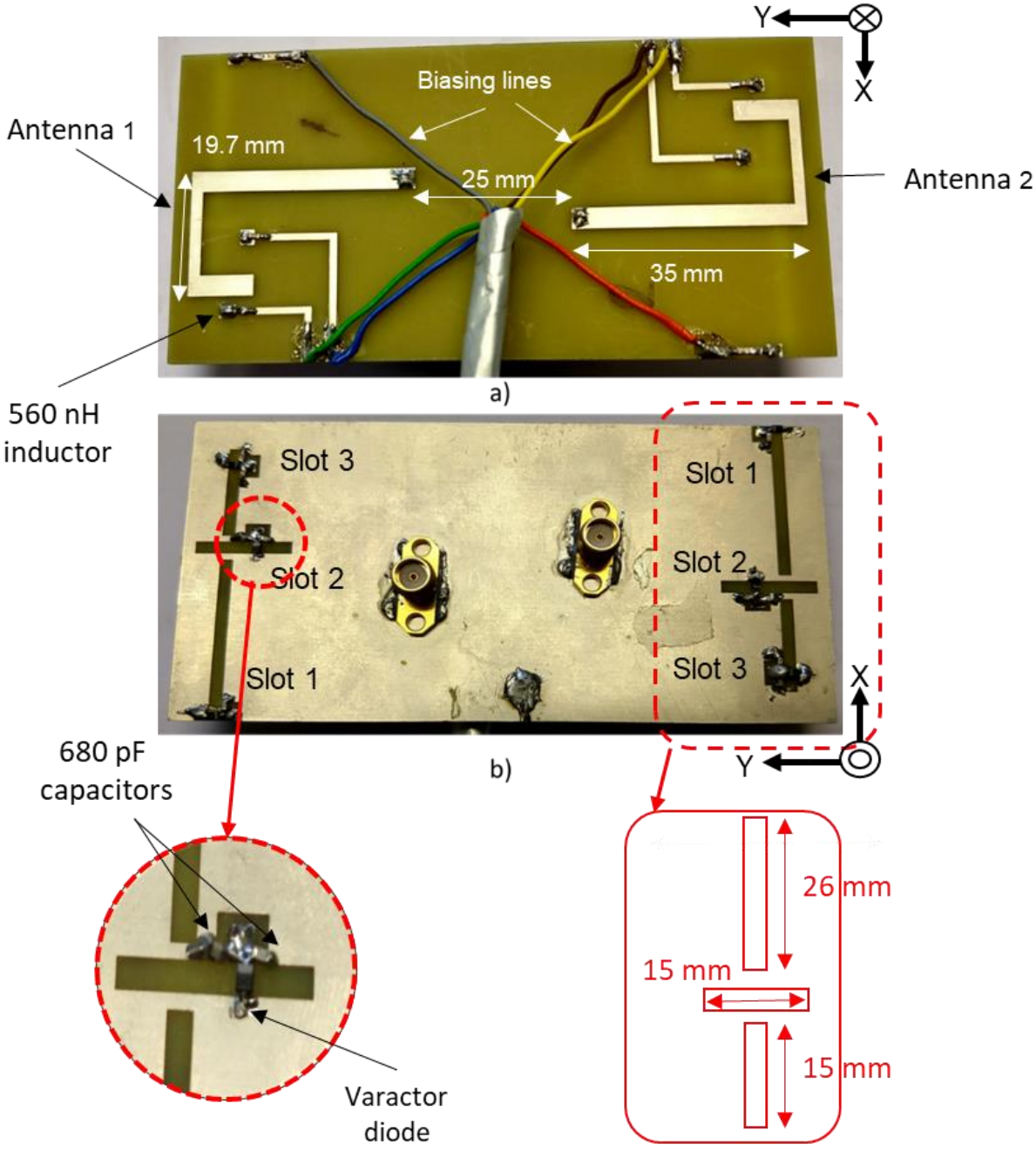

Fig. 60. Detailed and zoomed view of fabricated prototype MIMO 1.

Furthermore, each of the fabricated prototypes will be presented, including its respective elements, including the DC biasing lines. In Fig. 61 (a) feed line view and (b) ground plane view of MIMO 1 are shown respectively, the corresponding location of components and DC biasing voltage lines can also be observed.

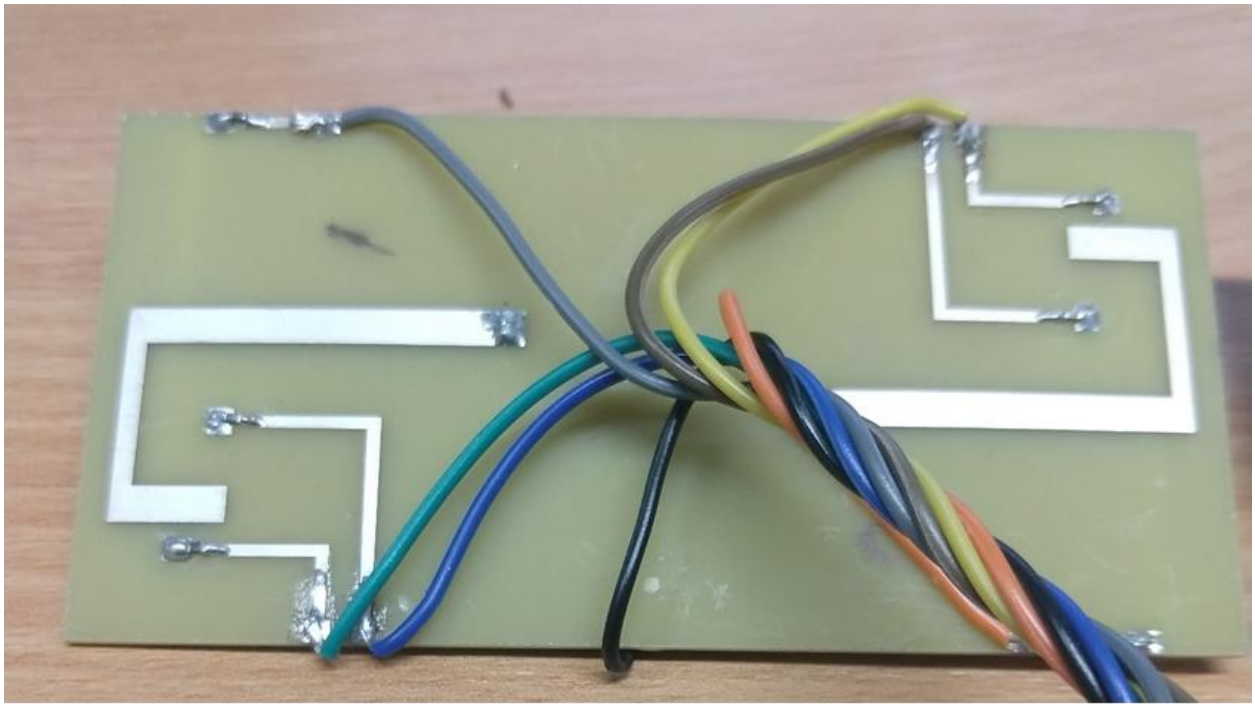

a)

b)

Fig. 61 Feed lines and ground plane views of fabricated prototype MIMO 1.

Secondly, in Fig. 62 the fabricated prototype for MIMO 2 is presented. Showing the (a) feed line view and (b) ground plane view including their DC biasing voltage lines and components and their different position of elements.

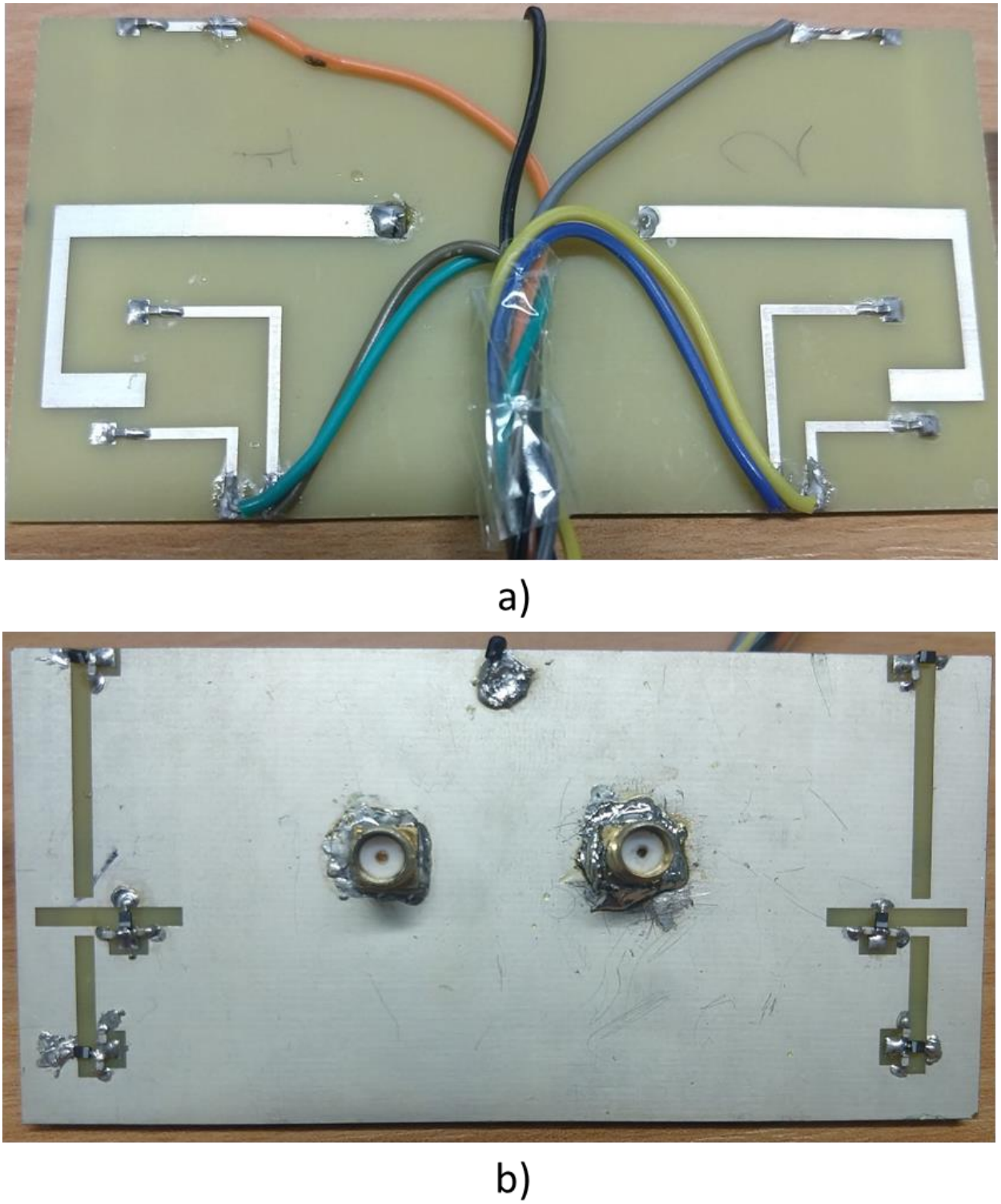

Fig. 62 Feed lines and ground plane views of fabricated prototype MIMO 2.

Finally, in Fig. 63, the fabricated prototype for MIMO 2 is presented. Where the (a) feed line view and (b) ground plane view are observed with their DC biasing voltage lines and components and clearly highlighting the opposite position of each antenna.

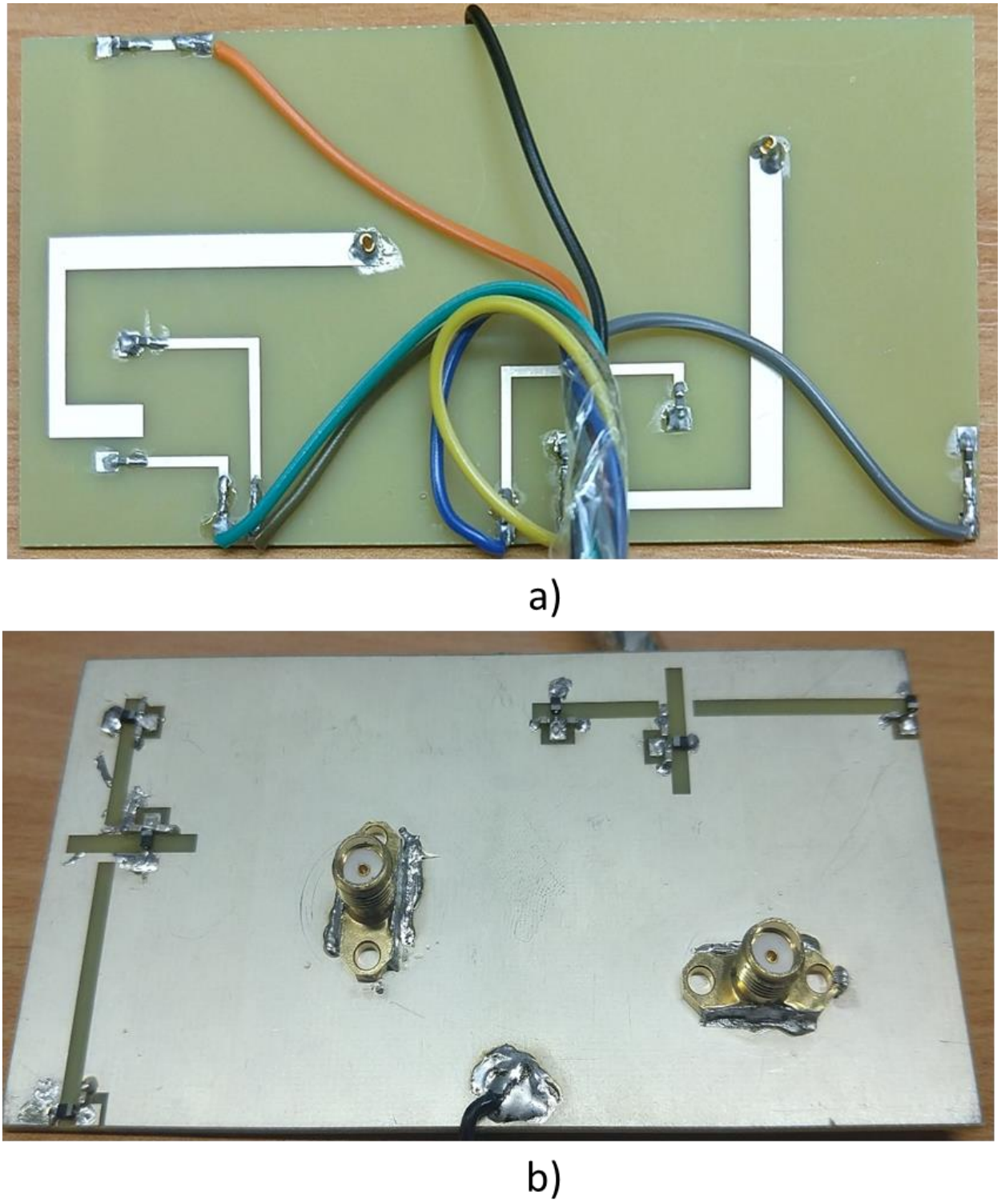

Fig. 63 Feed lines and ground plane views of fabricated prototype MIMO 3.

3.3.2. Measured S-Parameters.

With the fabricated prototypes described, this section discusses the measured reflection coefficients, using the same values of capacitance varied in simulation. The used varactor (Infineon BB833) offers a tunable capacitance from 9.3 pF to 0.75 pF when voltages from 1V to 28V are applied respectively after consulting the datasheet of varactor Infineon BB833. As presented in Table 3 below.

Band 1, voltage applied in biasing line and capacitance of D1	Band 2, voltage applied in biasing line and capacitance of D2	Band 3, voltage applied in biasing line and capacitance of D3
4.1 V – 4.0 pF	4.1 V – 4.0 pF	9.0 V – 1.5 pF
4.7 V – 3.5 pF	4.7 V – 3.5 pF	10.3 V – 1.0 pF
5.2 V – 3.0 pF	5.2 V – 3.0 pF	15.0 V – 0.7 pF
6.1 V – 2.5 pF	6.1 V – 2.5 pF	20.0 V – 0.6 pF
7.0 V – 2.0 pF	7.0 V – 2.0 pF	25.0 V – 0.5 pF
9.0 V – 1.5 pF	8.0 V – 1.7 pF	
10.3 V – 1.0 pF	9.0 V – 1.5 pF	
25.0 V – 0.5 pF	10.3 V – 1.0 pF	

Table 3 DC voltages and their respective capacitance values for D1, D2 and D3 in each fabricated prototype.

The method used to measure the fabricated prototypes was to apply a voltage through each varactor diode loading their respective slot in order to vary their capacitances. With a view to demonstrate that each band as an independent tuning, we applied a voltage to the three varactors in each antenna simultaneously, keeping two bands fixed and tuning one. For this purpose, we will use three different power supplies which are gradually controllable and will provide fix voltages and a tuning value for the band studied in question.

Fig. 64 shows the protocol used to measure the tuning range for each board using the network analyser that will plot the resonant frequencies when varying the voltage of the band being tuned and the fixed resonant frequencies for the un changed bands as well as the antennas being measured and one of the power supplies used to tune capacitances.

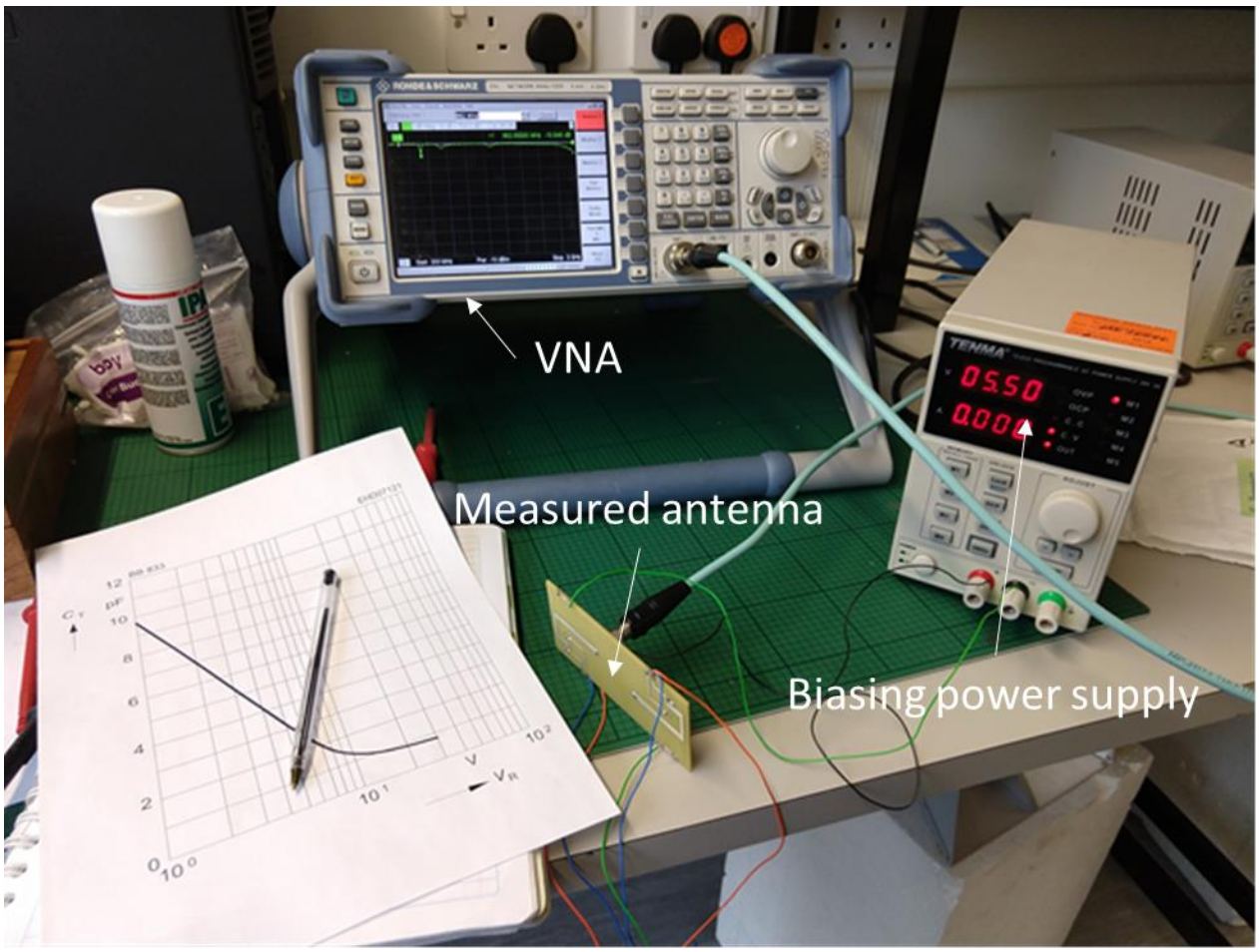

Fig. 64 Network analyser system measuring tuning ranges of MIMO 1 using a variable power supply.

The complete measured frequency range achieved via tuning when varying D1, D2 and D3 capacitances was 0.572 GHz to 2.73 GHz. detailing for each band as follows:

- Band 1 frequency range 0.572 – 1.17 GHz.
- Band 2 frequency range 1.15 – 1.98 GHz.
- Band 3 frequency range 1.68 – 2.73 GHz.

The set of measurements carried out using the protocol above described corresponds to the independent reconfiguration in frequency for each slot and the full coverage in frequency of the studied devices.

Overall, the band tuned in question does not affect the performance of the other two bands. The measured reflection coefficients will be now discussed, comparing the three boards tuning at the same capacitance similar to the results discussed in section 3.2.2 specifying the values for the voltage and hence the capacitance for the band tuned and also for the fixed bands remaining unaltered.

For MIMO 1, in Fig. 65 are shown the measured S_{11} parameters corresponding to Antenna 1 in boards (a) MIMO 1, (b) MIMO 2 and (c) MIMO 3 when tuning Band 1 varying the DC biasing voltage applied in D1 from 4.1 V – 25.0 V and hence controlling their capacitance from 4.0 – 0.5 pF. Keeping the voltages of D2 and D3 statically at 6.1 V / 2.5 pF for Band 2 and 10.3 V / 1.0 pF for Band 3, respectively.

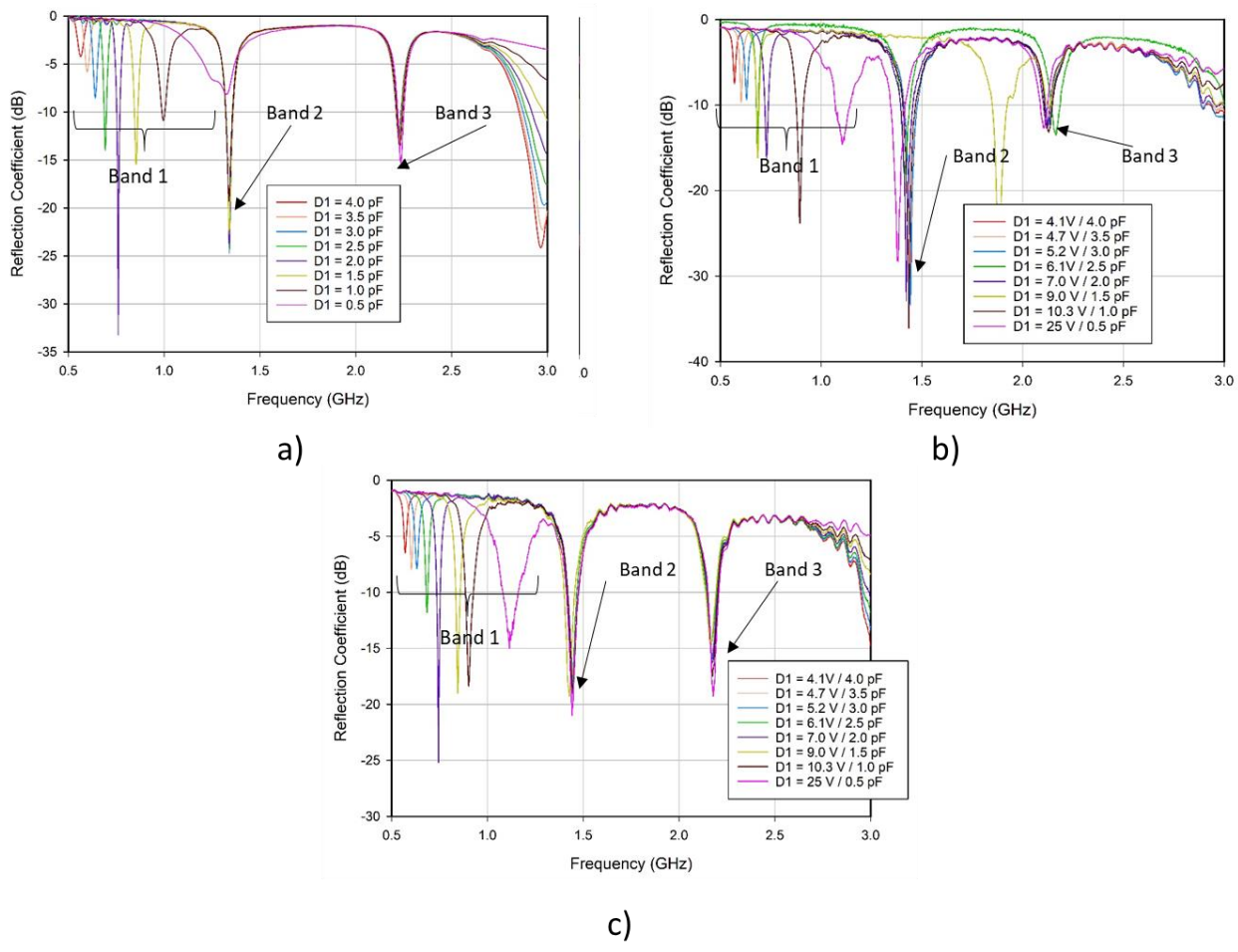

Fig. 65 Measured S_{11} Parameters for MIMO 1, 2 and 3 tuning Band 1.

Also for MIMO 1 but now analysing Antenna 2, in Fig. 66 are shown the measured S_{22} parameters corresponding to Antenna 2 in boards (a) MIMO 1, (b) MIMO 2 and (c) MIMO 3. Similar to the previous figure when tuning Band 1 varying the DC biasing voltage applied in D1 from 4.1 V – 25.0 V and hence controlling their capacitance from 4.0 – 0.5 pF, with the voltages of D2 and D3 remaining at 6.1 V / 2.5 pF for Band 2 and 10.3 V / 1.0 pF for Band 3 respectively.

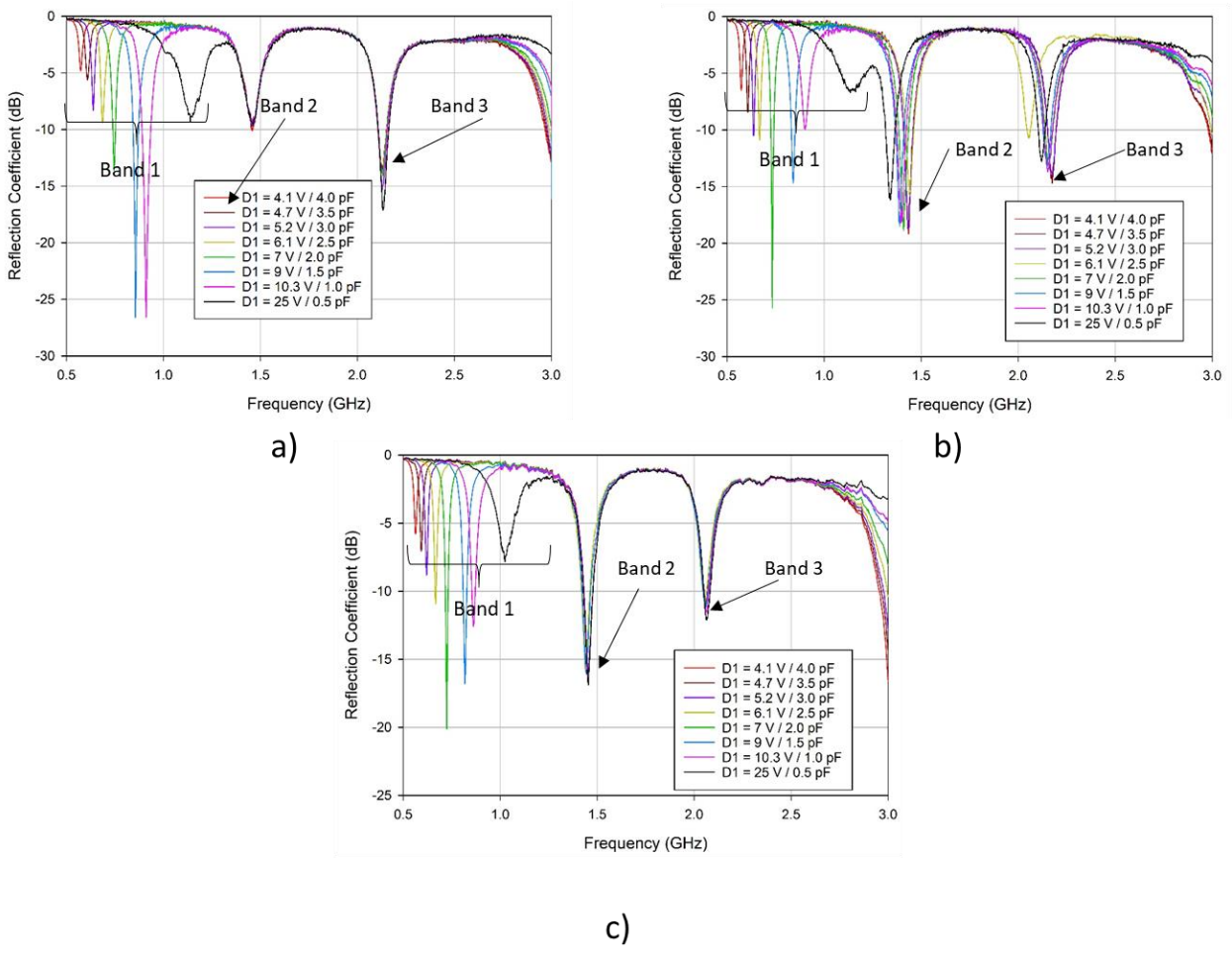

Fig. 66 Measured S_{22} Parameters for MIMO 1, 2 and 3 tuning Band 1.

Secondly, for Band 2, in Fig. 67 are presented the measured S_{11} parameters corresponding to Antenna 1 in boards (a) MIMO 1, (b) MIMO 2 and (c) MIMO 3 while the frequency band is being tuned by varying the DC biasing voltage applied in D2 from 4.1 V – 10.3 V controlling therefore their capacitance from 4.0 – 1.0 pF, with the voltages of D1 and D3 remaining at 6.1 V / 2.5 pF for Band 1 and 10.3 V / 1.0 pF for Band 3 respectively.

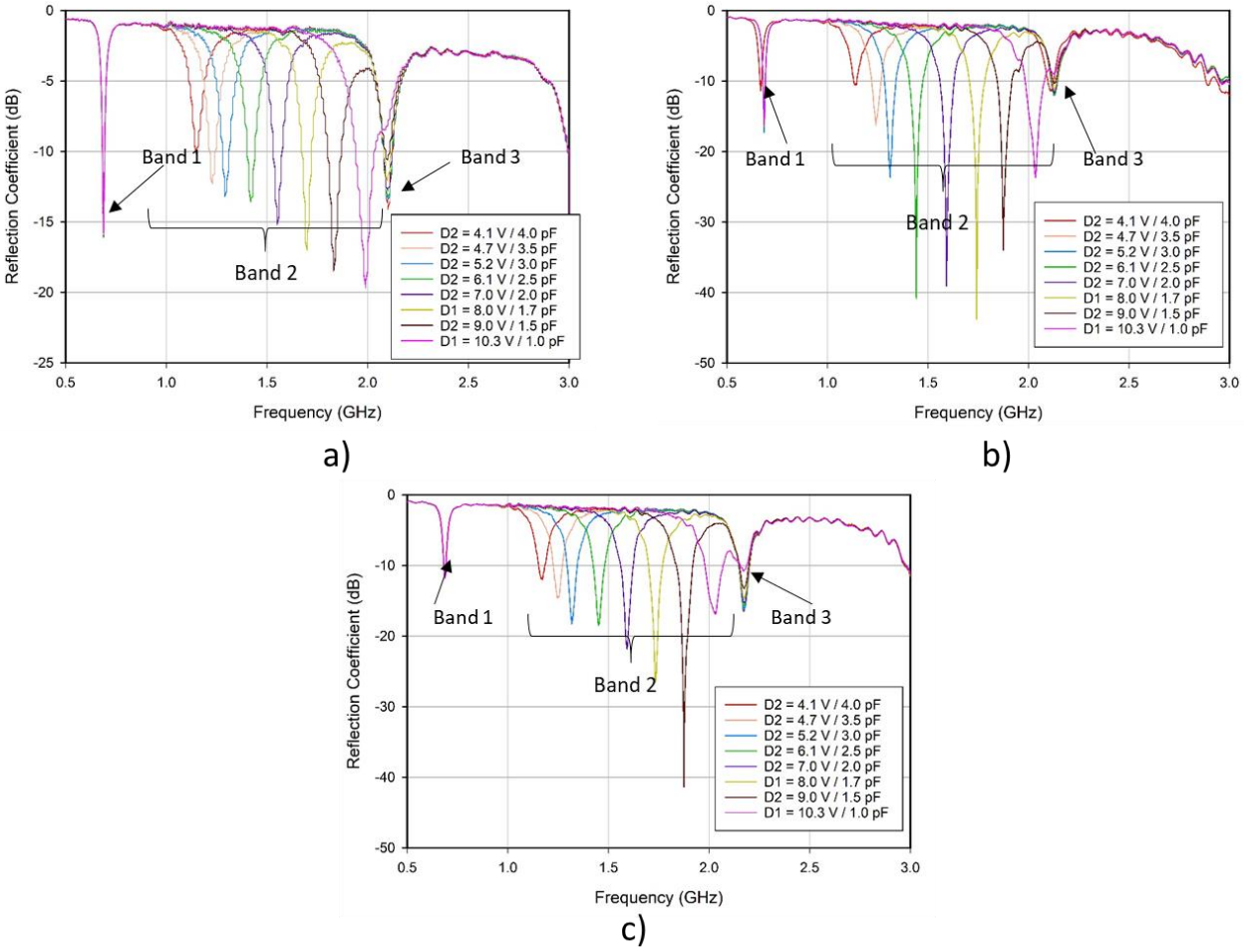

Fig. 67 Measured S_{11} Parameters for MIMO 1, 2 and 3 tuning Band 2.

Now for Antenna 2, in Fig. 68 the measured S_{22} parameters are presented corresponding to Antenna 2 in boards (a) MIMO 1, (b) MIMO 2 and (c) MIMO 3 while Band 2 is being tuned by varying the DC biasing voltage applied in D2 from 4.1 V – 10.3 V controlling therefore their capacitance from 4.0 – 1.0 pF, with the voltages of D1 and D3 remaining at 6.1 V / 2.5 pF for Band 1 and 10.3 V / 1.0 pF for Band 3 respectively.

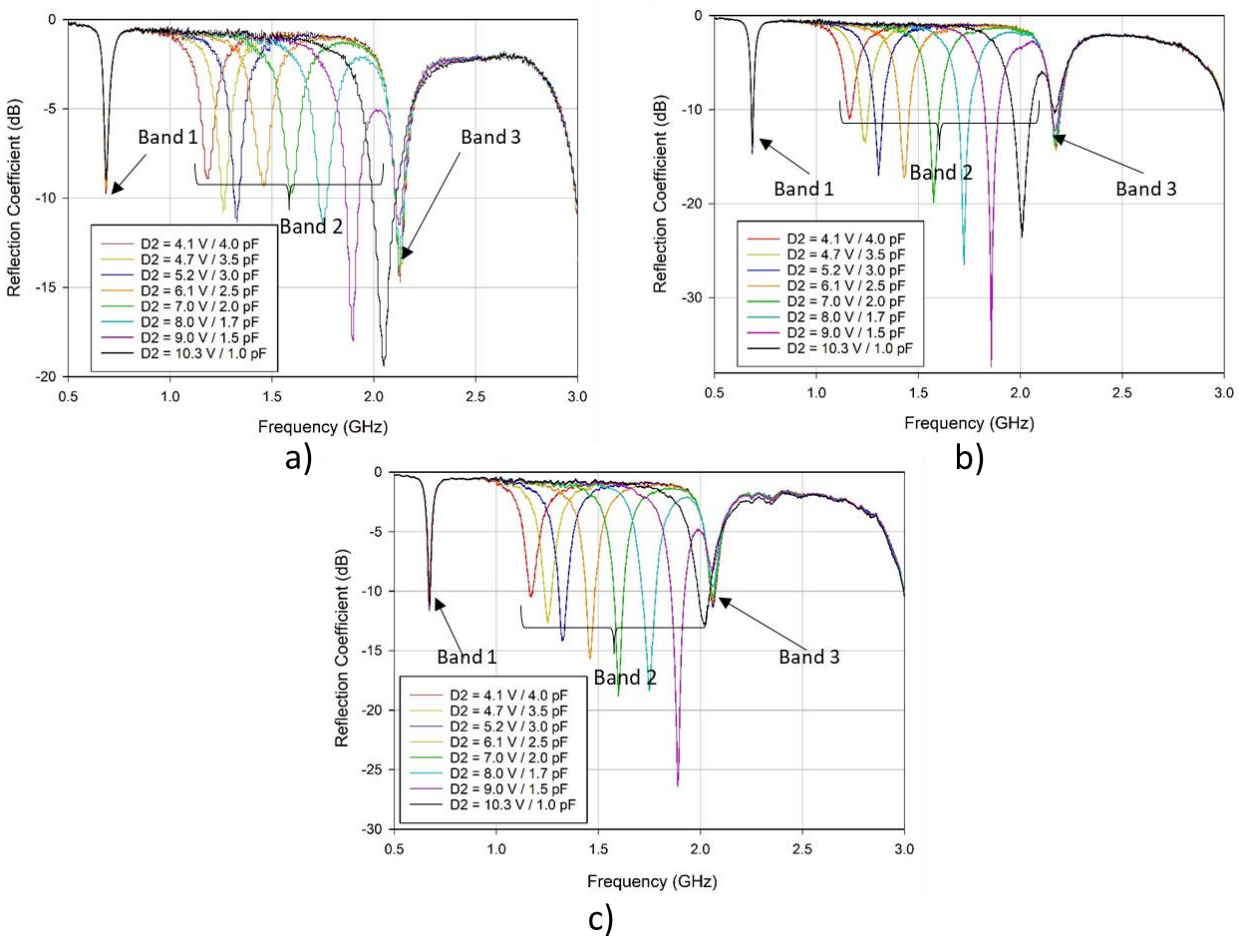

Fig. 68 Measured S_{22} Parameters for MIMO 1, 2 and 3 tuning Band 2.

Finally, for the S-parameters analysis, in Fig. 69 the measured S_{22} parameters are presented corresponding to Antenna 1 in boards (a) MIMO 1, (b) MIMO 2 and (c) MIMO 3 while Band 3 is being tuned by varying the DC biasing voltage applied in D3 from 9.0 V – 25.0 V controlling hence their capacitance from 1.0 – 0.5 pF, given these values are in the non-linear region of the characterisation of the varactor Infineon BB833. With the voltages of D1 and D2 kept at 6.1 V / 2.5 pF for Band 1 and Band 2.

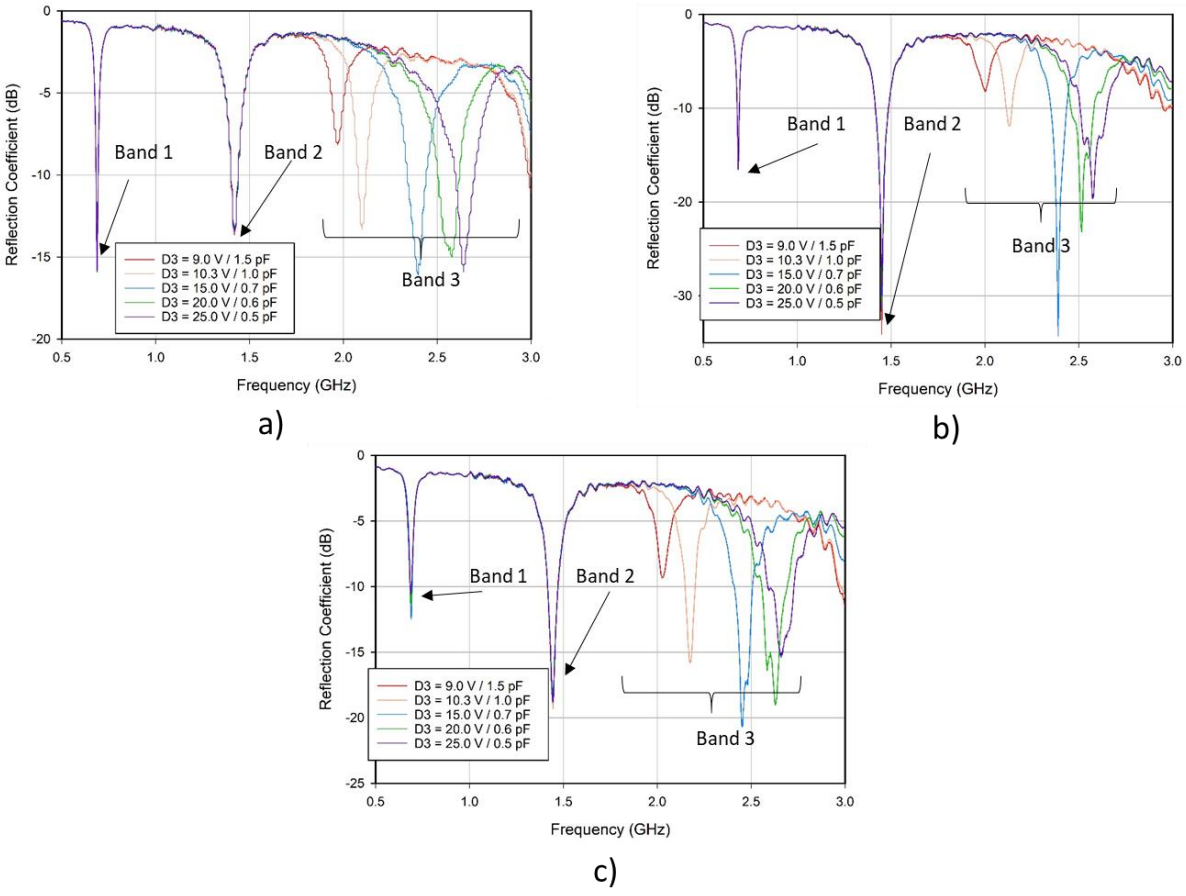

Fig. 69 Measured S_{11} Parameters for MIMO 1, 2 and 3 tuning Band 3.

In Fig. 70, the measured S_{22} parameters are shown corresponding to Antenna 2 in boards (a) MIMO 1, (b) MIMO 2 and (c) MIMO 3 while Band 3 is being tuned by varying the DC biasing voltage applied in D3 from 9.0 V – 25.0 V controlling hence their capacitance from 1.0 – 0.5 pF, with the voltages of D1 and D2 kept at 6.1 V / 2.5 pF for Band 1 and Band 2.

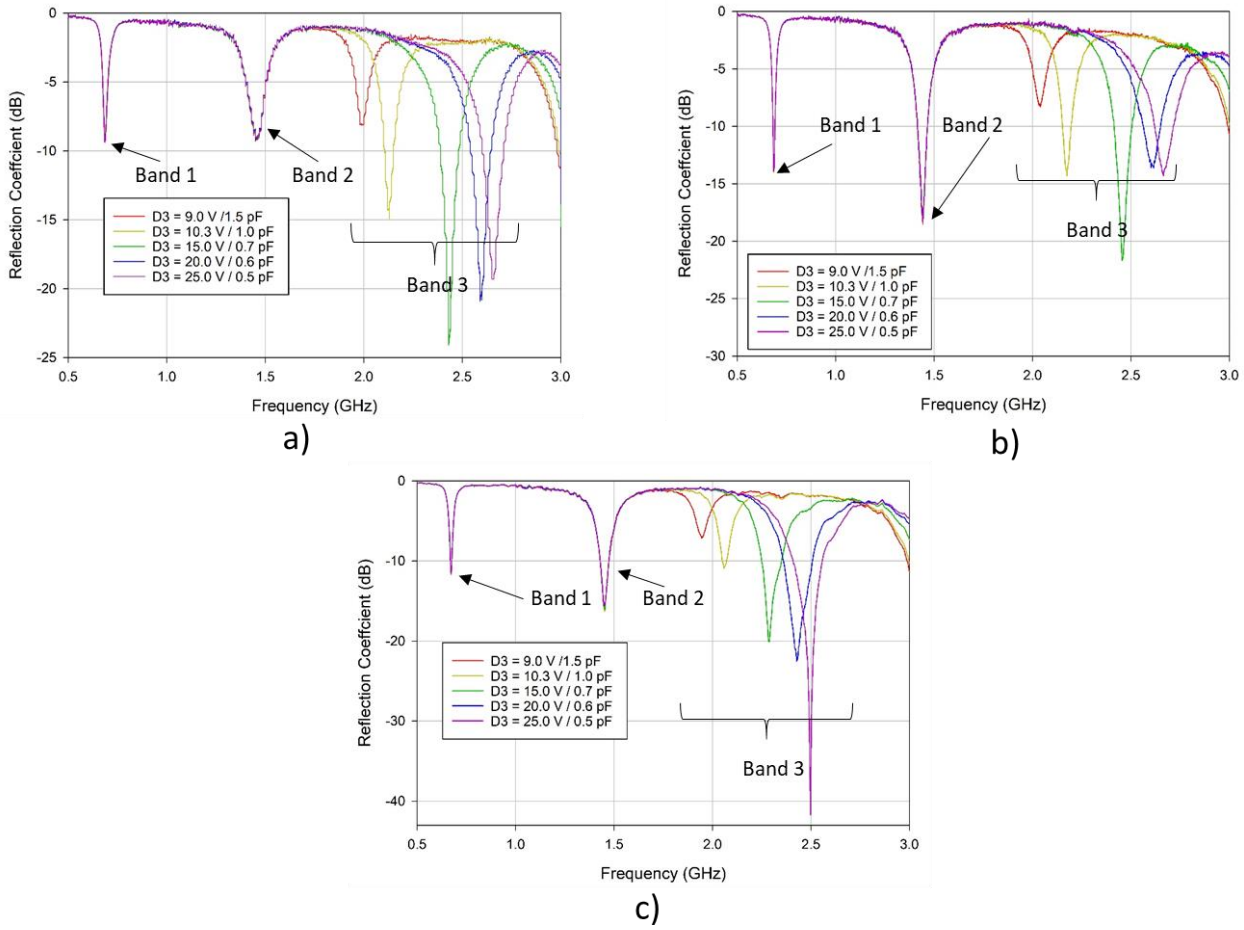

Fig. 70 Measured S_{22} Parameters for MIMO 1, 2 and 3 tuning Band 3.

After analysing the measured reflection coefficients in the previous figures, it was observed that the frequency bands are tuned independently and do not affect the unaltered resonant frequencies which happens not only from slot to slot but also from antenna to antenna, proving that the independent tuning is achievable in a board with two antennas simultaneously operating.

Furthermore, when comparing the three prototypes at the same frequency, the following Fig. 71, Fig. 72 and Fig. 73 are discussed next. This analysis presents the three prototypes working at the same given frequencies in order to analyse the agreement among prototypes.

In Fig. 71, the comparison of MIMO 1, 2 and 3 when tuning D1 at 7V / 2.0 pF is shown, where an agreement for S_{11} and S_{22} parameters for each board is observed. Nevertheless, the unchanged bands 2 and 3 differ slightly from a board to the other.

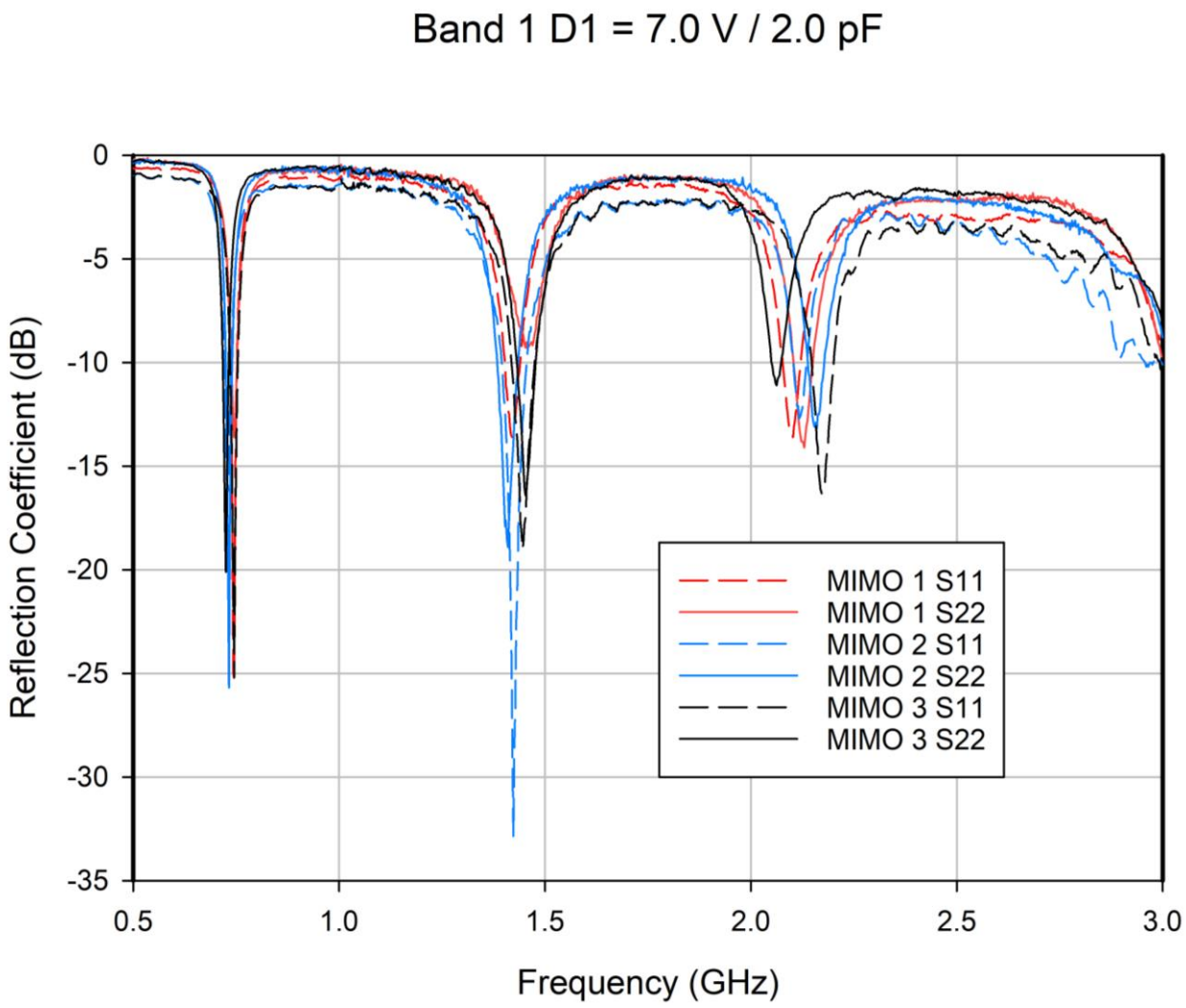

Fig. 71 Comparison of MIMO 1, 2 and 3 tuning their D1 at the same value.

In Fig. 72, the comparison of MIMO 1, 2 and 3 when tuning D2 at 7V / 2.0 pF is presented, similar to previous figures a good agreement for S_{11} and S_{22} parameters is observed for each board. Bands 2 and 3 which are not tuned have not dramatically change from a board to the other.

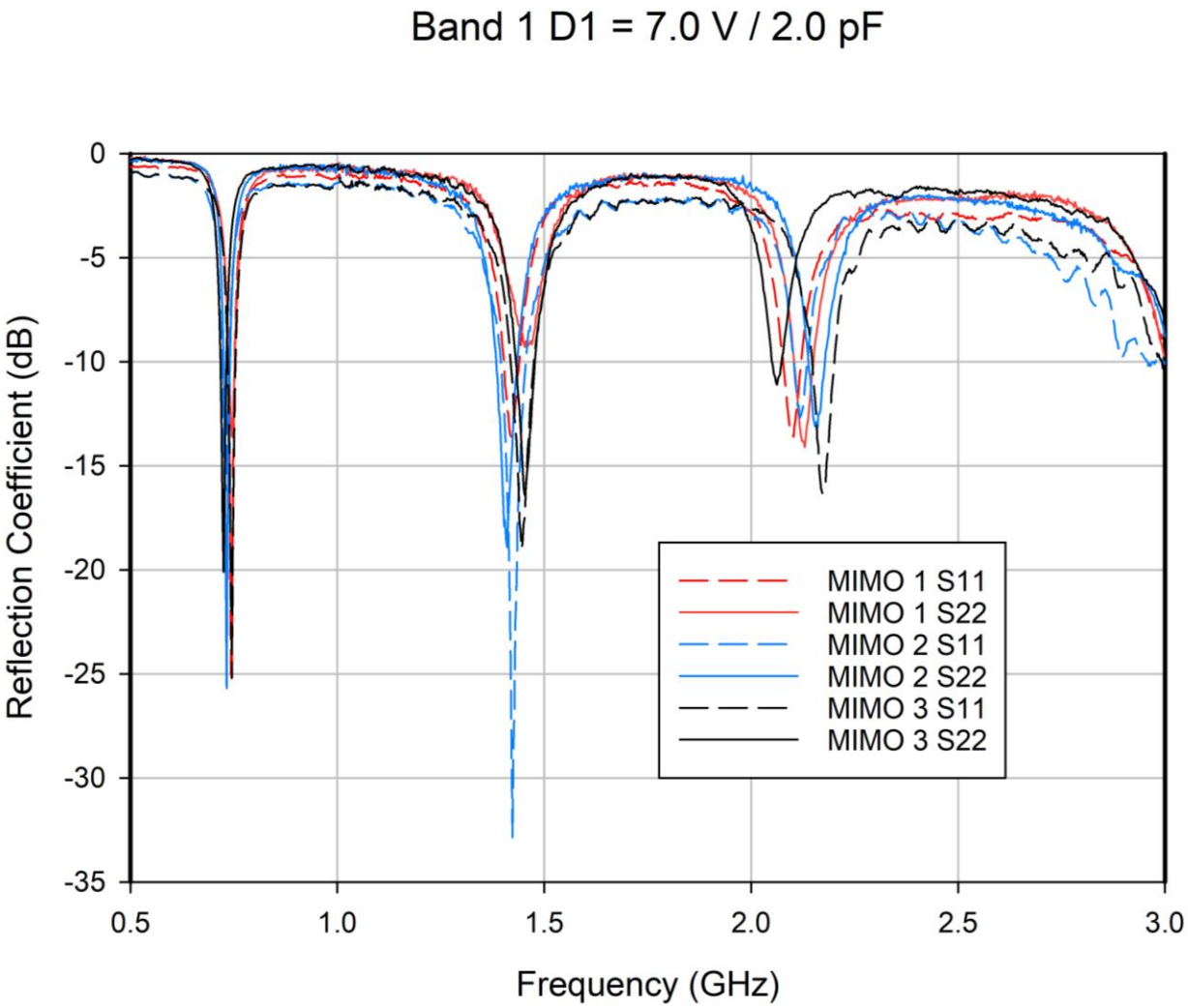

Fig. 72 Comparison of MIMO 1, 2 and 3 tuning their D2 at the same value.

In Fig. 73, the comparison of MIMO 1, 2 and 3 when tuning D3 at 15 V / 0.7 pF is shown. As expected, the agreement between S_{11} and S_{22} parameters for each board is not as good as in the previous two figures but it is still appropriate. Nevertheless, the unaltered bands 1 and 2 differ slightly.

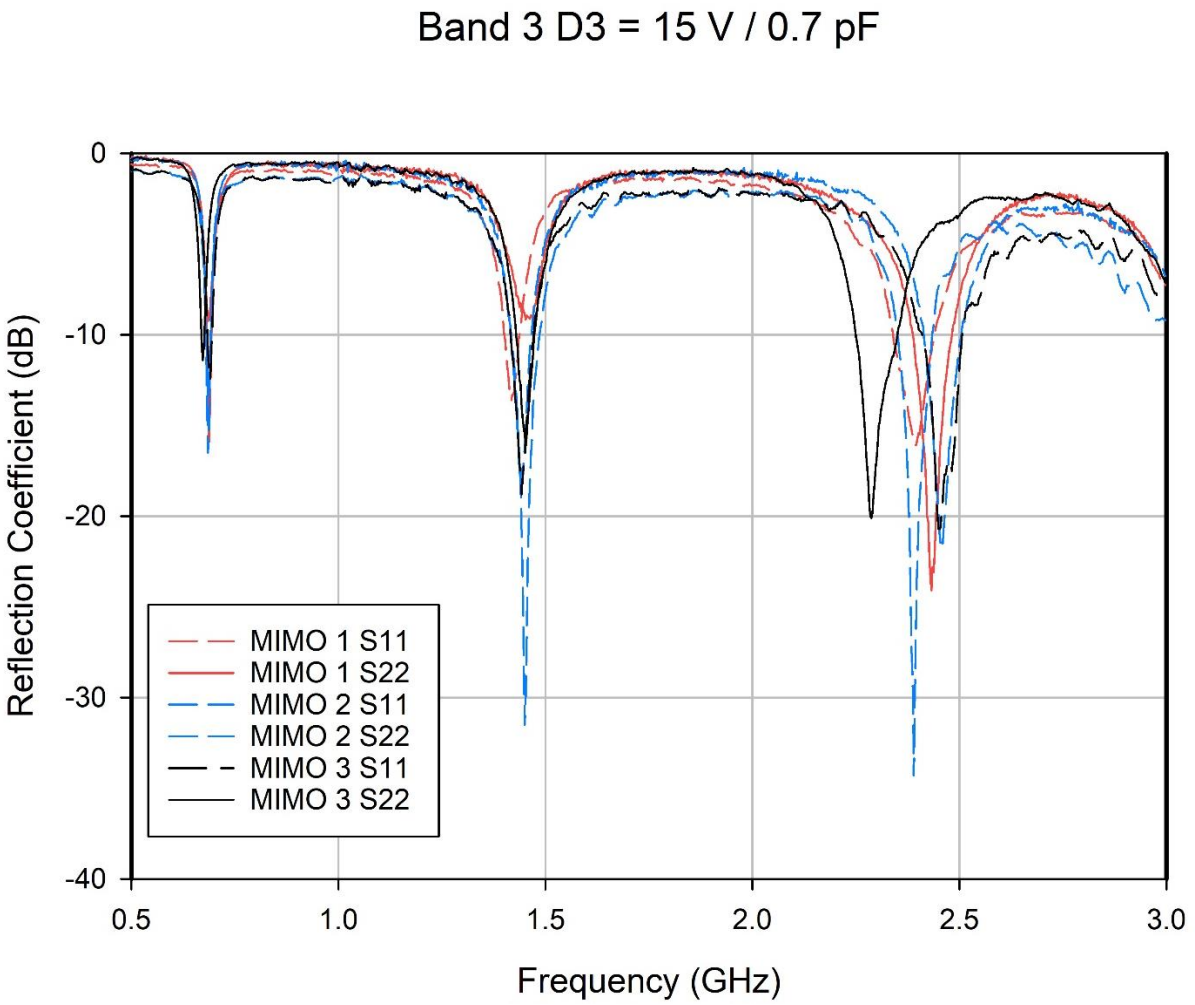

Fig. 73 Comparison of MIMO 1, 2 and 3 tuning their D3 at the same value.

As a conclusion of this section, it has been proved that independent tuning has been achieved for two identical set of resonant slots working in the same board which can be used for multipath purposes and MIMO applications which will be discussed later in this thesis.

Agreements between prototypes have been measured and do not represent a major issue in the performance of this antenna. This is discussed in the following figures where a detailed comparison between the measured and simulated reflection coefficients will be presented.

Firstly, for Band 1, In Fig. 74 Comparison between simulated and measured reflections coefficients for Band 1 for the three prototypes. above, the comparison between the simulated and the measured reflection coefficients for MIMO 1 (a), MIMO 2 (b), and MIMO 3 (c) is presented. The simulated results are displayed in solid lines while the measured numbers are in dashed lines as described in the scale. An appropriate agreement is observed between simulations and measurements for the three prototypes, especially for MIMO 2 where the frequency shift is lower than 50 MHz. For MIMO 1 and 3 there is an evident shift between simulated and measured results, probably due to the effectiveness of the shielding wrapping the DC biasing lines to control the frequency tuning. In terms of the unchanged bands, an agreement can also be observed and is optimal for MIMO 2, while for MIMO 1 and 3 this is slightly bigger but accepted.

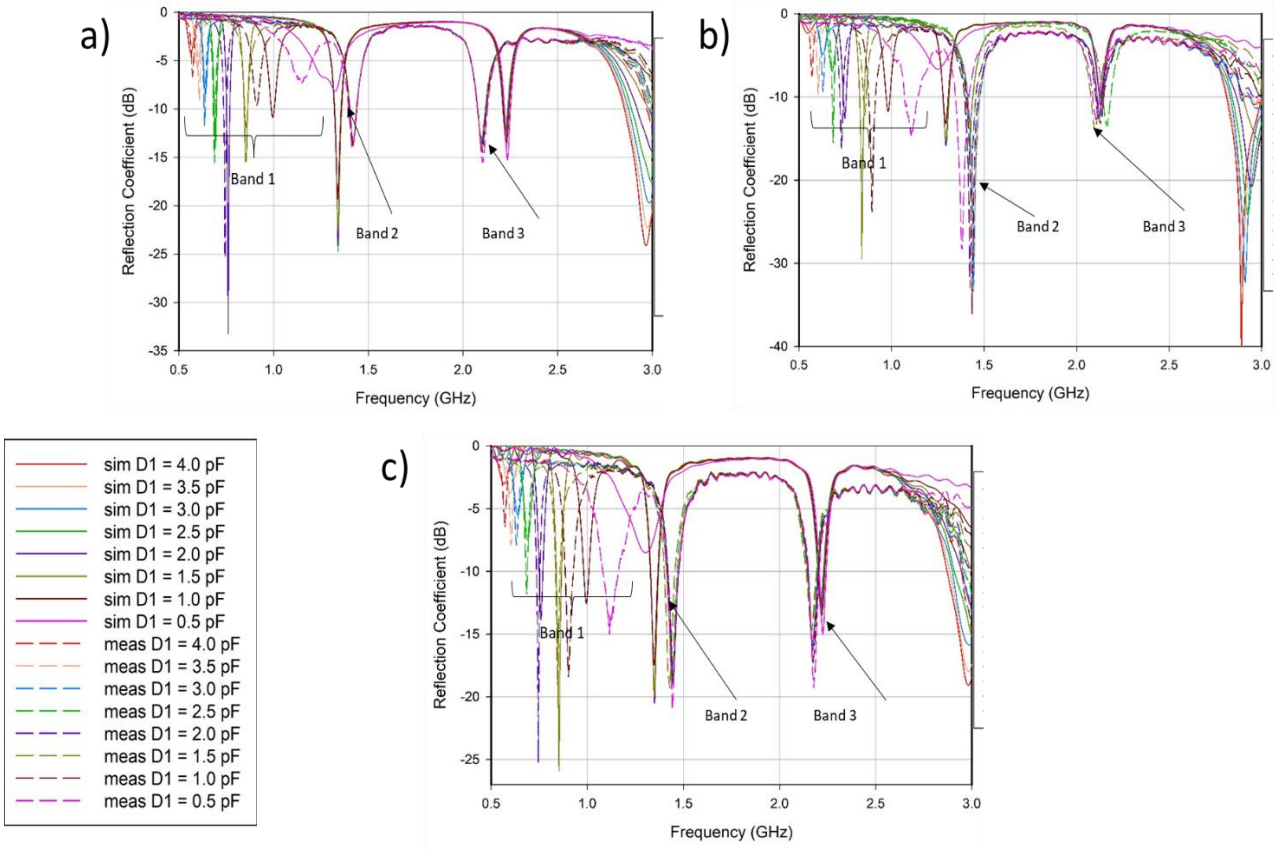

Fig. 74 Comparison between simulated and measured reflections coefficients for Band 1 for the three prototypes.

Then for Band 2, a good agreement is observed between simulations and measurement as observed in Fig. 75 for MIMO 1 (a), MIMO (b) and MIMO 3 (c). A frequency shift is observed in the three cases; however, it does not represent a significant issue in terms of simulations - measurements agreement. Similar to the previous figure, this comparison presents an appropriate similarity between the numbers obtained by CST Microwave Studio and the reflection coefficients measured in the laboratory. The closest agreement is observed for MIMO 1 and MIMO 2, where the frequency shift is below 50 MHz. Moreover, for MIMO 1, the frequency shift is uniform, i.e. the simulations are slightly lower than the measurements, separated by less than 40 MHz from each other, which highlights this prototype as the ne agreeing the most with simulations for frequency tuning of Band 2.

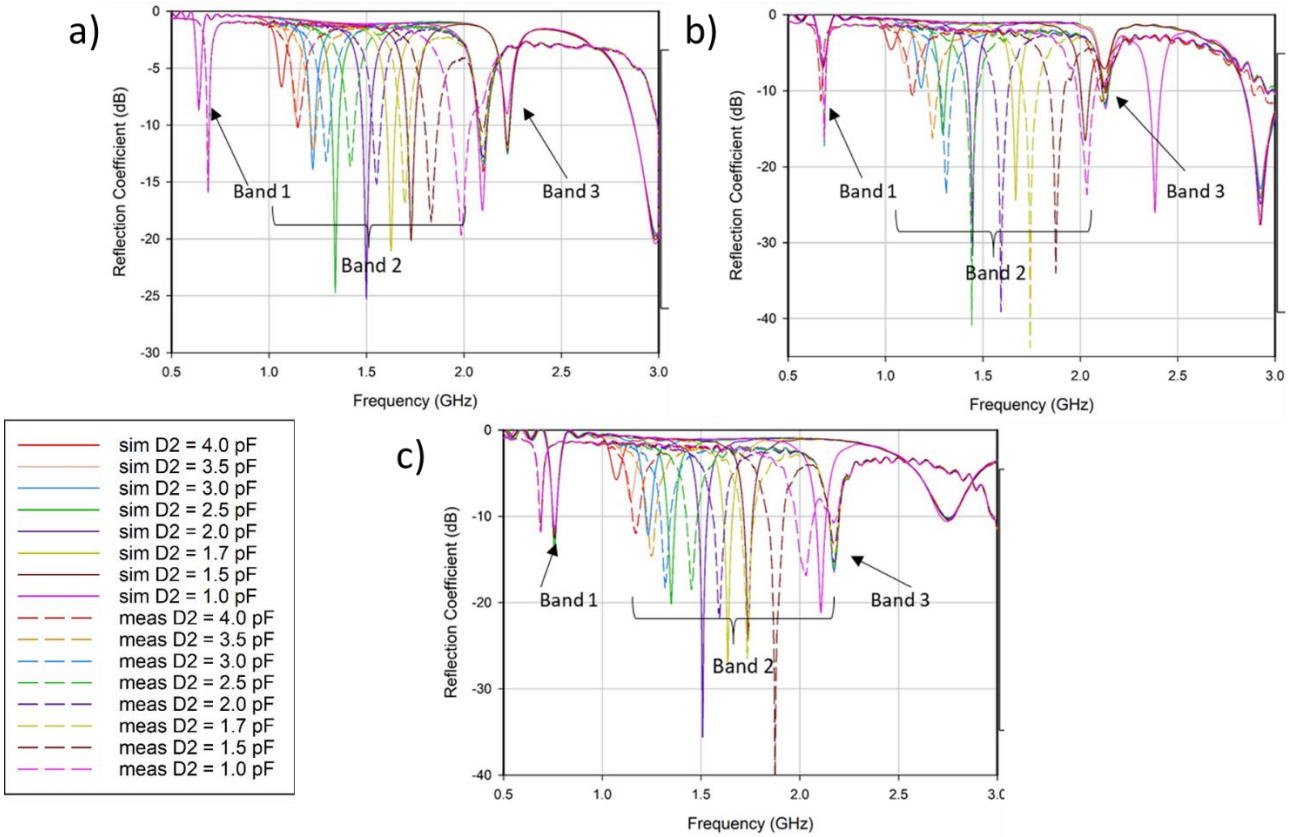

Fig. 75 Comparison between simulated and measured reflection coefficients for Band 2 for the three prototypes.

Finally, for Band 3 in Fig. 76 below, the comparison between simulated and measured reflection coefficients is presented. The analysis is made for MIMO 1 (a), MIMO (b) and MIMO 3 (c), respectively, similar to the previous comparisons. As the frequency tuning for Band 3 is carried out in the highest frequencies for the designs, the shift between simulations and measurements was more unpredictable, however, MIMO 3 presents the best agreement with a frequency shift below 60 MHz and a near ideal agreement for the unchanged bands.

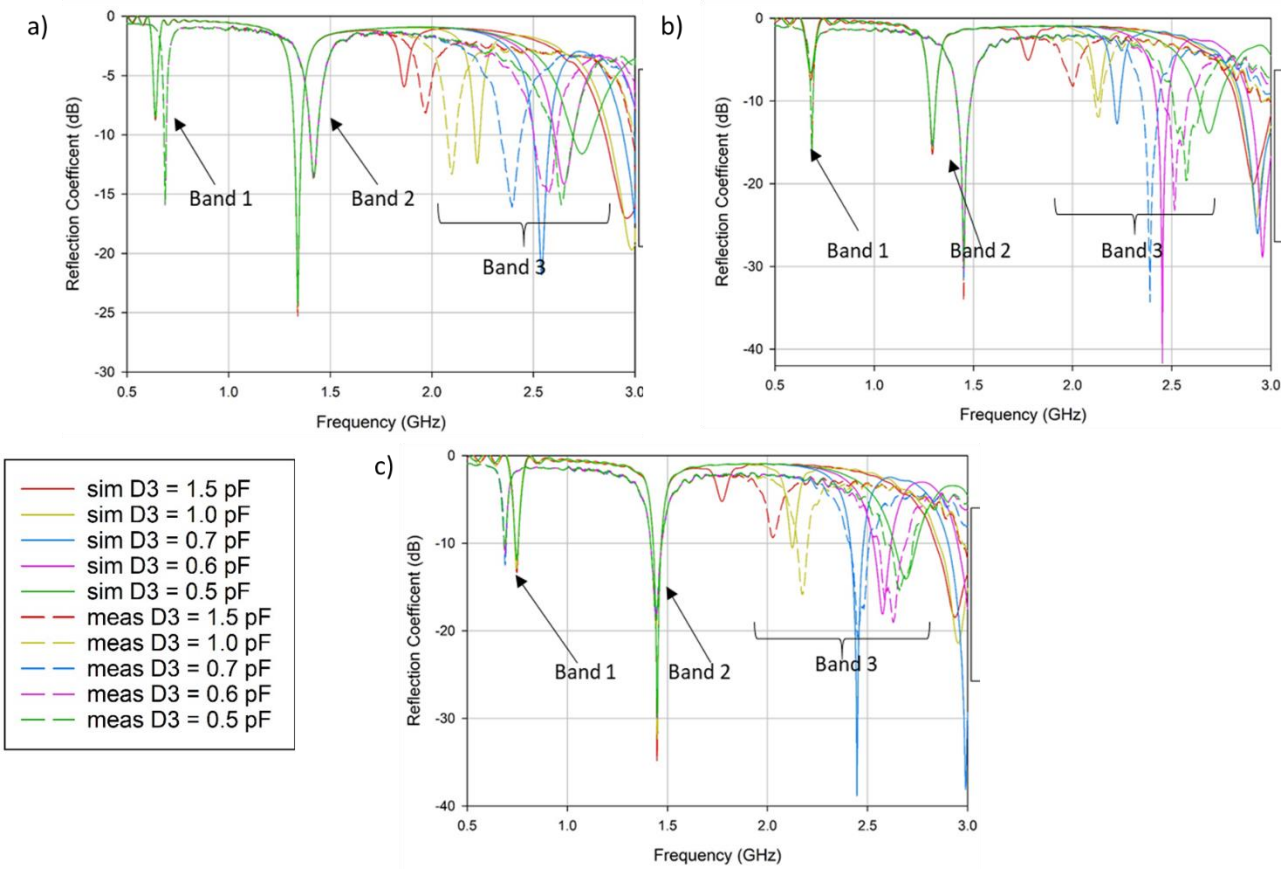

Fig. 76 Comparison between simulated and measured reflection coefficients for Band 2 for the three prototypes.

Overall, for the three comparisons presented previously, an appropriate agreement between simulations and measurements is observed. The frequency shifts observed are accepted and expected. These could be significantly reduced further with improvements in the shielding for the boards or a change of components, which could be a lead for future work. The comparisons carried out in the previous figures is discussed for the S_{11} parameters for each board corresponding to Antenna 1 in each case, for illustrative purposes only. The comparisons for the S_{22} parameters are similar. A full presentation of the comparison between simulated and measured reflection coefficients is presented in Appendix A of this Thesis.

In terms of isolations between the two set of slot antennas in each board, a good level is observed for each case. In addition to the surface current distribution, an appropriate isolation between Antenna 1 and Antenna 2 is observed in X below, this supports the surface current analysis carried out in section 3.2.3. MIMO 1 (a) presents the least optimal numbers while MIMO 2 (b) and MIMO 3 (c) show a better isolation. The isolation can be improved by increasing the separation between antennas and gradually analysing the results. This study will be further discussed next in Chapter 4.

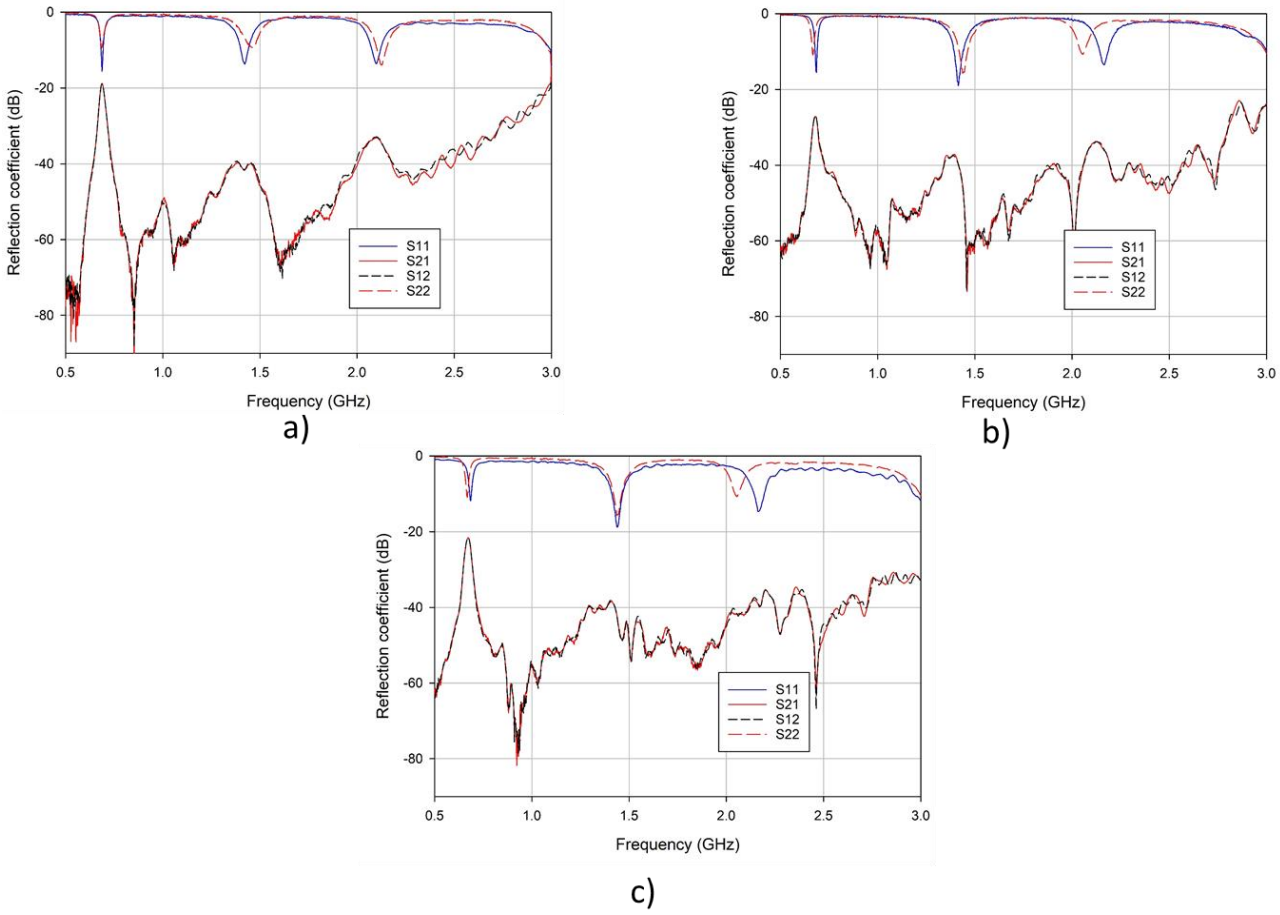

Fig. 77 Isolation between antennas in each board.

3.3.3. Measured radiation patterns.

Measured radiation patterns for the manufactured boards will be discussed in this section. In order to measure accurately each prototype, the position of the board was varied depending the orientation of the slot and the plane being measured in question. In Fig. 78 is presented the interior of the anechoic chamber of the communications group in the University of Sheffield, corresponding to the Electronic and Electrical Engineering (EEE) department of the University. The measurement system is shown in (a) where the mechanical arm holding the antenna varies the position of the antenna in a 360º rotation whilst a horn antenna HF906 is transmitting a signal towards the antenna being analysed. In (b) the antenna position in the mechanical arm is presented, with both sets of slots facing towards the horn reference. The position of the slot analysed in question is rotated with an additional step motor in the mechanical arm, this is normally a 90º rotation which corresponds to the slot positions and the plane that is required to be measured.

Fig. 78 Anechoic chamber of the communications group in the University of Sheffield and antenna measured in question.

The measured and normalised radiation patterns for these prototypes are presented from Fig. 79 to Fig. 87. In these figures, the (a) X-Z and (b) Y-Z planes are presented for each board at a given frequency band, these resonances were achieved when applying biasing voltages of 10.3 V, 9 V and 20 V to varactors D1, D2, D3 respectively for each antenna for each board.

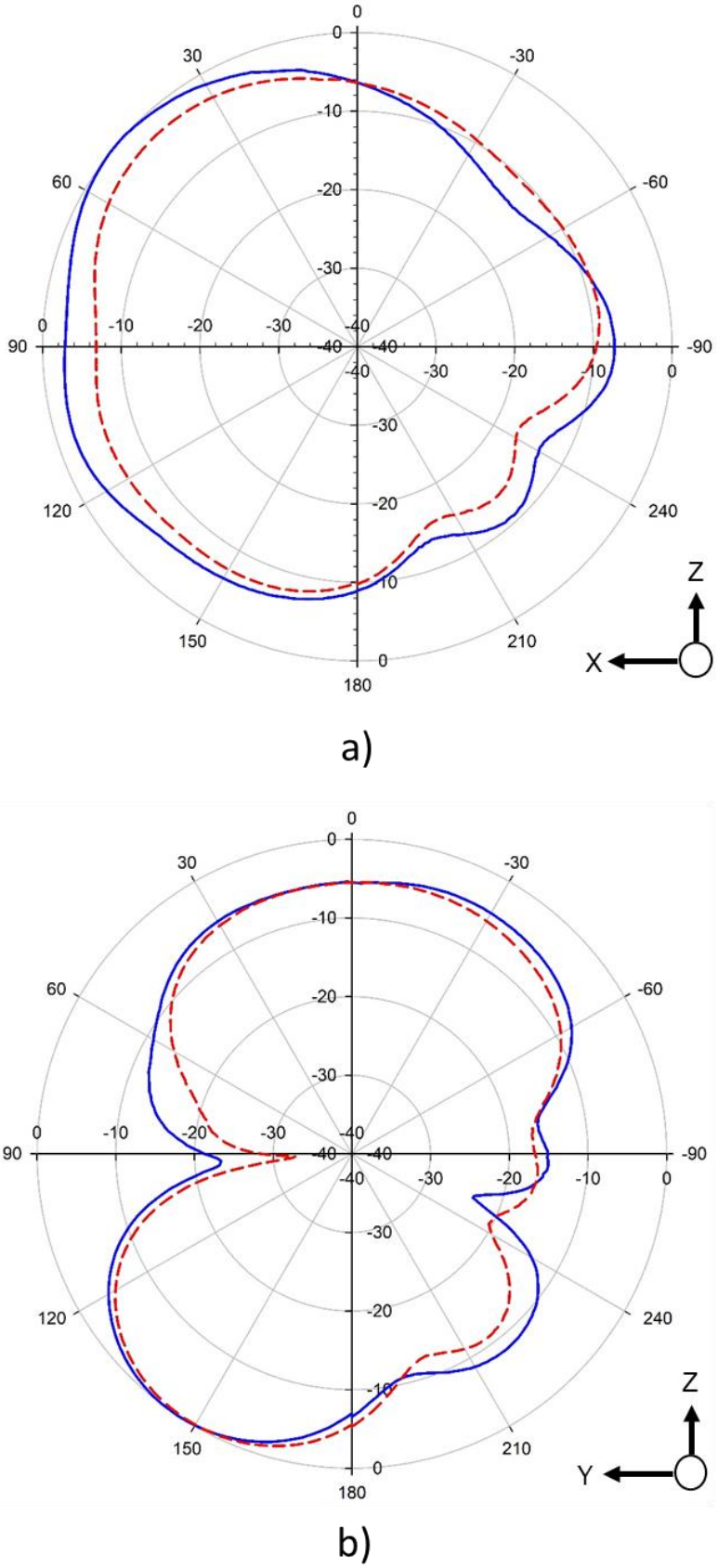

Fig. 79 Measured, normalised radiation patterns for MIMO 1 at 0.907 GHz.

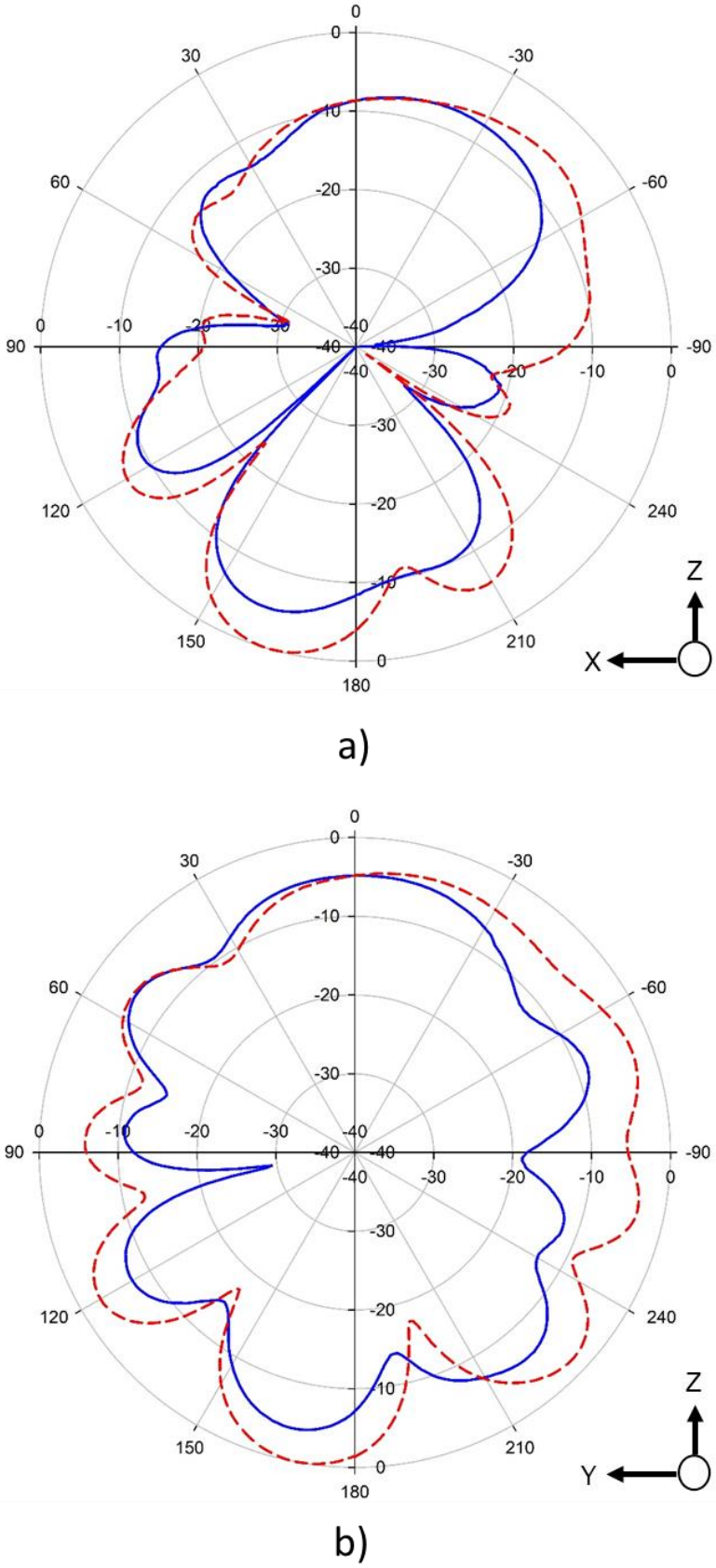

Fig. 80 Measured, normalised radiation patterns for MIMO 1 at 1.85 GHz.

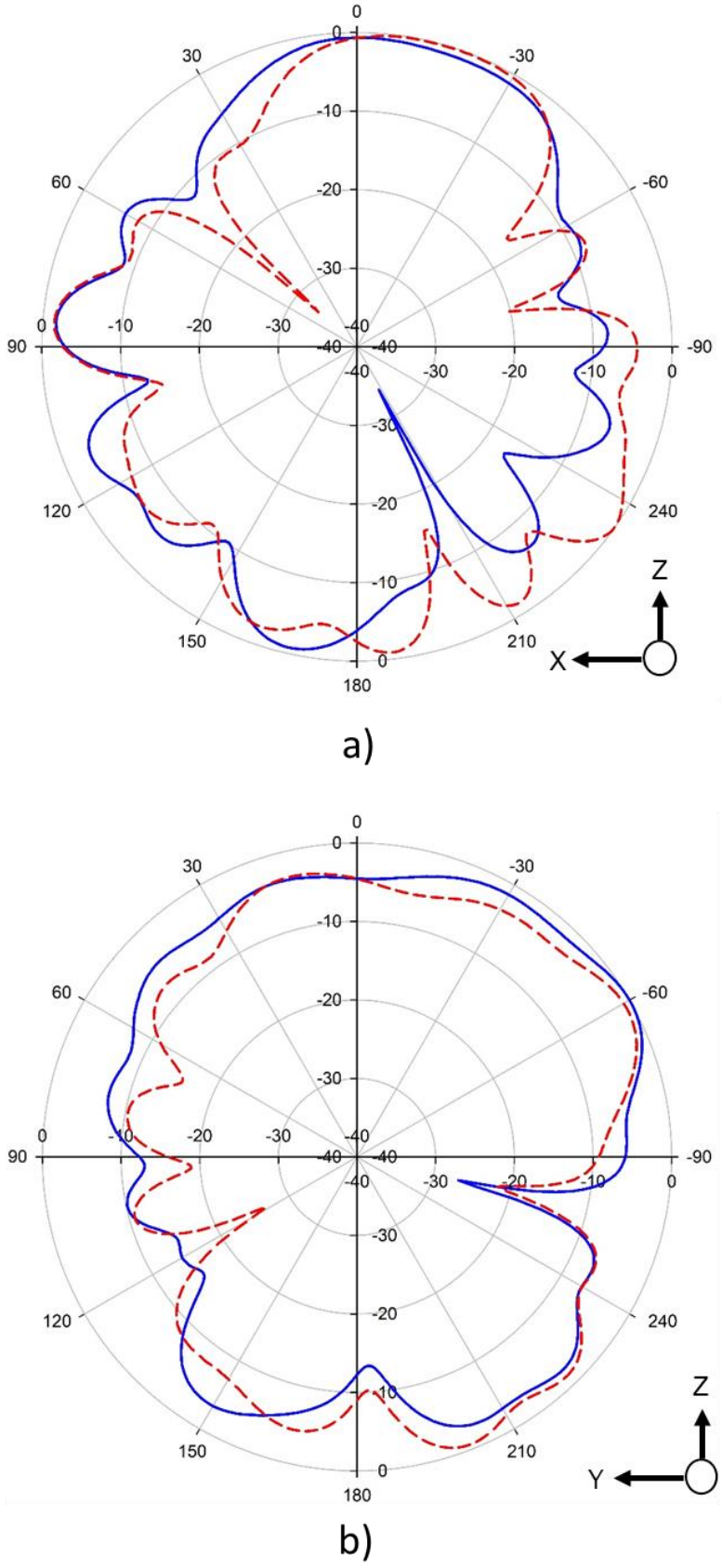

Fig. 81 Measured, normalised radiation patterns for MIMO 1 at 2.60 GHz.

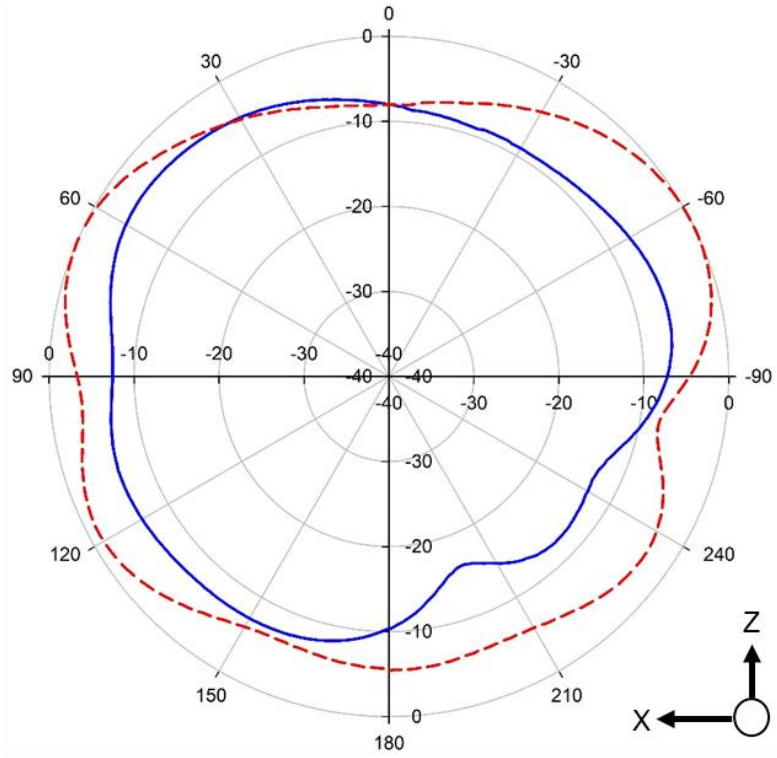

a)

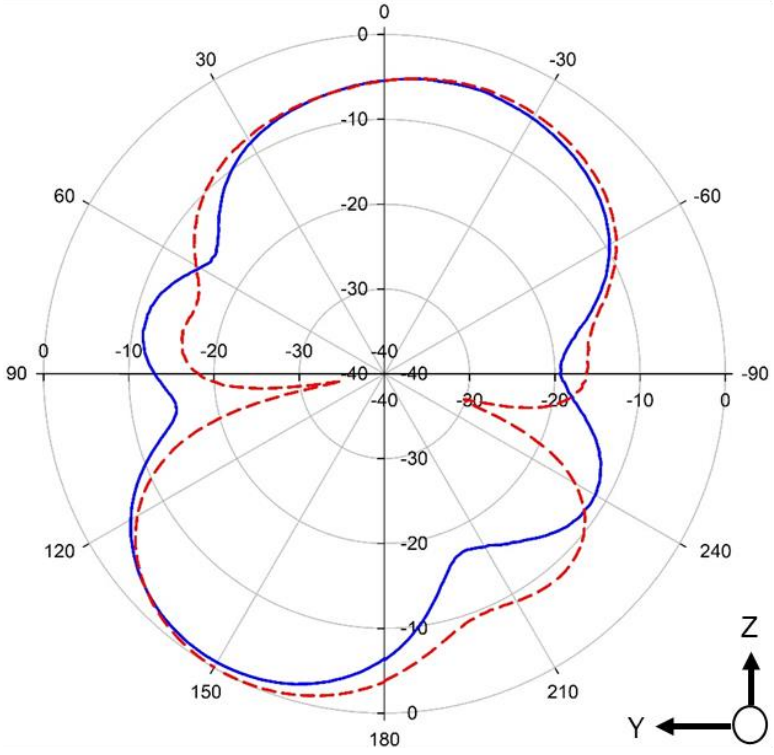

b)

Fig. 82 Measured, normalised radiation patterns for MIMO 2 at 0.907 GHz.

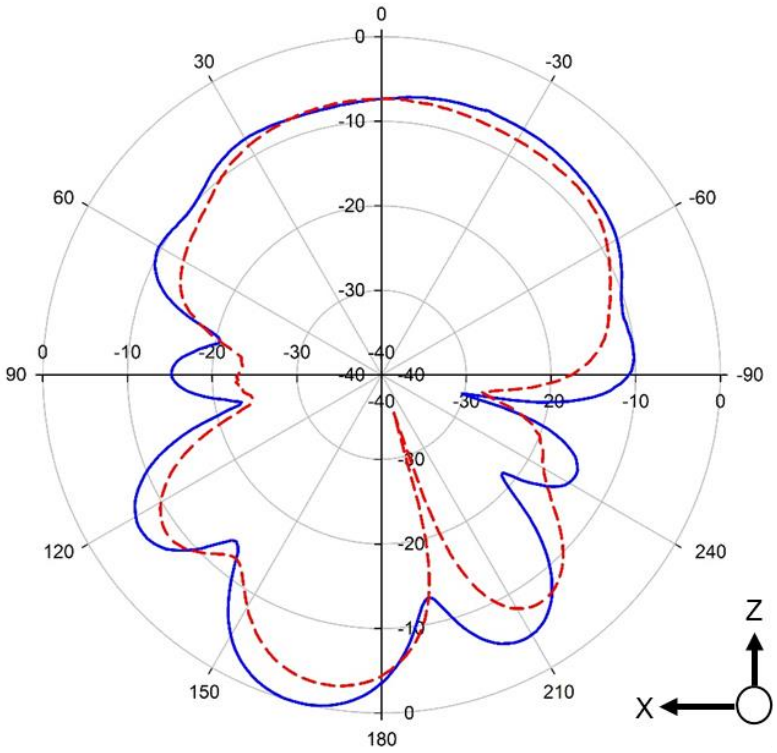

a)

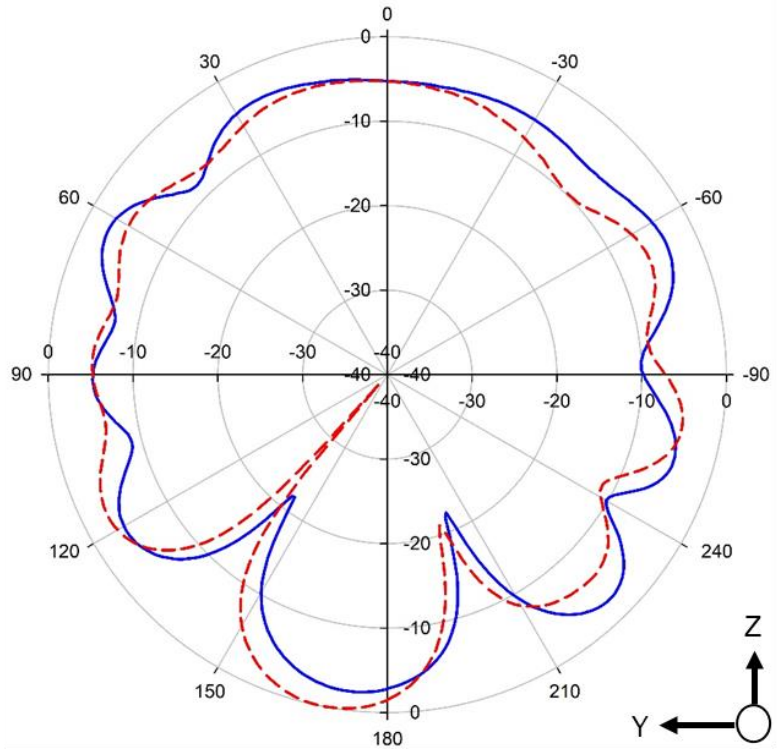

b)

Fig. 83 Measured, normalised radiation patterns for MIMO 2 at 1.85 GHz.

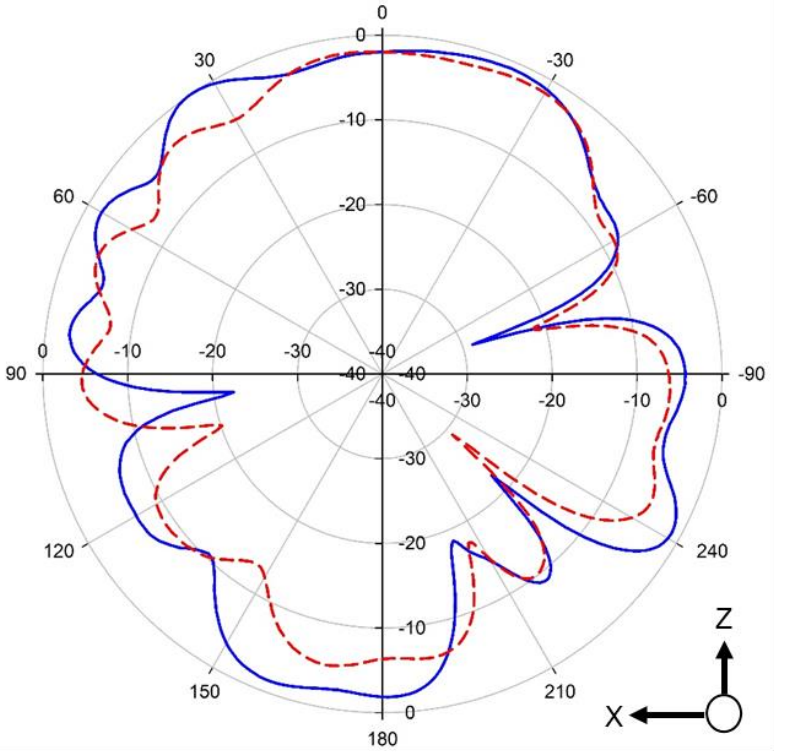

a)

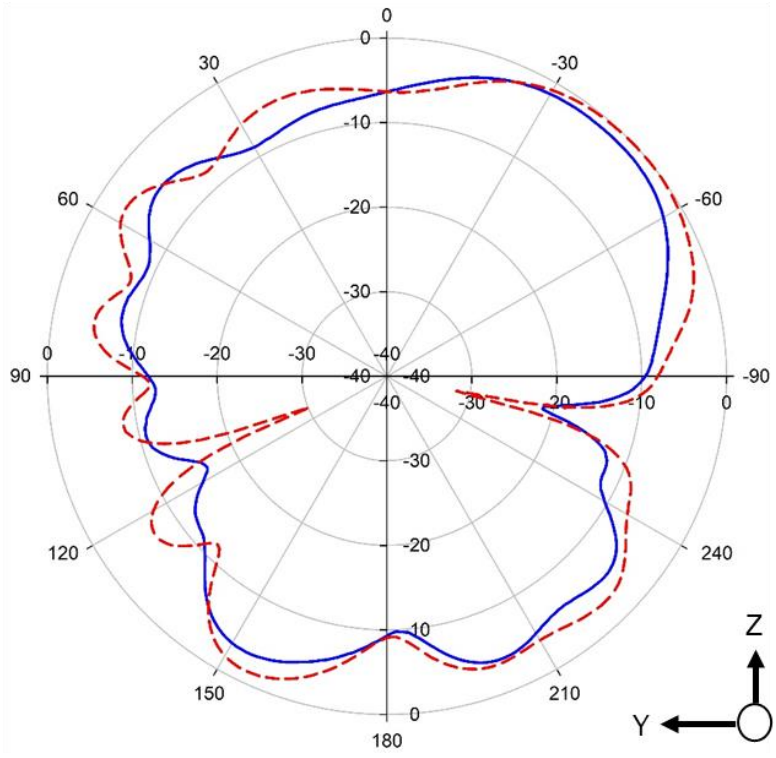

b)

Fig. 84 Measured, normalised radiation patterns for MIMO 2 at 2.60 GHz.

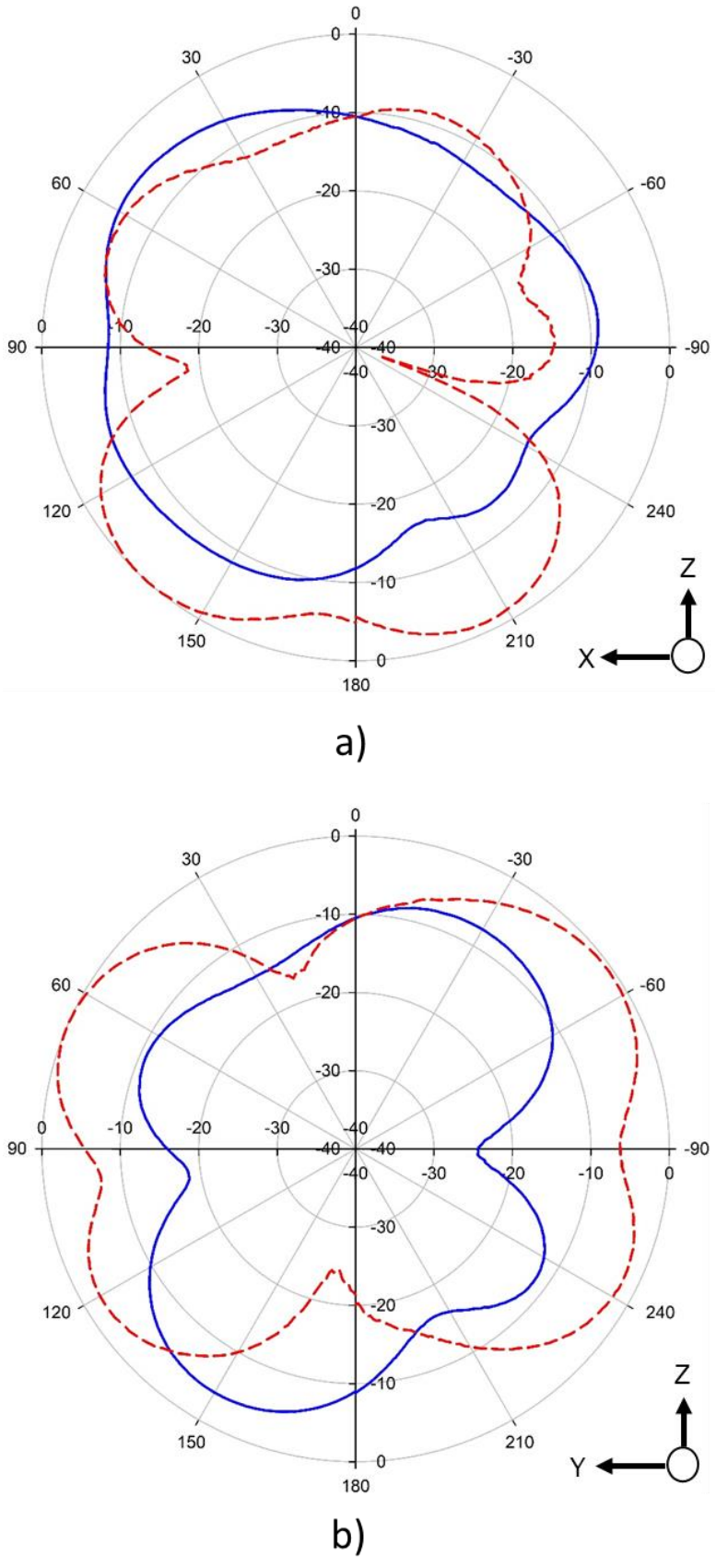

Fig. 85 Measured, normalised radiation patterns for MIMO 3 at 0.907 GHz.

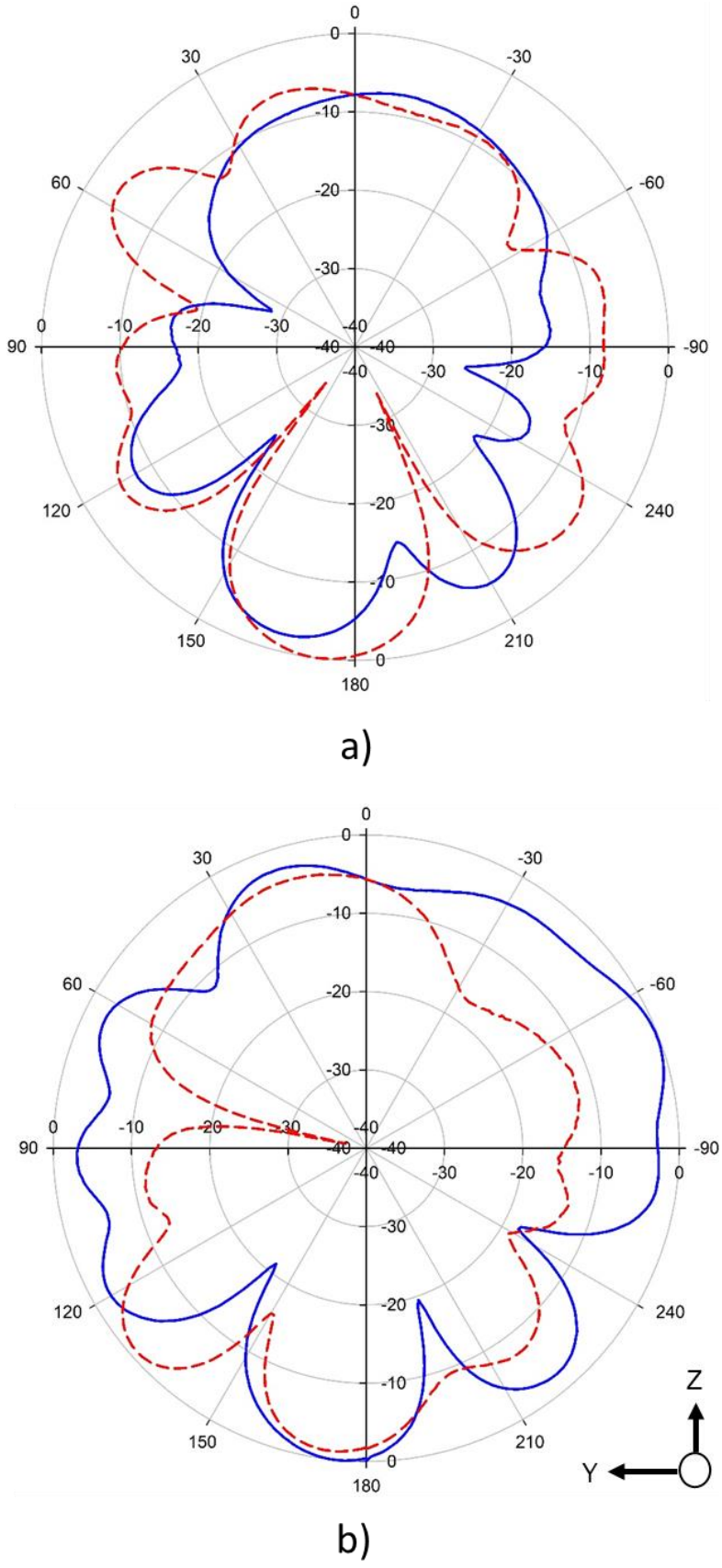

Fig. 86 Measured, normalised radiation patterns for MIMO 3 at 1.85 GHz.

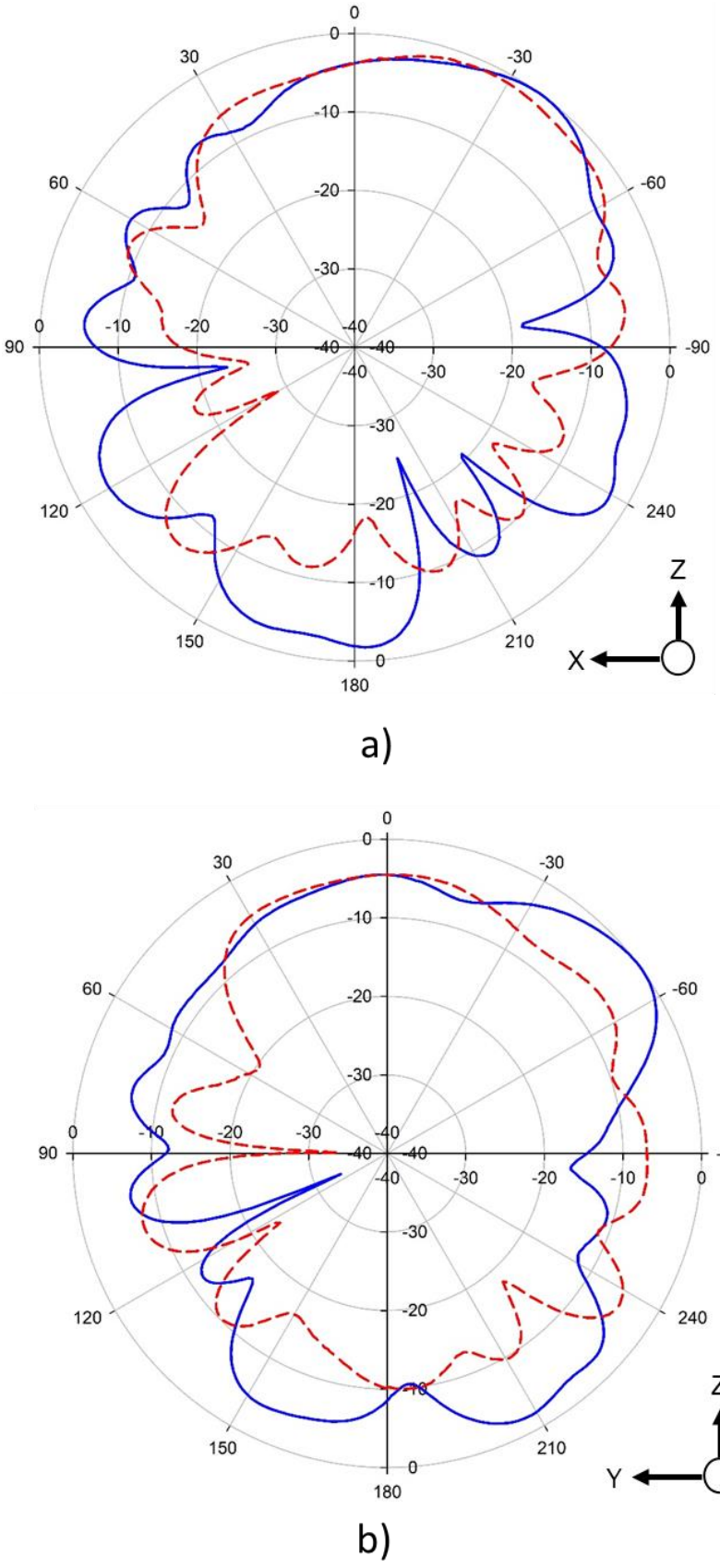

Fig. 87 Measured, normalised radiation patterns for MIMO 3 at 2.56 GHz.

The radiation patterns for the three manufactured prototypes were measured in the anechoic chamber at a number of different frequencies. The results presented for three frequencies, 0.907 MHz, 1.85 GHz and 2.60 GHz, one in each band, are representative of typical results within these bands. For MIMO 1 and MIMO 2 there is little pattern diversity between the antennas at any frequency band. However, the measured radiation patterns for MIMO 3 show diversity at all three frequencies indicating that placing the antennas orthogonally to each other brings obvious advantages even on a small device. The gain for these patterns was calculated as follows:

$Gain_{Eplane/Hplane}$ = Max value at Given frequency + Measured S_{21} horn-horn + Gain at given frequency from horn.

Which leaded to the following table of gains Table 4 .

	MIMO 1		MIMO 2		MIMO 3	
	H-Plane	E-Plane	H-Plane	E-Plane	H-Plane	E-Plane
0.7 GHz	-1.22 dBi	-1.35 dBi	-3.34 dBi	-2.86 dBi	-1.87 dBi	-2.45 dBi
1.85 GHz	-6.73 dBi	-8.96 dBi	-5.36 dBi	-7.82 dBi	-5.47 dBi	-6.95 dBi
2.60 GHz	-5.26 dBi	-2.14 dBi	-4.91 dBi	-3.54 dBi	-5.36 dBi	-1.98 dBi

Table 4 Calculated measured gains for each board at given frequencies.

Significant gains due to spatial diversity for any of the MIMO configurations were not expected due to the small dimensions of the board. Low gains corresponded to an agreement between the simulated radiation patterns and the measurements discussed in this section. The patterns measured corresponded to omnidirectional coverages which agree with the low gains.

3.4. Conclusions for Chapter 3.

In conclusion for this chapter, three different boards with two sets of independently tunable slots are presented. The designs presented are three 1×2 MIMO triple-slot antennas that were designed, simulated, fabricated, and measured. The designs were based on a previous work that presented a triple-slotted antenna in a PCB with independent reconfigurable slots. The designs carried out aimed for the study of different positions of two identical sets of three slots in the same board. The selection of the components used in these antennas was carried out in order to secure the electronic control of the antenna performance as well as protect the systems from external interferences. Computerised models were implemented for each prototype and fully simulated in CST Microwave Studio.

Each board offered three independent frequency bands that do not affect the remaining bands when varying the band in question for both simulated and measured results. The frequency range achieved by the measured prototypes is around 690 MHz – 2.80 GHz for the three different boards differing slightly from one prototype to the other. The set of measurements for the reflection coefficients and isolations as well as the simulations for current distributions demonstrate that the two sets of antennas in each board are practically uncorrelated, which is a desirable feature for multi antenna systems and highlights the designs as candidates for MIMO applications. This will be analysed next in Chapter 4.

The radiation patterns offered for these designs in general omnidirectional coverages. Little pattern diversity is observed for MIMO 1 and 2, however, for the third prototype MIMO 3, which explores lateral positions of the antennas, the patterns cover two different areas.

Overall, the designed antennas presented in this chapter offered innovative features and adaptive performances that are appropriate for 5G technologies. Nevertheless, further development is expected if these designs are taken as the base of future development of novel devices. The work carried out in this chapter has been published in [89] at Loughborough Antennas Propagation Conference in November 2018.

CHAPTER 4. MIMO AND DIVERSITY METRICS FOR OF INDEPENDENTLY TUNABLE TRIPLE-SLOT 1×2 MIMO ANTENNAS.

When multiple antennas work simultaneously in a system, we have different ways or paths of propagation. The trend for novel devices is to send large amounts of data as expected in 5G mobile communications generation equipment. This is a promising research opportunity to study sending the same data through multiple paths with a view to enhance the system performance. This is known as diversity in communications engineering and will be studied in the antennas analysed in the previous chapter 3. In this study, the focus is on spatial diversity, with a view to determine the MIMO reliability of the 1×2 triple-slotted antennas studied previously. The objective of these diversity techniques as mentioned previously is to improve the performance of the system, for this, two essential diversity and MIMO metrics that evaluate the compatibility for MIMO applications will be discussed [90].

4.1. Diversity techniques and metrics.

A radio channel presents a dynamic behaviour and yet unpredictable behaviour due to the effects of multipath and Doppler fading which can substantially affect the system performance. Diversity techniques are implemented with a view to avoid these distortions at relatively low costs allowing implementations in transmitters and receivers.

Diversity techniques benefit from the randomness of the natural radio channel behaviour by using more than one version of the transmitting signal and studying each of these versions [91]. In Fig. 88 a block diagram illustrates a communication system benefitting from a diversity scheme being introduced into it. In this system the original signal is replicated and is being transmitted it through a N number of channels. If these channels vary independently the likelihood of a deep fading in all of them is low. In practical cases it is expected that the N number of channels might not be ideally uncorrelated. However, a low correlation index would be enough to achieve a significant reduction of the signal-to-noise ratio (SNR) so that System SNR > one MIMO channel SNR, which is an essential parameter in order to achieve a given unavailability probability. These reduction of SNR is known as diversity gain (DG) [92] a parameter which will be discussed and used later in this chapter and a useful parameter that determines if a device is compatible with MIMO applications.

The different duplicates of the original transmitted signal are combined in the receiver and then sent into a demodulator and detector circuit as shown in the figure below.

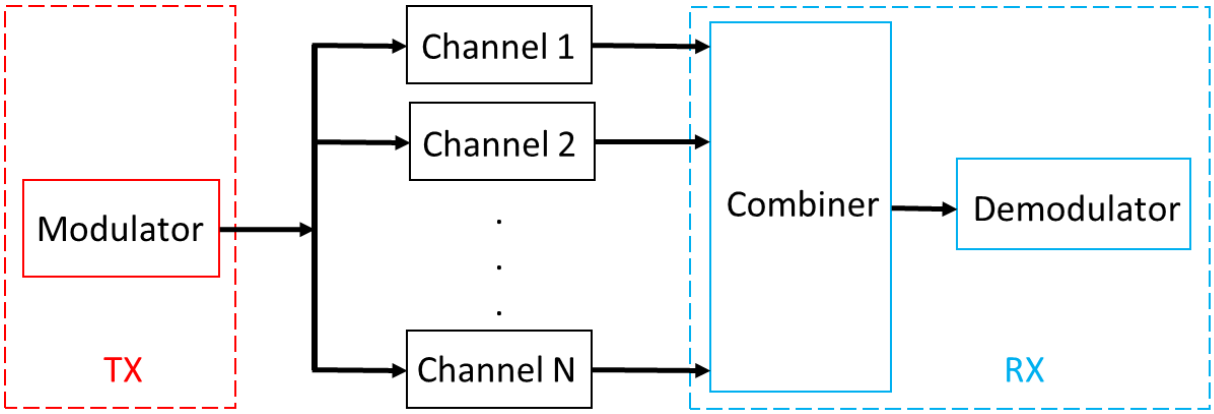

Fig. 88 Communication system with a diversity scheme.

The classification of diversity techniques will be now discussed. This classification depends entirely on the end in which the diversity scheme is implement, either transmitter or receiver. It also depends on the kind of signal processing used on the multiple duplicates of the original signal or the physical feature exploited to obtain these replicas partially or totally uncorrelated.

4.1.1. Spatial diversity.

Also known as antenna diversity, is a diversity scheme achieved by simply implementing multiple antennas for the transmitter or for the receiver. If the antennas are separated by a gap too wide their signals will suffer from fading independent from each other. The required gap between antennas depends directly on the local dispersion of the medium and on the carrier frequency. E.g. in a mobile handset system in which the device is near the ground and is surrounded by high dispersion and the channel suffers distortions over little distances in the space of propagation. However, for BTS or systems installed in masts the gap can be up to ten times this distance. As mentioned previously, diversity schemes can be implemented in the transmitter using multiple antennas and known as MISO systems (Multiple Input Single Output) as well as in the receiver which are called SIMO systems (Single Input Multiple Output). Novel systems combine these two schemes and are hence denominated MIMO (Multiple Input Multiple Output) [93]. In Fig. 89 (a) a SIMO system, (b) a MISO system and (c) a MIMO system are presented.

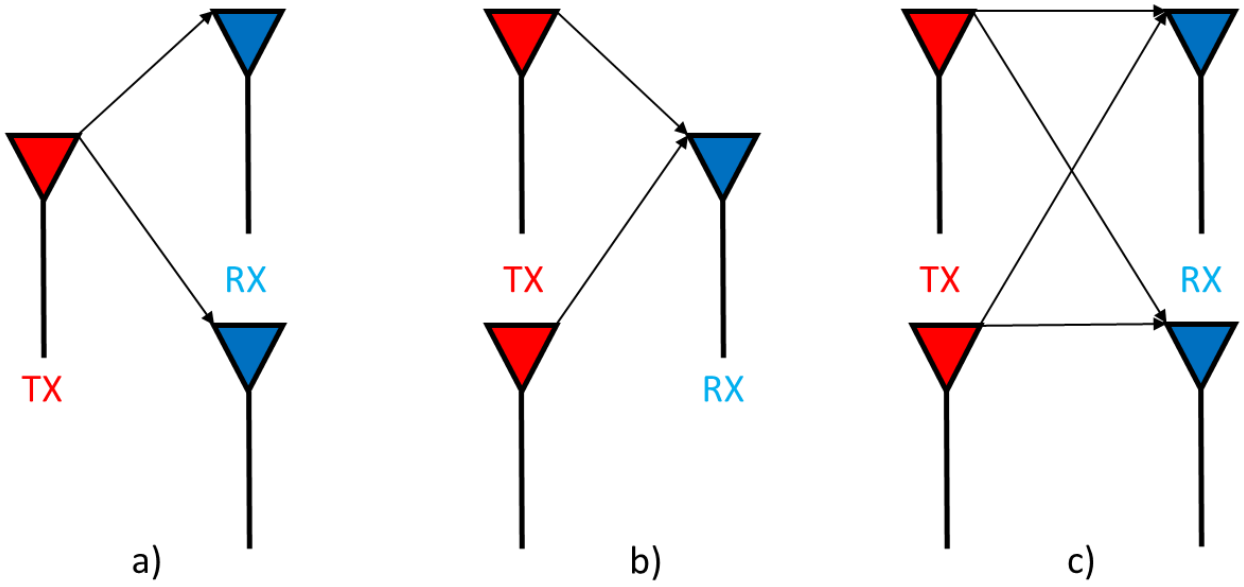

Fig. 89 Spatial diversity schemes.

4.1.2. Frequency Diversity.

When this scheme is used, the information is transmitted in more than one carrier so that signals presenting a major frequency shift will not be affected by the same fading. This is carried out considering the separation between signals as a necessary parameter to achieve partially or totally uncorrelated channels. This separation might correspond to an important proportional fraction of the total bandwidth, which therefore requires that this technique will only be applied on systems offering a significant large bandwidth with a number of receivers equal to the number of transmitters. However, Frequency diversity is usually applied in communication links by line of sight using Frequency Division Multiplexing (FDM). In transmission, is possible to implement frequency diversity via space-frequency codes [16] [92].

4.1.3. Time Diversity

Time diversity is achievable by calculating an average fading in the channel as a function of time. Normally, the coherence time of channel is between ten and hundred times the symbol time. Hence the channel is highly correlated through consecutive symbols, so the information is transmitted repeatedly every given time slot so that this repetition is carried out under fading-free conditions. An effective manner to achieve to implement this scheme is using entwined encoders. For instance, if we transmit a signal $x = [x_1, \ldots, x_L]$ with a length of L number of symbols and the received signal is given by $y_i = h_i\, xi + w_i$,

with $i = 1, \ldots, L$. assuming an ideal cross-correlation in which the symbols x_i are transmitted with enough separation among them, it can be therefore assumed that h_i are independent. L is also known as the number of diversity branches or level of diversity. This scheme has an inconvenience so is a not recurrent one due to the reduced transmission data rates given the time separation must be higher than the average duration of each duplicate of signal. This therefore produces a high latency [16] [94].

4.1.4. Polarisation diversity.

It has been experimentally proved that signals horizontally and vertically polarised present a significant uncorrelation when comparing them. This difference is due to the multiple reflections in the channel between the transmitter and the receiver with a different reflection coefficient for each kind of polarisation which leads to multiple amplitudes and phases for each signal. After many random reflections signals show a higher uncorrelation which increases the diversity gain in this scheme [95].

4.1.5. Selection diversity.

When classifying the different techniques depending on the signal processing carried out to the received or transmitted signals, one of the simplest methods is the diversity selection scheme. Once this scheme is implemented into the receiver, a system similar to the one described in Fig. 90, can be observed, where N demodulators and N RF streams are used to provide N diversity branches. The diversity selection occurs when the branch with the highest SNR is selected or when using N antennas, a single demodulator and a single RF stream selecting the branch with the highest carrier-noise ratio (CNR). If a scheme like this is implemented in transmission, the receiver ought to monitor every channel periodically and report the channel with highest envelope correlation to the transmitter, however, in case every branch have the same average SNR the amplitude of the output signal of the combiner is simply the magnitude of the strongest signal [92] [90].

Selection diversity-ruled systems are particularly sensitive to SNR differences among their branches. Diversity gains reach their maximum levels when all the branches present the same average SNR suffering gradually from external distortions proportionally to the increment of the difference between SNRs.

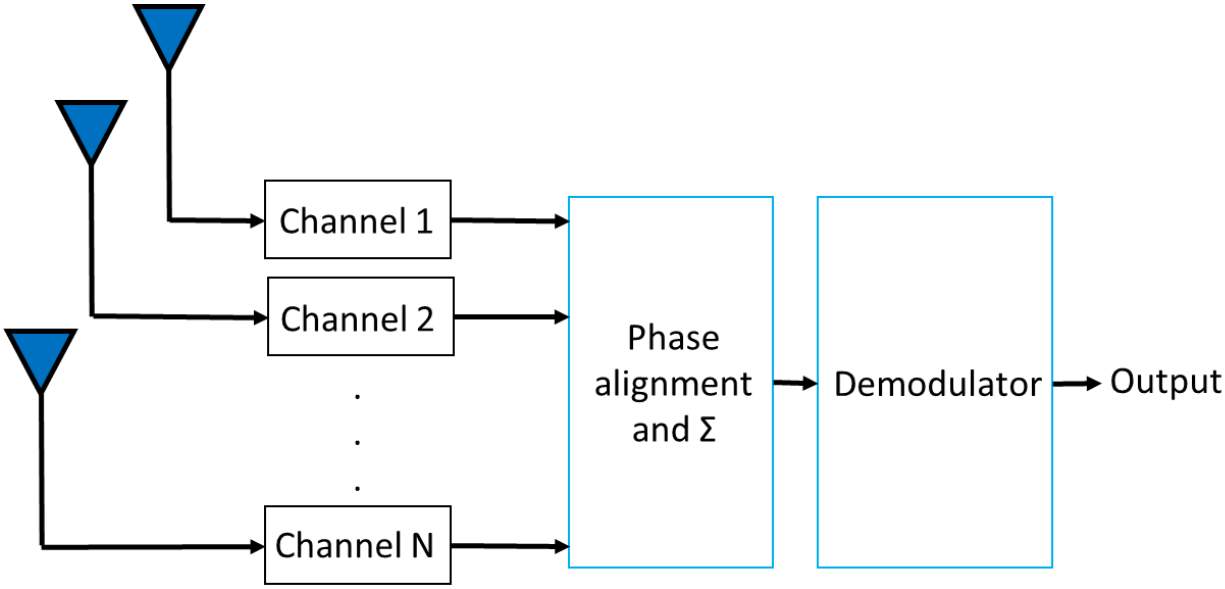

Fig. 90 Communications system with a selection diversity scheme.

4.1.6. Commutation Diversity.

Similar to selection diversity, this technique monitors all the channels, however, instead of selecting the best of N signals the monitor process is carried out until a channel triggers a detector when a signal goes above a certain and established level. The channel keeps its metrics until it drops below the triggering level and the search restarts. Fading statistics are slightly less favourable compared to the ones obtained by selection diversity, however, this technique have an easier implementation as only a receiver is detected, in Fig. 91, a diagram of a communications system in which this technique has been implemented is presented [96].

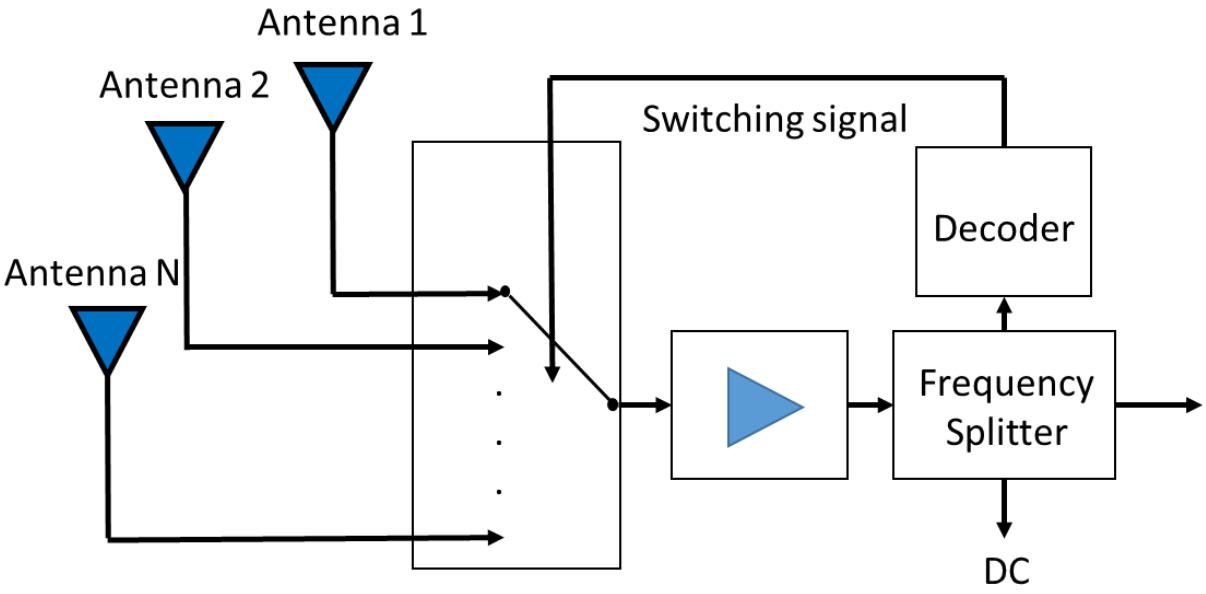

Fig. 91 Communications system with a commutation diversity scheme.

4.2. MIMO metrics for 5G communications standards.

The diversity techniques described in the previous section can be implemented into transmitters and receivers. In practice, diversity techniques are widely used in highly dispersive mediums. Hence, spatial diversity is widely used to reduce fading and losses due to multipath and has proved to be a very effective technique. A typical solution is to use multiple antennas together with combination methods in order to improve the quality of the received signal. However, some of the issues when using spatial diversities are the high costs, sizes of devices and energy consumption given the number of selection and commutation circuits turning MIMO systems into bulky devices for mobile communication equipment.

The next generation of mobile communications 5G aims for large amounts of data being transmitted simultaneously by multiple antennas using diversity schemes combined with novel versatile devices such as reconfigurable antennas. After reviewing numerous devices with these schemes in section 2.3.2 the analysed devices highlighted essential diversity metrics such as envelope correlation coefficients and diversity gain.

In this section we will discuss these two parameters recurrently cited and analysed in previous reconfigurable antennas applied to the MIMO prototypes studied in Chapter 3 as each board has two antennas and are highly uncorrelated which, after analysing diversity schemes in the previous section 4.1, is highly desirable for these applications [92].

4.2.1. Envelope correlation coefficient (ECC).

A recurrently used parameter in MIMO antennas is the envelope correlation coefficient (ECC). Given the number of antennas in a multi-antenna system, where a diversity scheme has been implemented it is essential to determine numerically the interaction among them. It is known that antennas have a duality property which means there are capable of transmit and receive a signal. ECC is a parameter that determines the independence between two antennas in a system with a diversity scheme. By analysing the proportional energy that affects an antenna when another one is transmitting a signal. Hence, this parameter is only applicable in a binary analysis, namely, it can only be calculated for two antennas at a time since it is a dual operation [15].

ECC can be determined by two different expressions. Basically, the equations are based on essential antenna metrics such as radiation patterns and reflection coefficients (S-parameters). A first expression for envelope correlation coefficient depends on the magnitude

of radiation patterns of the two antennas analysed in question, specifically on the polarisation of the patterns. Ideally, if the polarisation of the evaluated antennas are completely opposite e.g. vertical and horizontal, then the envelope correlation coefficient is 0 which means the antennas are not correlated [97], [98]. Equation (28) describes the expression of this parameter as follows:

$$\rho_e = \frac{\left|\int_{4\pi}\int\left[\overrightarrow{F_1}(\theta,\varphi)\cdot\overrightarrow{F_2}(\theta,\varphi)\right]d\Omega\right|^2}{\int_{4\pi}\int\left|\overrightarrow{F_1}(\theta,\varphi)\right|d\Omega^2\int_{4\pi}\int\left|\overrightarrow{F_2}(\theta,\varphi)\right|d\Omega^2} \quad (28)$$

Where $F_1(\theta, \varphi)$ and $F_2(\theta, \varphi)$ are complex functions in spherical coordinates describing the radiation patterns for antennas 1 and 2 evaluated in this parameter. Equation (28) describes the variation of radiation patterns over a spherical space, and compares both $F_1(\theta, \varphi)$ and $F_2(\theta, \varphi)$ specifically the vector describing their polarisation which is the direction of the electric field. So that, in case $F_1(\theta, \varphi) = F_2(\theta, \varphi)$ then the correlation coefficient is $\rho_e = 1$ and the antennas are therefore totally correlated. Consequently, when $F_1(\theta, \varphi) \neq F_2(\theta, \varphi)$ the correlation coefficient is described as: $1 < \rho_e \leq 0$.

Overall, as ECC is a number between 0 and 1 that proportionally evaluates the correlation between antennas, being 0 for ideal uncorrelated antennas and 1 for totally correlated antennas. For MIMO systems it has been quantified that correlation coefficients below 0.5 are borderline acceptable for their implementation systems introducing spatial diversity schemes. Figures lower than 0.3 are good for uncorrelated antennas in a MIMO system understanding that a correlation coefficient 0 is highly unlikely to achieve.

There are many techniques used to improve, hence, to reduce the ECC between antennas with a view to achieve low interactions and increase the performance of the system they are implemented in. Polarisation diversity among antennas is a recurrent technique in multi-antenna arrays as two differently polarised antennas would imply lower correlations. E.g. if an antenna A is vertically polarised and we compare it with an antenna B horizontally polarised then their ECC is an ideal 0. Moreover, if the antennas separation gap is increased, they will be proportionally less correlated as long as their farfields are separated enough in order to not interfere each other. However, if two antennas with identical performances are radiating towards the same direction, they can be uncorrelated enough if they are separated by an adequate space, which is typically $\lambda/2$ [15].

The simulator CST Microwave studio relies on this expression to calculate the ECC and base its results on the simulated radiation patterns comparing their positions and polarisations. It involves complex calculations and several parameters contained in the functions that turn the calculations too difficult to manually reproduce and making a simulator such as CST an essential tool to determine this parameter.

Another expression for envelope correlation coefficient involves the dispersion S-parameters which describe the input – output ratio on a two-ported network. This is therefore applicable to a binary antenna system which will study the relationship between their respective ports. Being S_{11} and S_{22} the reflection coefficients for port 1 and port 2 while S_{12} and S_{21} will evaluate the power transferred between ports described by each parameter according to the notation, so that, S_{12} studies the power from port 2 to port 1 and S_{21} evaluates the transfer from port 1 to port 2.

The expression involving the S-parameters of a system of two antennas is described by Equation (29) as follows:

$$\rho_e = \frac{|S_{11}{}^* S_{12} + S_{21}{}^* S_{22}|^2}{(1 - |S_{11}|^2 + |S_{21}|^2)(1 - |S_{22}|^2 + |S_{12}|^2)} \tag{29}$$

Where S_{11}, S_{22}, S_{12} and S_{21} are the scattering parameters described previously in an antenna system studying the power transfer between ports as a two-ported electric network and the operator (*) represents the complex conjugate. Nevertheless, and despite the simplicity of this calculation compared to equation (28) this expression assumes the antennas studied in question have high efficiencies.

4.2.2. Diversity Gain.

This parameter was briefly described in the diversity techniques of section 4.1. essentially this metric determines the proportional reduction of the power in a system when multiple antennas are working simultaneously according to their SNR when spatial diversity is implemented in a communication system. If “n” antennas are used in a system, its corresponding signals ad up in phase, the noise adds up to, although incoherently. Diversity gain can also be considered as the reduced required SNR in reception from “n” antennas. This depends on the bit-error-rate (BER) and the fading margin due to the diversity scheme. The lower the fading margin is reduced for each antenna, the higher the diversity gain. Hence, the diversity gain could be higher than the array gain for a multiantenna system with a reduced number of radiators. Nevertheless, the diversity gain is saturated at the fading margin for each

antenna. The mathematical expression for Diversity gain DG is based directly on the calculation for the envelope correlation coefficient ECC described in section 4.2.1. Equation (30) describes the expression for DG. In practical terms, two ideal uncorrelated antennas that will offer an envelope correlation coefficient of $\rho_e = 0$ will therefore present a diversity gain DG = 10 dB [99].

$$DG = 10 \cdot \sqrt{1 - |\rho_e|^2} \tag{30}$$

When evaluating a multi-antenna system as a two-port network the S_{12} and S_{21} parameters are essential to corroborate the correlation between antennas. As mentioned previously, it is assumed that for antennas presenting high efficiencies equation (29) determines the envelope correlation coefficient. However, given antennas offer a dual property of transmission and reception also known as reciprocity, a system of two antennas will therefore evaluate that if antenna 1 in the scheme transmits a signal, then antenna 2 will receive a quantity of energy proportional to the correlation coefficient turning equation (29) as a suitable expression to determine this essential diversity metric for MIMO devices.

Although the analysis of S_{21} provides an essential figure for the interaction between two antennas in a multiantenna system, the study of envelope correlation coefficient is a complimentary analysis that evaluates the mutual interaction in a ratio from 0 to 1 which is specialised for MIMO systems. It is intended to optimise the proposed boards as MIMO candidates and therefore the complimentary analysis will determine in part the suitability of the designs presented.

The simulated envelope correlation coefficients and diversity gains calculated by the CST software package will be presented next. The obtained figures will help the estimation of the correlation between the two triple-slotted antennas operating in each prototype MIMO 1, 2 and 3. Then in the sequential order these simulations will be supported by the calculations of the same metrics using the measured S-parameters presented in section 3.3.2. and will evaluate in concrete numbers the compatibility of the MIMO 1, 2 and 3 prototypes for 5G applications according to these parameters.

For the analysis of simulated diversity parameters presented next, a fixed resonant frequency for each band offered by each prototype was selected. The capacitance values for D1, D2 and D3 are as follows in each antenna: D1 = 2.5 pF corresponding to a resonant frequency for Band 1 at 0.69 GHz, D2 = 2.5 pF tuning Band 2 at 1.34 GHz and D3 = 1.0 pF which achieves a resonant frequency of 2.22 GHz for Band 3.

4.3. Simulated diversity metrics for MIMO 1, 2 and 3.

As mentioned previously, the simulator CST provides the calculation of diversity metrics such as the reviewed Envelope Correlation Coefficient and Diversity Gain. For the simulated ECC, the software carries out the calculation using the simulated radiation patterns which have been presented in section 2.3.4. Hence, the CST software package uses equation (28). Moreover, the expression in CST used for the calculation of Diversity Gain is given by equation (30) as it only depends on the previously calculated correlation coefficient. Then, the description for the simulated figures will be carried out for ECC and DG for each board at a given frequency next. The proposed fixed values for this purpose are as follows: Band 1 = 0.69 GHz, Band 2 = 1.34 GHz and Band 3 = 2.22 GHz.

4.3.1. Simulated envelope correlation coefficient for MIMO 1, 2 and 3.

For each simulated board, a value for their respective ECC was obtained by the simulator itself. Overall, low correlation levels were observed for each board, for each band at their corresponding resonant frequency. The highest values, yet low correlations, are observed at resonant frequencies corresponding to Band 1 and are slightly above the standard 0.5 corresponding the highest values for MIMO 1 and MIMO. Nevertheless, for the rest of the frequency bands the numbers stay well below 0.3 which classifies these results as good and hence suitable for MIMO applications. Besides the observed simulated numbers in Band 1, correlations are nearly 0 for the rest of frequencies which correspond to resonant frequencies for Band 2 and Band 3, especially beyond the 1.0 GHz mark.

In Fig. 92, the envelope correlation coefficients simulated in CST Microwave studios for Band 1, Band 2 and Band 3. Agreement is observed from one board to other, overall, the correlations are higher in frequencies lower than 750 MHz. As the conditions are ideal in the simulator and do not consider any external distortions, the highest correlation levels indicate a higher interaction between antennas at the indicated frequencies, this is probably due to the proximity between the elements in the board, i.e. the mutual coupling effects are relatively stronger at lower frequencies. Nevertheless, the numbers presented in this analysis are accepted as they are below 0.5 in terms of correlation.

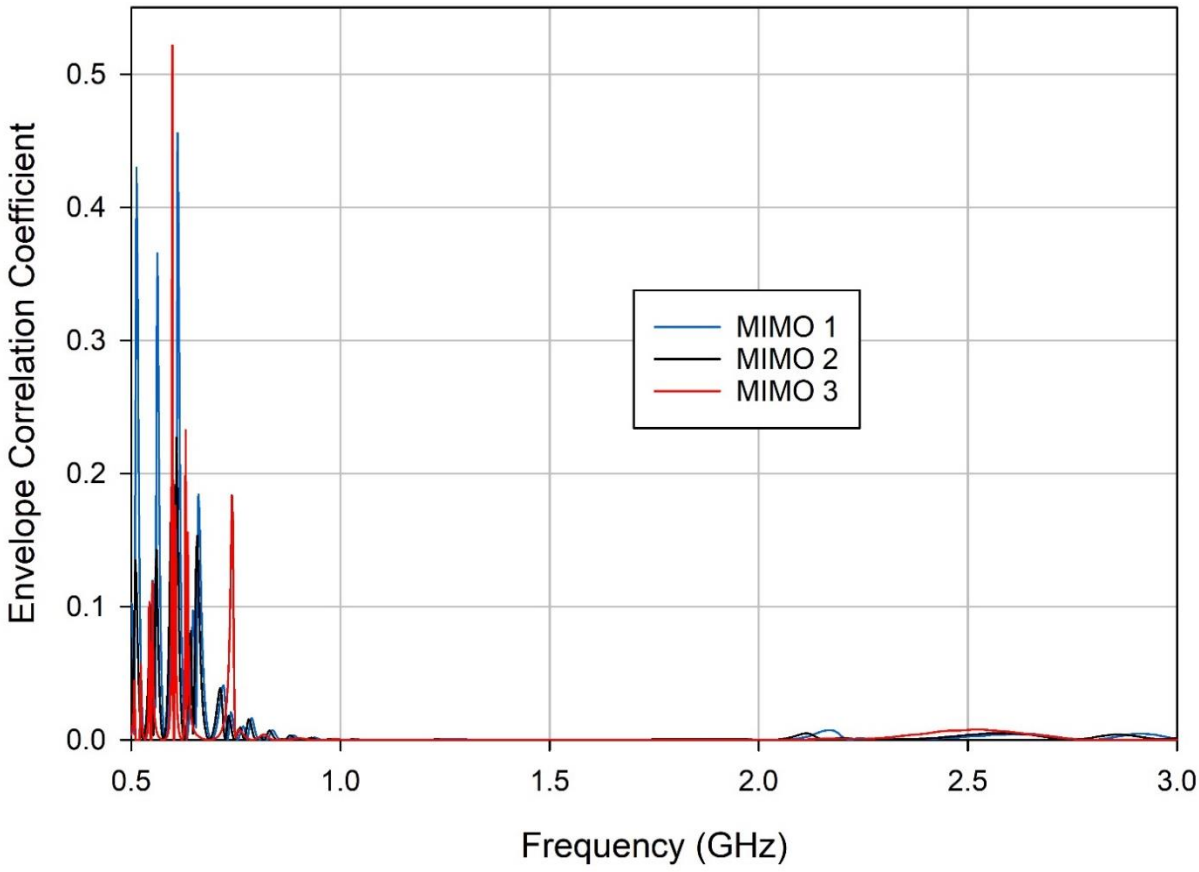

Fig. 92. Comparison of simulated Envelope Correlation Coefficient for each prototype.

4.3.2. Simulated diversity gains for MIMO 1, 2 and 3.

Furthermore, the simulated diversity gains which are depending on the correlations presented in Fig. 92 have been also obtained straight by CST Microwave studio. Diversity gains for each board reach their lower numbers in frequencies corresponding Band 1, resembling results are found in each board. Levels near the ideal 10 dB are observed in the remaining of the frequency except for Band 1 frequencies, similar to the ECC analysis. Diversity gains reaching 6.8 dB are observed at is lowest values which have been observed for MIMO 2. However, these ranges offer good levels of diversity gain after the 800 MHz mark which then proves that simulated MIMO 1, 2 and 3 are overall suitable for MIMO applications, corroborating the metrics for ECC in an ideal condition simulated environment. In Fig. 93, the simulated diversity gains for MIMO 1, 2 and 3 are presented, where similar results are observed from a board to board.

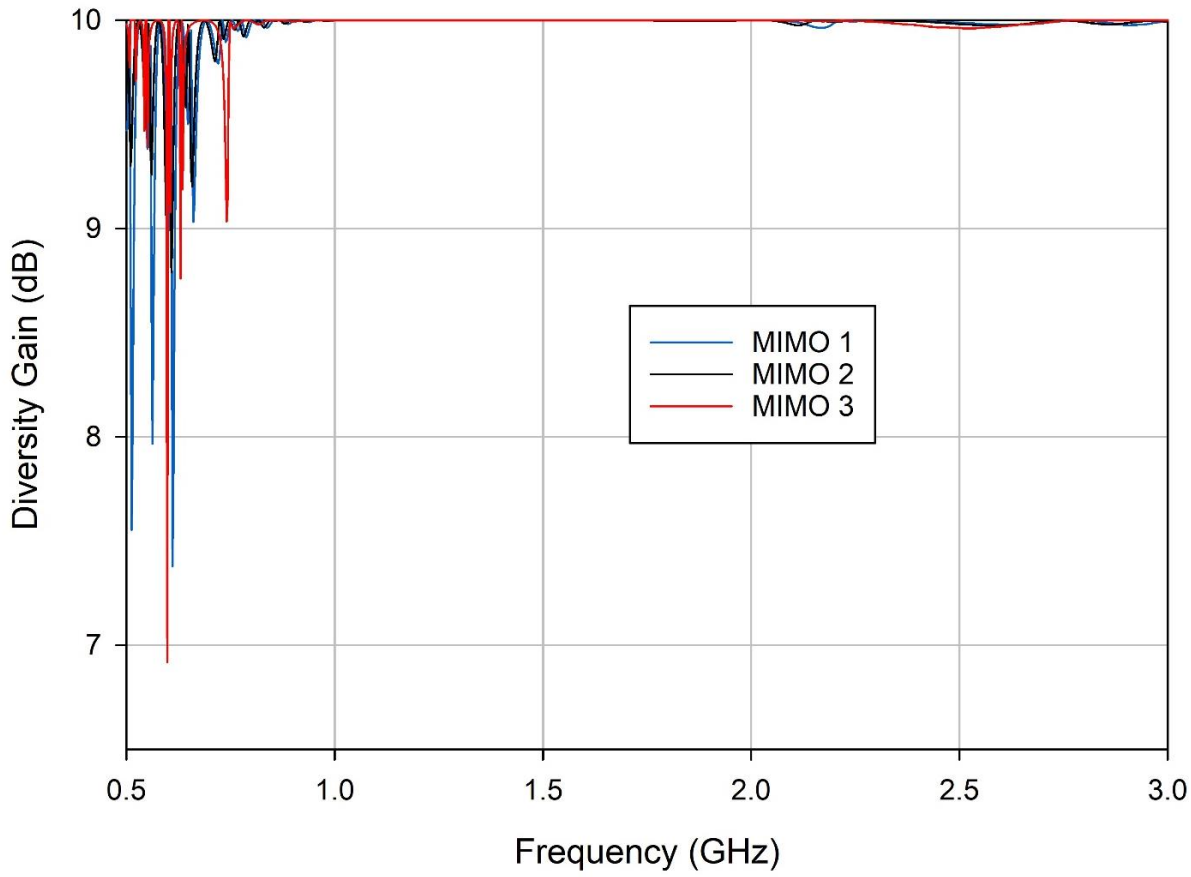

Fig. 93. Comparison of simulated diversity gains for each prototype.

4.3.3. Simulated isolation in S-parameters.

The simulated diversity metrics ECC and DG presented previously can be corroborated by analysing the simulated S-parameters, including the numbers presented in section 3.2.2 and adding the simulated mutual couplings S_{21} and S_{12} for each prototype.

In Fig. 94, the simulated isolations given by S-Parameters obtained in CST Microwave Studio are presented. These metrics are associated to the previously analysed ECC and DG. As discussed previously, when a multi-antenna system is analysed as a multi-port electric network, we can evaluate the contributions between ports using S-Parameters. Therefore, the isolation is observed as the ratio between the reflection coefficients S_{11}, S_{22} and the transmission coefficients S_{21}, S_{12} for (a) MIMO 1, (b) MIMO 2 and (c) MIMO 3 respectively.

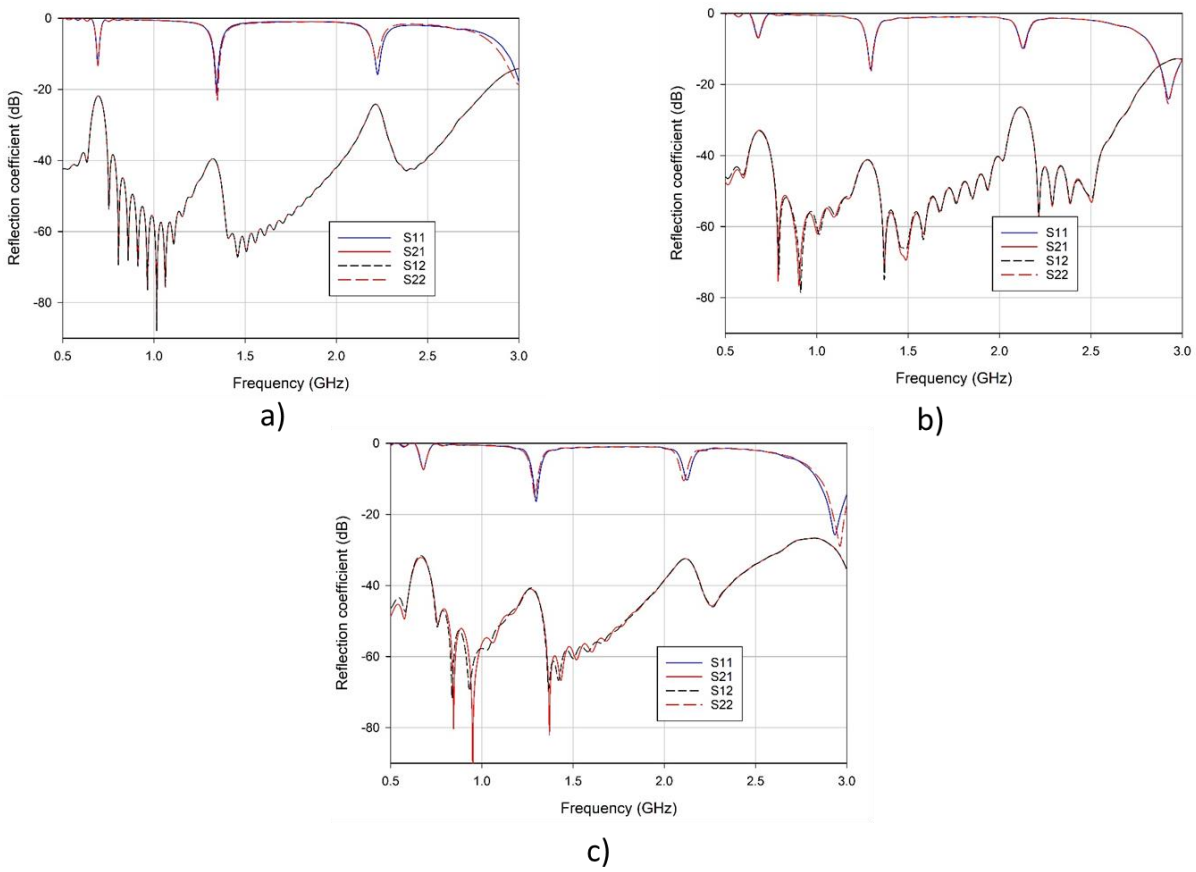

Fig. 94 Simulated isolation for each prototype.

It was observed in the previous figure that good isolations are presented for the three prototypes, which correspond to 12 dB in their lowest figures, typically located in Band 1 frequencies. Isolation S_{21} is interpreted as power transmitted from Antenna 1 to Antenna 2 and vice versa for S_{12}. the best isolation levels are above 25 dB and correspond to Band 2 for the three boards as the results are highly resembling. Overall, the isolation levels help to corroborate the low correlation between antennas in the MIMO prototypes as they determine the mutual coupling effects between two sets of antennas.

4.3.4. Calculated envelope correlation coefficients and diversity gains using simulated S-parameters for MIMO 1, 2 and 3.

Given that the correlations obtained in simulation are calculated using the simulated radiation patterns of the prototypes, this section will assess the use of equation (29) in order to calculate the ECC.

Using the previously presented S-Parameters obtained in simulation. These numbers have first to be converted in their magnitude forms prior to be used in a calculation. With a view to obtain these results I have developed a simple code in MATLAB implementing equation (29) using the magnitude form of the simulated S-Parameters. In Fig. 95, the calculated ECCs for MIMO 1, 2 and 3 are presented. These metrics were calculated by the programming in MATLAB using the respective simulated S-Parameters presented in section 3.2.2. The observed numbers for calculated ECCs are similar to the simulated ECCs obtained straight from CST Microwave Studio. These numbers correspond to high correlations of 0.7 for frequencies near 600 MHz which correspond to slightly higher mutual couplings at the indicated frequencies and practically negligible correlations beyond the mark of 700 MHZ for the rest of the range.

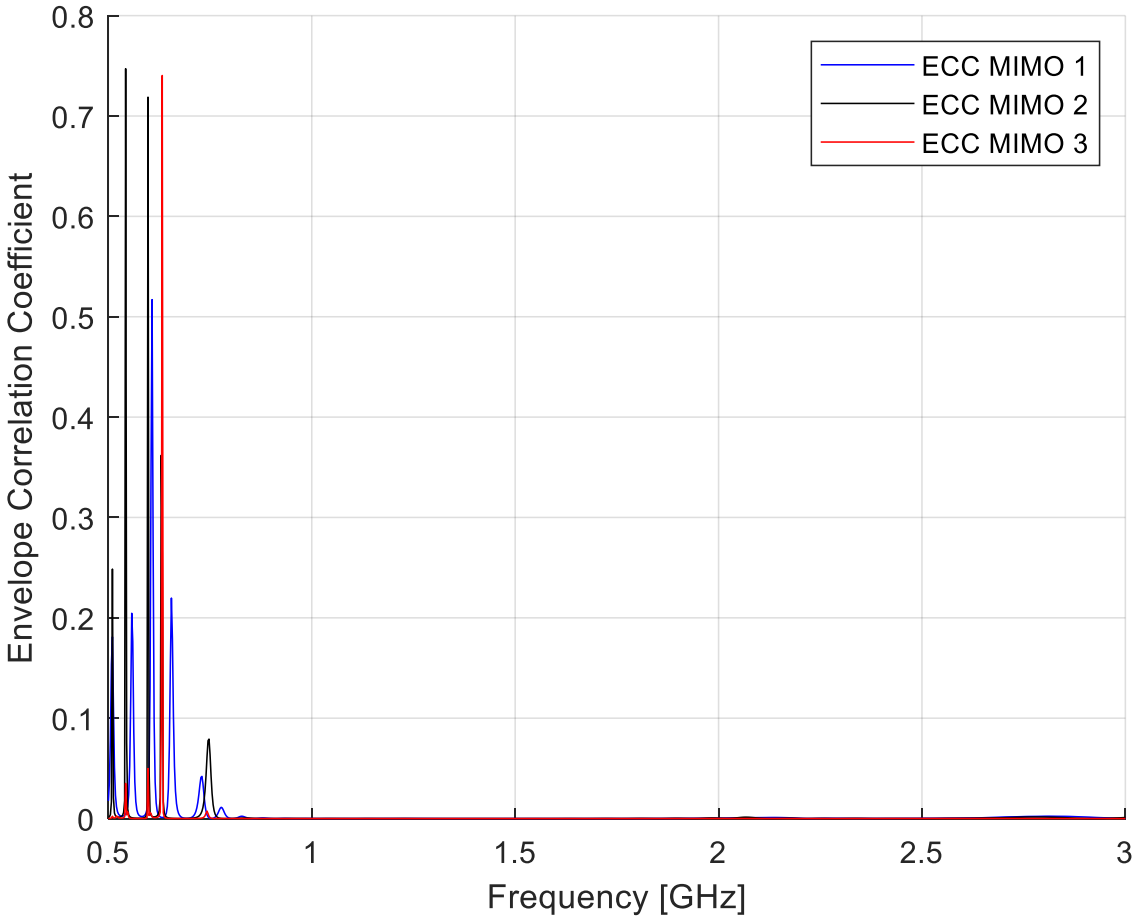

Fig. 95 Calculated envelope correlation coefficients for MIMO 1, 2 and 3 using simulated S-Parameters.

Once the envelope correlation coefficients were calculated, the diversity gains were obtained also using the numbers presented in Fig. 95 and implementing equation (30) in the MATLAB coding. Similar to the simulated diversity gains, the calculations showed the lowest peaks in frequencies surrounding 600 MHz where gains not lower than of 6.7 dB are shown. However, for the rest of the range we see ideal figures of 10 dB with very slight variations for the rest of the range. In Fig. 96 below, the calculated diversity gains using simulated results are presented for the three boards.

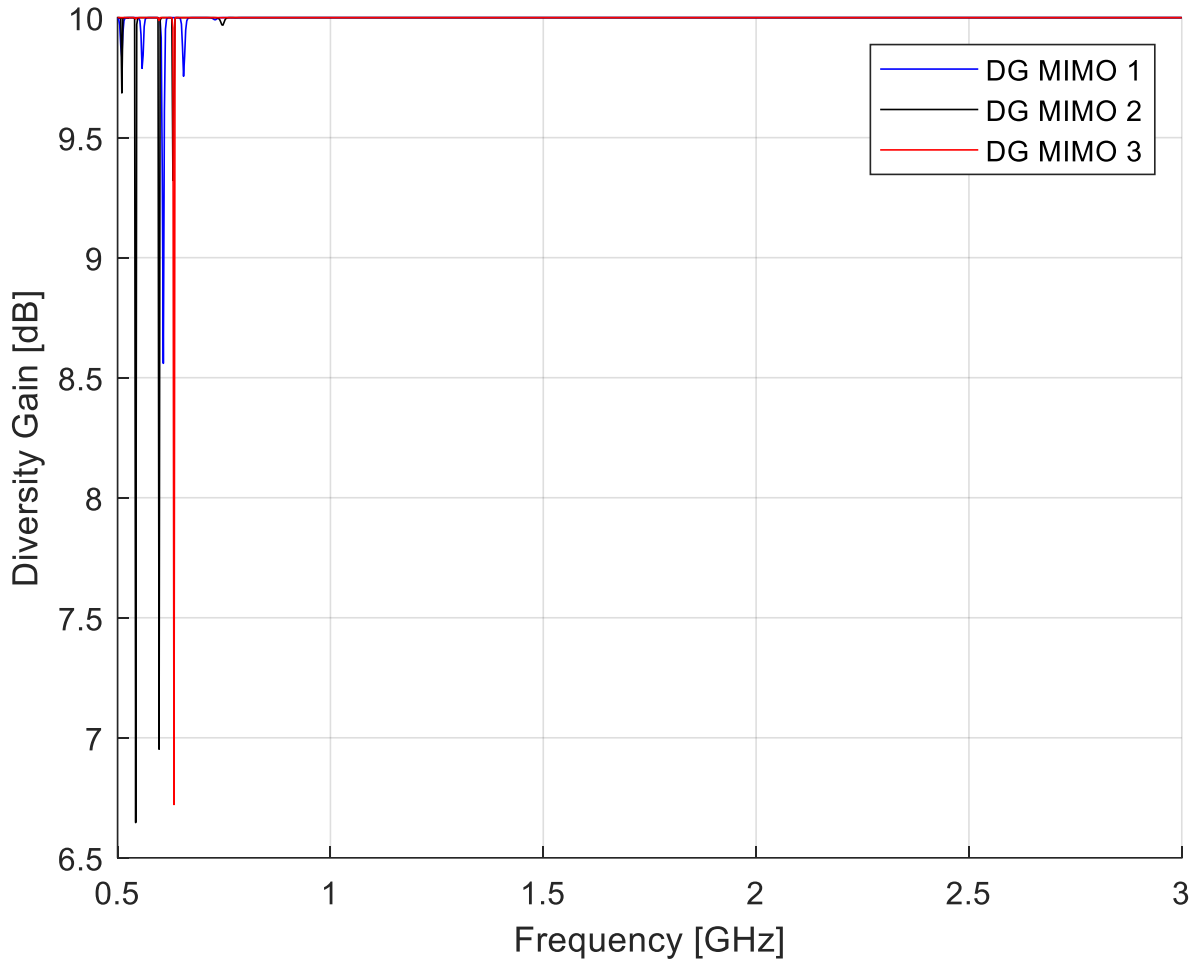

Fig. 96 Calculated diversity gains for MIMO 1, 2 and 3 using simulated S-parameters.

As an additional comparison, and in order to prove the similarities between both methods, two graphs are presented in Fig. 97 below, where dashed lines describe the simulated metrics obtained by CST Microwave Studio while dotted ones present the calculated metrics derived from the simulated S-Parameters. The graphs presenting this comparison are below for (a) Envelope Correlation Coefficient and (b) Diversity Gain.

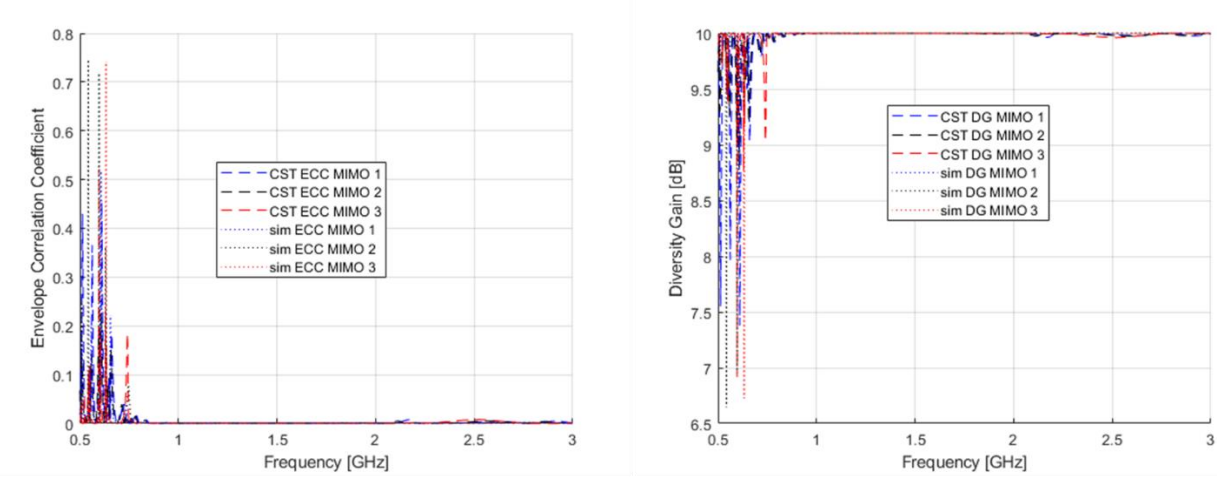

a) b)

Fig. 97 Comparison between simulated by CST and simulated S-parameter derived diversity metrics.

One could take as a reference the numbers simulated by CST as a more accurate model, since it involves physical characteristics for the boards. Since CST numbers and the calculated metrics using simulated S-Parameters agreed in general with slight variations. Hence the accuracy has been proved for equations (29) and (30) and can therefore be used to calculate diversity parameters using measured S-Parameters.

Overall, for simulated diversity metrics, both obtained straight from CST Microwave Studio and calculated using simulation S-Parameters, relatively high correlations were observed for frequencies corresponding to Band 1 where we do not observe significant resonant frequencies for the antenna performances. However, after the mark of 750 MHz, where slots 1 start to achieve properly matched resonant frequencies we observe ideal numbers for both ECC and DG. The numbers simulated for prototypes MIMO 1, 2 and 3 highlight them as suitable candidates for MIMO applications.

CST Microwave Studio offers to calculate the total efficiencies for each board. Considering antenna efficiency as the ratio between the radiated power and the input power, namely: $e_r = \frac{P_{radiated}}{P_{input}}$ where e_r is the antenna total efficiency. This parameter is essential when attempting to calculate ECC for the simulated MIMO prototypes given equation (29) is valid for antennas presenting high efficiencies.

As the simulated efficiencies reached the values described in Table 1 below the limitation of the use of the envelope correlation coefficient calculated by equation (29) was a concern, as this expression is based on isolation and suggests that by improving S_{12} the correlation coefficients will be reduced.

	Simulated efficiency for MIMO 1	Simulated efficiency for MIMO 2	Simulated efficiency for MIMO 3
Band 1 = 0.69 GHz	45.7 %	49.5 %	44.1 %
Band 2 = 1.34 GHz	19.4 %	14.2 %	17.5%
Band 3 = 2.22 GHz	26.3 %	33.7 %	28.9 %

Table 5 Simulated efficiencies for MIMO 1, 2 and 3.

In Table 5, low efficiencies are presented. These numbers do not classify the MIMO prototypes into highly efficient antennas. Nevertheless, the accuracy of equation (29) offers decent agreement with simulations despite its suitability for antennas with high efficiencies. Which provides us with an adequate approximation of the correlation coefficient basing on S-Parameters when comparing it to the numbers calculated by the simulator using radiation patterns.

On the accuracy of equation (29), although it is designed to be suitable only for highly efficient antennas it is a useful mathematical tool determine an approximation for envelope correlation coefficients and consequently diversity gains using a simpler expression than equation (28) that requires complex functions which are difficult to obtain using measurements easily obtained on a network analyser. Hence, the correlation coefficient equation (29) has been implemented using the measured results for each board. The calculated numbers using measured S-Parameters are presented in the next section.

4.4. Calculated metrics using measured results for MIMO 1, 2 and 3.

Once the simulated diversity metrics have been analysed in the previous section, the calculated envelope correlation coefficients and diversity gains will be discussed, using the measured S-Parameters presented in section 3.3.2 for each board. As explained in the simulated diversity calculations, these parameters determine how optimal an antenna system is when a diversity scheme is applied. In diversity techniques, the same amount of information is sent across independent channels to combat fading which has to be corroborated by measured numbers of the prototypes MIMO 1, 2 and 3. In real-life measurements we observed good isolation levels that imply low correlations between the two antennas on each board. Moreover, a good agreement with the simulated results has been observed, which therefore implies that similar envelope correlation coefficients and diversity gains will be obtained with measured results.

In this section, the numbers calculated for ECC and DG are discussed using the measured figures for MIMO 1, 2 and 3 presented in section 3.3.2. For practical purposes, I will refer to these metrics as measured ECC and measured DG despite not being obtained straight from a Vector Network Analyser (VNA). For the calculation of envelope correlation coefficients and diversity gains, a set of resonant frequency references was selected for each independently tunable frequency band similar to the ones presented in section 4.3 as reference which are as follows:

Band 1 → D1 = 6.1 V / 2.5 pF → 0.68 GHz.

Band 2 → D2 = 6.1 V / 2.5 pF → 1.42 GHz.

Band 3 → D3 = 10.3 V / 1.0 pF → 2.11 GHz

These results have slight variations for one board to the other but present similar frequencies for each prototype. As a good agreement was observed between CST simulated and simulated S-Parameters derived, a similar agreement was expected between the previously analysed figures and measured ECCs and DGs. In the following sections 4.4.1 and 4.4.2.

Moreover, a MATLAB code was implemented for the calculation of ECCs and DGs presented, similar to the previous section and an imperative conversion of S-Parameters into their magnitude forms was carried out for this calculation.

4.4.1. Calculated envelope correlation coefficients using measured S-parameters.

Using the measured scattering parameters for each board and following the reference frequencies described previously. The following numbers were obtained using equation (29), similar to the operations carried out in section 4.3.4 and acceptable numbers for Envelope Correlation Coefficients are observed. ECCs above 0.68 are observed in their highest peak values near 600 MHz similar to the calculated and simulated ECCs. Moreover, after the mark of 1.0 GHz, correlations below 0.4 are observed, which is considered good MIMO applications. Another set of peak values that do not go above 0.3 except for MIMO 2. It is important to point out that measured results ideally uncorrelated antennas are very unlikely to be achieved, however the metrics are adequate and similar to simulations.

In Fig. 98, the measured envelope correlation coefficients are presented for the three prototypes that have been calculated using the measured S-Parameters.

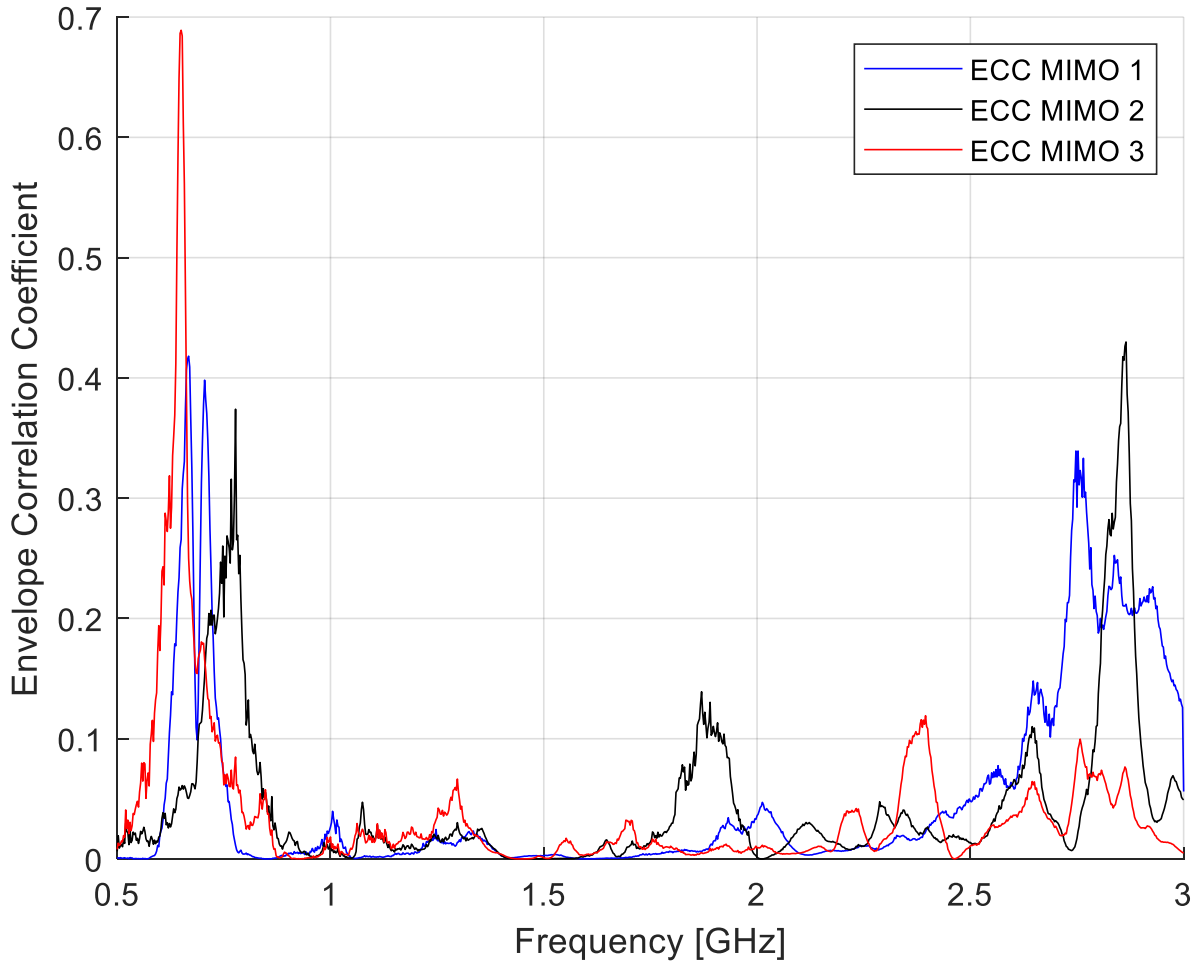

Fig. 98 Measured envelope correlation coefficients for the manufactured prototypes.

4.4.2. Calculated diversity gains using measured envelope correlation coefficients.

For the measured diversity gains, the numbers presented in the previously shown Fig. 98 and carried out the calculation using equation (29). In Fig. 99, the calculated DGs for MIMO 1, 2 and 3 are presented, using their respective measured correlation coefficients. Diversity gains are observed with similar numbers to the simulated figures obtained in CST Microwave Studio and the ones calculated in section 4.3.4. the lowest gains close to 7.2 dB are observed near 600 MHz and correspond to Band 1, similar to simulated results. Diversity gains close to 10 dB are observed in the remaining of the frequency range two slight peaks measured for MIMO 1 and 2 at frequencies near 2.75 GHz which correspond to Band 3. However, these numbers are not as significant as the peaks observed for Band 1.

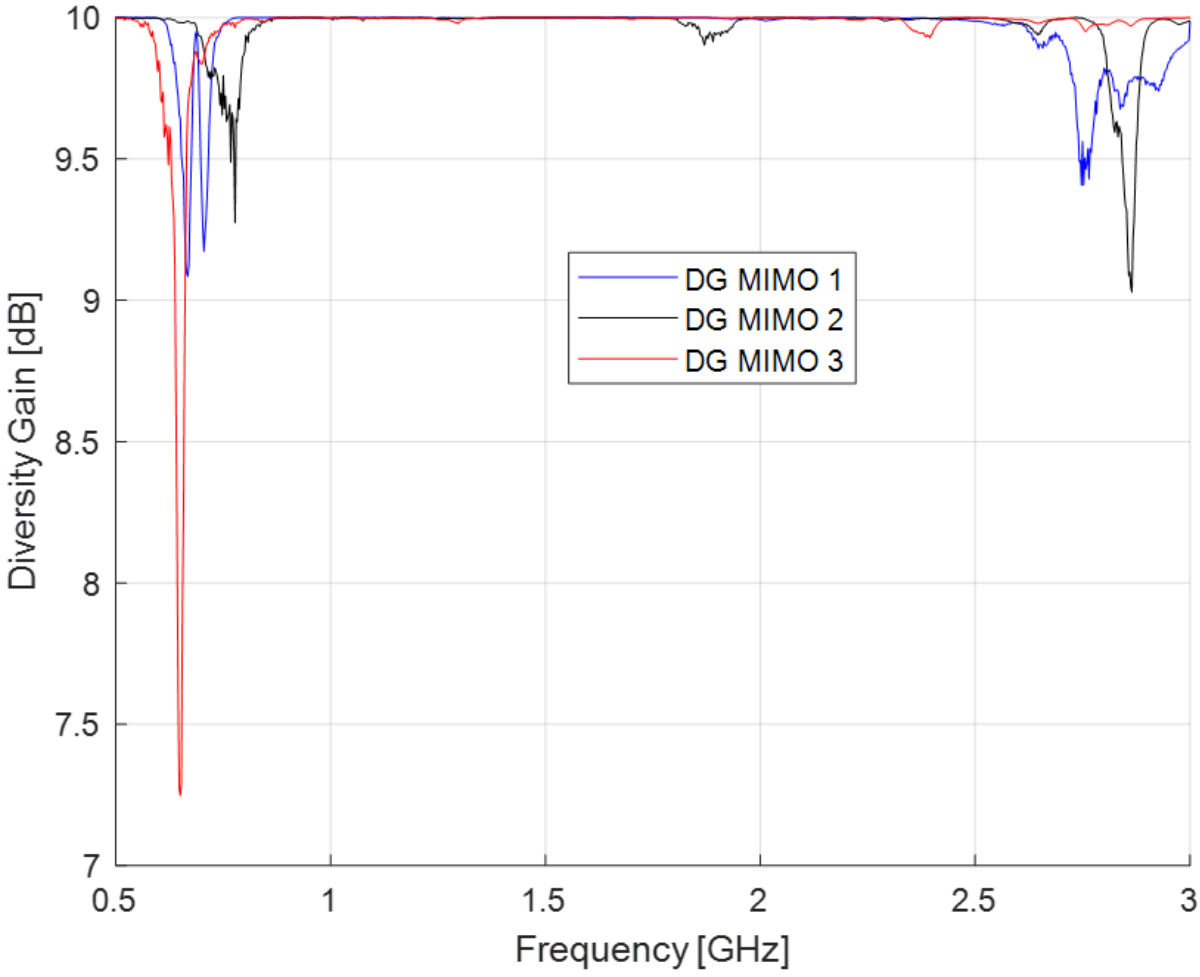

Fig. 99 Measured diversity gains for the manufactured prototypes.

Additionally, a comparison between simulated (both CST and S-parameters derived) and measured Diversity calculations will be now discussed. Firstly, the comparison for ECCs will be analysed. For this, Fig. 100 presents the analysis corresponding the Envelope Correlation Coefficient for (a) MIMO 1, (b) MIMO 2 and (c) MIMO 3. The blue solid line represents the measured numbers, the red dashed lines corresponds to the simulated S-Parameters derived calculated by the MATLAB code and the black dotted line stands for the CST simulated ECC.

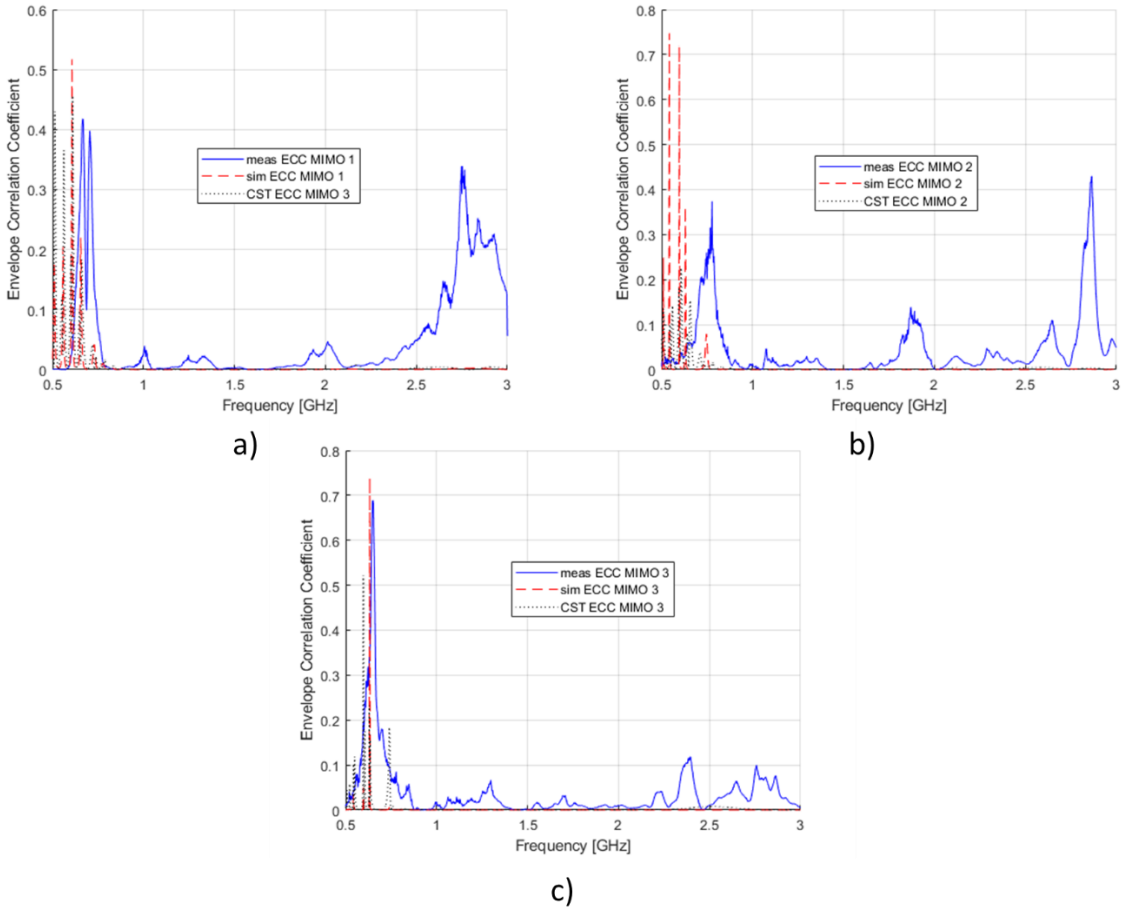

Fig. 100 Comparison between simulated and measured ECCs for the three boards.

In this comparison, an agreement is observed for the high correlations in frequencies below 800 MHz, which correspond to Band 1, nevertheless, there is an unexpected peak for the measured numbers, located at frequencies near 2.6 – 2.9 GHz, which was not observed for any of the simulated methods. These are a set of correlations near 0.3 and 0.4, especially for MIMO 1 and 2, however, these are still below the 0.5 mark which is an appropriate mark. These numbers are probably related to component's SRF or a poor shielding.

Then, for the comparison between simulated and measured diversity gains, the analysis carried out will be discussed next. The analysis compares the set of simulations against the measurements. In Fig. 101, the comparison is presented for (a) MIMO 1, (b) MIMO 2 and (c) MIMO 3.

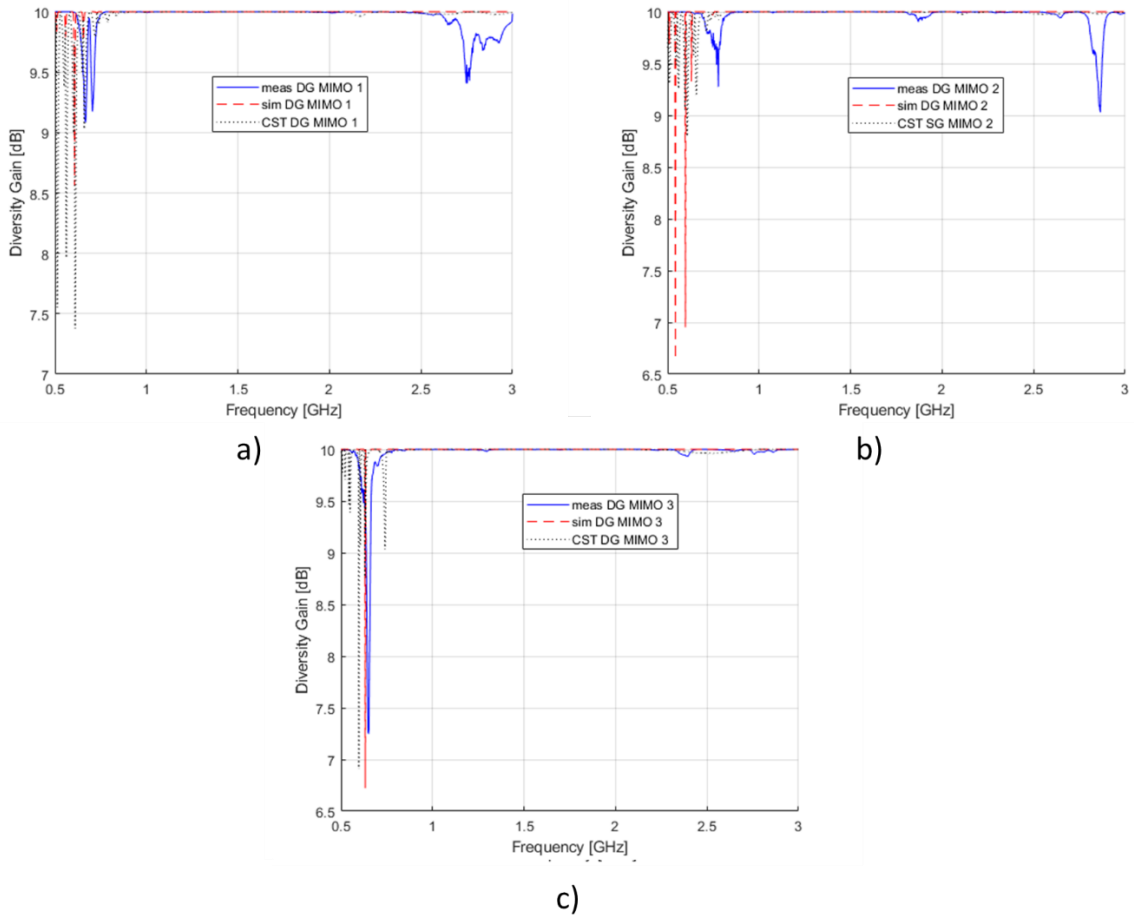

Fig. 101 Comparison between simulated and measured ECCs for the three boards.

Similar to the comparison for ECC, an unexpected peak is observed for frequencies near 2.6 – 2.8 GHz, nevertheless, this is still below the limit recommended. Overall, for measured envelope correlation coefficients and diversity gains, s which high correlations of more than 0.68 for where observed for frequencies starting at 600 MHZ which are resonant frequencies of Band 1 but low acceptable numbers on the rest of the range. And is totally improvable by replacing the shielding for better assessed one. This classifies the prototypes MIMO 1, 2 and 3 good candidates for MIMO applications at frequencies higher than 750 MHz. Moreover, in terms of diversity gains we observed the lowest levels at frequencies for Band 1 near 600 MHz, agreeing with the frequencies where the highest correlations have been measured and correspond to a diversity gain of 7.2 dB.

4.4.3. Measured isolation in S-Parameters.

Similar to the simulated numbers, the measured diversity metrics ECC and DG can be corroborated by analysing the measured S-parameters where the figures analysed in section 3.3.2 together with their corresponding mutual couplings S_{21} and S_{12}. In Fig. 102, the measured isolation is presented for (a) MIMO 1, (b) MIMO 2 and (c) MIMO 3 where similar numbers to those observed in simulation and corroborate the adequate independence between antennas for MIMO applications are presented.

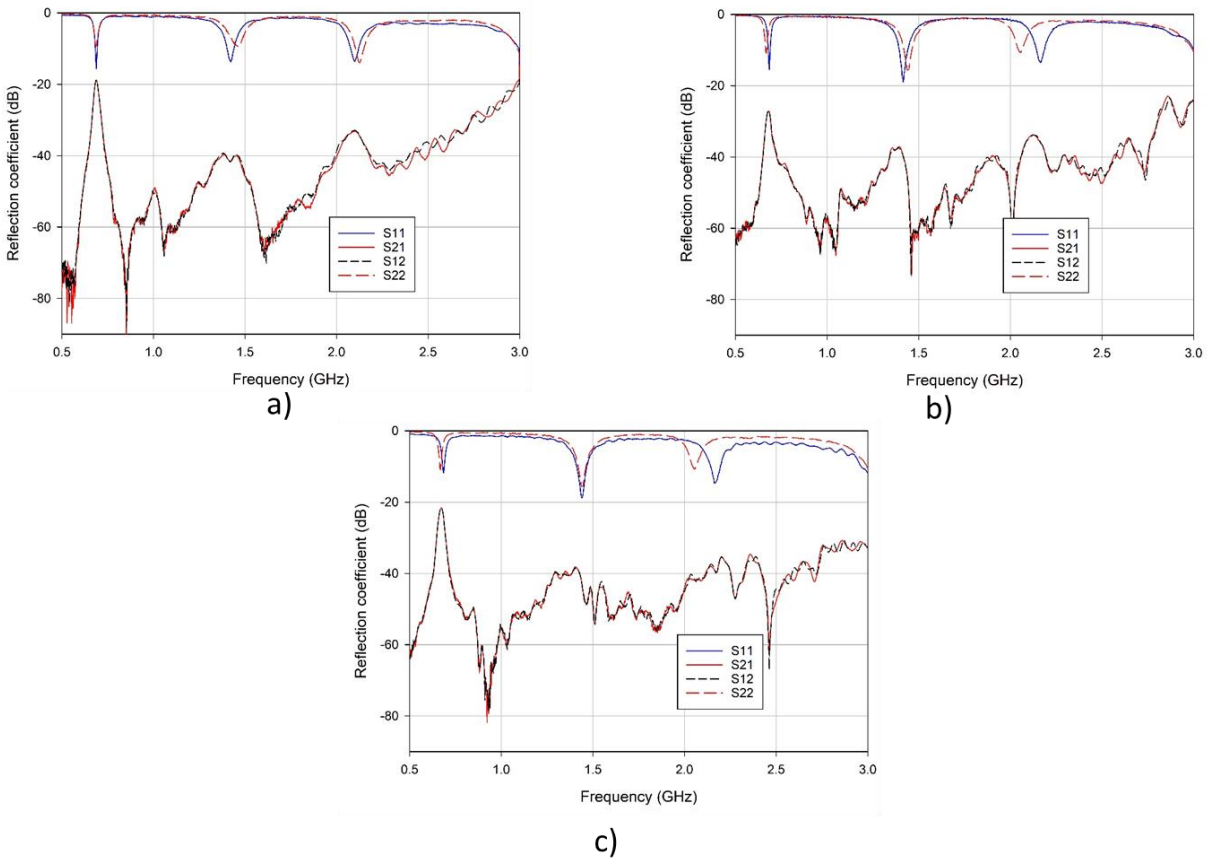

Fig. 102. Measured isolation for each manufactured prototype during simultaneous tuning.

Furthermore, on commenting on the isolation between antennas, the particular case of MIMO 1 presents higher correlations at frequencies in Band 1. In Fig. 103, the measured isolation for MIMO 1 is presented, when D1 varies its capacitance from 2.5 pF to 2.0 pF. This figure shows an isolation near 8 dB at the staring value for D1, then at the respective capacitance, a low isolation is observed which implies a high correlation for the antennas in the board. However, for the rest of the frequency range the isolation is maintaining at high levels which correspond to low correlations and hence diversity gains near 10 dB corroborating the observed numbers of ECC and DG observed in simulation and measurements.

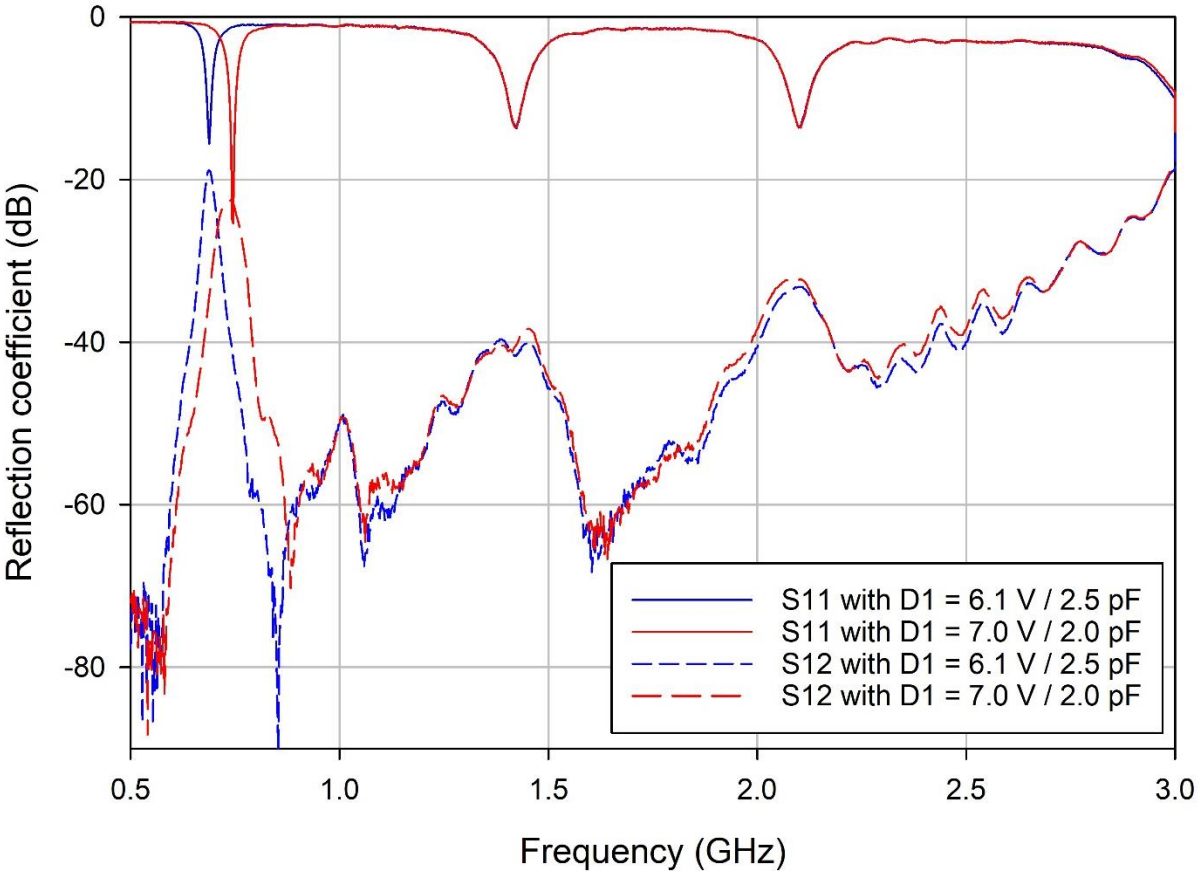

Fig. 103 Measured Isolation when tuning two different values for D1.

By proving what the isolation effects are as described in what the multi-port electrical network theory dictates, the set of analysis carried out in this chapter corroborate that enhancing the mutual couplings S_{12} and S_{21} will have a positive effect on reducing the correlations between antennas. Consequently, if the aim of a diversity study is to assess methods to reduce the correlation between two single antennas, the most recurrent and effective method is to increase the S-Parameters-based isolation by implementing any of the techniques explained in section 4.2.

Overall, the study of isolations carried out in this section has helped and corroborated the metrics presented in the ECC and DG studies in previous sections. Overall, the simulated and measured diversity parameters presented ideal numbers for bands 2 and 3 but higher numbers for Band 1, which is also presented in the isolation readings. In the case of measured ECC and DGs, there are peaks at higher frequencies near 2.6 – 2.9 GHz which are also reflected in the transmitted power observed in the measured isolation metrics as the correlations are higher for these frequencies.

4.5. Conclusions for Chapter 4.

In conclusion to the analysis of diversity parameters carried out in this chapter, the metrics simulated, and calculated using simulated and measured S-Parameters for the designed prototypes are useful to determine its suitability for MIMO applications. Parameters such as ECC and DG are specific metrics required to assess the performance for MIMO systems and the mutual interaction between antennas in a diversity scheme. Although a simpler assessment of the antenna isolation S_{21} can determine the amount of power transmitted from one antenna to other, these analysis are a complimentary study which help determine useful anomalies such as the ones presented by measured ECCS and DGs at frequencies above 2.6 GHz. Nevertheless, the obtention of these readings highlight the proposed prototypes as suitable for MIMO applications in frequencies above 750 MHz where low correlations and diversity gains near 10 dB are observed which are within the boundaries of good results for diversity parameters.

An agreement has been found between simulated and measured metrics frequencies from 500 MHz to 2.6 GHz where low correlations and high diversity gains are observed. However, measured reading s present unexpected peaks at frequencies above 2.6 GHz which do not agree with any of the simulated metrics. Nevertheless, the initial agreement corroborates not only the accuracy of the software CST Microwave Studio in estimating diversity metrics but also proves the effectiveness of the equations that determine the correlation coefficients based on the scattering parameters despite these are dedicated to highly effective antennas and this is not the case for the MIMO prototypes. Overall, these devices present diversity metrics within the recommended limits for 5G diversity standards and classify as good candidates for MIMO applications as the correlations are overall low and the diversity gains obtained are uniformly high. The suitability of the presented boards is corroborated by the study the isolations S_{12} and S_{21} in simulation and measurements which determine the power transmitted from Antenna 1 to Antenna 2.

As a result of these studies, many solutions are suggested to reduce the transmission coefficients S_{12} and S_{21} and consequently ECCs and DGs, e.g. increasing the separation between antennas or changing the polarisation for each of the antennas. These hypothetical modifications in the system will have a positive effect on reducing the correlations and keeping diversity gains near 10 dB which is the main goal for improving multi antenna systems. Moreover, we could observe diversity patterns in section 3.3.3 for MIMO 3 which is also desirable for MIMO metrics optimal for 5G technologies.

CHAPTER 5. DESIGN, SIMULATIONS, MANUFACTURE AND MEASUREMENTS OF 3D-PRINTED FREQUENCY RECONFIGURABLE RECTANGULAR DIELECTRIC RESONANT ANTENNAS FOR MM-WAVE APPLICATIONS

As discussed in Chapter 2, the next generation of mobile communications demand large amounts of data being exchanged and consequently, high frequencies of operation. This is a research opportunity for dielectric resonator antennas. Despite being discovered in the late 40's this technology has now been recalled with a view to overcome the difficulties of high metallic losses when working at high frequencies given the non-metallic nature of these radiators. This is also a promising research opportunity for novel materials with interesting properties that have not been assessed yet in wireless communication engineering applications. For the development of this chapter, I am proposing the assessment for low-cost unconventional dielectric materials as DRAs in simulation and sequentially in real-life measurements.

In this chapter, a discussion for novel materials for DRAs will be carried out, then the assessment of mathematical tools to estimate the geometry of a RDRA will be presented and finally the design and simulations of a reconfigurable DRA will be discussed. The aim is to achieve a tunable 3D-Printed dielectric resonant antenna suitable for mm-wave frequencies which controls its resonant frequencies by changing the permittivity of different materials contained inside the dielectric resonator With a view to achieve frequency reconfiguration, the modification of an essential parameter such as the dielectric permittivity of the material analysed in question can be tuned and therefore control the resonant frequency.

The extrapolation of this study suggests that a reconfiguration mechanism will be achieved by an electrically tuned material or substance that can alter its properties by controlling an electric signal. Some of the materials with the desired properties were facilitated by the silk fibroin research group of the chemical and biological engineering department of the University of Sheffield. A collaboration was fulfilled between the research groups with a view to achieve a useful application in communication engineering for the materials that are developed in the CBE department.

5.1. Research opportunities for 3D-Printed low-cost materials as DRAs.

After reviewing many publications in the literature review, the most common material used for the construction of dielectric resonators is a wide variety of ceramics. Ceramics are optimised to perform in microwave applications as their relative permittivities are high, their structure provides an ideal dielectric waveguide path and can be manufactured in miniaturised shapes and maintain their properties in reduced sizes [101]. However, using ceramics implies elevated costs for manufacture given the high grade of precision is required to be achieved in the structure of the resonator which is only possible through specialised manufacture methods, which increases considerably the cost of the DRA and hence the additional components such as the connectors and substrates which consequently, require a high precision grade.

5.1.1. 3D-Printing bioplastics as dielectric resonator antennas.

One of the objectives of this thesis is to assess novel materials as the constituting dielectric for a DRA. In the reviewed literature and state of the art for dielectric resonators antennas, practically all the published works are incorporating ceramic-based resonators. Given the recurrent use of ceramics, the overall costs for the manufacture of DRAs is high as it requires precise manufacture methods and refined materials which are difficult to achieve by simple construction methods. In order to overcome this gap in knowledge and to assess alternative materials to significantly reduce the cost of DRAs, I propose the use of an alternative material with numerous applications in 3D printing fabrication, this is the case of the polylactic acid (PLA). This material is derived from biological waste sources such as biomass as well as a biodegradable polymer also known as a bioplastic. It is widely used in medicine, chemistry, biology, materials engineering and more.

However, PLA is not commonly used in electronics and electrical engineering applications, specifically in communications engineering. Therefore, the opportunity to explore the use of a bioplastic in the fabrication of a dielectric resonant antennas was an ideal opportunity to study the suitability for such innovative material in communications engineering. It is known that the electric properties for materials such as PLA vary form one kind to other, however, the estimation for the relative permittivity of these bioplastics is from 2.5-3 depending on some factors related to the production of the material. Normally, a permittivity above 10 is used for DRAs materials, however, the elevated cost of production for a ceramic resonator is generally elevated. PLAs offer an easier way to manipulate its structure and hence manufacture multiple shapes such as 3D-Printing. Being one of the most recurrent

methods for fabrication of part nowadays, 3D-Printing is widely used for the production of parts with applications in multiple disciplines DRAs are not an assessed approach for published work as the materials involved do not present the high precision features that ceramics offer. Nevertheless, a faster and cheaper construction technique for a DRA, as well as the assessment for the suitability of PLA as dielectric resonators will be discussed throughout this chapter.

The researchers from the silk-fibroin research group in the Chemical and Biological Engineering (CBE) department are exploring the applications of 3D-printing polymers based on silk proteins and bioplastics for diverse applications on biological engineering. They have provided some materials for this Thesis and will be discussed later in this chapter. A set of the materials facilitated by the CBE department and some of the work developed for the silk-fibroin research group are presented in Fig. 104 below, where a PLA-based part is being manufactured in the 3D printer of the CBE laboratory is shown in (a), while (b) and (c) present the silk-fibroin based 3D-Printed process carried out by the research group.

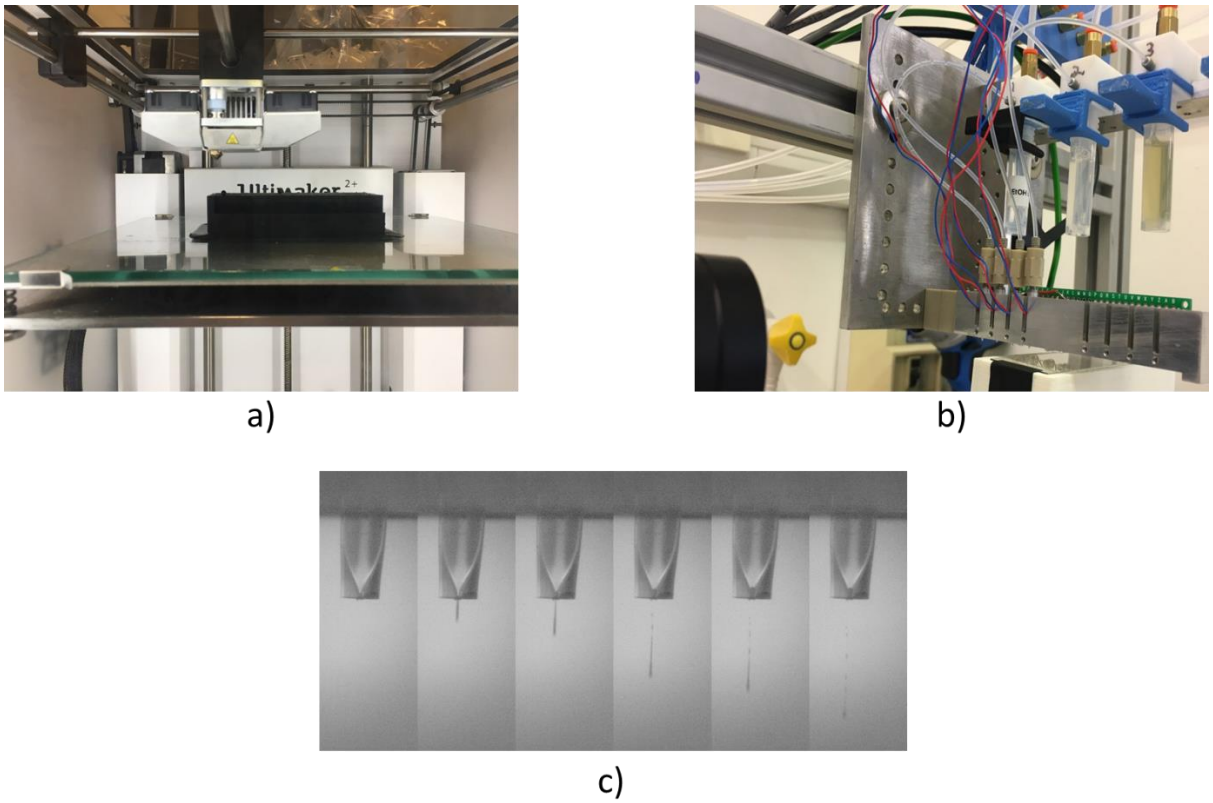

Fig. 104 3D-Printing manufacture of polymer-based applications in the CBE department.

Additional remarks concerning the preparation of materials used in this thesis that have been facilitated by the CBE department and the silk-fibroin research group are presented in Appendix B of this Thesis.

5.1.2. Electronically tunable materials for frequency reconfiguration.

In terms of frequency reconfiguration, many tunable materials have been considered for the DRA itself, for the tuning element or the substrate. Nevertheless, the most sensible approach is to create a dielectric resonator that will contain another material, preferably tunable, with a relative permittivity different from the one of the dielectric resonators. The difference between permittivities will create a frequency shift that can be controlled electronically. Some materials that present these features will be assessed in this section such as liquid crystals and graphene. These materials rearrange their internal structure in presence of an electric field or signal and have been used previously as tuning elements for communications equipment related to frequency agile applications.

As reviewed in Chapter 2, one of the most recurrent substances used in communication, RF and microwave engineering applications are liquid crystals. They are a versatile material easy to manipulate by a DC voltage to control its relative permittivity. LC are mainly used in printed antennas and enclosed devices; however, they are difficult to manipulate physically without the appropriate protection equipment and imply high costs in their transport, containment, and incorporation to the system in question. Hence, the idea of incorporating liquid crystals to the proposed 3D-printed antenna was discarded due to the setbacks presented. Nevertheless, there is a gap in knowledge for tunable substances as it is quite unusual to incorporate a liquid or colloidal element in an antenna. Therefore, another substance is proposed as it was facilitated by the silk-fibroin research group which is graphene oxide (GO).

Graphene oxide is derived from the oxidation of graphite itself and produced by numerous chemical and mechanical techniques with a view to achieve its reduction [112]. Graphene oxide is the product of a simpler and a lower cost method of production of graphene, highlighting it as a financially suitable form of graphene keeping all the innovative properties offered by graphene. Having graphite as the base material of this innovative produce, we can consider it as a stock of several millions of graphene layers that will be strongly oxidised by the aid of external agents. Once the oxidation occurs, the graphene layers will separate by a larger gap and will allow the material to be compatible with water. If a single layer is produced at the end of this complex process, then it will be called graphene oxide. Consequently, numerous layers will be considered graphite oxide [113]. Graphene oxide is constituted by a nanotubes-based structure which allows the material to have multiple useful and innovative

properties that can solve many of the current environmental, medical, and structural problems of our daily life.

Although graphene and graphene oxide have been recently used in novel applications such as water filtration and cancer cure, it has also been explored in electronic communications engineering, using as sensors in high accuracy circuits, always basing on its dielectric permittivity and techniques to control it. Graphene oxide permittivity depends on multiple factors and is a parameter difficult to calculate as it depends on many complex variables which is why a simulation for this material could not have been simulated. However, many techniques have been carried out to characterise the electric properties of graphene and graphene oxide. Dielectric permittivity of graphene and graphene oxide could have been estimated by some experimental protocols that have obtained numbers depending on many parameters which do not specify a starting point for a concrete value [114], [115]. Nevertheless, graphene oxide has been recently used in some applications in communications engineering as temperature sensor in highly calibrated systems by using thin layers of graphene oxide having an estimation for dielectric permittivities close to 53 [116]. In Fig. 105 are presented (a) a sample of the GO solution and (b) an enclosed application provided by the CBE department.

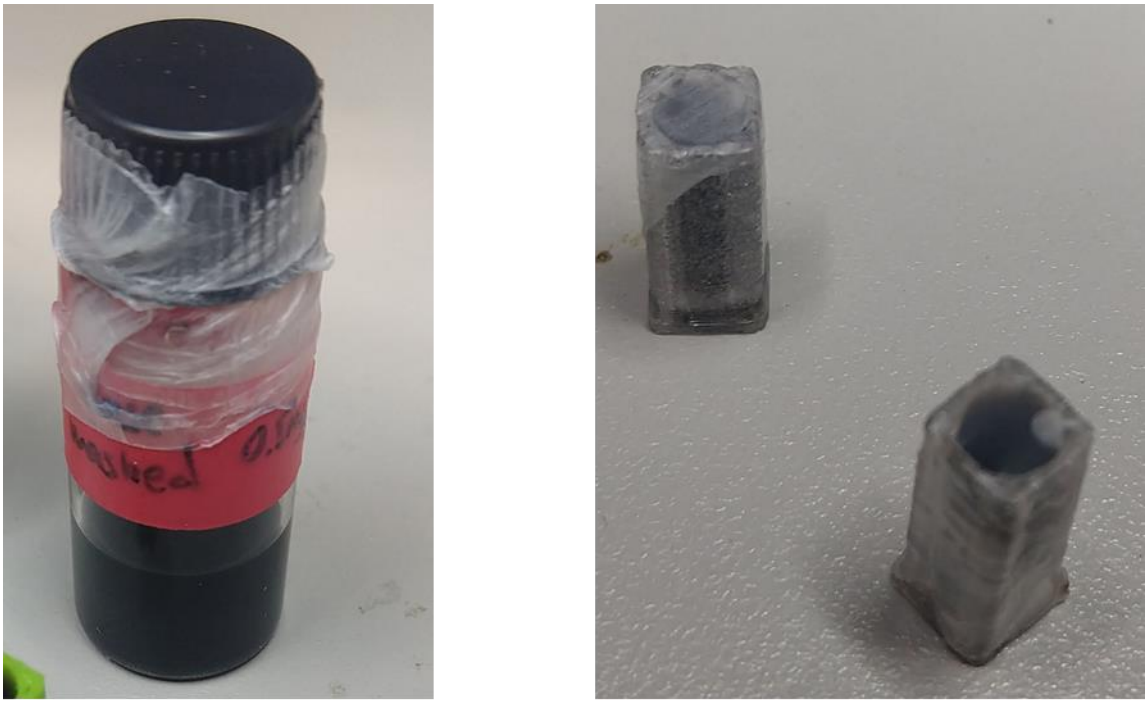

a) b)

Fig. 105 graphene oxide solution facilitated by CBE.

5.1.3. Substrates for mm-wave applications.

Concerning substrates, permittivities for mm-wave are within 3.4 – 3.6 which typically correspond to Rogers RO4000 series materials given the thickness of these substrate is a given parameter and essential for the calculation of the dielectric resonator dimensions and widely used in high frequency applications [102], [103]. Rogers RO4000 series are delicate materials with reduced thickness that allow the optimal performance for high frequencies applications that provide precise numbers and specific bespoke performance when applied as dielectric substrates. The Rogers series are one of the most recurrent materials for substrates employed in communications equipment and printed antennas for mm-wave applications, which justifies the selection for this material. This substrate will hold a metallic ground plane in one face with a carved slot that will create the coupling with the DRA. The dielectric will be sitting on top of this aperture. In the opposite face of the board a microstrip transmission line will be placed to feed the aperture and consequently the DRA. In Fig. 106 is shown an example of substrate constituted by the above discussed material with a printed antenna for microwave engineering applications.

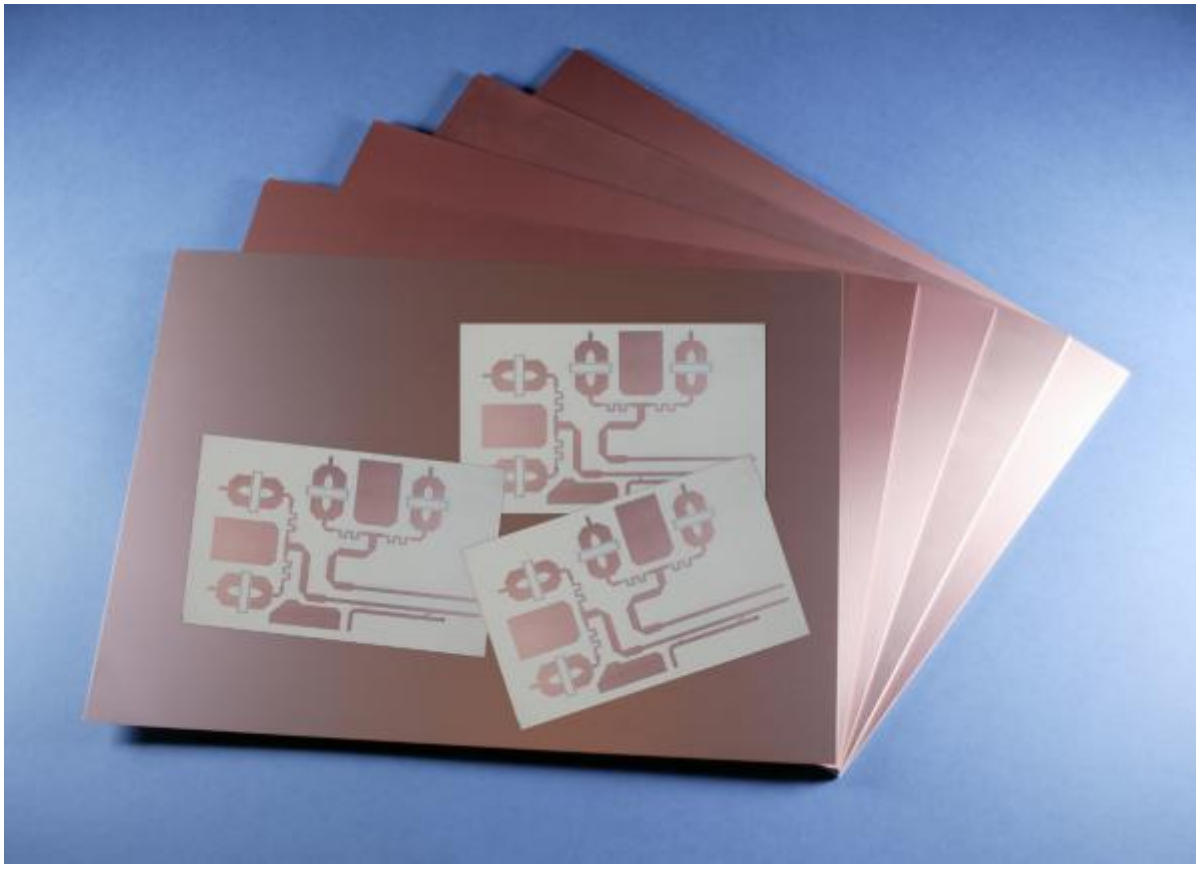

Fig. 106 PCBs with Rogers RO4000 substrates for microwave engineering applications.

5.2. Accuracy of approximation equations for the geometry of DRA.

An essential step of the design of a dielectric resonant antenna is the simulation process. The versatile and sometimes unpredictable behaviour of dielectric resonators is based on the adaptive properties of the materials used in their manufacture. Normally dielectric resonant antennas are made of materials with high dielectric constant / relative permittivity ε_r of the order of 10-100 and high Q factors [100]. Following the guidelines reviewed in Chapter 2, the properties of dielectric resonators using conventional materials were assessed. This has been carried out reviewing the techniques often used in mm-wave applications with a view to be implemented in 5G systems that will carry out exchanges of large amounts of data.

The sequential step prior to produce a simulated model is to determine the dimensions for a proposed antenna following the mathematical tools derived from the complex theory reviewed in Chapter 2. Posteriorly, using the calculated estimations for the DRA geometry, an implementation in CST Microwave Studio will be discussed. Essential metrics obtained in simulation such as S_{11} parameters and radiation patterns will be assessed in this section for the simulated models. The objective of the creation of this model is to prove the accuracy of the design equations derived from the waveguide model for a dielectric resonator analysed in section 2.4.7.

5.2.1. Design equations for approximation of dimensions of a rectangular DRA.

In this section, the suitability and accuracy of a set of equations to obtain the geometry for a rectangular DRA will be discussed in this section. As reviewed in Chapter 2, the rectangular dielectric resonant antenna is a suitable shape for dielectric resonators and is often recurred in the reviewed works as it provides a complete control of the supported modes and resonant frequency by modifying its geometry. The expressions derived from the supported modes included in the waveguide theory are discussed in the approximation equations from [104], [105] and will be implemented with a view to corroborate the effectiveness of the mathematical tools for the final produce aimed in the objectives for this thesis.

Hence, a rectangular dielectric resonator aimed to resonate at 50 GHz, was designed using the following parameters: for the substrate, the selected material is Rogers RO4350 with a relative permittivity of $\varepsilon_r = 3.48$ and a thickness of $h_s = 0.5$ mm. Then, for the dielectric constant, which usually takes values from 10-100 as this helps the size reduction and improves coupling but affects the bandwidth. The selected permittivity for the material $\varepsilon_{dra} = 10$.

Then for the geometry approximations, and the equations from [104], [105] have been used to determine the dimensions of the resonator having specified the parameters discussed above. The first ratio that has to be followed by the equations is that the DRA size can be approximated by equation (31) such that the condition is fulfilled (1>w>h).

$$DRA_{size} \propto \frac{\lambda_0}{\sqrt{\varepsilon_r}} \tag{31}$$

Where the desired resonant frequency for the DRA is f_r = 50 GHz, therefore the wavelength corresponds to λ_0= 6mm. Then the total height of DRA is given by equation (32) .

$$h_t = h_{dra} + h_s \tag{32}$$

Where h_s is the effective thickness of substrate and h_{dra} is the effective height of the DRA and are calculated as follows:

$$h_s = \frac{0.3c}{2\pi f\sqrt{\varepsilon_s}} = \frac{0.3(3\times10^8)}{2\pi(50\times10^9)\sqrt{3.48}} = 1.54\times10^{-4}m$$

$$h_{dra} = \frac{\lambda_0}{4\sqrt{\varepsilon_{dra}}} = \frac{6\times10^{-3}}{4\sqrt{10}} = 4.74\times10^{-4}m$$

Hence $h_t = 4.74\times10^{-4}m + 1.54\times10^{-4}m = 6.28\times10^{-4}m$.

This model considers an effective dielectric constant which involves the DRA and substrate thicknesses combined in the following equation (33) .

$$\varepsilon_{reff} = \frac{h_t}{\frac{h_{dra}}{\varepsilon_{dra}} + \frac{h_s}{\varepsilon_s}} = \frac{6.2\times10^{-4}}{\frac{4.7\times10^{-4}}{10} + \frac{1.5\times10^{-4}}{3.48}} = 6.86 \tag{33}$$

This parameter is used in the guide wavelength of the DRA given by equation (34) below.

$$\lambda_g = \frac{\lambda_0}{\sqrt{\varepsilon_{reff}}} = \frac{6\times10^{-3}}{\sqrt{6.86}} = 2.30\times10^{-3}m \tag{34}$$

Then, the approximation for the geometry for the coupling slot feeding the DRA are given by (35) and (36) .

$$l_s = \frac{0.4\lambda_0}{\varepsilon_{reff}} = \frac{0.4(6\times10^{-3})}{6.86} = 3.50\times10^{-4}m \tag{35}$$

$$w_s = 0.2l_s = 0.2(3.50\times10^{-4}) = 7.00\times10^{-5}m \tag{36}$$

Finally, the guide wavelength λ_g is used in the stub length of the resonator as well. This is given by equation (37), this stub length is the space that must exceed the feed line where the slot is placed.

$$l_{stub} = \frac{\lambda_g}{4} = 5.75 \times 10^{-4} m \tag{37}$$

Given this antenna is on a single mode area, (TE_{111}) these equations suggest a scaling of up to 10 times the dimensions obtained, in this case, the dimensions were multiplied by 3 as the designed antenna is expected to resonate in higher-order modes due to its resonant frequency [105]. The equations are used as a starting point for determining the dimensions of the dielectric resonator. This is when the simulation process starts to become essential in the design process as it allows the modification of the geometry obtained by this set of calculations and refines the design prior to manufacture.

5.2.2. Simulated models and metrics for designed RDRA.

Using the dimensions calculated in the previous step, the creation of a computerised model in CST Microwave Studio was carried out for the DRA and substrate. In order to create an accurate model of the material used for the dielectric resonator, the material simulated was alumina which is a microwave-enhanced material. The material created was named RDRA with permittivity ε_{dra} = 10, although customised materials can be designed in the simulator. In Fig. 107 an isometric view of the designed dielectric resonator antenna and its corresponding coupling PCB is presented.

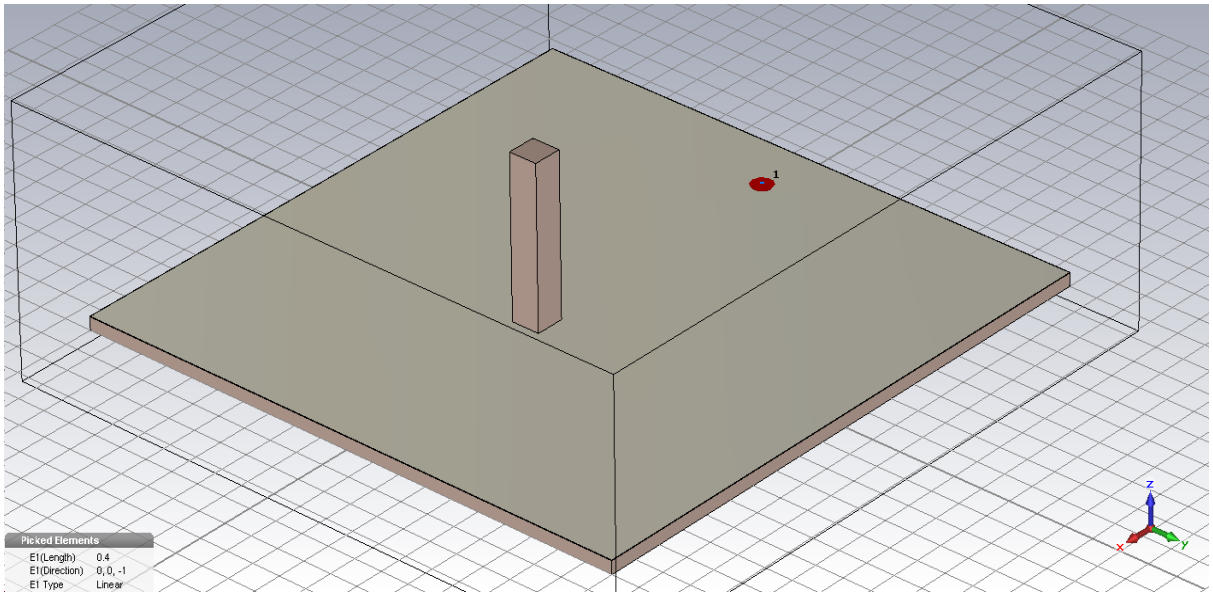

Fig. 107 Rectangular dielectric resonator designed to work on 50 GHz.

As the resonant frequency was selected as f_r = 50 GHz in the parametric initial conditions to design the dielectric resonator, we will now analyse the simulated antenna metrics in order to evaluate the accuracy of the simulation.

In Fig. 108 the simulated reflection coefficient of the designed DRA is shown. The simulated S_{11} present a resonance around 51 GHz, with a return loss of -22 dB which represents a good matching.

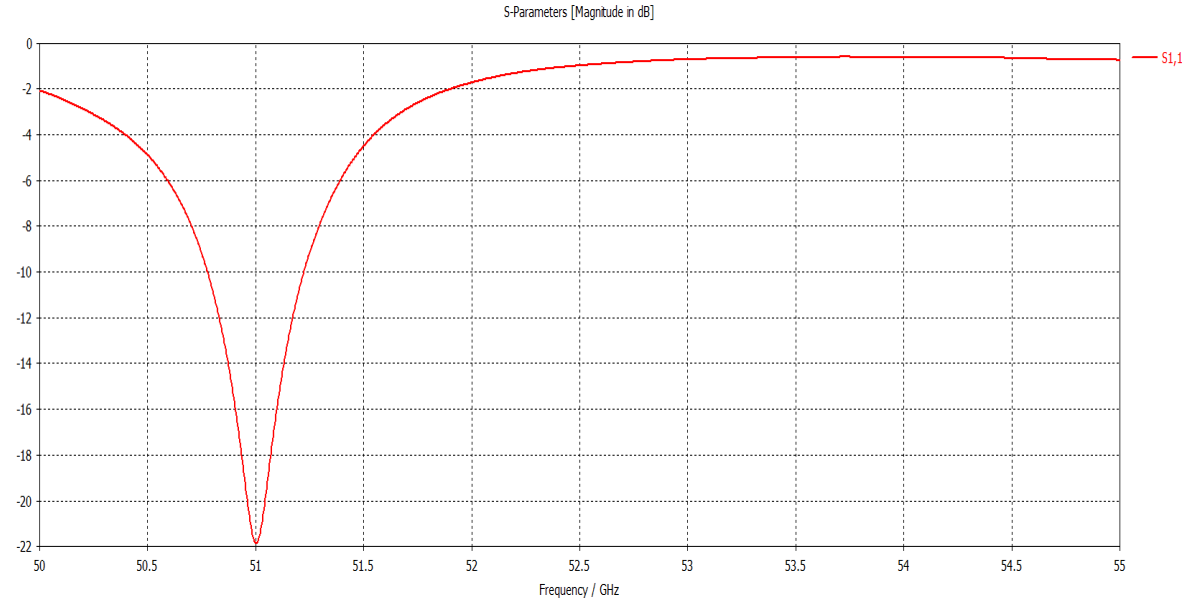

Fig. 108 S_{11} Parameters of simulated rectangular DRA.

The resonant frequency achieved by the simulated DRA is near the frequency the dielectric resonator was designed for in section 5.2.1 which corresponds to 50 GHz. As the analysis for this antenna is carried out for high frequencies shifts are expected of a relatively small proportional part in the frequency range which includes this shift as an acceptable variation and an adequate accuracy for the mathematical model carried out previously which has been corroborated by simulation.

Moreover, on simulated results, the simulated radiation patterns will now be discussed. As explained in section 2.4.3, dielectric resonant antennas typically offer rather directive radiation patterns in the direction of the **z** axis. These patterns are highly directives and hence present good gains, as this indicates the dielectric is well coupled to the slot in the PCB and the waves are bouncing back and forth in the walls of the dielectric resonator. In simulation, this kind of radiation patterns are observed as well with a high intensity lob and secondary lobes with lower intensities but still focusing towards the direction of propagation.

In Fig. 109 the simulated radiation pattern for the designed DRA is presented. The figure shows the YZ plane in its polar plot. Where the high intensity lobe is located in the direction of propagation. This is therefore adding to corroborate the accuracy of the designed model and the simulator as the results correspond to a typical behaviour in a rectangular DRA.

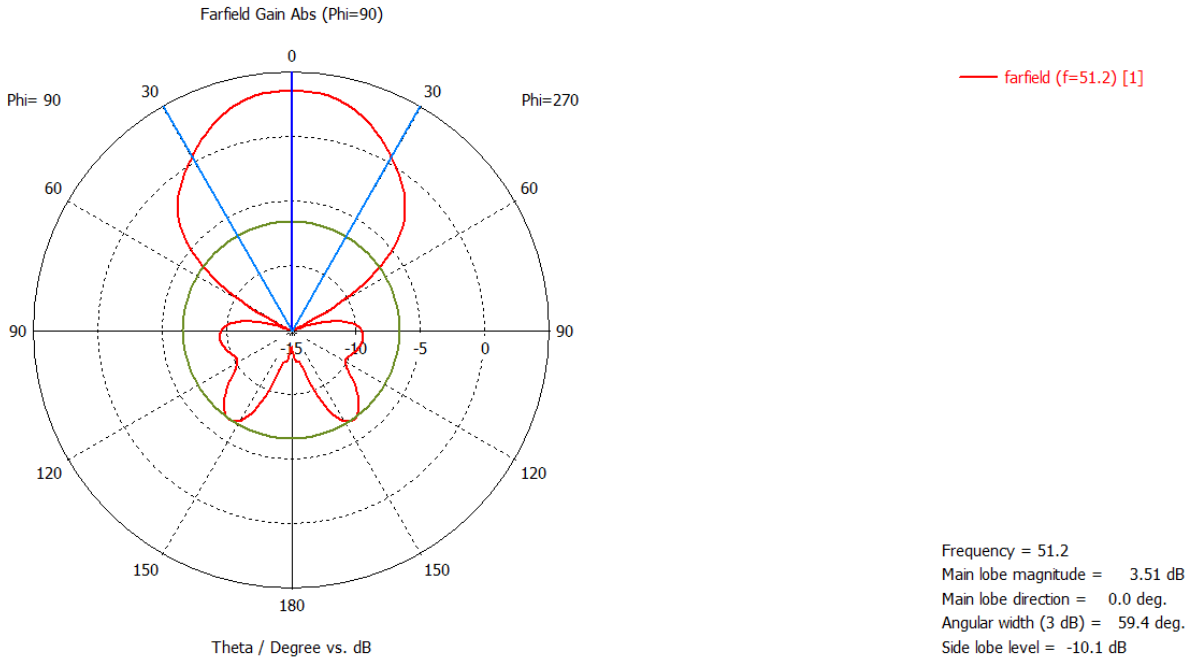

Fig. 109 Rectangular DRA simulated radiation pattern.

If a higher precision in the dimensions of the resonator and therefore in the simulated results is required, then one can slightly and gradually modify the parameters introduced for the simulation model and evaluate their effect on the simulated performance of the model. Overall, the design equations are derived from the waveguide model reviewed in section 2.4.7 and are considered as starting points of the dimensions.

Once the dimensions are calculated, these can be modified in the computerised model with a view to refine the expected results and therefore avoid manufacture costs which are not definitive until the simulated results are as close as possible to the expected results. By proving that the design equations used to determine the dimension approximations present a ana appropriate precision grade with respect to the expected results we conclude that the equations are suitable to conceive a fabricated dielectric resonator based on these calculations. The following sections will explore the simulated reconfiguration mechanisms of DRAs using different techniques.

5.3. Frequency reconfiguration in computerised models of DRAs.

As part of the 5G technologies, tuning mechanisms are expected be implemented into the novel signature antenna systems of the generation, including the dielectric resonator antennas. For this purpose, numerous methods to achieve reconfiguration in DRAs have been reviewed in section 5.2. However, all of them include the use of passive and active electronic components in order to control the radiation patterns and frequency tuning of the systems. In this section the use of novel materials that are capable to control their performance by altering its properties using external signals is discussed. These materials have been reviewed in section 2.1.3 and 2.1.4 and are liquid crystals and graphene, novel and versatile substances that are more commonly used not only in communications engineering but also in medicine, architecture, mechanics, electronics, textiles etc.

A set of variation for some essential parameters was carried out in order to evaluate the effect on the performance of the antenna designed in the previous section. The modified parameters are related to the operation principles of the dielectric resonators theory with a view to achieve a foreseeable frequency reconfiguration. Mainly, this study is based on the fact that the permittivity of the dielectric resonator and the substrate are essential parameters which are initial conditions for the design of the antenna and if modified the performance of the system will be consequently affected. Hence, if there is a technique to control electronically these parameters then the frequency will also be proportionally controlled.

5.3.1. Simulations of a DRA varying permittivity of substrate.

Using the antenna designed previously, the relative permittivity of the substrate for this model was varied. This modification alters the corresponding resonant frequency of the antenna. In the software CST Microwave Studio, we carried out a parameter sweep analysis with slight variations of the substrate permittivity with a view to explore the range of frequencies that can be achieved by altering this parameter. Consequently, further investigation can be carried out to control the substrate permittivity to tune the antenna. Using the previously discussed computerised model working at 50 GHz was modified according to the above discussed permittivity of the substrate. Hypothetically, an additional container filled with an electrically tunable substance placed in the substrate can alter the effective permittivity of the system. This was changed from 3.4 to 3.0 achieving frequencies from 51.6 GHz to 54.5 GHz as presented in Fig. 110. The S_{11} parameters of the achieved tuning range present an evident frequency shift with a lost on the matchings proportional to the increment on frequency.

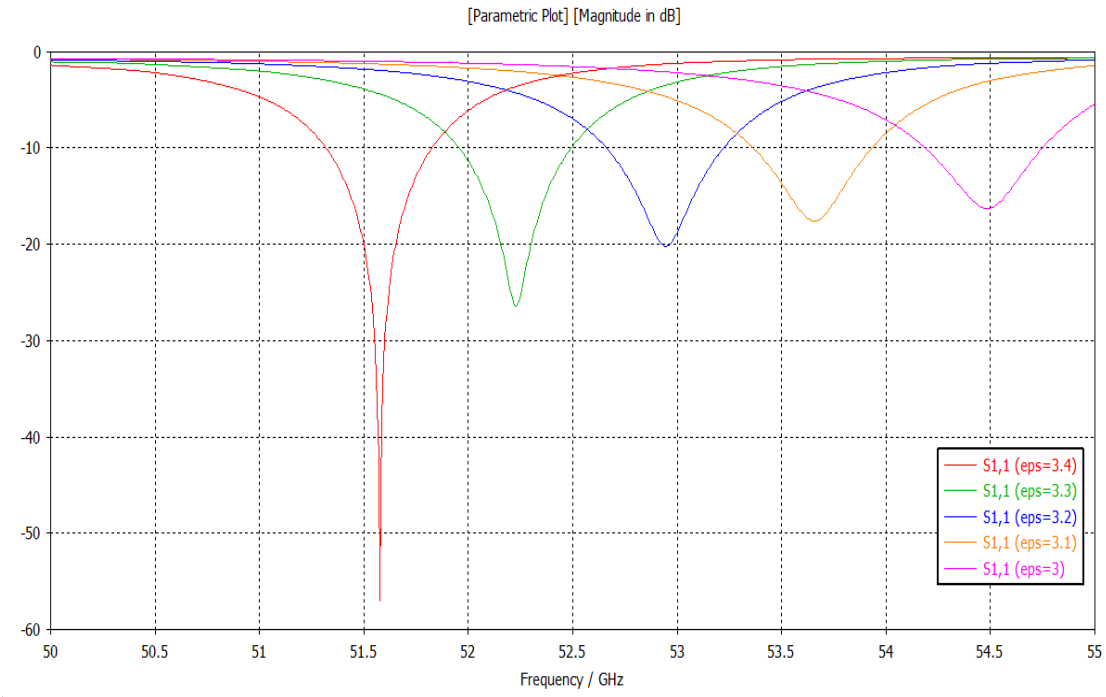

Fig. 110 Tuning range of different values of dielectric constant of substrate.

Using the design equations from section 5.2.1, the design of another DRA was carried out, aiming to operate at 20 GHz, choosing dielectric permittivities ε_{dra} = 10 for the dielectric resonator, and ε_r = 3.48 for the substrate with a thickness of 1.5 mm. After using the approximation calculations, the dielectric resonator dimensions are as follows: 5.0 mm × 10.0mm × 8.12 mm. This DRA has also been simulated in the CST suite and is presented n Fig. 111 above.

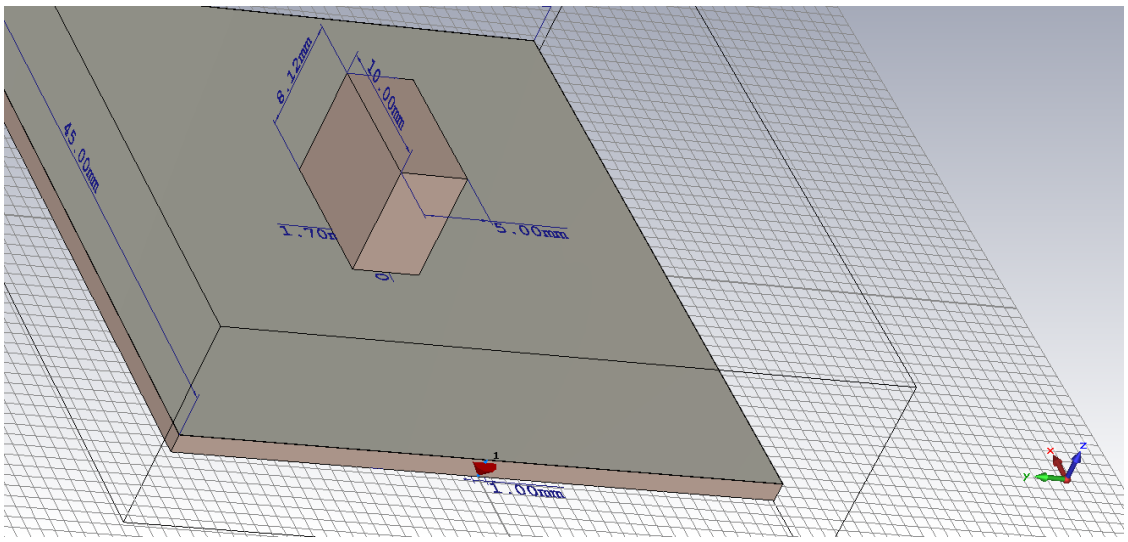

Fig. 111 Modelled DRA designed to operate at 20 GHz.

In order to evaluate the performance for the designed DRA the simulated reflection coefficient for this model was analysed. The figures showed a main resonance at 19.96 GHz with a good matching below -21 dB. Having obtained a resonance close to 20 GHz corroborates again the approximation equations (31) – (37). In Fig. 112, the simulated reflection coefficient for the designed antenna are shown.

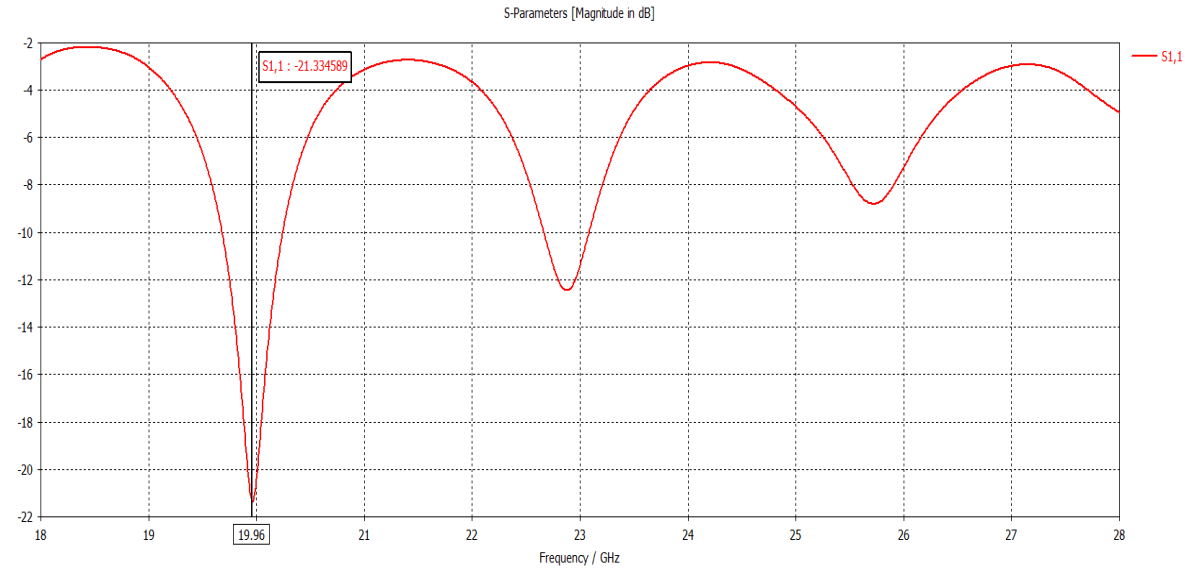

Fig. 112 Simulated reflection coefficient for the DRA designed to work at 20 GHz.

Moreover, based on the fact that the permittivity of the substrate alters the antenna performance when changed, it is likely that a frequency reconfiguration mechanism can be implemented to control the resonant frequencies of the antenna in question based on varying the substrate permittivity. Since the substrate of the antenna occupies a relatively large space compared to the rest of the DRA elements, a cavity can be created in its structure. This can be therefore filled with a ferroelectric material that can changes its properties such as liquid crystals. It was discussed in section 5.1.2 that this substance is able to alter its properties when an electric signal is introduced in its structure. The electric signal rearranges the molecules of the substance, depending on the voltage amplitude, or current intensity. Then its internal structure is reorganised and changes its conductivity, permittivity, and other electrical properties useful to the antenna performance.

Therefore, the creation of a cavity in the substrate of the computerised model of DRA simulated by CST Microwave Studio was carried out. The cavity geometry is as follows 10.0 mm × 10.0 mm × 1.0 mm and was filled with a created customised material with an equivalent volume. The customised material aimed to emulate the properties of liquid crystals.

In Fig. 113 the simulated model of the antenna containing liquid crystals in its substrate is presented.

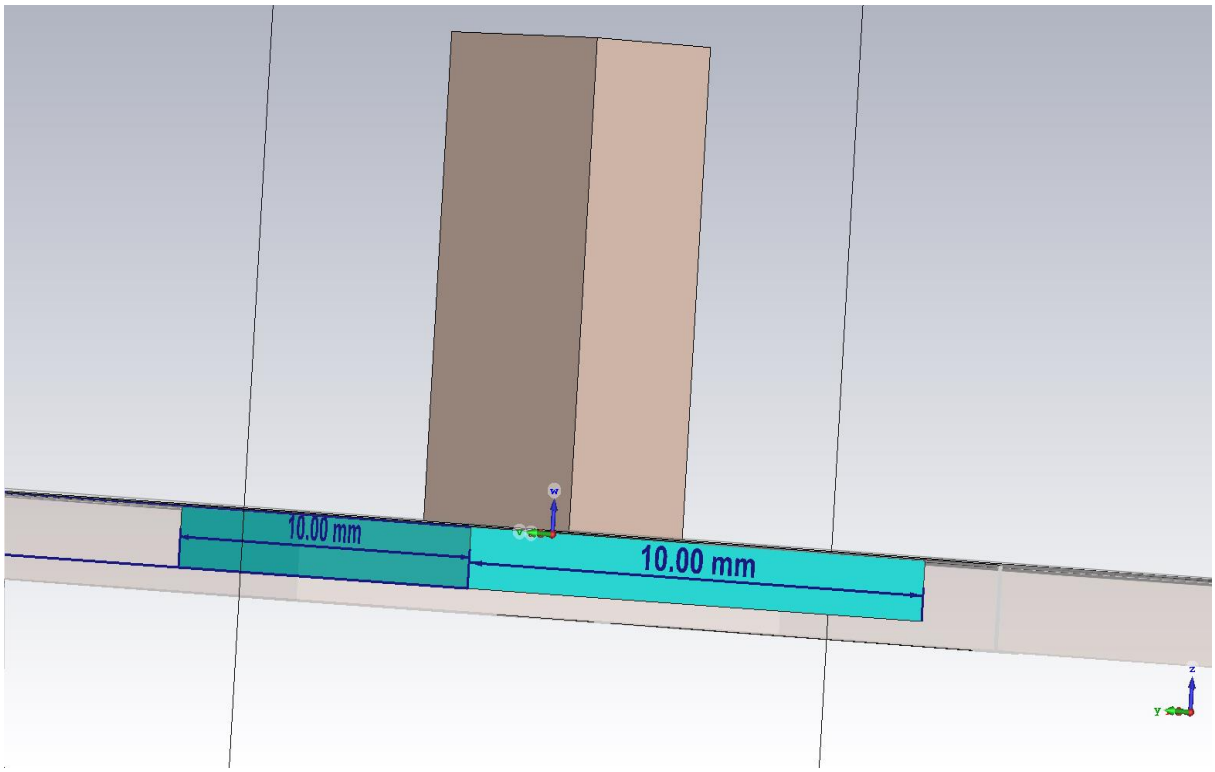

Fig. 113 Simulated DRA with liquid crystals in substrate.

Then, the permittivity of the generic substance emulating liquid crystals was varied. The simulated reflection coefficient as a function of the varies permittivity evaluated how it affected gradually the resonant frequencies of the system. The selected values for the permittivity of the liquid crystals ε_{LC} went from 3 to 4, varying this parameter in the order of 0.1 each step. The tuning achieved for their resonant frequencies covered two frequency bands from 20.3 GHz to 21 GHz and from 24.8 GHz to 25.7 GHz, respectively.

The achieved reconfiguration reaches a bandwidth less than 10% of the resonant frequency, which is not optimal for DRAs, moreover, creating a cavity in a Rogers RO4000 series substrate is very unlikely to manufacture as the thicknesses of this material do not go above 0.5 mm. Consequently, further techniques to achieve reconfiguration will be discussed, Nevertheless, it was proved that the manipulation of the relative permittivity has repercussions in frequency. In Fig. 114, the simulated reflection coefficients resulting from varying the permittivity of the tunable generic substance are presented.

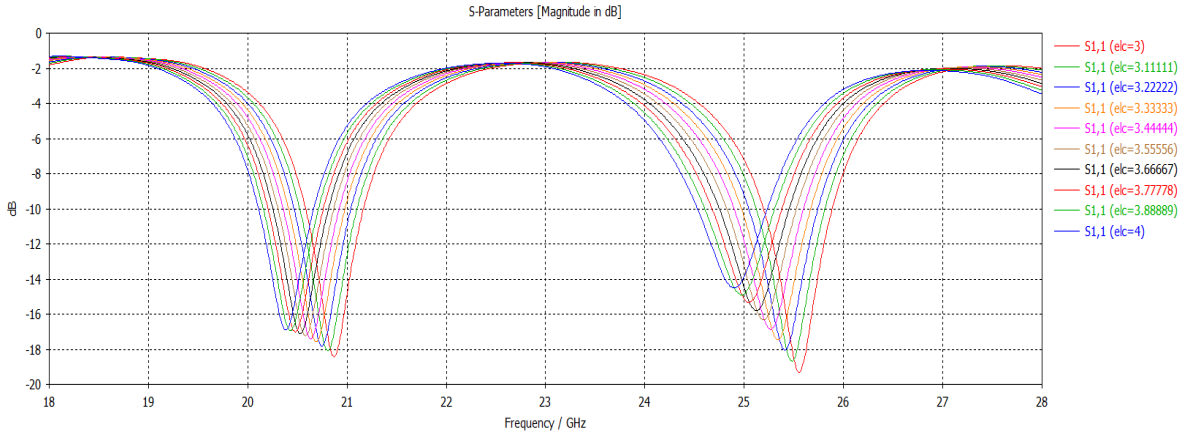

Fig. 114 Simulated tuning range for designed DRA when varying the liquid crystals permittivity.

5.3.2. Simulated effects of metallic electrodes incorporated to a tunable DRA.

Having proved that controlling the dielectric constant of the substrate of a DRA system tunes the resonances and as a liquid crystal requires an external voltage in order to control its permittivity it was required to evaluate a tunable material inside the dielectric resonator itself. Placing a ferroelectric or alterable material via an electric signal inside of the DRA structures it's a more likely alternative to achieve reconfigurability. Avoiding the complex manipulation of the substrate which can damage its structure due to the fragility of Rogers RO4000.

With a view to provide an electric signal to control the properties of the material contained in the DRA, the effect of metallic elements, i.e. electrodes, will be assessed. These elements will bring the biasing voltage to the tunable material. The biggest concern of adding metallic elements in the DRA structure is a considerable increment of the metallic losses at high frequencies. However, electrodes placed in the external walls of DRAs can be analysed as the effect of parasitic patches placed in the DRA, a technique that has been reviewed previously with positive effects in terms of antenna efficiency. Despite adding metallic losses these have been proved to be nearly negligible in high frequencies when used in dielectrics with relatively low relative permittivities and Q-factors [106]. The tunable materials that can fill a cavity in the DRA can be therefore controlled using a signal trough an electric field injected to the DRA walls by discrete electrodes.

For the analysis of metallic elements in a DRA some simulations were carried out with a view to assess its effect on the antenna performance, especially in the radiation patterns. A computerised model incorporating a pair of electrodes was simulated. The electrodes were two identical metallic cylinders with a diameter of 1.0 mm each. These cylinders were placed next to the DRA walls keeping a symmetrical proportion. With a view to analyse its effect on the antenna performance. In Fig. 115, the designed DRA in 5.2.1 with the addition of a pair of metallic electrodes is presented.

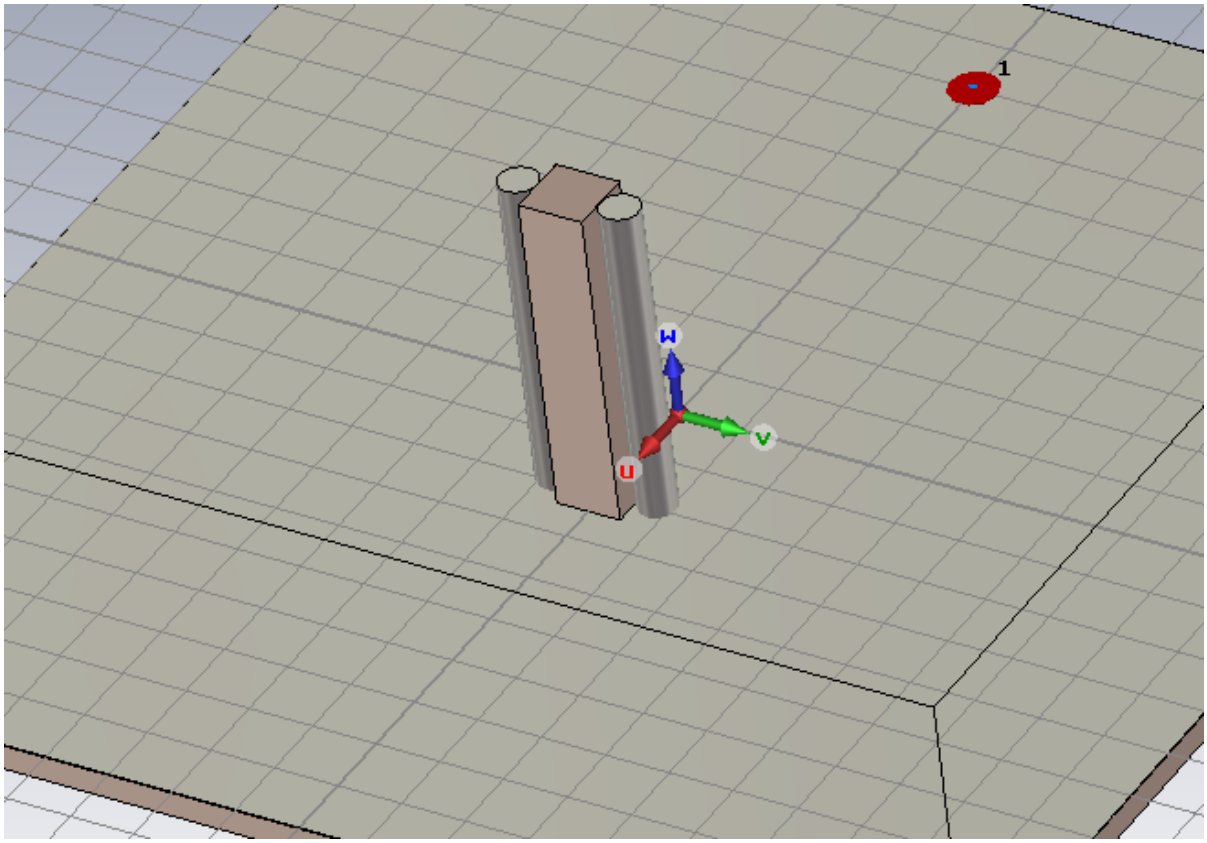

Fig. 115 Rectangular DRA with electrodes.

Furthermore, the frequency response does not suffer any alteration as observed in the simulated reflection coefficients, which, compared to the results observed in Fig. 108 are very similar, as the resonant frequency remain the same. However, the matching suffers a reduction of near 6 dB. This represents then that the reflection coefficients are not significantly affected by this incorporation. However, an appropriate assessment for the radiation patterns was carried out as well. These suffer a slightly considerable reduction of the gain in the characteristic main lobe as well as the eradication of the secondary lobes. These differences are notorious when compared to the one presented in Fig. 109.

In Fig. 116, the simulated S_{11} parameters for the DRA with a pair of electrodes are shown. The commented reduction on the matching as well as the maintained resonant frequency are observed.

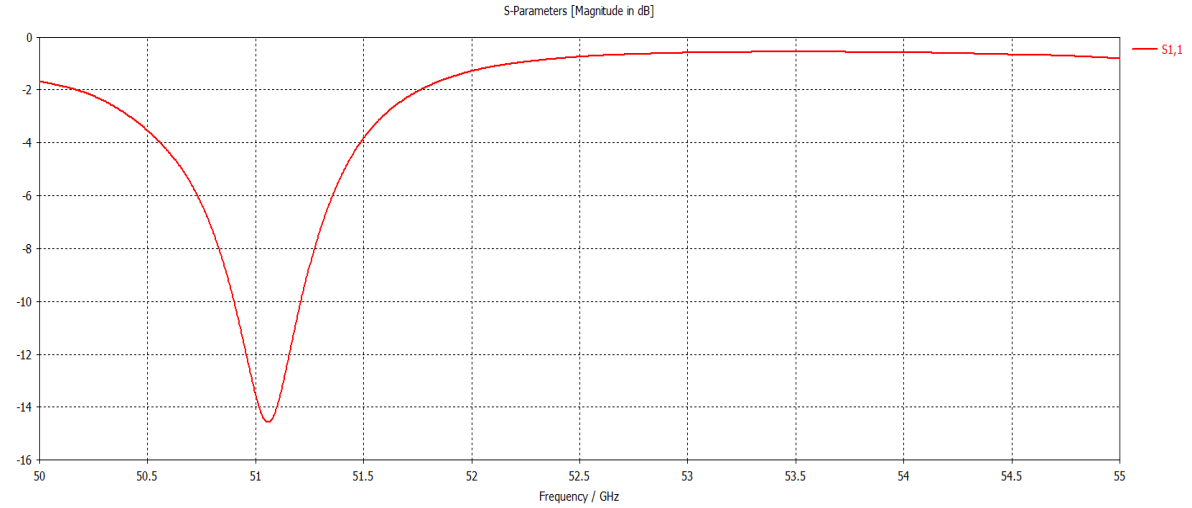

Fig. 116 S_{11} parameters of DRA with electrodes.

In Fig. 117, the affected radiation pattern in its polar plot is shown. This figure presents the YZ plane cut where the reduction of lobes is observed when comparing it to the pattern simulated in section 5.2.2.

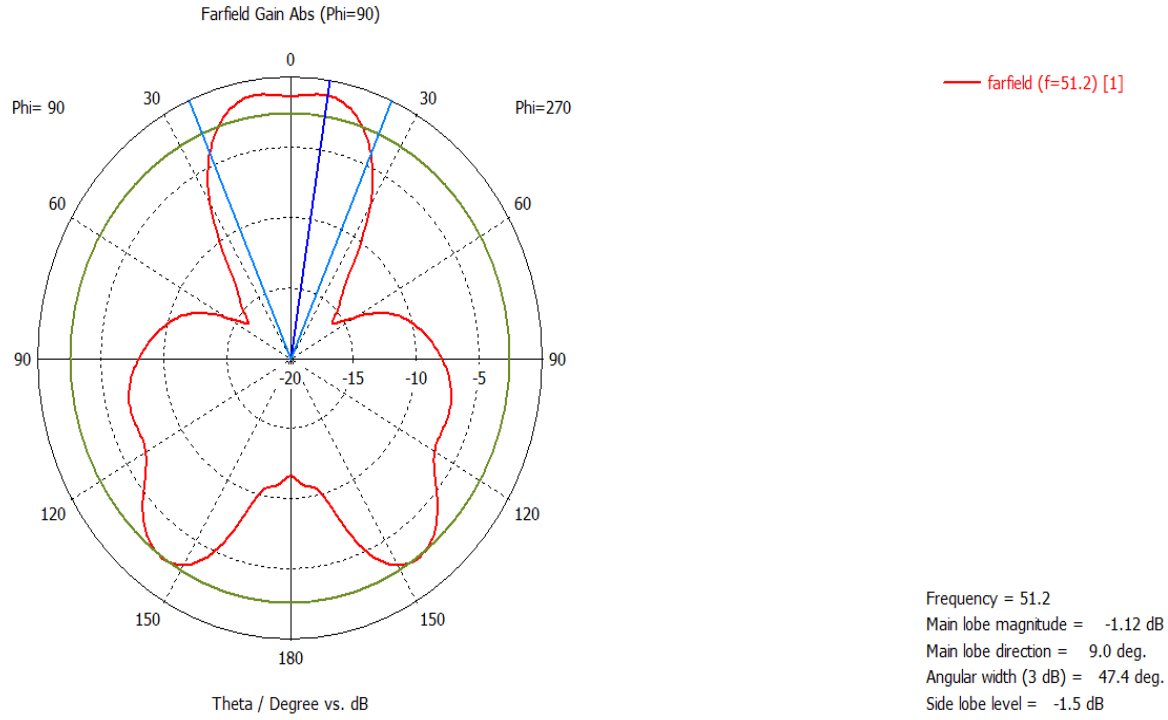

Fig. 117 Radiation patterns of DRA with electrodes.

5.3.3. Simulated effects of metallic cladding surrounding a tunable material-based DRA.

A further analysis has been performed aiming to achieve the control of a tunable material contained in the dielectric resonator itself. This will therefore involve the use of more discrete electrodes to provide the controlling signal. A different shape of electrodes such as cladding is proposed, as the previous models including the cylindrical electrodes implied a significant effect on the characteristic performance of a DRA. For this purpose, another model was carried out modifying the shape of the DRA and turning it into a cylindrical one. Keeping the dimensions of the base as diameter = 1 mm and height = 5 mm. In Fig. 118, the simulated model of cylindrical DRA is presented, using a generic material with tunable relative permittivity but with a fixed ε_{dra} = 10 for initial conditions.

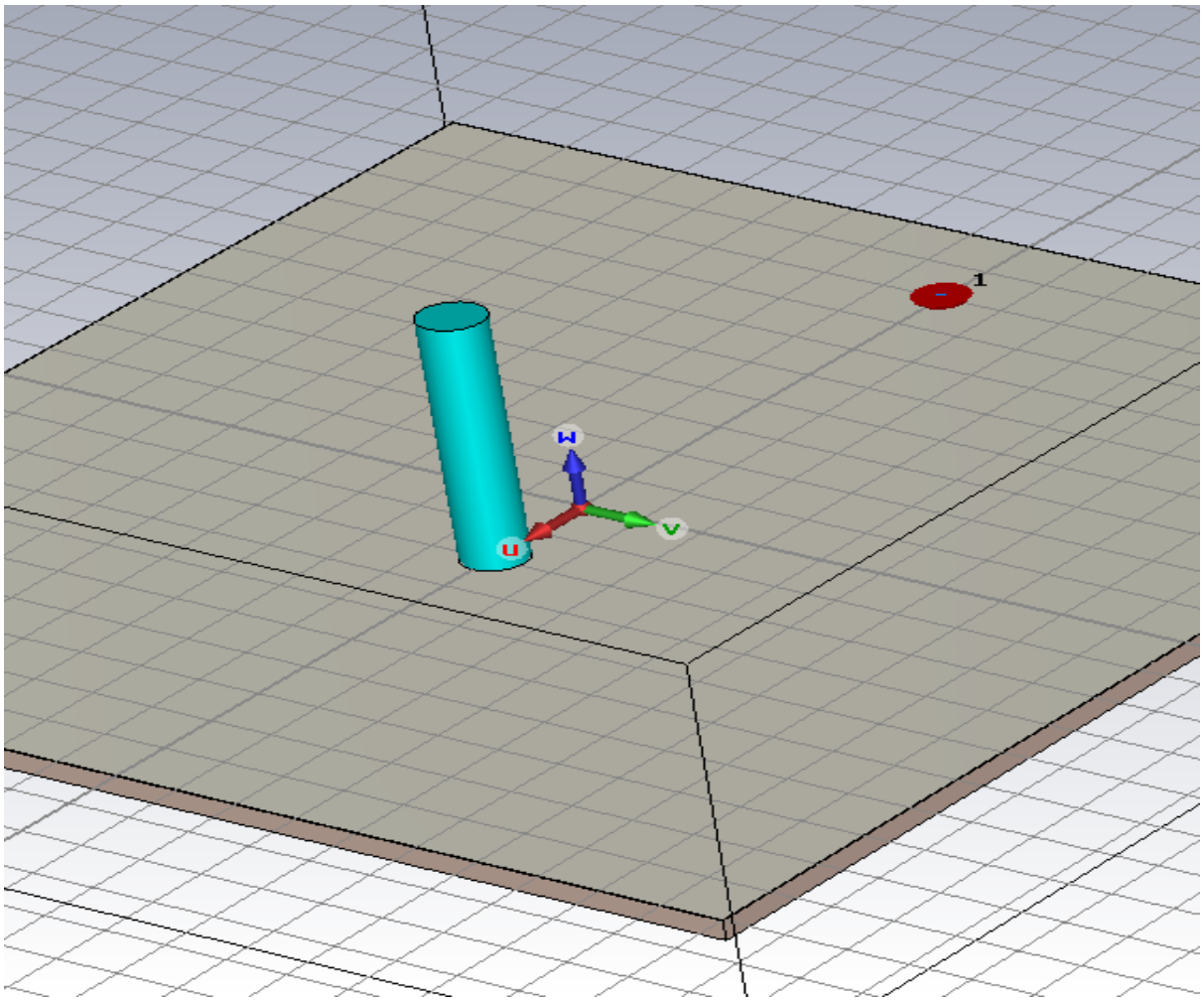

Fig. 118 Simulated Cylindrical DRA.

The model was expected to have similar results to a rectangular dielectric resonator antenna similar to the one designed in section 5.2.1. A full analysis of its metrics was carried out in the simulator CST Microwave Studio and will be fully discussed in the following figures. In Fig. 119, the simulated S_{11} parameters for the cylindrical shape of DRA are presented. A resonant frequency of 51, similar to the rectangular DRA, however, the matching has suffered a reduction.

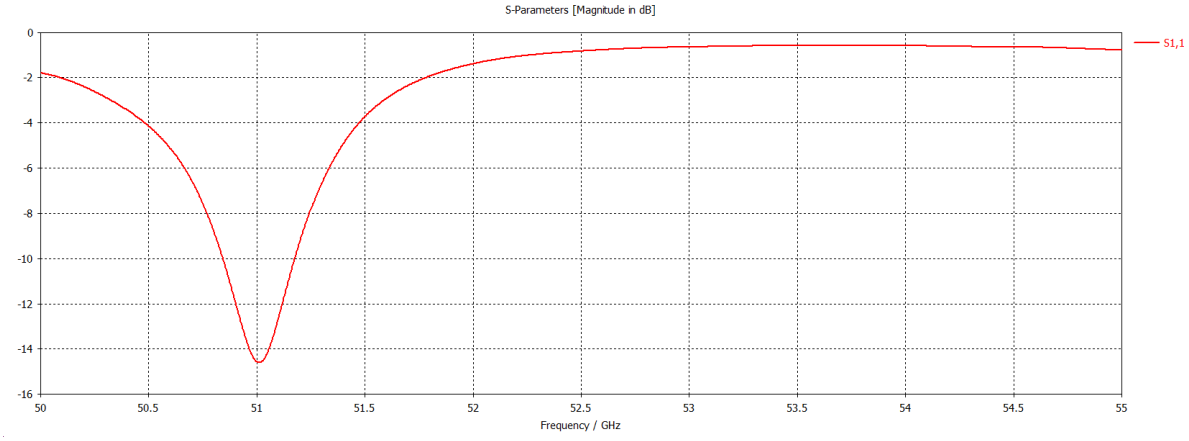

Fig. 119 Simulated S_{11} cylindrical DRA.

Moreover, the simulated radiation pattern was assessed in its polar plot from the CST simulator. In Fig. 120, the YZ plane of this plot is presented where a reduction in the main lobe and the gain compared to the rectangular resonator are observed.

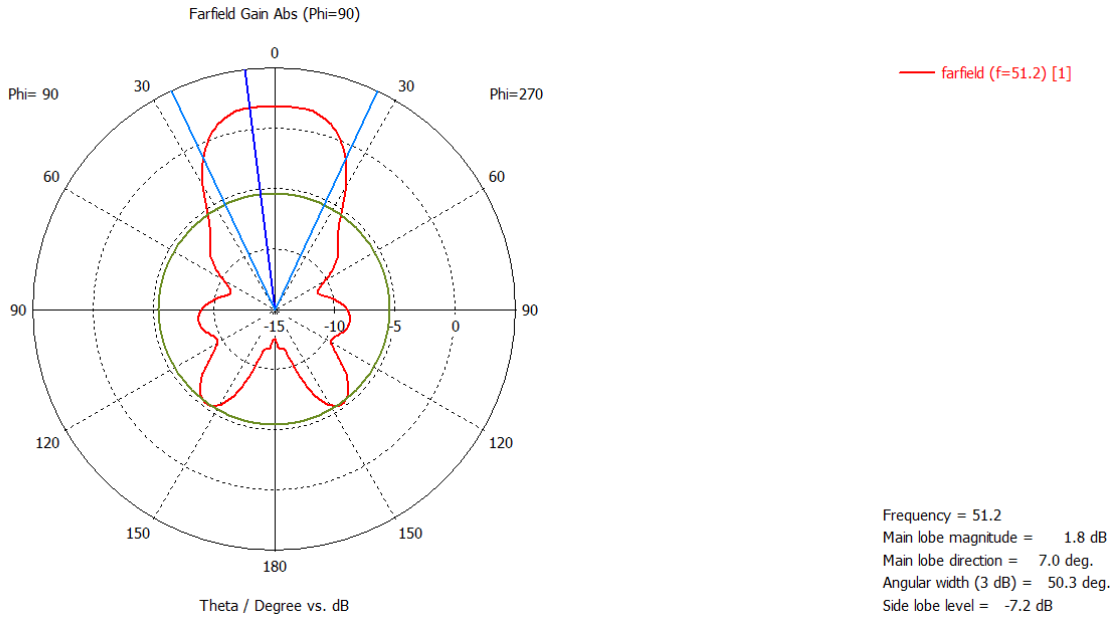

Fig. 120 Simulated radiation pattern of cylindrical DRA.

In order to inject an electric signal into the tunable substance it is appropriate to assess the effect of a metallic layer such as the previously proposed cladding. For this purpose, the simulation of a conductive layer surrounding the cylindrical DRA acting as electrode was carried out. This layer was not grounded and is expected to bring an uniform current distribution, however, a negative effect on the radiation of the system was also expected. In Fig. 121, the model of the metallic cladding surrounding the dielectric resonator simulated in CST Microwave Studio is presented.

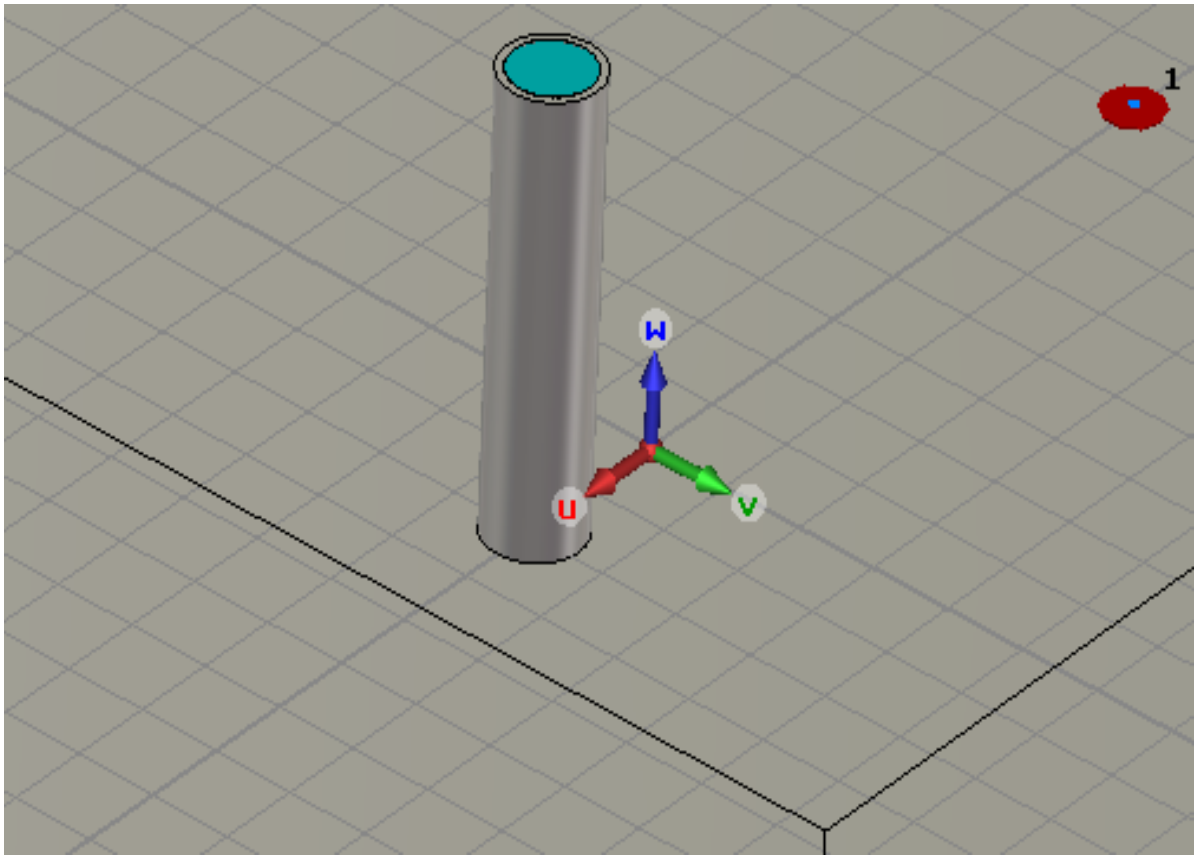

Fig. 121 Cylindrical DRA incorporating a cladding.

The effect of this layer was assessed in terms of the frequency response, for this purpose, the simulated reflection coefficient is presented in Fig. 122. A slight shift in the resonant frequency is observed, this is another negative effect produced by the cladding. In addition to this, a reduction in the matching is also presented, a matching barely below -12 dB is reached at a resonant frequency of 51.1 GHz.

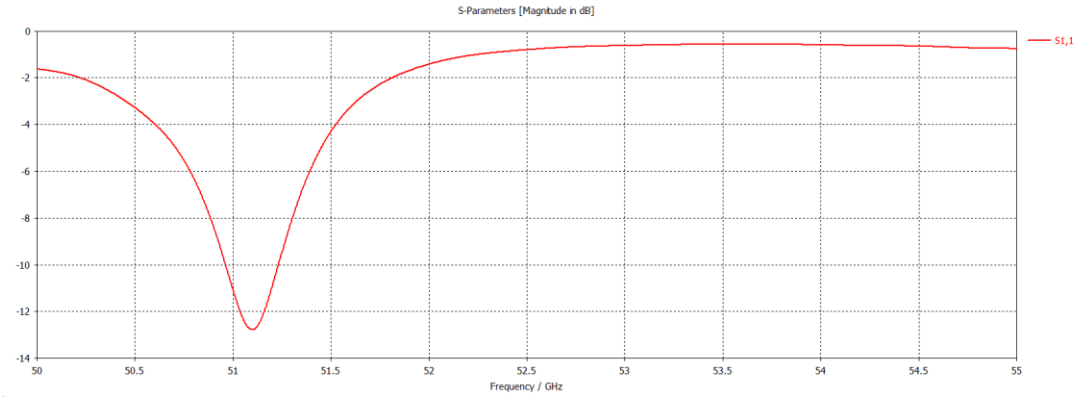

Fig. 122 Simulated S11 of cylindrical DRA with electrode.

Although the frequency shift is not representing a significant affectation to the overall performance for the DRA, the effect on the radiation must be assessed with more relevance than the reflection coefficient as the addition of metallic losses to the DRA due to the incorporation of a metallic layer surrounding the dielectric resonator.

The simulated radiation patterns for this set of elements, are presented in its polar form in Fig. 123 the YZ cut of the pattern in shown. Overall, we see a similar pattern to the one observed in Fig. 117. A significant reduction of the main lobe is observed, the highest intensity of radiation is located in the lower half of the structure, which corresponds to undesired radiation's coming from the PCB.

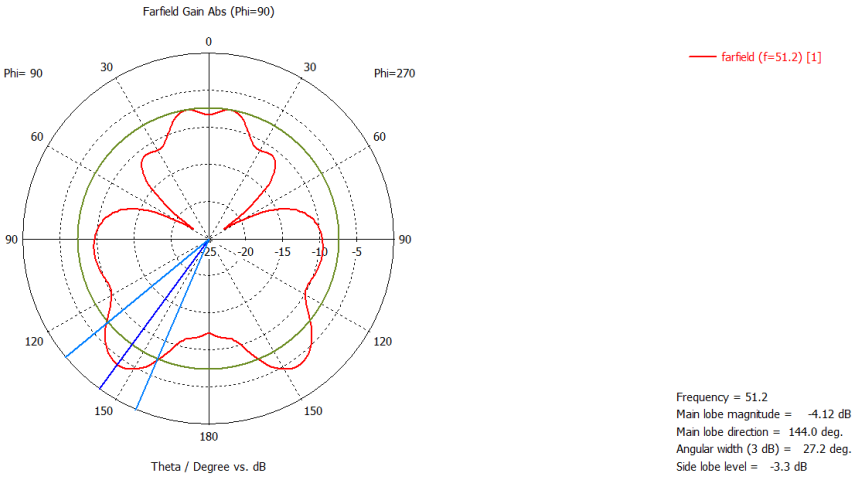

Fig. 123 Simulated radiation pattern of cylindrical DRA with electrode.

As a conclusion of metallic electrodes in the walls of a DRA, , significant negative effects are observed as the insertion of metallic losses is a consequence of the incorporation of metallic elements bringing a controlling DC biasing signal to the structure of the antenna. Nevertheless, this suggests that the electrodes should be rather narrow and covering a smaller arear in the surface of the walls of the DRA. This will then reduce the significant effects on the radiation patterns and therefore improve the overall performance of the antenna. In terms of the reflection coefficients, no significant effects in the resonant frequencies were observed, except for the matchings, which was expected due to the inserted metallic losses.

As recapitulation, Table 6 below, presents a summary for the simulations carried out in this section. This table compares the different effects observed in each of the models incorporating additional elements with a view to introduce a control signal to achieve frequency reconfiguration as well as the parameter controlled in question.

Model	Element incorporated	Major setback	Alternative solution proposed
DRA with liquid crystals inside a cavity in the substrate.	An amount of electronically tunable liquid crystals.	The cavity in the substrate is extremely difficult to achieve due to the reduced thickness.	Incorporate the tunable substance in a cavity in the resonator instead. Switch from LC to GO.
DRA with metallic electrodes.	Two cylindrical electrodes attached to the walls of the dielectric resonator.	Significant alteration of characteristic radiation patterns.	Change the shape of electrodes as a metallic layer attached to the dielectric resonator.
DRA with metallic cladding.	A metallic layer surrounding the cylindrical DRA manufactured in a tunable material.	Reduction of matching in reflection coefficients and a significant effect to radiation patterns.	Reduction of the area covered by the electric layers.

Table 6 Summary of simulations and proposed solutions.

5.4. Design and simulation of a 3D-printed frequency reconfigurable RDRA for mm-wave.

Basing on the knowledge assessed in the previous sections of this chapter, the design of an alternative DRA will be discussed in this section. The assessment for electronically tunable substances, effects of metallic electrodes and claddings and design equations for dielectric resonators and was carried out, obtaining as a conclusion certain guideline to be followed in the development of an alternative solution to overcome the discussed setbacks.

For this, I propose the design of a rectangular dielectric resonant antenna using low-cost polymers used in the novel and versatile manufacture method known as 3D printing. This fabrication technique is widely used in different industries involving the heating of a filament made of a dielectric material, generally derived from plastics, and then manipulate the shape of it while hot in order to achieve a desired form, consistency and size. For the manufacture of DRAs the most common material used in the reviewed works is a wide variety of ceramics which have high relative permittivities, typically 10, However, for this study, I selected a material from the available variety in the Chemical and Biological Engineering (CBE) department laboratory whom have collaborated with this project and provided some of the materials studied in this work.

By using a different material, an assessment of simulations must be carried out first prior to the manufacture of dielectric resonators. Following the work discussed in the previous section, a tunable material that changes its permittivity was modelled in CST Microwave Studio with a view to estimate the frequency range achieved by an electrically tunable substance. The study on electrodes attached to the walls of the dielectric resonator has determined that narrow and discrete electrodes will have a reduced effect on the performance of the DRA system as a result of the analysis carried out in the previous sections. The use of electrodes is necessary due to the electric signal required to control the electronically tunable substance.

The hypothesis of this proposed system is that an electrically tunable substance contained inside a dielectric resonator will achieve a frequency reconfiguration through an incident electric field between two discrete electrodes. In this section, the design and simulations for a dielectric resonant antenna operating at 28 GHz based on an unconventional low-cost polymer for 3D printing as the material for the resonator. Then the modelling of a tunable substance and the simulated frequency response as well as radiation patterns will be presented.

5.4.1. Design methodology of 3D printed RDRA.

I propose the design of a DRA operating at 28 GHz which has applications for mm-wave. The DRA has been designed considering a foreseeable manufacture through 3D printing, hence the calculations were carried out basing on a common material in 3D printing but an unconventional one for DRA which is polylactic acid (PLA). This material is a thermoplastic polymer derived from bio-waste which, different from other plastics that are derived from petroleum-based composites. PLA can be considered as an environmental-friendly bioplastic as it is derived from biomass [107]. Therefore, for calculations carried out using approximation equations (31) – (37) I based the numbers on the relative permittivity for PLA, which after consulting the manufacturer for such specific product, is $\varepsilon_r = 2.5$.

The aim of this design process was to achieve a rectangular dielectric resonator antenna working at 28 GHz, then hollow it by a cavity which will be filled with an electrically tunable substance. The rectangular dielectric resonant designed measures 6.0 mm × 6.0 mm × 16.12 mm. the dielectric resonator will be sitting on top of a PCB measuring 30.0 mm × 30.0 mm × 0.5 mm constituted by Rogers RO4350 with a permittivity $\varepsilon_s = 3.66$. a metallic ground plane holds the calculated coupling aperture measuring 2.77 mm × 0.47 mm. the system is therefore fed by a microstrip transmission line place in the opposite face of the substrate. A model in CST microwave studio has been carried out and is presented in Fig. 124.

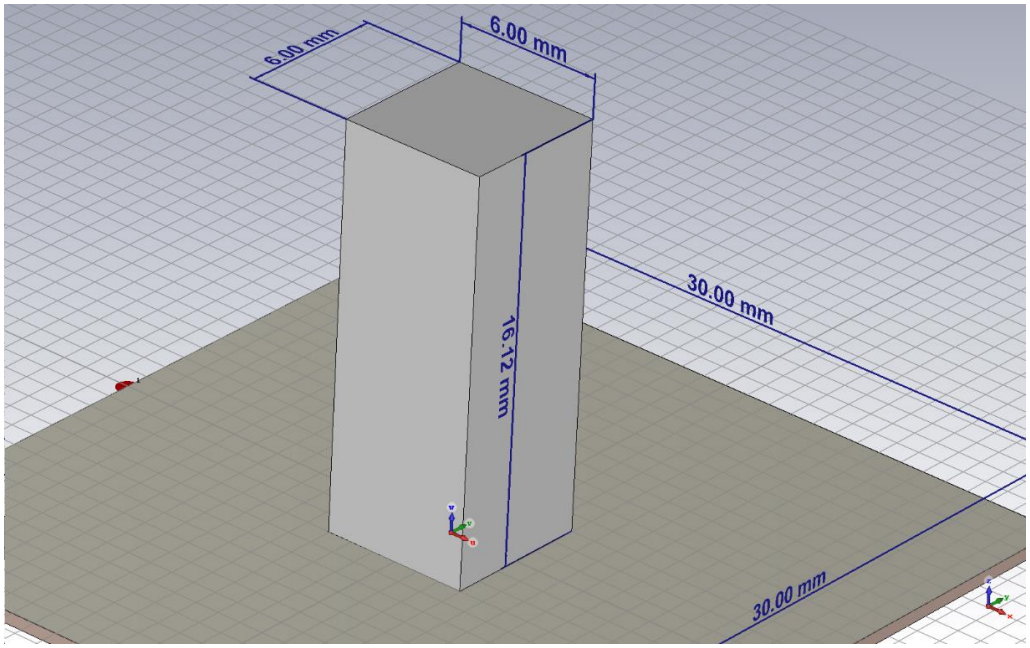

Fig. 124 simulated model of DRA working at 28 GHz.

Furthermore, in simulations, the simulated reflection coefficient for this model was assessed in order to evaluate the frequency response of the designed DRA model, as well as the accuracy of the equations. In Fig. 125, the simulated S-Parameters for the designed DRA are presented. A resonant frequency of 28.59 GHz is observed, with an appropriate matching of -17.5 dB, however, a second resonant frequency is observed at 30.3 GHz with a matching of -13.1 dB.

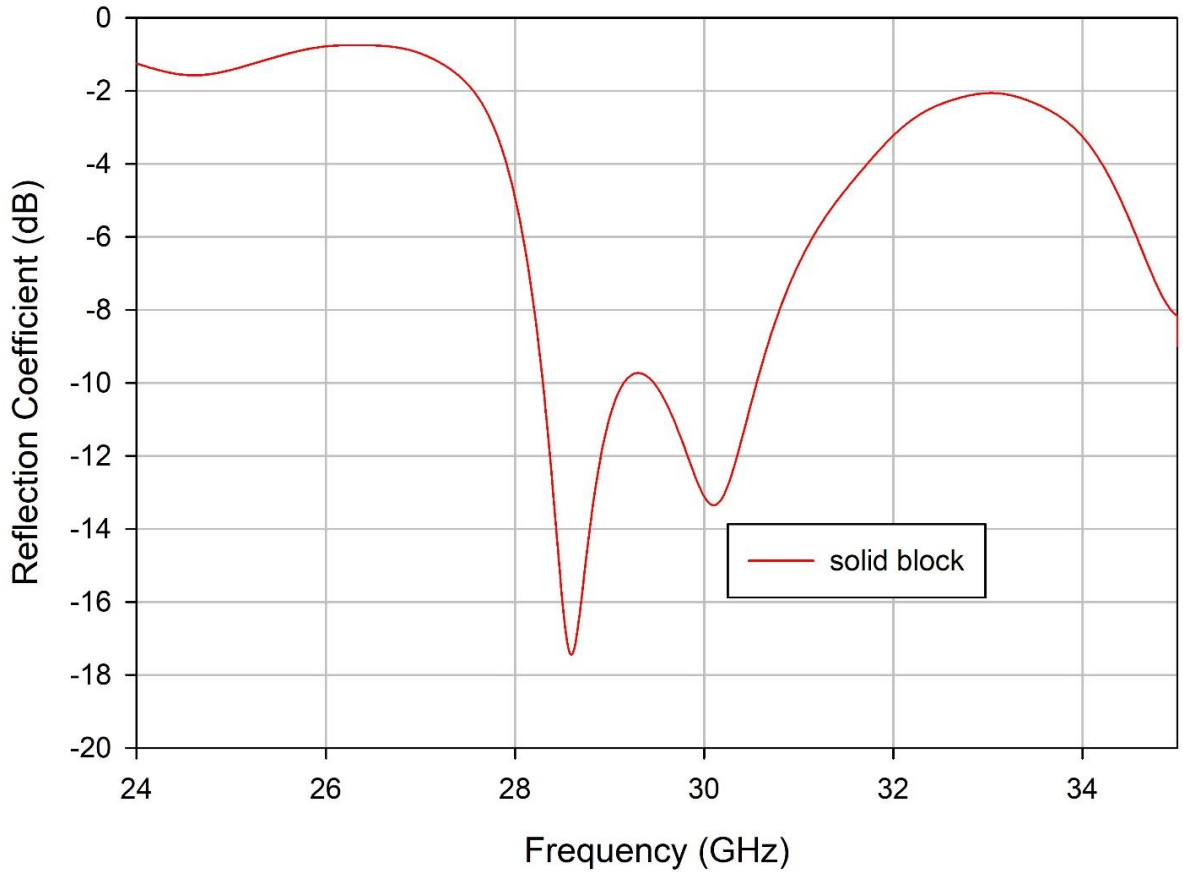

Fig. 125 Simulated reflection coefficient for DRA designed to work at 28 GHz.

Furthermore, the radiation patterns of this model were assessed. The simulated metrics correspond to typical figures offered by dielectric resonant antennas which is a main lobe in the direction of propagation of the z axis and secondary lobes adjacent to the main one.

In Fig. 126 the simulated radiation patterns for this designed DRA are presented in their polar forms (a) XZ cut, (b) YZ cut and meanwhile the 3D pattern is presented in (c) where the typical lobes discussed previously are observed. These figures correspond to typical radiation patterns for dielectric resonant antennas.

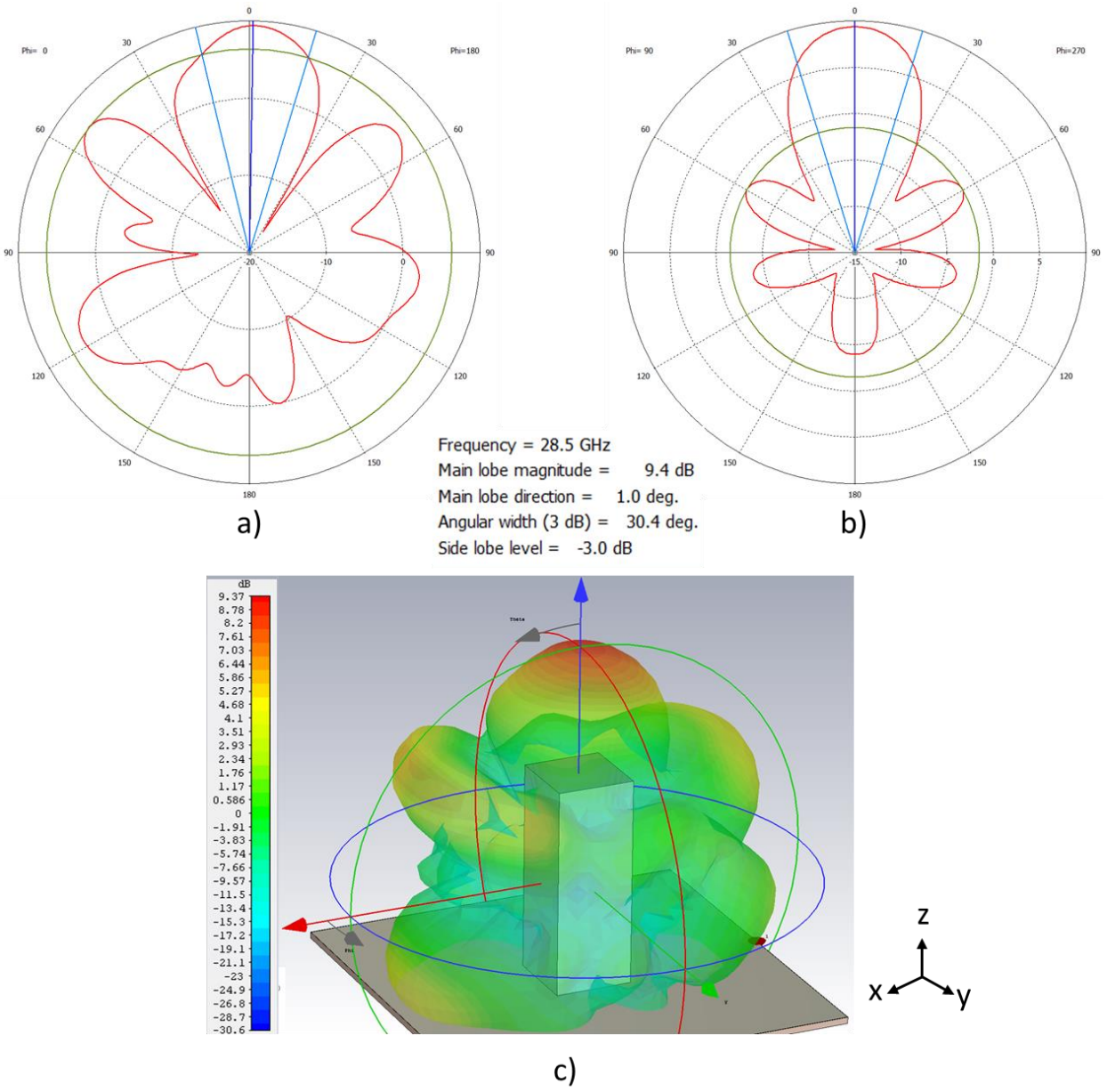

Fig. 126 Simulated radiation patterns for DRA designed at 28 GHz.

Overall, for this designed rectangular dielectric resonant antenna, the observed performance which is considered appropriate for mm-wave applications despite the DRA is constituted by a dielectric material which is not optimised for its use as dielectric resonator. As the simulated metrics corroborate the accuracy of design equations and the operation of a DRA with a relatively low permittivity ($\varepsilon_r = 2.5$) is achievable, the next step was to create a cavity in the DRA which is projected to be filled with an electrically tunable substance or material that will control the resonant frequency of the system.

A cylindrical-shaped cavity with a radius r = 2.5 mm and a height h = 15 mm was concentrically placed inside the rectangular dielectric resonant antenna turning the main structure of the resonator into a recipient the shape presented in Fig. 127 with the isometric view of the dielectric resonator in (a) and a plane cut view of the structure in (b) where the depth of the cavity is shown as well as the base of the DRA. Moreover, the tunable material is observed in (c), where two permittivities coexist within the structure of the dielectric resonator ε_{DRA} and ε_T and corresponds to the addition of an effective permittivity that will be controlled in order to achieve the frequency reconfiguration for this system. Although, ε_T will be the varying parameter in order to control the resonant frequencies of the system.

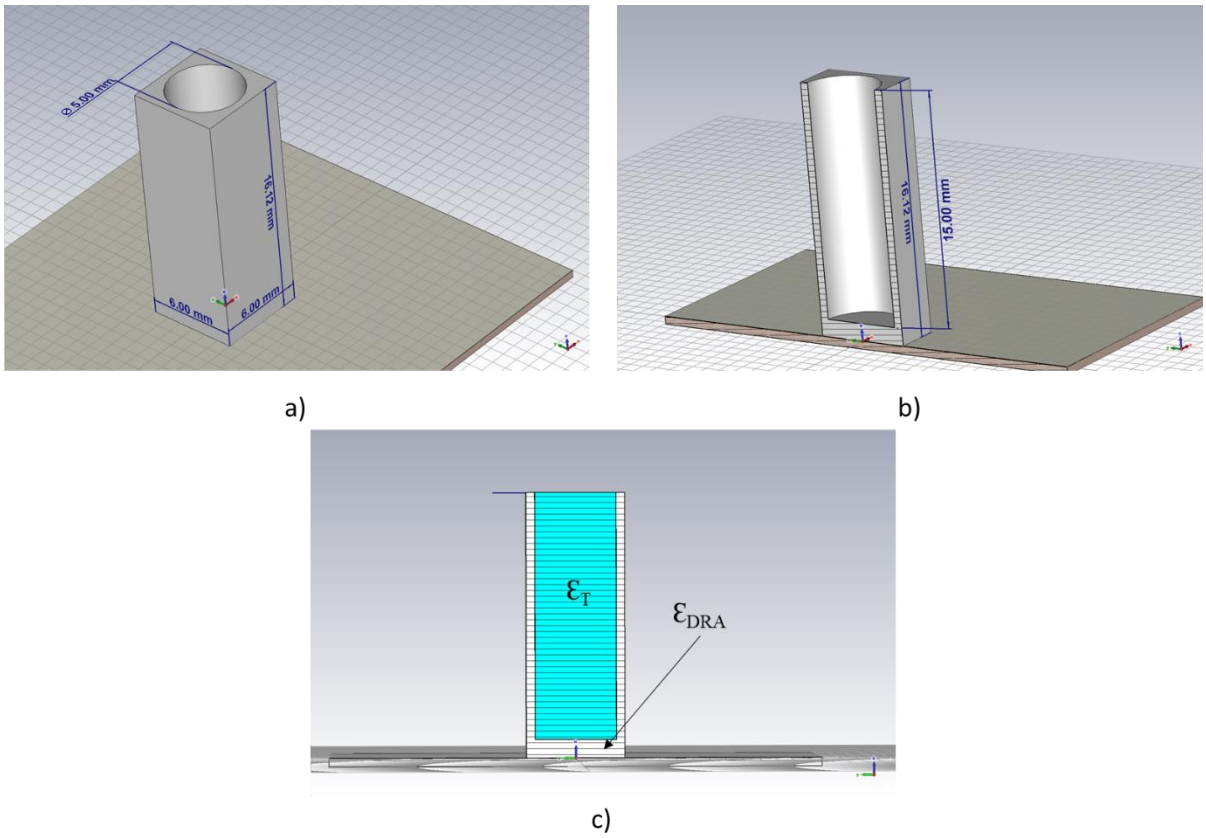

Fig. 127 Views of hollowed designed DRA.

With this cavity incorporated to the geometry of the dielectric resonator, the simulation for the cavity filled by a customised tunable material was carried out in terms of the antenna performance. This material varied its properties in simulation with a view to assess whether frequency reconfiguration is achievable through the proposed technique. It has been reviewed that a DRA containing two different permittivities can coexist and achieve an appropriate performance with potential frequency agility [108].

5.4.2. Simulated S-Parameters for 3D-Printed DRA when tuning internal cylinder.

The effects of changing the dielectric constant or relative permittivity of the simulated tunable material have been analysed in a parameter sweep carried out in CST Microwave Studio. The relative permittivity ε_T has been varied from 1.0 to 5.0 as a sensible range to assess the potential tuning. The obtained simulated metrics will be analysed in the next sections including reflection coefficients and radiation patterns.

The first steps for the simulation analysis of this model were carried out by varying the relative permittivity of the tunable material as discussed previously. This variation achieved resonant frequencies from 28.2 GHz to 31.2 GHz according to the varied values for ε_T. As expected, the simulated reflection coefficient presented a set of resonant frequencies corresponding to each of the values for the relative permittivity of the tunable material ε_T. This tuning range is presented in Fig. 128 below.

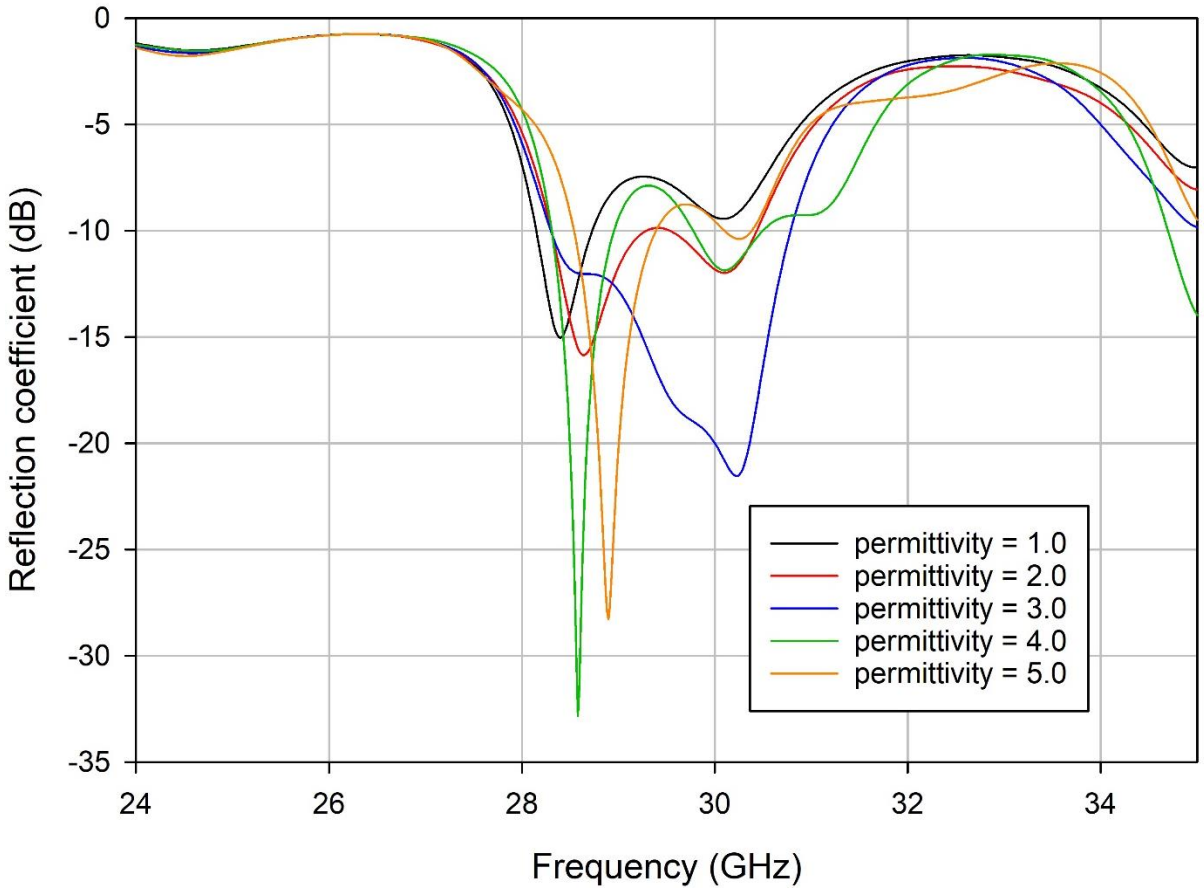

Fig. 128 Simulated tuning range of DRA when changing permittivity of internal cylinder.

As an abrupt frequency shift is observed when varying 1.0 for the relative permittivity in each case, a more detailed analysis was carried out in simulation. For this case ε_T was varied from 2.5 to 3.5 with an increment of 0.1 each case. This sin shown in Fig. 129 where the different resonant modes for the designed DRA are being changed in function of the permittivity.

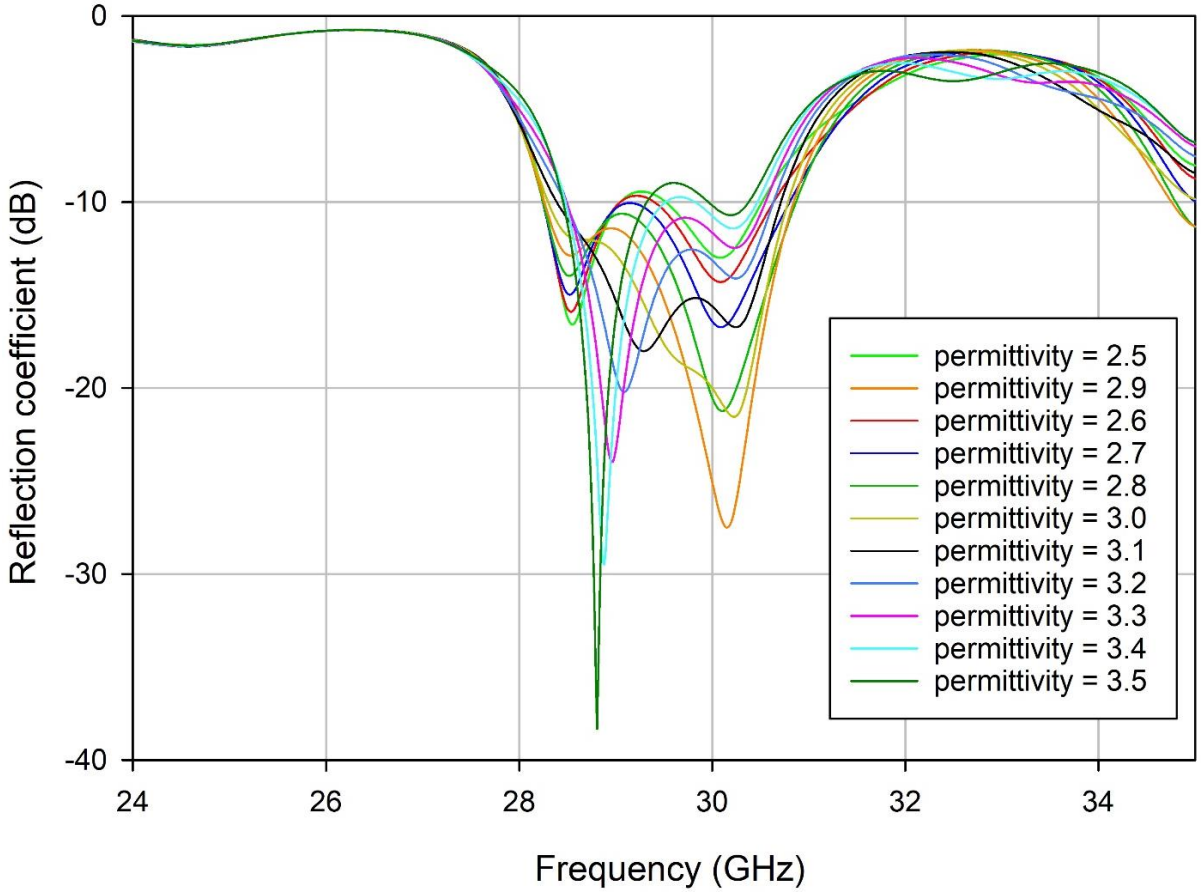

Fig. 129 Simulated reflection coefficients for DRA when internal cylinder varies its permittivity from 2.5 to 3.5.

Given the created tunable material was modelled as a generic substance that can change its permittivity, the simulation of the designed hollowed DRA was carried out with materials in the library of CST Microwave Studio, materials that are available to be simulated inside the dielectric resonator. As a reference, the solid block created in section 5.4.1 was used for this purpose, incorporating a cylinder constituted by the same material as the dielectric resonator (PLC) inserted in in its cavity.

Then, the simulated models for cylinders constituted of different materials were carried out. The aim of this set of studies is to assess the simulated response for a hollowed DRA with different materials in the created cylindrical cavity with the dimensions discussed in section 5.3.3. For this first set of simulations, four models were created, incorporating a different material filling the cylindrical cavity in each case. For the first case, the original solid block was taken as a reference. Then for the second model, the cavity was only filled with air, which permittivity is 1.0. Finally, two of the materials available to use, provided by the CBE laboratory, were included in the simulation. These materials are silk and graphite with relative permittivities of 4.2 and 12 respectively. The inclusion of these materials available in the silk-fibroin research group laboratory was interesting in order to assess the use of alternatives of manufacture that can provide a promising starting point for future development. In Fig. 130, the simulated reflection coefficient for each of these discussed cases are presented.

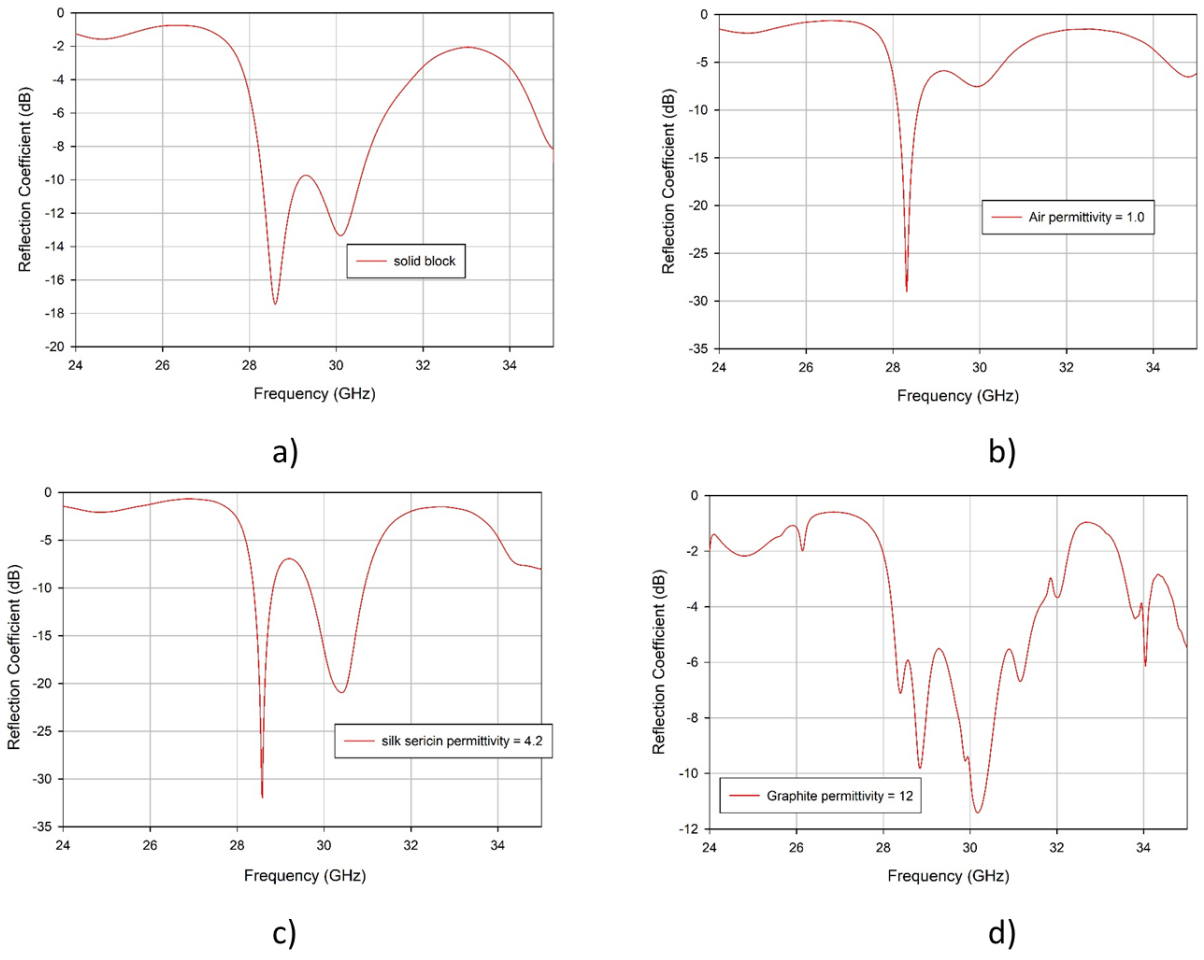

Fig. 130 Simulated reflection coefficients for different materials introduced in the DRA.

5.4.3. Simulated radiation patterns for 3D-Printed RDRA with different materials in internal cylinder.

As a sequential step, the assessment for the radiation patterns of the simulated models was carried out obtained radiation patterns for each of these materials with different permittivities. Despite achieving different resonant frequencies in function of the relative permittivity it was also imperative to study the effect of these materials in terms of the radiation patterns especially the non-confined materials for mm-wave propagation but are available for testing in the laboratory such as silk and graphite.

As analysed in Fig. 130, different resonant frequencies were observed for each material filling the cavity in the DRA, which, proves the correspondence between resonant frequency and relative permittivity in the simulated models. Therefore, the assessment of the radiation characteristics will be discussed accordingly. The radiation patterns for the originally designed DRA were discussed in Fig. 126 and corresponded to characteristic radiation intensities for a dielectric resonator.

The simulated polar and 3D patterns for the models of the DRA filled with air, silk and graphite in the following Fig. 131, Fig. 132 and Fig. 133 where the respective XZ an YZ plane cuts for the three cases are presented as well as an isometric view of their corresponding 3D patterns. As dielectric materials typically offer high gained radiation patterns in their main lobes, generally accompanied by secondary lobes with relatively lower gains then similar results were expected in practice for the dielectric materials used in the modelling for this DRA. The relative permittivities analysed in simulation in function of their corresponding resonant frequencies achieved are presented in Table 7 below. As a prediction for these resonant frequencies, a set of calculations using the mode determining equations were briefly carried out and agree with the simulated metrics in CST Microwave Studio.

	air	silk	graphite
Relative permittivity	1.0	4.2	12.0
Resonant frequency	28.4 GHz	28.5 GHz	30.1 GHz
Material nature	gas	gel	solid

Table 7 Properties of simulated materials contained in the DRA cavity.

The first model discussed was the hollowed DRA containing only air inside the cylindrical cavity. In the simulated material a relative permittivity of 1.0 is given by the computerised model. The simulated radiation patterns for this model are presented in Fig. 131. The simulated radiation patterns present an appropriate performance with typical numbers and shapes for DRAs. The figure presents in (a) the XZ plane cut and in (b) the YZ plane cut for the polar representation of these radiation patterns, while in (c), the 3D radiation pattern for this model is shown, where a main lobe with high intensity is observed.

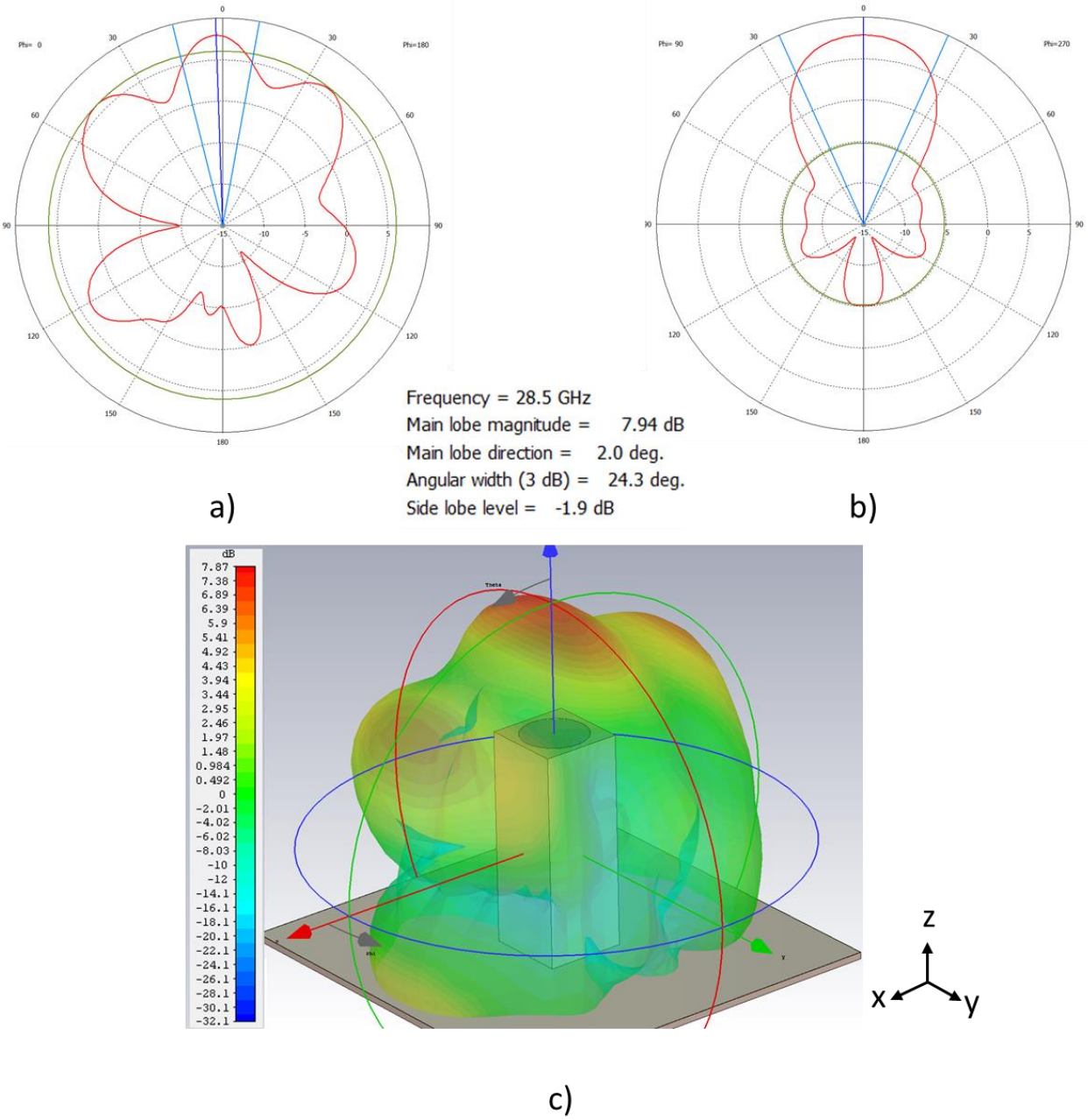

Fig. 131 Simulated radiation patterns for DRA filled with air at 28.4 GHz.

Secondly, the radiation patterns for the DRA containing silk in its cylindrical cavity are discussed. Commonly, silk is found as electromagnetic radiation absorbers [109]. Some properties of silk in gel forms have proved to aid the transmission in textile wearable devices [110] which is why this material was interested to be detailly analysed in its radiation characteristics. The corresponding simulated radiation patterns at their respective resonant frequency 28.5 GHz are shown in Fig. 132 where are presented in (a) its XZ plane cut, in (b) its YZ plane view and in (c) its 3D representation where typical main lobe and secondary lobes are shown but the shape is not presenting high gain.

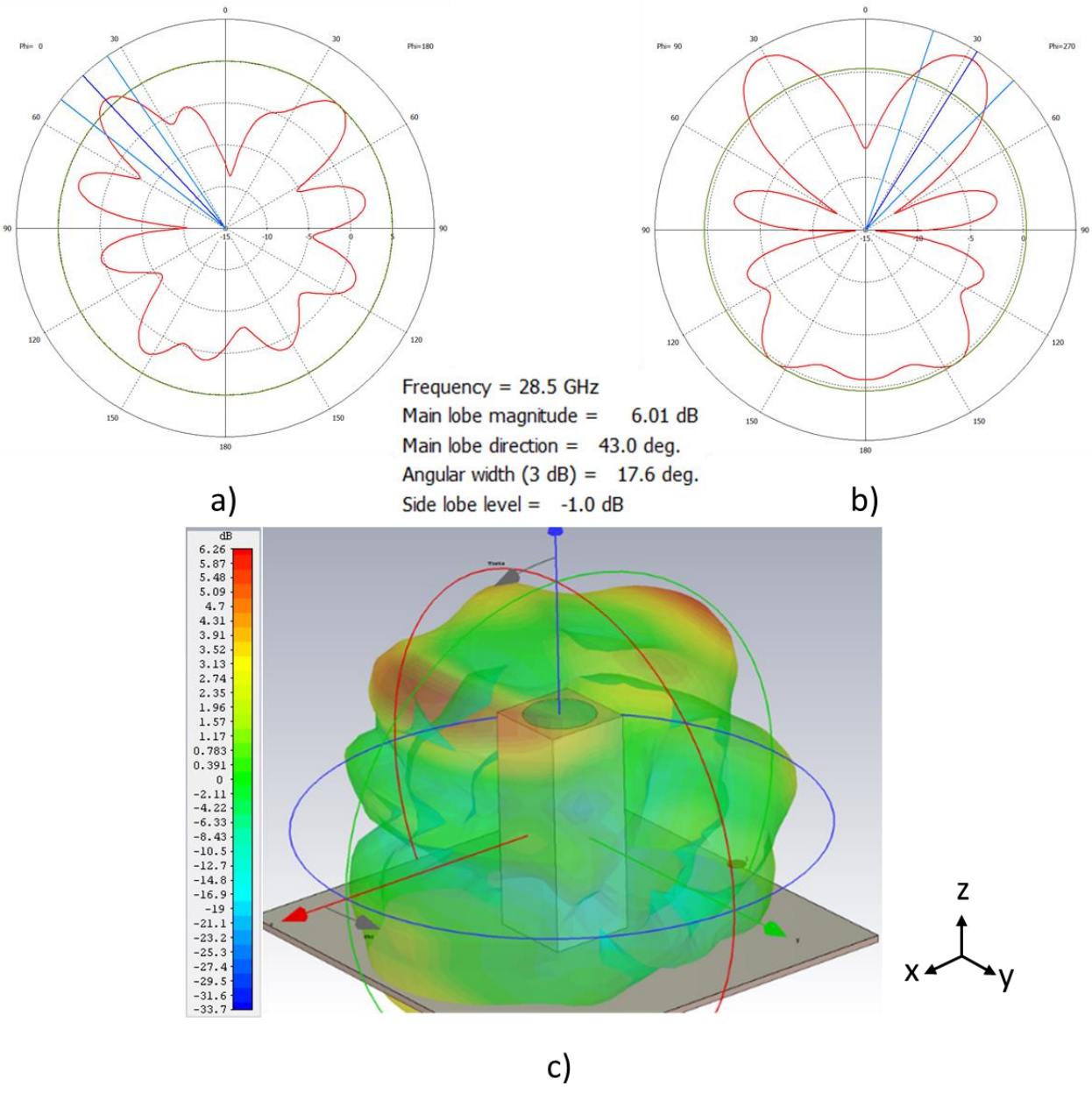

Fig. 132 Simulated radiation patterns for DRA filled with silk sericin gel at 28.5 GHz.

Finally, the third material analysed was a graphite cylinder inside the DRA cavity. Graphite is a very useful and versatile material that contains nano tubes in its internal structures which can have potential applications in microwave engineering as nano electrodes for electromagnetic radiation emissions [111]. The simulated radiation patterns for DRA containing graphite are presented in Fig. 133. It is observed in (a) the XZ plane view and in (b) the YZ plane view for the polar plots and in (c), the 3D radiation pattern for this model is presented where a typical high lobe and secondary lobes with lower intensities but a rather oddly shaped main lobe with higher gains in different places on top of the main lobe is seen.

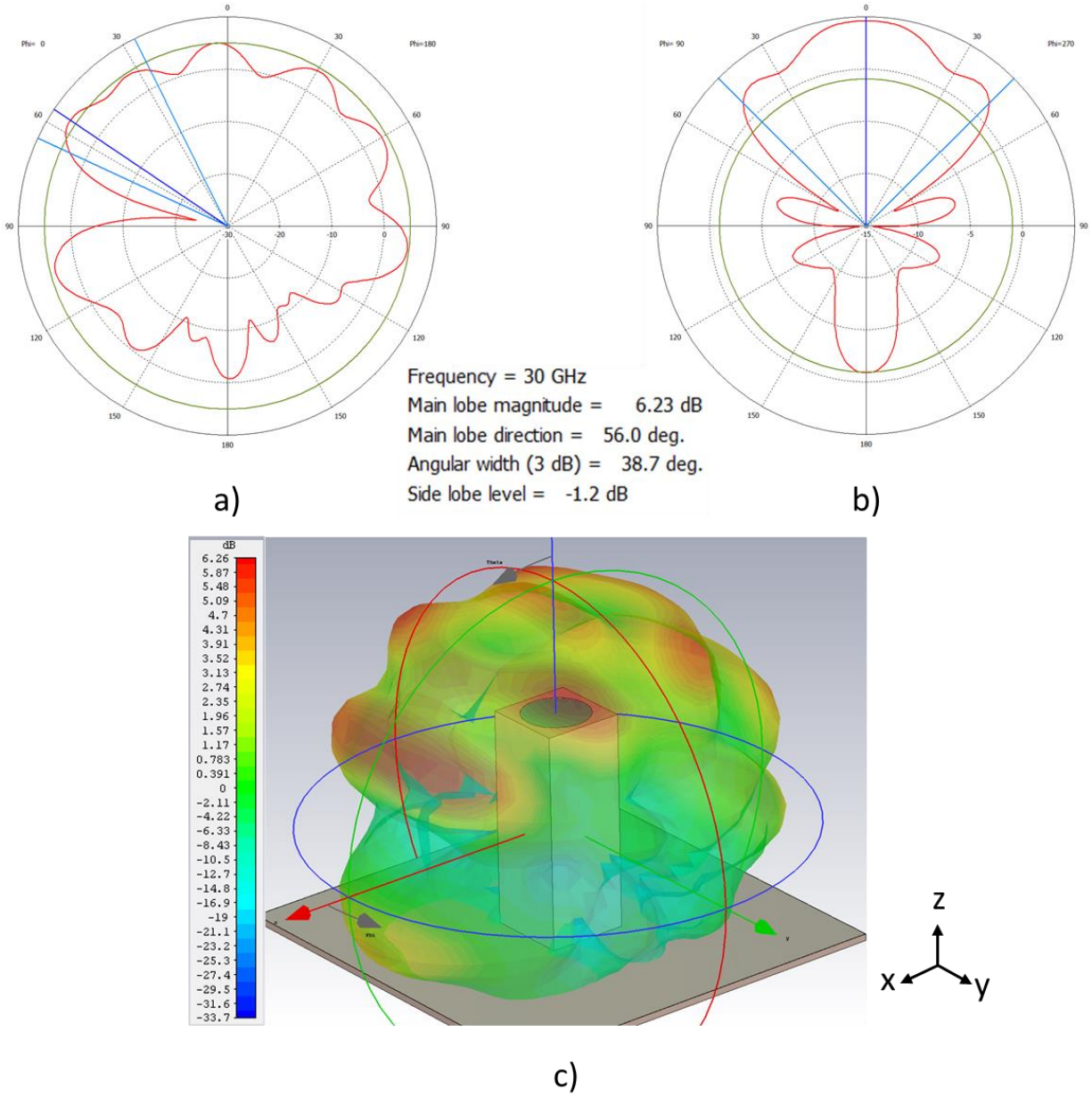

Fig. 133 Simulated radiation patterns for DRA with graphite at 30.1 GHz.

Moreover, a novel material, derived from graphite, able to vary its relative permittivity through external incident electric fields will be discussed. This is the case of Graphene Oxide (GO) which was briefly mentioned in section 5.1.2. Such material was provided by the chemical and biological engineering department laboratory. Involving the use of graphene in mobile communication engineering is one of the most innovative trends currently studied as the material has multiple and proven applications in many research fields such as medicine, architecture, mechanics, aerospace, electronics and electrical engineering, etc. This material has not been completely analysed in full due to its unpredictable behaviour which is based in the Nanotubes based structure that randomly rearranges in presence of an external factor which can be an electric signal.

As an amount of graphene oxide was expected to fill the cylindrical cavity in the rectangular DRA, an external electric signal was also required to be brought to the DRA walls in order to alter the dielectric constant of it. For this purpose, a simulation in CST Microwave Studio was carried out. This model incorporated a set of electrodes following the simulations discussed in section 5.4.2 and 5.4.3 with a view to analyse the effect of metallic elements placed in the external walls of the DRA. The ideal and recommended addition to the dielectric resonator is a set of discrete, thin metallic patches which, after the analysis previously carried out, do not represent a significant, negative effect on the antenna performance. The negligible effect for these patches is due to the reduced metallic losses of reduced inserted. These small conductive layers are incorporated to the computerised model measuring 2.0 mm × 4.0 mm over the external walls of the DRA in opposite faces.

An appropriate assessment of the performance in simulation of the proposed model will be now discussed. Firstly, the simulated reflection coefficients are commented. As a comparison with previous models, no significant effects are observed when compared to Fig. 130. This preliminary proves the proposed shape for electrodes present reduced effects at least in the reflection coefficients. However, it was imperative to analyse the simulated radiation patterns with a view to fully assess the effect of the proposed electrodes in the antenna performance. In Fig. 134, the simulated radiation patterns for the DRA model with the proposed electrodes are presented. The polar forms in are shown (a) for XZ plane and (b) for the YZ cut where slight differences in intensities are seen compared to the patterns without electrodes which is corroborated by the 3D pattern in (c). Also, a surface current analysis has been carried out specifically in the electrodes which did not present high current densities representing negligible radiation intensities to the patterns as shown in (d).

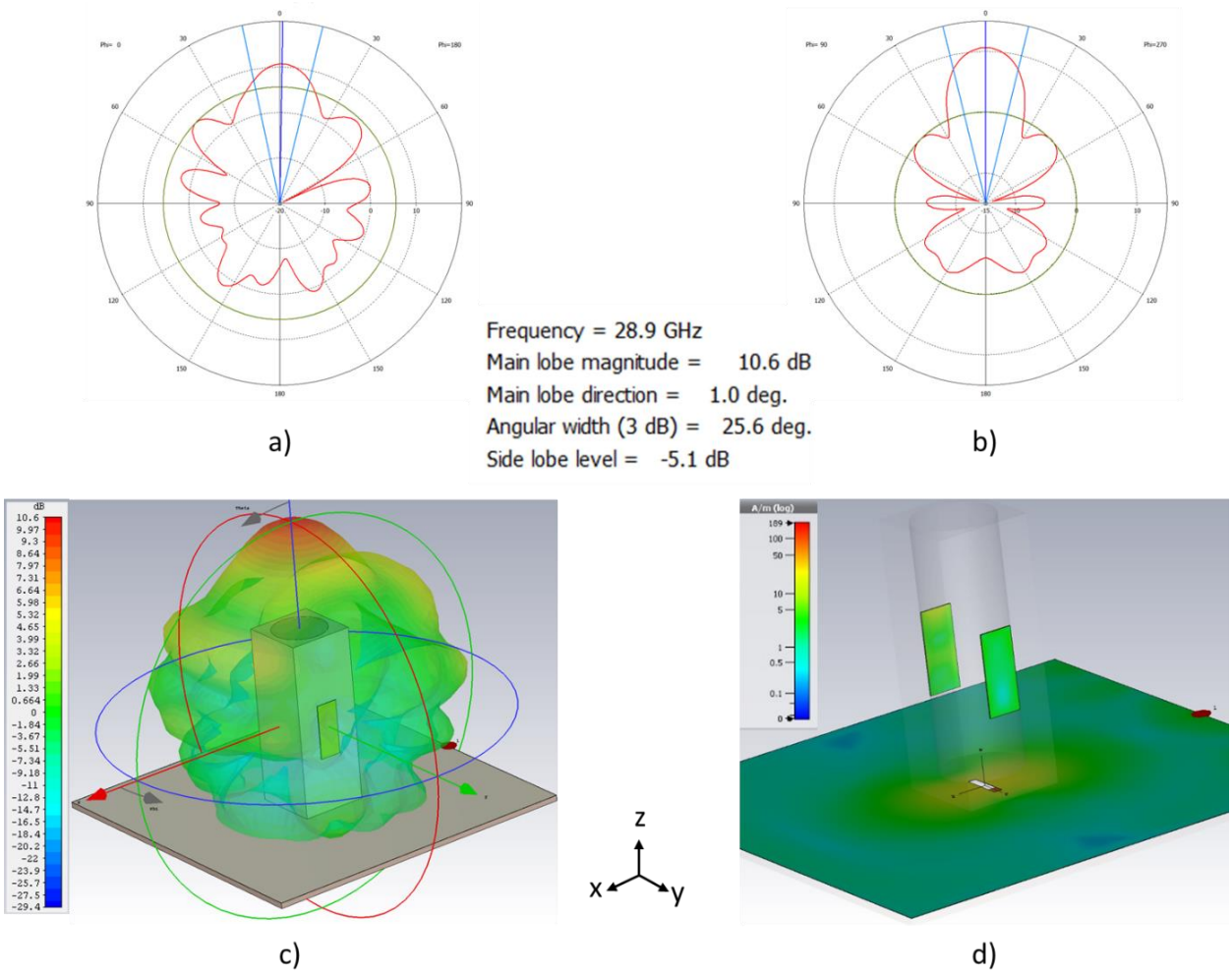

Fig. 134 Simulated radiation patterns for DRA with tunable cylinder and electrodes.

Another useful feature offered by the CST package is the H-field analysis. This tool is especially profitable for dielectric resonator antennas as it aids to determine the resonant modes supported by the DRA analysed in question. The mode theory that a waveguide can support only certain propagation modes, and, in the case of a dielectric waveguide, only TE modes are supported, which correspond to H-waves describing the magnetic field in its internal structure. Using the H-field analysis, the plot of the number of short magnetic dipoles that are supported by the dielectric resonator and therefore determine the supported TE modes for the analysed DRA.

The resonant modes supported by a waveguide have different essential features such as the intensity of modes described by the number of short magnetic dipoles contained in the waveguide. The lowest number of short magnetic dipoles supported by a waveguide is denominated fundamental modes, other modes different from this simplicity are known as

higher order modes which are not supported by all the waveguides, different from the fundamental modes which are present in every waveguide. In Fig. 135, the H-field analysis for this dielectric resonant antenna is presented. It is clearly observed that 14 short magnetic dipoles are located at the top and a last one at the bottom, which, due to the reflection offered by the ground plane counts as a reflected dipole counting on the notation as one only. However, analysing the modes on the other axis Y and X only the fundamental mode is observed. Hence, the notation for the supported modes by the designed DRA is TE_{1115} and correspond to higher order modes for this dielectric waveguide.

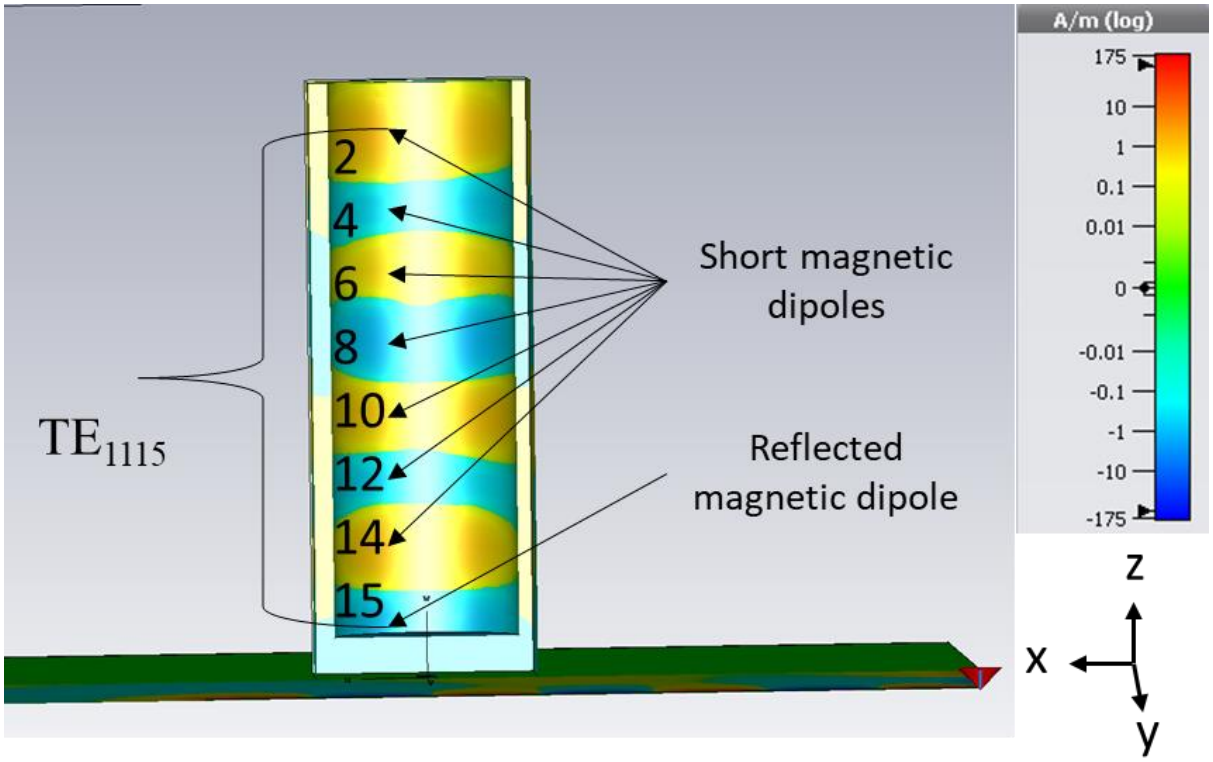

Fig. 135 Simulation of resonant modes for filled DRA.

Having analysed the supported resonant modes for the designed DRA one can conclude that the dielectric resonator operates in higher order modes, which is beneficial in high frequencies for mm-wave applications. It is only by computerised full wave antenna analysis that such conclusions on essential operating features for dielectric resonators can be obtained accurately. The results suggest that the cylindrical material is therefore the radiating part for this antenna, and the hollowed PLA dielectric resonator acts as a coating for the contained material. Since the higher order modes are supported by this designed DRA then a reduction of its Q-factor is expected.

In conclusion for the analysed simulated numbers in this section, the radiation patterns did not lose the typical shapes corresponding to DRAs. However, they are slightly affected in terms of the gain of the higher lobes which might represent reductions in the performance of the antenna when in practice. Moreover, for the simulated reflection coefficients, the control of relative permittivities for the material of the internal cylinder, an appropriate frequency shift was observed was well achieved when varying ε_T. This was valid for both a tunable bespoke material and the modelled materials included in the library of CST Microwave Studio. However, a proportional ratio permittivity – frequency was unlikely to predict as the DRA designed offer originally two resonant modes which are close to each other and hence affect the frequency tuning of either one or the other resonant mode. Nevertheless, this is a promising starting point in simulation for frequency tunable dielectric resonant antennas once proving the relative permittivity of the internal material can be electrically tuned with external signals. In the next section 5.5, the discussion for the manufacture process and measured results for the designed model analysed in simulation will be carried out.

5.5. Manufacture and measurements of 3D-Printed reconfigurable RDRA for mm-wave applications.

Basing on the promising results analysed in the previous section, corresponding to computerised models, the manufacture procedure will be now discussed. The proposed manufacture technique of 3D-Printing will be assessed in this section. The materials for the 3D-Printed dielectric resonators and its corresponding fillings were previously discussed and will now be assessed in practice. The novel technique for 3D-Printed parts has been growing in the past few years for multiple disciplines and industries. Nowadays, acquiring a 3D-Printer for a household is quite simple and can offer the construction of multiple objects for home appliances. This is a beneficial in terms of simplicity and relatively low costs for manufacture of complex structures. This thesis aims for an assessment of this technique now focused towards the construction of radiating elements such as DRAs. This study is needed as the simulations presented a promising starting point for the foreseeable manufacture, which posteriorly will be assessed in measurements using laboratory equipment. Moreover, in terms of materials, an electrically tunable substance will be incorporated in these manufactured prototypes. This substance will be filling the cylindrical cavity in order to evaluate the frequency reconfiguration, by assessing the real measurements for reflection coefficients and radiation patterns which will be discussed and compared with simulations.

5.5.1. 3D-Printing and manufacturing process of RDRAs.

As the origin of the materials used in the prototypes for the proposed DRAs has been discussed, further information on established quantities and preparations for tunable materials and substances is presented in Appendix B. In this section, the construction procedure for the designed DRAs will be carried out. Firstly, a material for the DRA was selected for the body of the resonator, this was the case of a transparent PLA, which, after corroborating with manufacturer, has a relative permittivity of ε_{DRA} = 2.5 corresponding to the properties simulated in section 5.4. In the chemical and biological engineering (CBE) department laboratory that assisted on this research, three different forms of PLA were available for use and, after consulting with manufacturer, had different relative permittivities each. A green PLA filament presents a permittivity ε_{DRA} = 2.7, while a dark blue filament offers another value ε_{DRA} = 2.9. The use of these materials will be discussed not only as DRAs but also as cylinders filling the respective cavity a solid DRA without cylindrical cavities has been 3D printed as well in order to evaluate the performance of the material itself.

For the feeding network printed circuit boards, the manufacture of layers of Rogers RO4350 with ε_s = 3.66 with a geometry measuring 30.0 mm × 30.0 mm × 0.5 mm were ordered. These specifications are only achievable by industrial manufacture carried out by specialised equipment. Concerning the ground plane for the PCB, a layer of copper covered one of the faces of the board having a concentric coupling aperture measuring 2.77 mm × 0.47 mm where the DRA and the material contained will sit concentrically on top of it as well, making it a versatile and easily changeable for the multiple DRAs to be analysed. In the opposite face of the board a microstrip feed line has been placed in order to feed the coupling aperture and consequently feed the DRA system. This feed line will be connected to a 2.4 connector suitable for frequencies up to 60 GHz. Hence, the ground of this connector will be connected to the ground plane of the board.

Finally, for the materials used in the cylindrical cavities of the prototypes, the 3D printing of three different PLA cylinders using the previously discussed available materials was carried out as well as the injection of a volume of the analysed materials. The collaborating staff of the chemical and biological engineering department assisted on the preparation of the silk sericin gel derived from naturally harvested worm silk that has numerous applications in biochemical scaffolds generally but also has been explored in electronic engineering applications.

Moreover, the staff facilitated a sample of a graphene oxide solution dispersed in water and prepared a gel based on this material. In Fig. 136, I present in (a) the 3D printing of one of the DRAs in (b) the materials prepared and facilitated by the CBE department, in (c) the DRA prototypes proposed sitting on top of the PCB and held by adhesive tape and in (d) the measurement protocol that will be analysed in the next section 5.5.2.

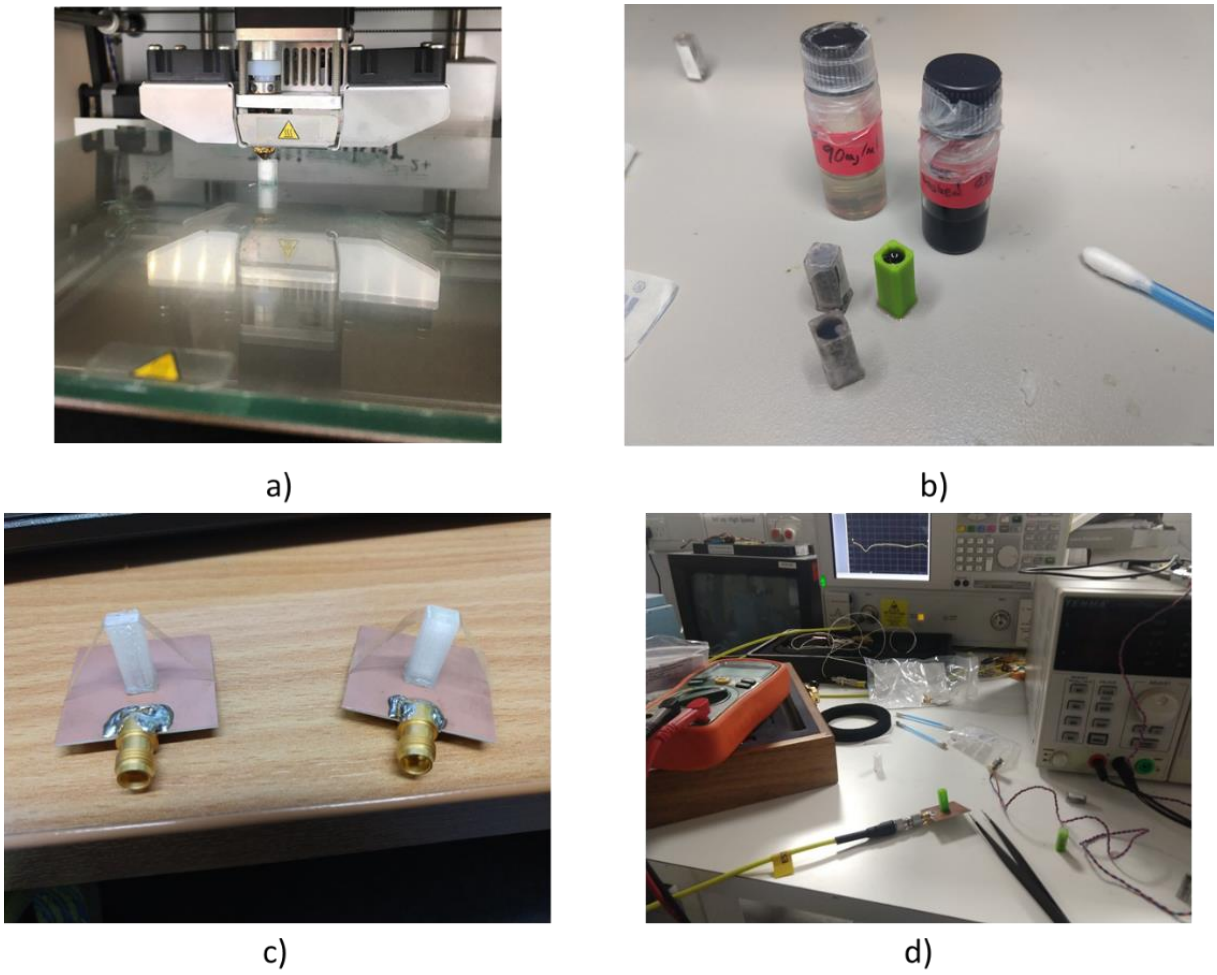

Fig. 136 3D printing process prototypes and measurement protocol for rectangular dielectric resonators.

Once these prototypes were prepared, a set of measurements was carried out in order to evaluate the performance for each of the materials previously analysed in simulation. The study will be discussed first for the materials discussed in the previous section that were filling the cavity and did not suffer the incidence of any external signals, i.e. silk, PLA, Air, etc. Then, the measurements for the performance of the antenna when containing a volume of electronically tunable graphene oxide will be assessed.

5.5.2. Measured S-Parameters for 3D-Printed RDRAs.

The respective set of measurements was performed in the laboratory using the VNA with the appropriate frequency range for applications of this purpose, different form the one used in section 3.3.2. Similar to section 5.4.2, the first element analysed was the solid block. The frequency response of this printed solid DRA presented a resonant frequency of 27.3 GHz and a matching well below -27 dB having the second resonant frequency with a week matching. This agrees in principle with the main resonant frequency expected from the design calculation and simulations. Then, the second model analysed was a hollowed DRA containing only air, this prototype measured a resonant frequency of 26.8 GHz and a matching near -30 dB, again, this corresponds with predicted calculations and simulations. Now for the filled resonators, the one containing the silk sericin gel provided by the CBE lab offered a resonant frequency of 27.2 GHz however, the matching was significantly reduced reaching nearly -22 dB which differs slightly from the calculated modes and the simulations. These reflection coefficients are presented in Fig. 137 for (a) the solid DRA made of transparent PLA, (b) the hollowed DRA and (c) the DRA filled with silk sericin gel.

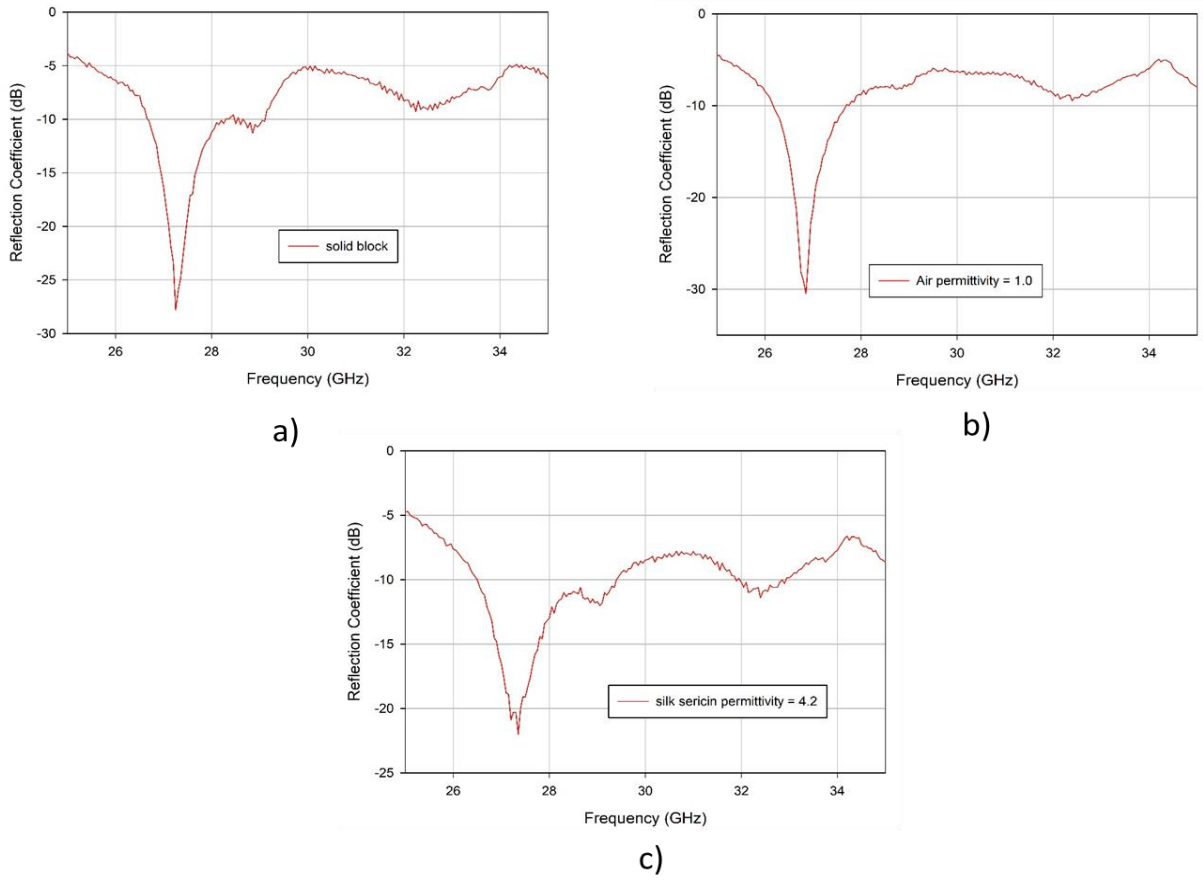

Fig. 137 Measured reflection coefficients for DRA filled with air, silk and solid block.

Further in measurements, two dielectric resonators containing two different preparations of graphene oxide. These preparations were carried out under the assistance and guidance from the CBE department staff. The two presentations of GO, a graphene oxide solution, and a graphene oxide gel, filled two dielectric resonators respectively. These were analysed similar to the previous sample filled with silk, securing its position on top of the feeding network PCB. Firstly, the DRA containing liquid graphene oxide offered a resonant frequency of 27.7 GHz and a matching near -35 dB. Then for the DRA filled graphene oxide gel, a resonant frequency of 27.5 GHz and a matching near -30dB dB were observed. In Fig. 138, the measured reflection coefficients for DRAs filled with (a) graphene oxide solution and (b) graphene oxide gel (b) are presented results.

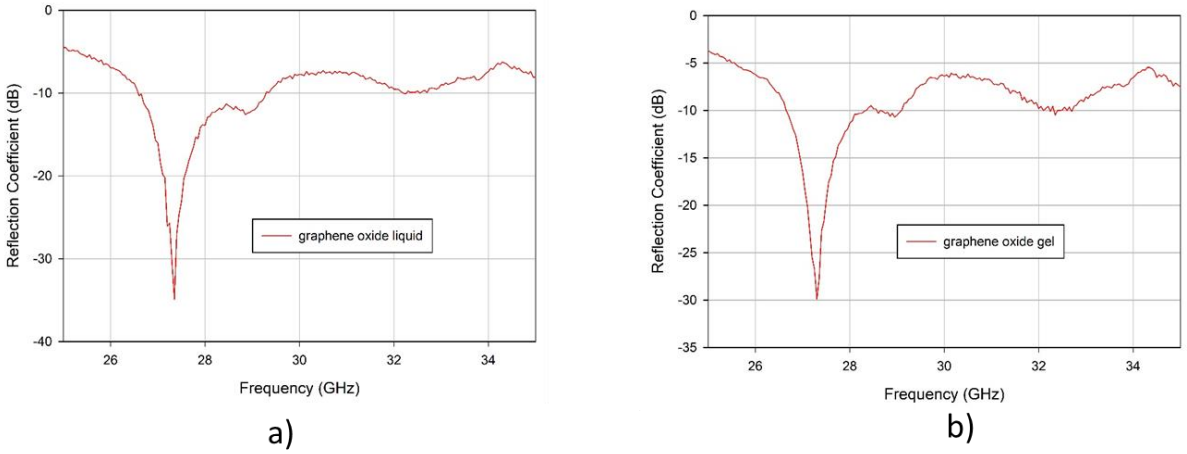

Fig. 138 Measured reflection coefficients for DRA filled with two presentations of graphene oxide.

According to the proposed methodology, with a view to explore the interaction of the two presentation of graphene oxide in presence of an incident electric signal, in incorporation of metallic elements was carried out. The use of discrete metallic electrodes providing an electric signal varying its voltage will be discussed, similar to the simulated model discussed in Fig. 134 (d). As, theoretically, an external electric field can cause the nanotube-based structure of graphene oxide rearrange its position, two discrete metallic electrodes measuring 2.0 mm × 4.0 mm were incorporated in one dielectric resonator. Since the simulated model proved to have negligible effects in the overall performance of the DRA, the geometry of these patches was reproduced in practice. The electrodes were produced using a 35 µm thick copper tape, which, after being cut in their corresponding rectangular shape, incorporated the soldering of a thin wire in each electrode. This procedure was carried out fr both DRAs filled with

graphene oxide solution and containing graphene oxide gel. As the wires were placed in the patches, a biasing voltage was applied to the DRA walls. Using a power supply, I varied the DC biasing voltage provided by it from 0 – 30 V and analysed its effects on the resonant frequencies. A frequency tuning, although not significant in high frequencies, was achieved in presence of different values of the incident signal.

In Fig. 139, the experimental procedures carried out for the measurement of the reflection coefficients for the DRAs are presented. Presenting in (a) the DRA with electrodes attached to its walls as well as DC biasing voltage lines, in (b) the VNA measuring the reflection coefficients and the power sources providing the electrical tuning signal, and the frequency range achieved by the DRA filled with (c) graphene oxide solution and (d) graphene oxide gel when the experimental measurement protocol is applied.

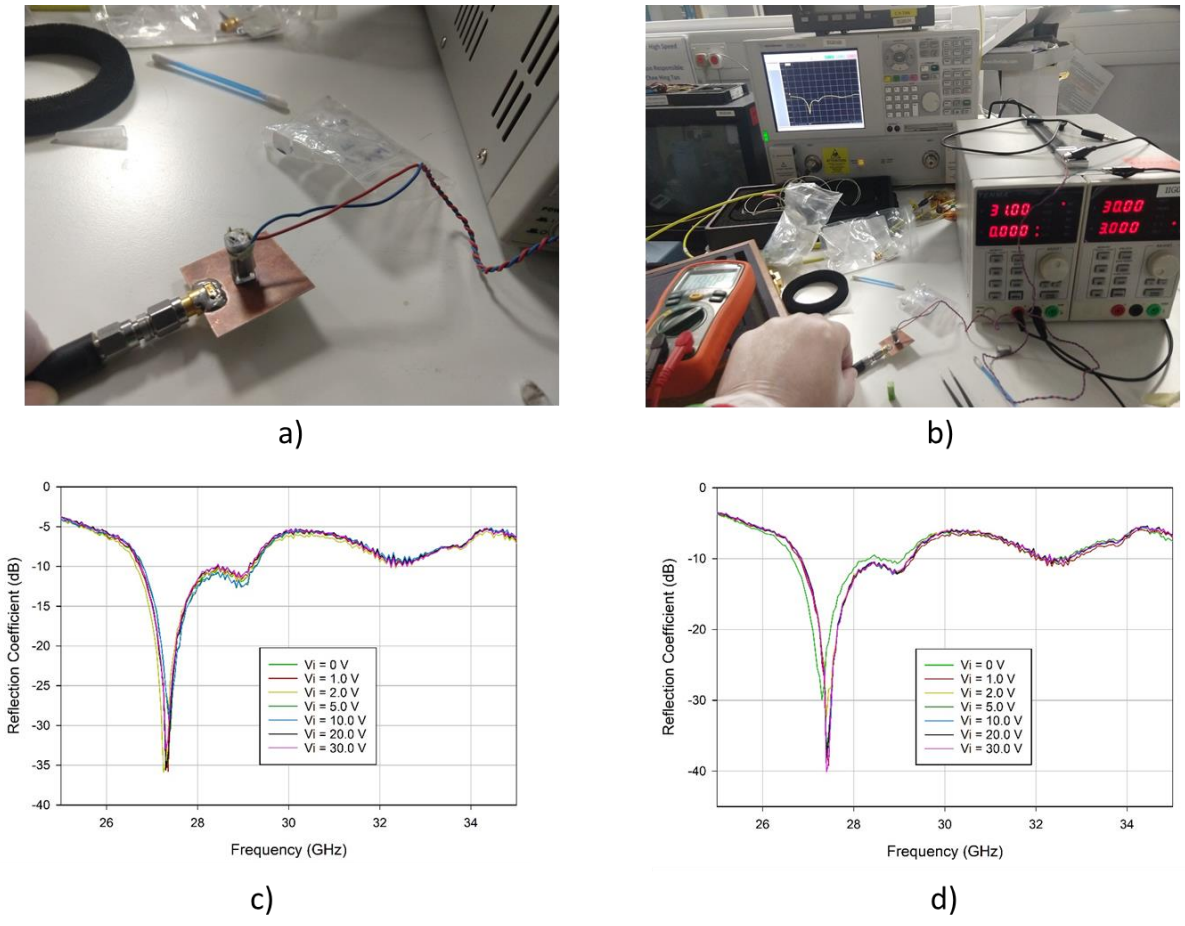

Fig. 139 Experimental protocol for measurement of resonant frequencies for DRAs filled with graphene oxide and its measured reflection in presence of a biasing DC voltage.

Despite the tuning achieved by the proposed DRAs filled with graphene oxide did not present significant changes when analysing it in high frequencies. Although, a detailed analysis of the achieved frequency ranges was carried out from 27.25 GHz from 27.42 GHz when varying the biasing voltage from 0 – 30 V. Given the many unknown properties of the graphene oxide samples used for these experiments, it is quite difficult to quantify the voltage – frequency ratio, which differs from the characterised varactors Infineon BB833 that achieved tuning for the reconfigurable 1 × 2 MIMO systems analysed in Chapters 3 and 4. Nevertheless, this is a staring point for future works potentially based on filled DRAs with electronically tunable materials.

In Fig. 140, the previously discussed detailed zoomed graphic is shown. The measured reflection coefficients for the tuning frequency range achieved for the DRA filled with graphene oxide solution is presented. The range achieved by the proposed DRA filled with graphene gel in presence of an external tuning electric signal is similar to the one presented in this figure.

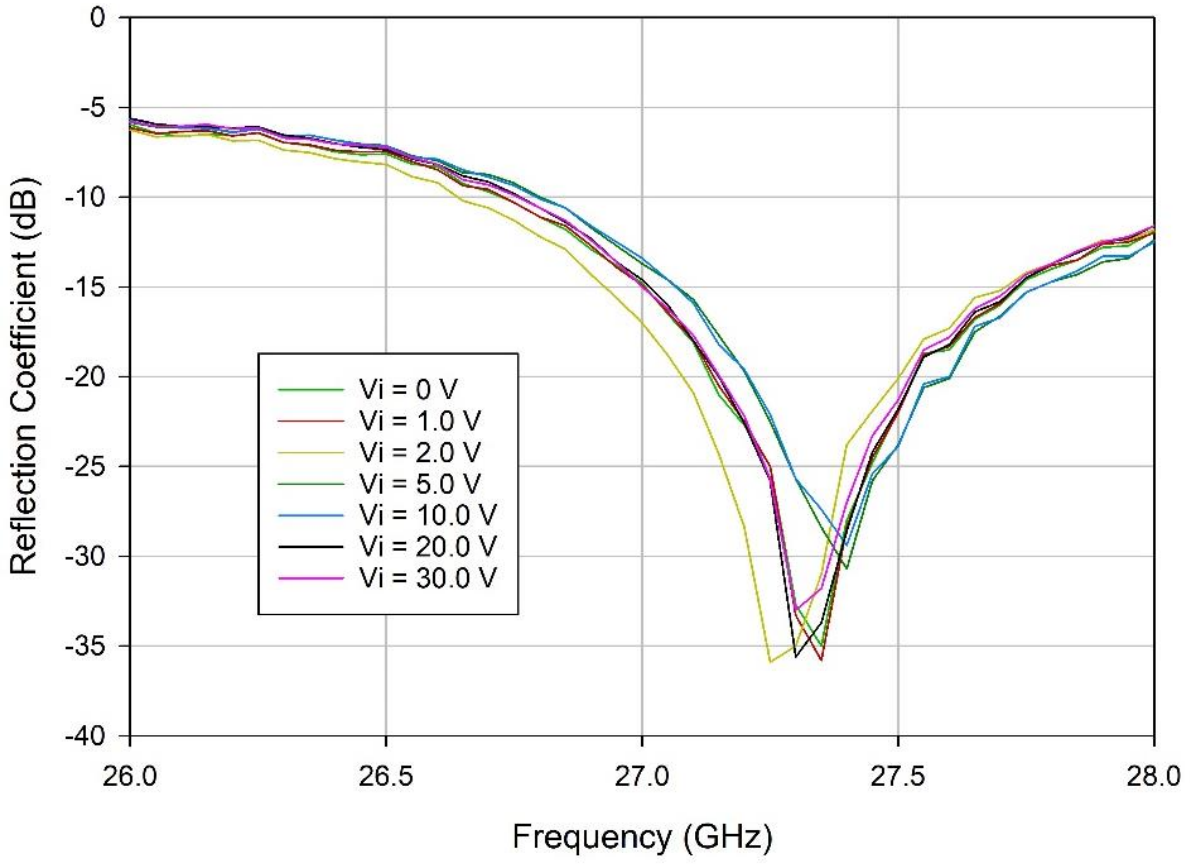

Fig. 140 Zoomed Measured reflection coefficients for DRA filled with graphene oxide liquid when applying a voltage.

Moreover, additional prototypes were prepared including 3D-Printed cylinders constituted by PLA of different pigmentations. Three additional DRAs incorporating 3D printed cylinders made of the transparent, green and blue PLA will be discussed and analysed with a view to add up to the study of a material with different permittivities. The 3D-Printed cylinders achieved different resonant frequencies each, as shown in the reflection coefficients, achieving different ranges for each material as follows: 27.15 GHz and matching of -26 dB for the transparent PLA cylinder, 27.22 GHz and -26 dB for the green cylinder and 26.91 GHz with -32 dB of matching. The analysis of these materials being contained inside the DRA although supposed to be from the original same material present different resonant frequencies due to the different values of relative permittivity for each variant of PLA. By analysing the case of the transparent cylinder inserted in the DRA we corroborate what the H-field analysis in simulation suggested, i.e. the resonant modes are supported by the cylindrical material, while the designed DRA acts as a coat. In Fig. 141, the measured reflection coefficients for the DRA containing the discussed 3D printed cylinders and their respective permittivities are presented.

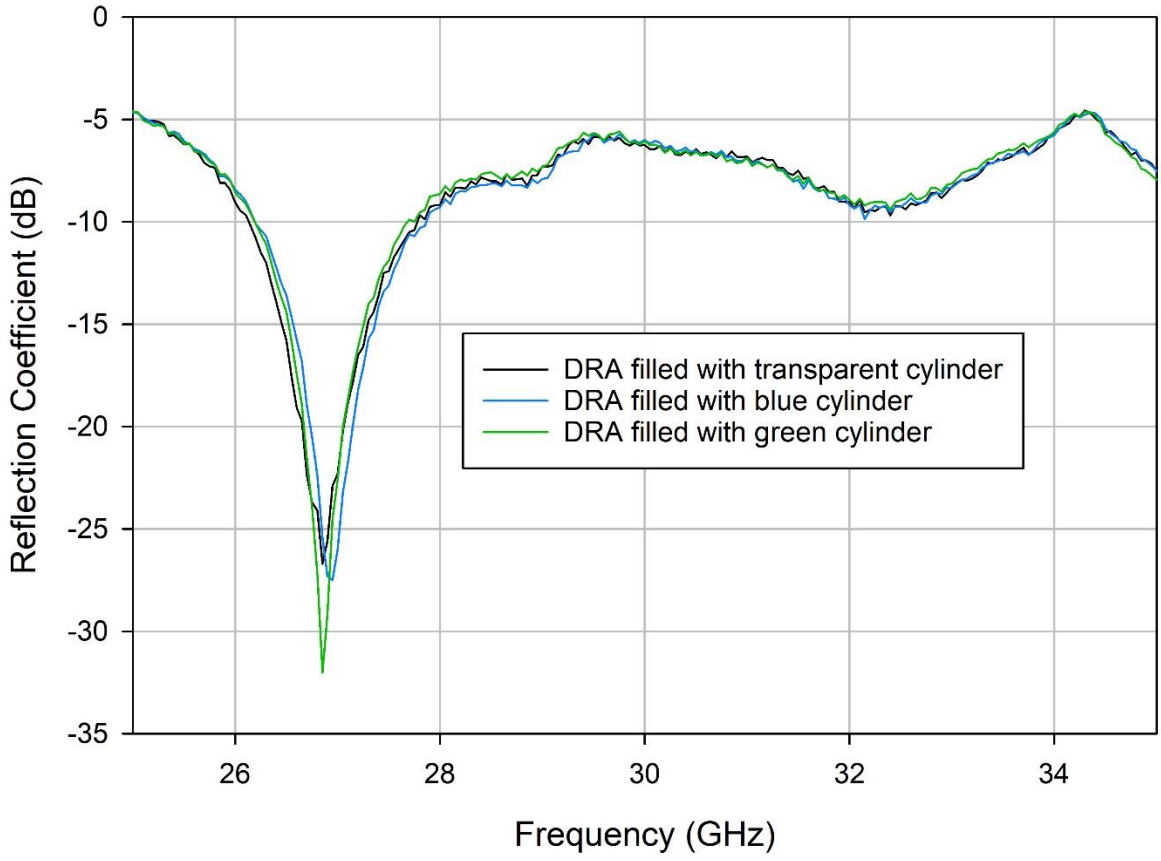

Fig. 141 Measured reflection coefficients for DRA filled with cylinders of different permittivities.

As an illustrative experiment, the measurements of the reflection coefficients for the 3D printed cylinders in the absence of the container DRA. As the coupling aperture dimensions allowed it, the cylinders were sitting on top of it and excited it acting now as dielectric resonators and achieved different resonant frequencies as follows: 27.23 GHz and a remarkably good matching of -57 dB for the transparent PLA cylinder, 27.48 GHz and a matching of -41 dB for the green cylinder and 27.68 GHz and a matching of -37 dB of matching. This analysis proves that the cylinders themselves support resonant modes and are suitable for mm-wave applications potentially if investigated further as well as a potentially achievable frequency reconfiguration if their permittivity is varied, this is shown in Fig. 142 below, the measured reflection coefficients for the three cylinders of different variants of PLA and different permittivities are presented.

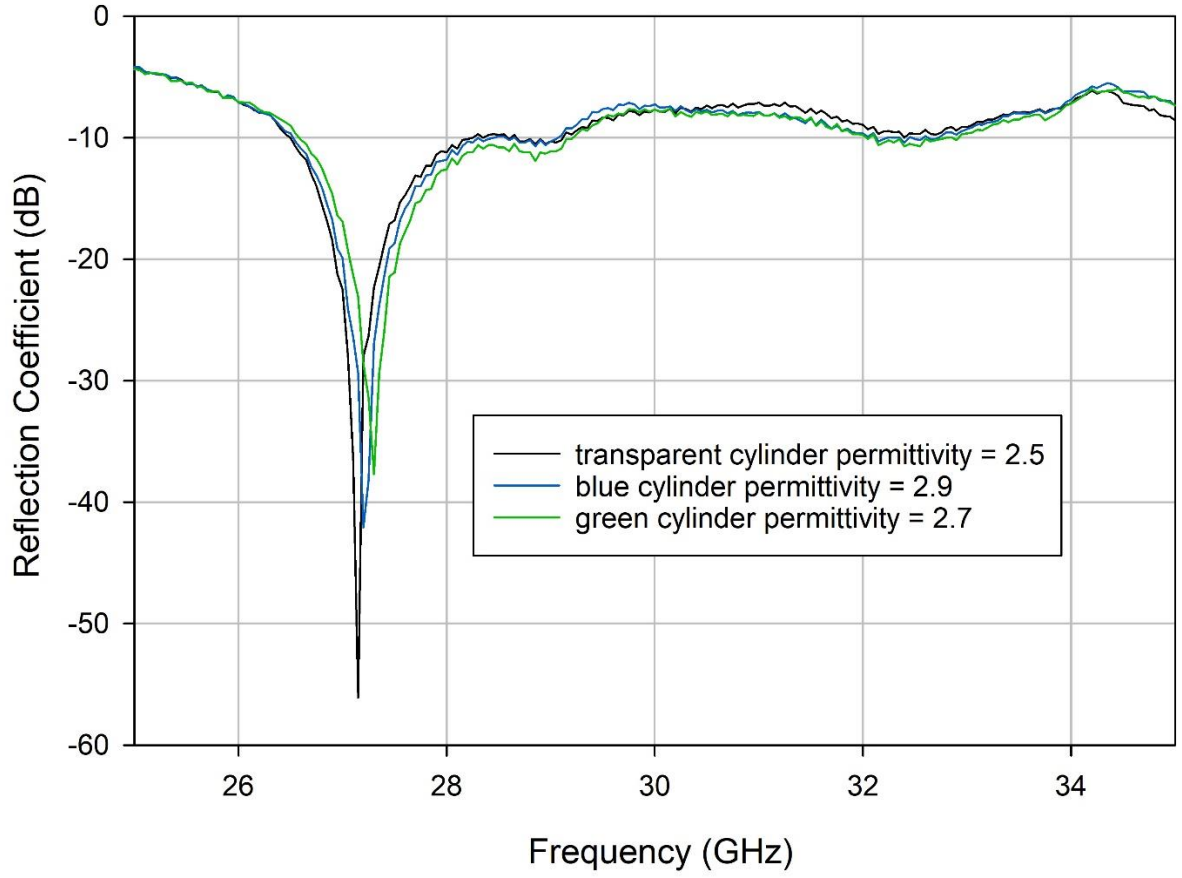

Fig. 142 Measured reflection coefficients for cylindrical dielectric resonant antennas with different permittivities.

Since a small difference in the permittivities was presented from one material to other, then a proportional shift was expected in these models, this was therefore expected and agreed with the numbers presented above.

As a final analysis in terms of measured S-Parameters, one can conclude that frequency reconfiguration on dielectric resonant antennas is potentially achievable in greater scale as proved in the discussed prototypes. Even a slight variation in the relative permittivity of the materials constituting the DRA would represent a proportional frequency shift.

For this purpose, Fig. 146 the summarised values for all the resonant frequencies achieved by all the materials contained in the DRA are presented in (a) as well as a zoomed detailed view of the tuning range in (b).

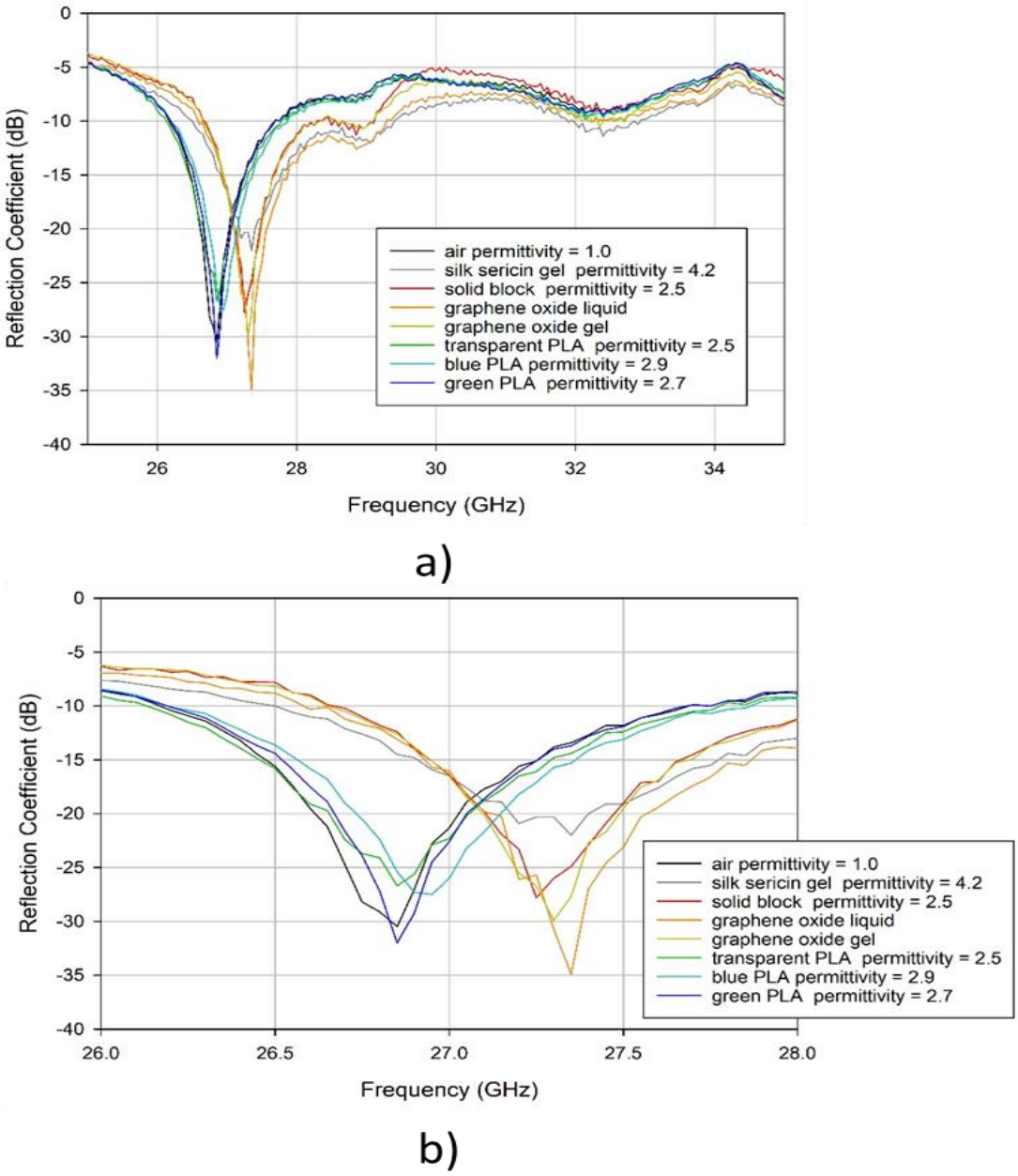

Fig. 143 Measured reflection coefficients for DRAs filled with all the studied materials.

The analysed measured S-Parameters have shown little agreement with the simulations. Overall, there is a gap observed in the analysis of reflection coefficients between simulated and measured readings. Nevertheless, the frequency response is similar for both analyses. The resonant modes are resembling for most of the prototypes despite the frequency shift which is between 800 MHz and up to 1.1 GHz. Relatively, this gap might represent a large frequency shift in general, however, this could be negligible in higher frequencies applications.

Below in Fig. 144, some comparisons between simulated and measured reflection coefficients for the proposed and assessed DRAs are presented, these correspond to (a) the solid block, and the hollowed DRAs containing (b) air and (c) silk sericin gel.

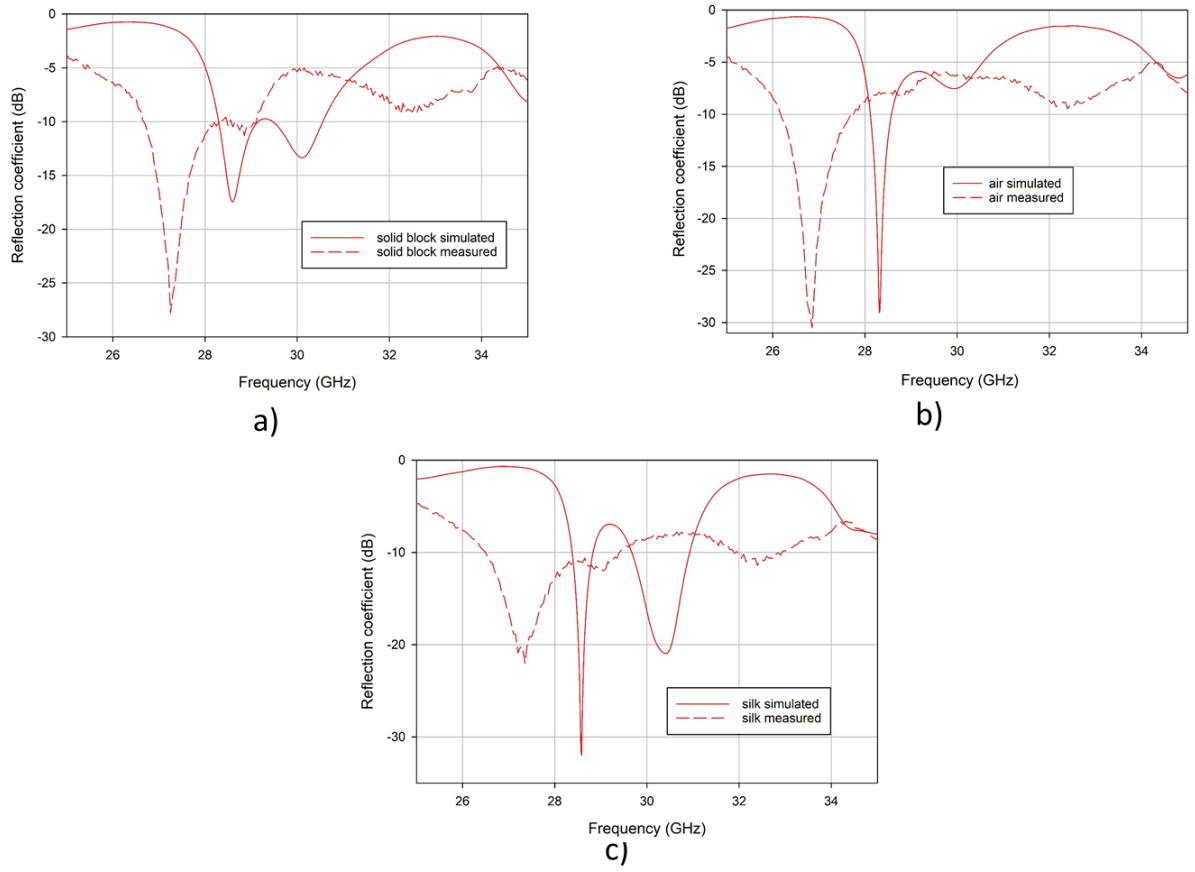

Fig. 144 Comparison between simulated and measured 3D-Printed DRAs.

The observed comparisons presented the previously discussed frequency shifts for each of the figures. The difference between simulated and measured antennas are probably originated by the 3D-Printing process for each of the resonators. The printed DRAs visibly present some wrinkles in the surface, due to the manufacture itself, while in simulation, the surfaces are ideally smooth. This could be potentially improved with higher precision 3D-printing incorporating smoothing techniques.

There are a set of unassessed electrical properties of graphene oxide that remain without a proper study. This Thesis has based the frequency reconfiguration in the response of an amount of GO in the presence of an external signal. However, there is little certainty of electrical properties e.g. relative permittivity and how it changes in the presence of different voltages. Some authors have estimated the ratio voltage – εr for a given concentration of graphene as a rise of 2 in the permittivity every 5.0 V [116]. This was taken as a reference for the development of the experimental protocol discussed in this section, however, the concentration of the liquid and gels derived from GO would definitely differ as this parameters were set for graphene, rather than for graphene oxide.

Nevertheless, this is a starting set of data that could help future development. In Fig. 145 is presented a comparison between the simulations and measurements for the tunable DRAs following the references previously discussed. There is a nearly negligible tuning in the measured S-Parameters compared to the evident tuning in simulation. Again, this is a subject to further development as there is limited information on the graphene oxide concentrations and additional parameters.

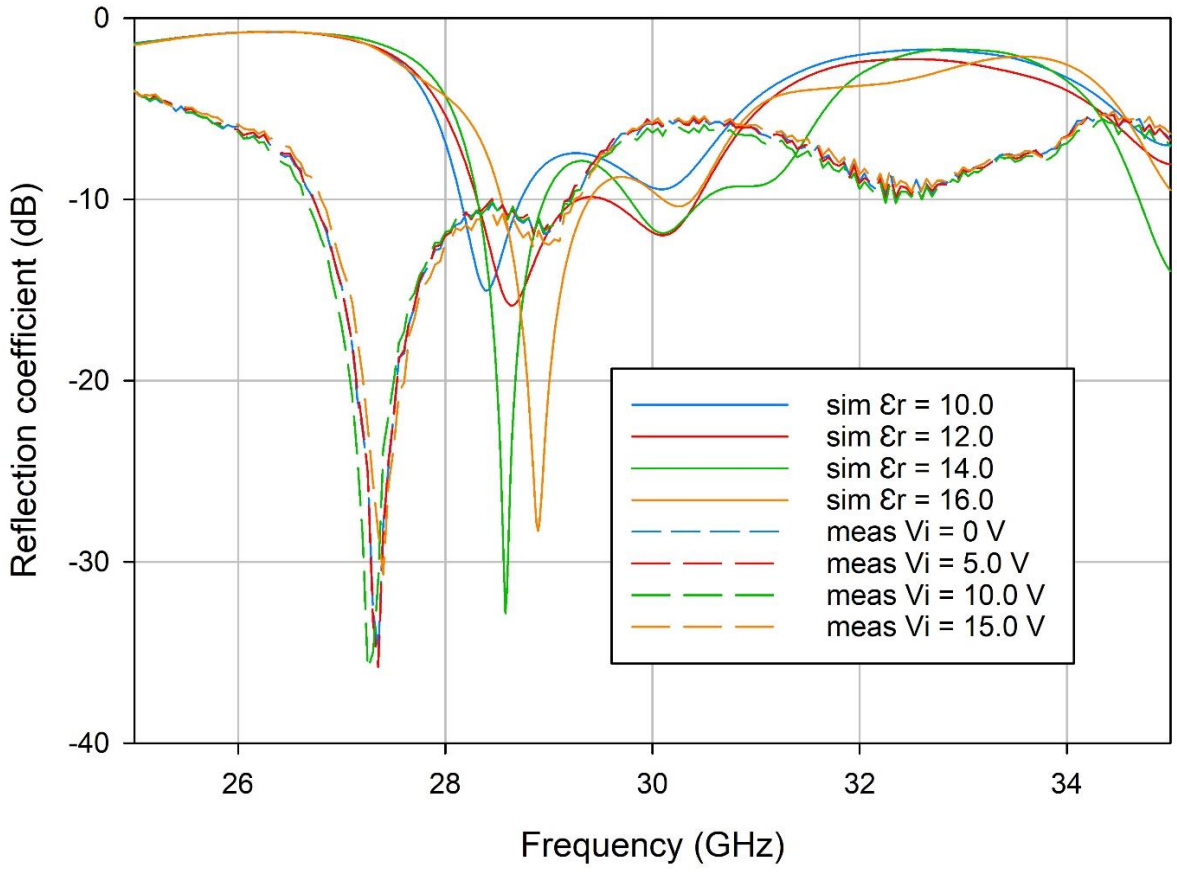

Fig. 145 Comparison between simulated and measured tuning ranges for 3D-Printed DRAs.

5.5.3. Measured radiation patterns for 3D-Printed RDRAs.

As the radiation patterns are essential metrics for the valuation of the antenna performance not only for dielectric resonator antennas but also for antennas in general, we also proceeded to carry out the measurements of radiation patterns using the mm-wave laboratory in the communications group of the University of Sheffield, recently inaugurated in 2019. This novel cutting-edge equipment is designed to perform measurements of radiation patterns at high frequencies up to 110 GHz. Similar to the anechoic chamber that performs radiation patterns measurements showed in Fig. 78, the mm-wave chamber has a reference antenna that radiates toward the antenna studied in question, however, it varies its position aided by a robotic arm that evaluates the radiation over 180º. As an additional note, gain was not possible to be determinate by this system as it still needs a significant amount of calculations and configurations to be put in place. In Fig. 146 the anechoic chamber of the mm-wave laboratory, in which the measurements were carried out, is presented in (a) as well as one of the proposed DRAs put in position for measurements in (b).

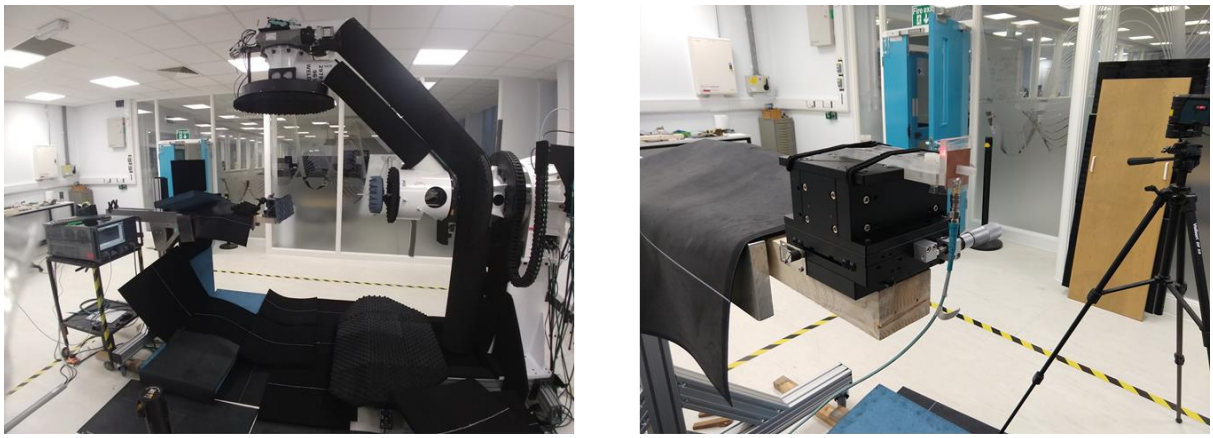

Fig. 146 Antenna measurement system of mm-wave state of the art laboratory of the University of Sheffield.

The measurements of the radiation patterns for the proposed DRAs previously analysed were carried out for their frequency response and using their respective resonant frequencies to determine the radiation pattern at that specific frequency. The analysed prototypes in the mm-Wave laboratory were the solid DRA, the hollowed DRA, the DRA filled with silk sericin gel, the DRA filled with graphene oxide solution and this last with the addition of electrodes attached to its outer walls.

Overall, the measured radiation patterns presented typical metrics for dielectric resonant antennas, which correspond to a main lobe with high radiation intensity in the direction of the propagation and secondary lobes with lower intensities compared to the main one. This typical reflected radiation is due to the coupling aperture and the ground plane acting as a reflector. In Fig. 147, the measured normalised radiation patterns in its polar form for (a) XZ plane and (b) YZ plane for the proposed solid DRA are presented.

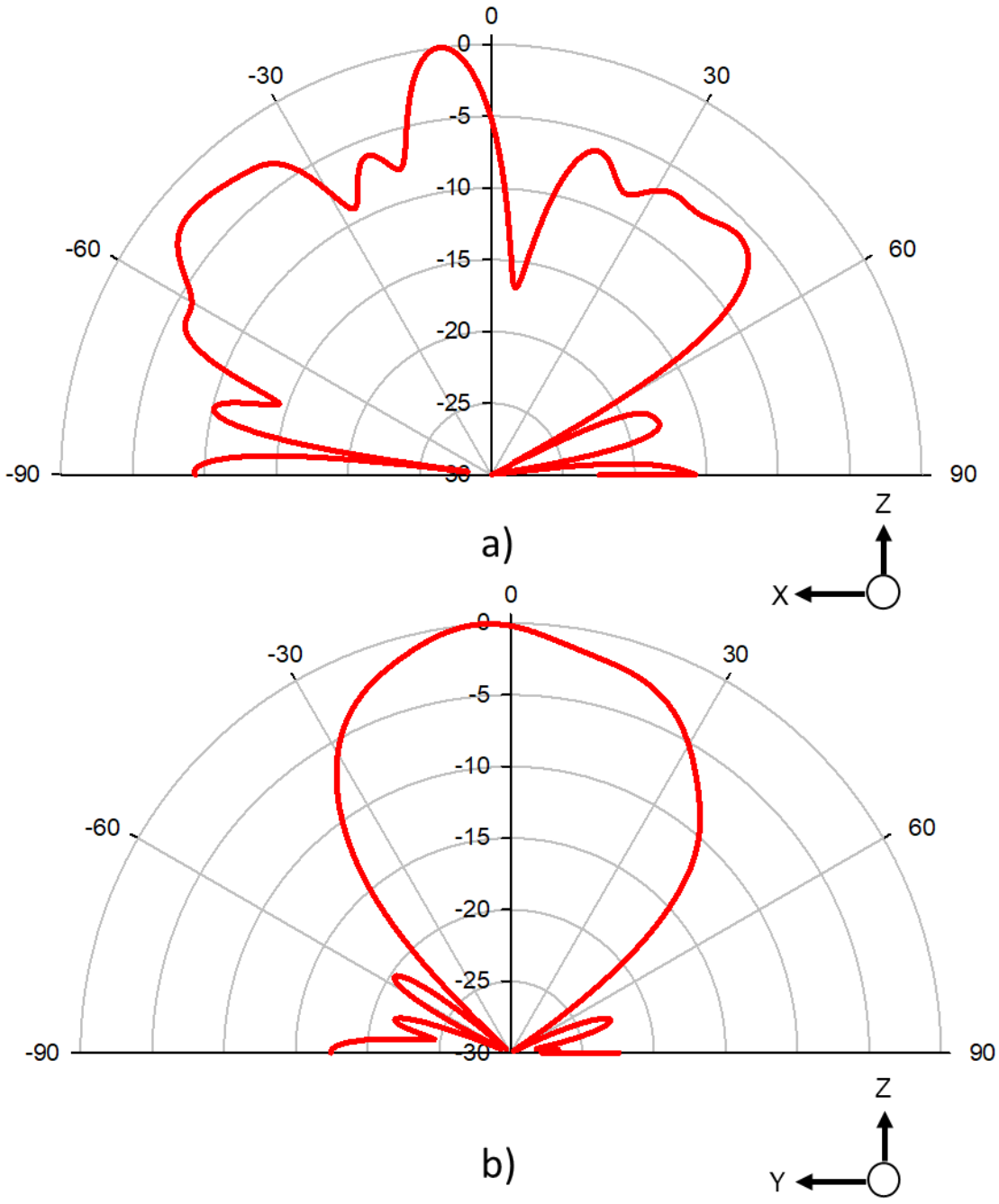

Fig. 147 Measured normalised radiation patterns for DRA solid block at 27.3 GHz

As the solid DRA presented typical shapes for dielectric resonant antennas, then the respective measurements were carried out for the hollowed DRA containing only air in its cylindrical cavity where also a high gained main lobe is observed, as well as the secondary lobes. However, and as expected, these patterns are not resembling to the measured ones for the solid DRA. This is presented in Fig. 148 for its (a) XZ plane and (b) YZ plane.

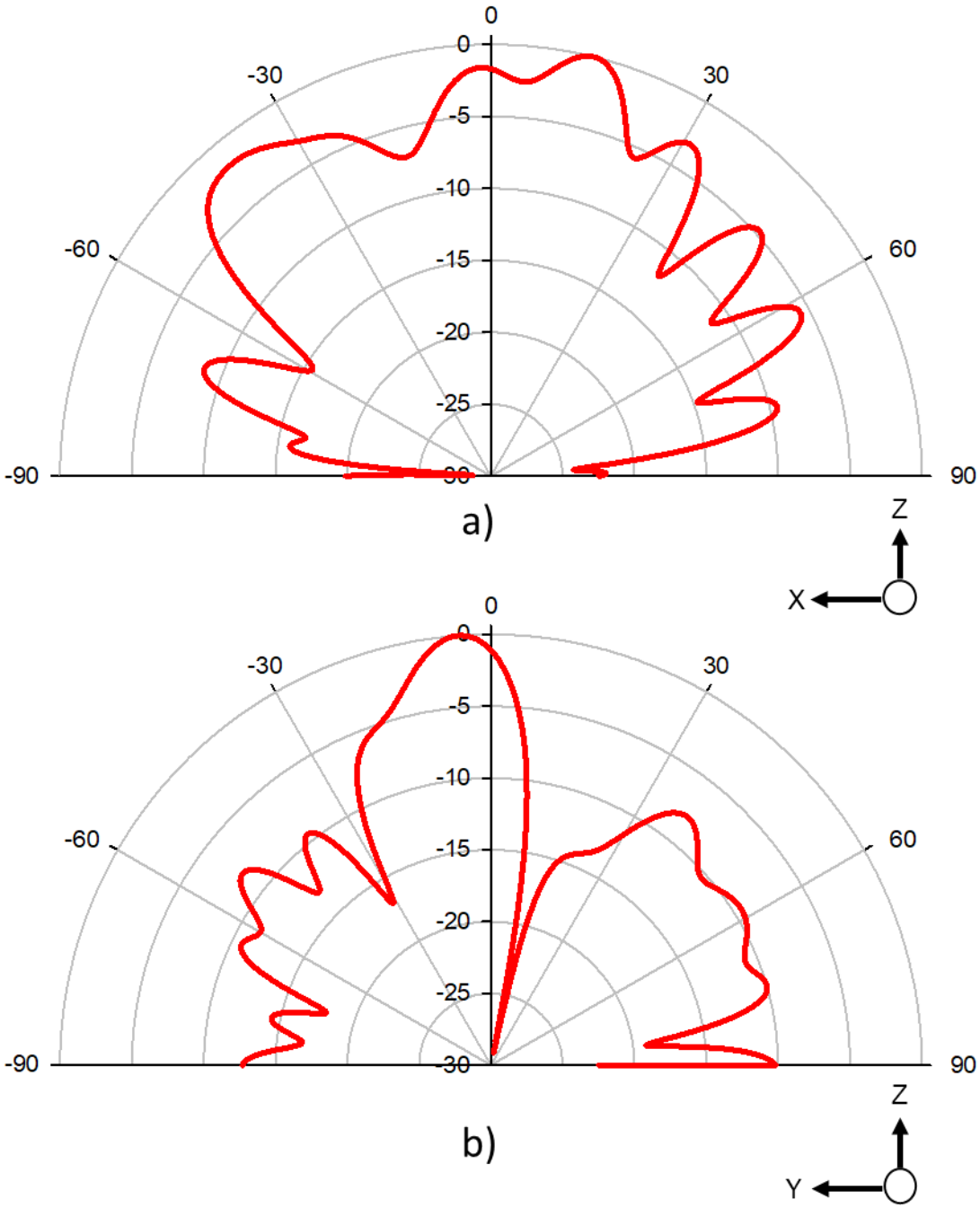

Fig. 148 Measured normalised radiation patterns for hollowed DRA at 27.9 GHz.

Now regarding the filled proposed prototypes, the DRA filled with silk sericin gel was analysed. As this was the least efficient material analysed in terms of frequency response, a typical DRA radiation pattern was not expected to be observed in practice, which was corroborated by the readings presented in Fig. 149 where an oddly shaped main lobe in the direction of propagation are observed as seen in (a) for its XZ plane and (b) for its YZ cut.

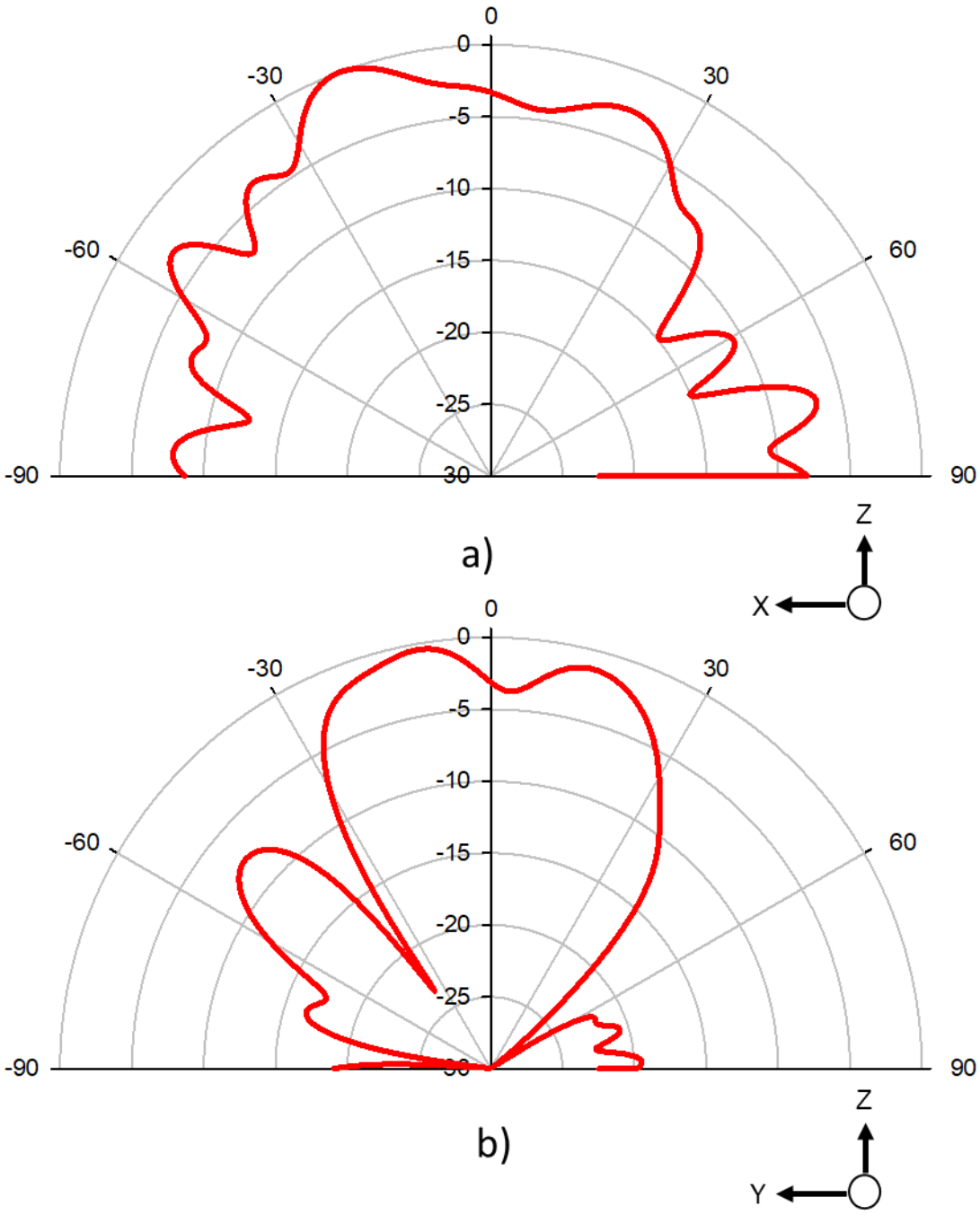

Fig. 149 Measured normalised radiation patterns for DRA filled with silk sericin gel at 27.9 GHz.

Further on filled DRAs, the radiation patterns for the DRA filled with graphene oxide liquid were suited in the mm-Wave laboratory. The measured radiation patterns for this prototypes are presented in Fig. 150 (a) XZ cut and (b) YZ cut where a main lobe is perfectly observed and their respective side lobes. This measurement might be slightly affected by a thin parafilm placed on top of the dielectric resonator to avoid leakages of graphene oxide fluid due to the position of measurement.

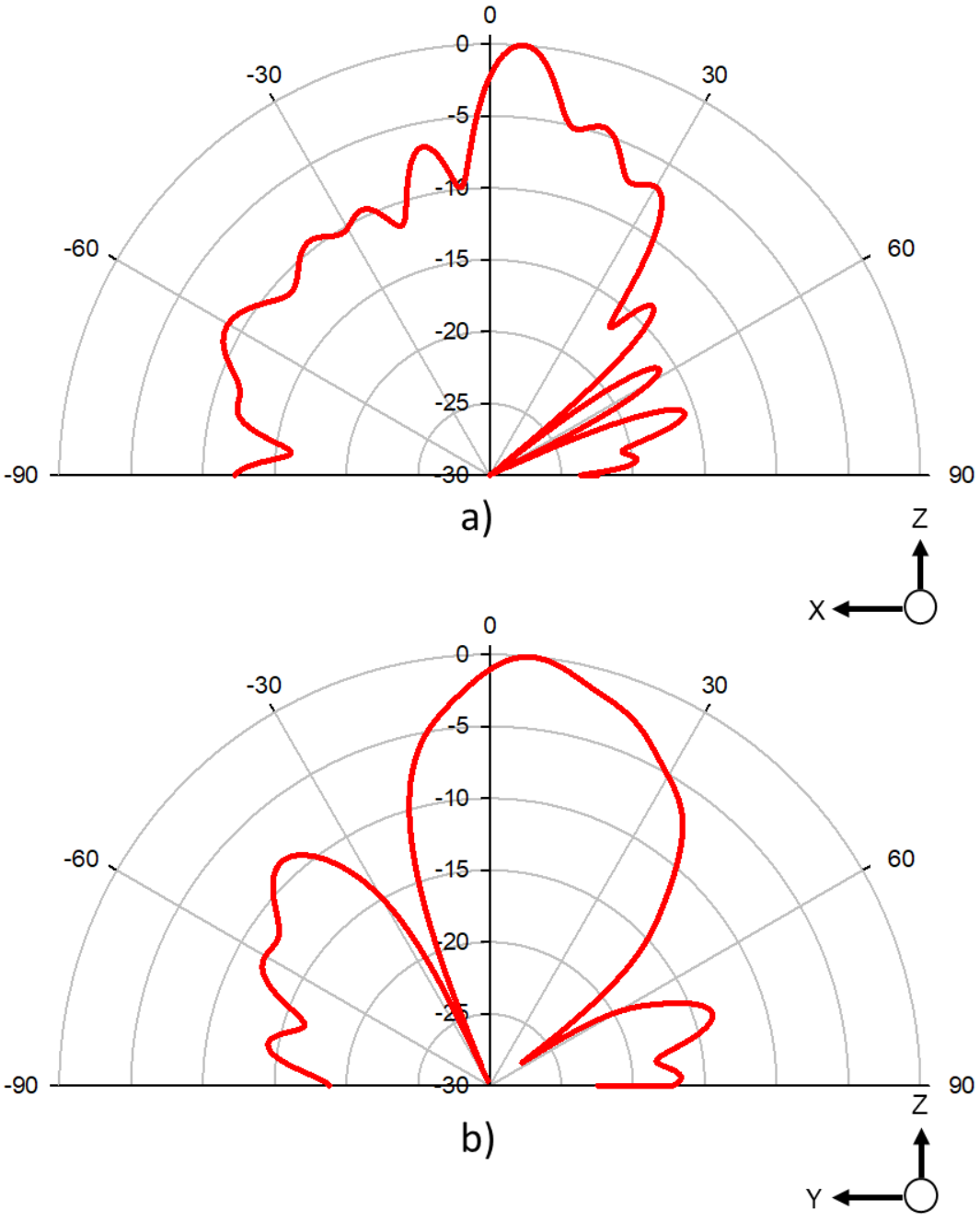

Fig. 150 Measured normalised radiation patterns for DRA filled with liquid graphene oxide at 27.8 GHz.

Finally, for the measurement of radiation patterns, those corresponding to the DRA filled with graphene oxide solution are presented. This prototype now incorporates with a set of metallic electrodes attached to its external walls. These readings are presented in Fig. 151 where slight differences with respect to Fig. 150 can be observed. This corroborates in practice the low interference of the metallic patches acting as electrodes in the performance of the DRA.

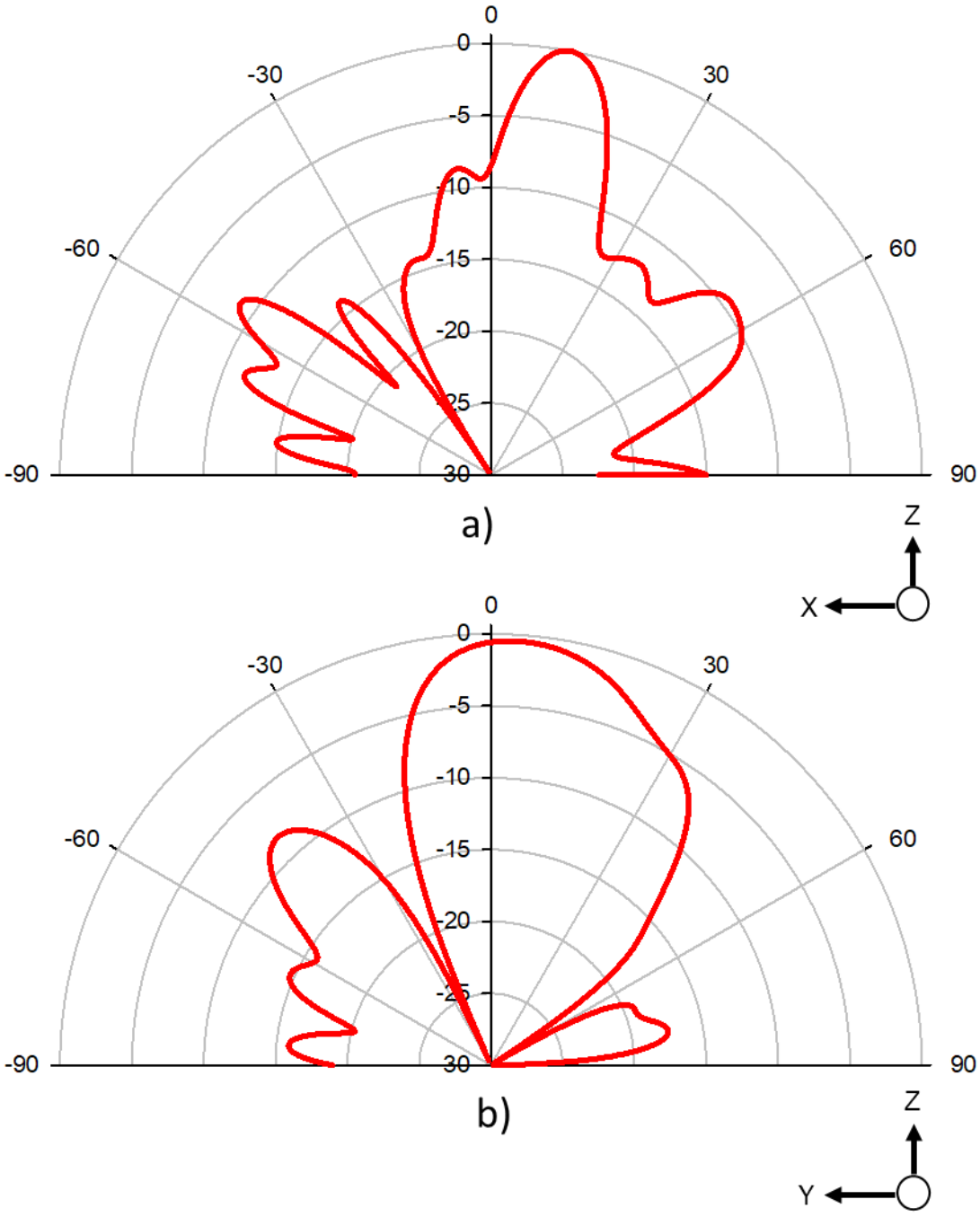

Fig. 151 Measured normalised radiation patterns for DRA filled with graphene oxide liquid and electrodes in their walls at 27.6 GHz.

5.6. Conclusions for Chapter 5

In conclusion for this chapter, a set of potentially reconfigurable dielectric resonant antennas were discussed. These proposed antennas used novel materials that are not commonly applied in communications engineering and possess high potential for cutting edge adaptive devices if further study is carried out basing on the presented results for the proposed devices.

Environment-friendly bioplastics that are not commonly used in industry for communications engineering have proved to be suitable as dielectric resonant antennas which normally are made of high precision ceramics that elevates the cost of production for these antennas. The assessment for PLA as DRA material was supported by the observed resonant frequencies and appropriate antenna metrics for the proposed antennas. This not only proved that reduction of costs is achievable but also eco-friendly biodegradable bioplastics can be used for the manufacture of mobile communications devices suitable for 5G applications in mm-wave.

Innovative, versatile materials such as graphene proved to be compatible when incorporated to the developed DRA technology. The DRAs filled with GO presented appropriate readings for reflection coefficients and radiation patterns. However, as the tuning range achieved did not represent a significant range for mm-wave frequencies, many more parameters must be further assessed in order to refine and improve the presented results such as a proper estimation of the dielectric permittivity and other electric parameters. The variables on which graphene oxide depends, such as concentration, must be analysed more in depth. As well as the preparation for suitable forms of graphene oxide such as gels or colloidal suspensions containing an appropriate concentration of this material in its pure form are also some of the parameters that must be analysed further with a view to obtain significant tuning ranges in mm-wave frequencies.

In terms of the measured and simulated performances for the proposed DRAs, typical metrics for dielectric resonant antennas were observed. A good agreement between the simulated and measured radiation patterns was presented. This agreement no only corroborates the accuracy of CST Microwave Studio in terms of estimate essential antenna metrics, but also helps to conclude on the suitability for PLA as dielectric resonant antenna material which will reduce the costs of manufactures for mobile communication equipment and will introduce environmental and eco-friendly bioplastics that will help to achieve sustainably developed antennas.

CHAPTER 6. CONCLUSIONS AND FUTURE DIRECTIONS.

In this thesis, two types of frequency reconfigurable antennas were discussed using innovative techniques and materials. A set of three prototypes for 1×2 MIMO reconfigurable triple-slotted antennas and a dielectric resonator antenna with frequency tuning were designed, simulated, manufactured, and measured.

Prior to the development of the developed prototypes discussed, a comprehensive literature review was presented in Chapter 2 involving frequency reconfigurable antennas using active components and arrays of DRAs, as well as the theoretical fundamentals for slot antennas and dielectric resonant antennas. Also, essential theoretical background on dielectric resonant antennas was discussed. Then in Chapter 3, the design steps were discussed for the proposed prototypes of 1×2 MIMO triple-slotted antennas including the computer-assisted design using CST Microwave studio, the simulated models, frequency responses and radiation patterns as well as the measured metrics. A study on the spatial diversity scheme introduced in the designed MIMO antennas was discussed in Chapter 4 where essential metrics helped to determine the suitability for the proposed prototypes in MIMO for 5G. Finally, in Chapter 5, the design, simulations, manufacture, and measurements for frequency reconfigurable dielectric resonant antennas were presented. The proposed prototypes successfully incorporated the use of 3D-Printing bioplastics, forms of graphene oxide and other materials with different relative permittivities.

The designs presented in this Thesis were assessed in terms of suitability in applications for 5G mobile communications. The MIMO triple-slotted prototypes have presented independent tunable frequency bands and showed good MIMO diversity metrics which determined the independence between the two antennas in each board. Moreover, the designed dielectric resonant antennas discussed offered good antenna performances that correspond to typical DRA reflection coefficients and directive radiation patterns in the direction of propagation, proving that a bioplastic such as polylactic acid (PLA) is a low-cost alternative material for the fabrication of dielectric resonant antennas that will be introduced in the foreseeable future as sustainable development for mobile communication devices that are biodegradable. Also, an innovative material such as graphene oxide was successfully introduced in the structure of the proposed DRAs as this material offers numerous advantages for adaptive performance which is a desirable feature for 5G requirements.

6.1. Multiband independently tunable MIMO antennas.

The designed MIMO prototypes discussed in Chapter 3 and 4 offered beneficial performances in terms of radio agility and adaption. Each antenna was formed by an array of three slot antennas loaded with varactor diodes that control their resonant frequency. The main feature for these proposed adaptive antennas is the independent frequency tuning achieved from slot to slot and from antenna to antenna in each board. It was observed in simulated and measured reflection coefficients for the three proposed prototypes that if a frequency band is tuned in question, then the remaining frequency bands do not present any alteration. This behaviour was observed for each of the two triple-slotted antennas in each board.

The independent frequency tuning for the three offered bands in each antenna are achieved by varactors incorporated in each slot. This incorporation offers a continuous tuning of the resonant frequencies of the slot by varying the capacitance of the varactors. The control of the frequency range is carried out by an electric tuning signal i.e. a DC biasing voltage. The frequency tuning is proportional to the characterisation of the varactor Infineon BB833 in terms of the ratio voltage – capacitance. The assessment of the frequency response assessed a range of resonances from 650 MHz to 2.8 GHz with potential applications in the commercial spectrum, i.e. Wi-Fi, Bluetooth, etc.

The proposed MIMO prototypes offered typical radiation patterns for slot antennas with omnidirectional shapes. Consequently, relatively low gains have been observed for measured radiation patterns for these antennas. Given that two sets of antennas are coexisting in the circuit board, it was imperative to carry out a diversity analysis offered in terms of radiation patterns. The coverage from one antenna to other represented little pattern diversity for MIMO 1 and 2 given the patterns are similar since the set of slots are placed in symmetrical positions but in opposite ends of the board. However, MIMO 3 presented the most remarkable pattern diversity of the three prototypes. MIMO 3 was a prototype designed to analyse the lateral positions of the triple-slotted antennas, which corresponded to antenna 2 in this case. Overall, the designed MIMO antennas offered good agreement between simulations and measurements for reflection coefficients and radiation patterns. These metrics support the classification of these antennas as suitable devices for radio frequency agile applications. The conferences proceedings for Loughborough Antennas Propagation Conference 2018 included a publication of this work.

6.1.1. MIMO and diversity metrics for independently tunable 1×2 triple-slotted antennas MIMO 1, 2 and 3.

Given the MIMO prototypes designed in Chapter 3 had introduced a spatial diversity scheme, a study in diversity metric for these antennas was in order and was carried out in Chapter 4. As two sets of slots are placed in each board with different positions, a study on the correlation levels between antennas has been carried out by determining diversity metrics such as envelope correlation coefficients (ECC) and diversity gains (DG) for the antennas 1 and 2 for each board. These metrics were supported by the study of antenna isolations through the analysis of transmission coefficients S_{21}. The correlation levels observed for each board corresponded to undesired high numbers in low frequencies where Slot 1 started to offered matched resonant frequencies, however for frequencies above 750 MHz the correlation coefficients presented appropriate numbers below the borderline value required for optimal low correlations in MIMO systems. Moreover, the diversity gains analysed for the MIMO prototypes presented ideal gains near the desired 10 dB for frequencies above 750 MHz similar to the range where the optimal correlation coefficients have been observed. Based on the DG metrics observed, these proposed MIMO prototypes reduce the power when needed since a diversity scheme has been introduced

Moreover, the simulated and measured isolations in S-Parameters supported the suitability of these prototypes for MIMO applications, as the mutual couplings S_{12} and S_{21} determine more detailly the independence between antennas. Appropriate readings for isolation were observed for frequencies above 750 MHz which correspond to the higher frequencies of Band 1 and the full range of Band 2 and Band 3. Further to spatial diversity, in the analysis of radiation patterns for the proposed MIMO 3 presented diversity in the measured radiation patterns for the two antennas in the board. Pattern diversity is potentially applicable in 5G.

Overall, a good agreement between measurements and simulations has been observed, except for frequencies above 2.6 GHz where unexpected peaks ere observed in the measured ECCs and DGs. This difference between simulations and measurements observed in the comparisons presented in the corresponding sections are caused by external interferences affecting the performance of the board. This suggests that an evident improvement must be carried out to the shielding implemented to the boards, specially to avoid the RF effects of the DC biasing cables, as well as the SRF from the components. Modifications to polarisations and space between antennas could significantly reduce the correlations between antennas.

6.2. 3D printed frequency reconfigurable DRA using bioplastics and graphene oxide.

For the presented dielectric resonant antenna in Chapter 5, innovative, versatile and adaptive novel materials have been assessed in simulation and then incorporated in practice for the fabrication of the proposed DRAs. The use of polylactic acid (PLA) in the manufacture of dielectric resonant antennas has been discussed as an alternative approach for dielectric resonators. A detailed analysis of the simulated and measured metrics for the proposed DRAs support the suitability of these materials. Also, the assessment suggests future directions basing on the presented works. These presented DRAs are based on biodegradable ecological and environmental-friendly bioplastics and include low-cost alternatives for graphene production which highlights these devices as low-cost and sustainable solutions for mobile communications in 5G capable of operate in mm-wave frequencies Solid and hollowed DRAs have been presented in this chapter and proved to be suitable for mm-wave applications as their respective antenna performances corroborated it. The hollowed DRAs were analysed for their antenna performances where they were filled with other PLAs with different permittivities as well as silk sericin gel and graphene oxide facilitated by the chemical and biological engineering department (CBE).

The use of innovative cutting-edge materials such as graphene turned the proposed DRAs as a capable of frequency tuning achieved by the alteration of the material using an external electrical signal. Although the achieved tuning range was not significant in higher frequencies, it was proved that graphene oxide forms assessed are altered in the presence of an electric field given the nanotubes-based internal structure is rearranged near a signal of this nature. Moreover, graphene oxide is presented to be a low-cost alternative for graphene, as it offers all the advantageous properties typical of graphene but significantly reduces costs of production and turns it as a financially sustainable alternative for commercial products. Further and essential information regarding the material compositions, specifically, the concentration quantities of the graphene oxide solutions could be beneficial in future directions taking the presented work as a starting point. Further on material improvements, a refinement in the manufacture procedure of the dielectric resonator is desirable in future works, specially the soothing of the s2D-Printing surface which will be closer to the expected resonances obtained in the mathematical design and supported by the simulations.

6.2.1. 3D printing of dielectric resonant antennas using bioplastics and their performance.

The introduction of PLA in the manufacture of dielectric resonant antennas is an innovative approach presented in this work, sustainable bioplastics derived from plants, have proved to be suitable in the fabrication of dielectric resonators as they have provides simulated and measured metrics that agree on optimal performances mm-wave frequencies. By the use of more bioplastics such as PLA, the manufacture of dielectric resonators will not only be benefitted from the suitability in terms of antenna performance but also in the ease of construction that can potentially replace the use of expensive ceramics that provide similar performances to the numbers offered by the proposed DRAs. Although ceramics provide a high quality and accuracy in terms of the antenna metrics when used as DRA as they are the most commonly used in this kind of antennas, the production costs remain very high and take large amounts of time to order specific equipment for specialised applications. However, with the introduction of PLA as DRA material, these costs can be significantly reduced as not only PLA offers a quick biodegradation and easy recycling but also provides a quick and effective manufacture time assisted by the innovative 3D printing production process.

6.2.2. Frequency reconfiguration for 3D printed dielectric resonant antennas using innovative materials presenting different relative permittivities.

Further on the dielectric resonant antennas proposed in Chapter 5, the use of materials that have offered good results when used in medicine, biology, mechanics and architecture was discussed. Such as the silk sericin gel that filled the cylindrical cavity of the proposed dielectric resonator. Silk sericin gel is a material typically used as a dielectric absorber, however, it has been used previously as sensor in electronics engineering and having a relative permittivity within the studied range of dielectrics analysed for this work, its use as resonant material for mm-wave frequencies was analysed and it was determined that the suitability for this material is adequate as its corresponding metrics suggested in simulation and in measurements. Moreover, the use of two presentations of graphene oxide, in liquid fluid and in a colloidal gel, not only proved to be suitable materials for a dielectric resonant antenna as their numbers in antenna performance showed that they can achieve optimal metrics but also achieved a frequency tuning in presence of an electric field brought to the DRA walls by an external set of biasing DC voltage lines.

Although the tuning range did not represent significant frequency reconfiguration, it is appropriate to point out that graphene oxide depends on a large number of variables that have not been specified by a manufacturer as this substance has been produced empirically in a laboratory and there was little certainty on electric parameters. Essential information must be specified with certainty such as the essential dielectric permittivity that the dielectric resonant antennas base their resonant frequencies on. However, the use of external agents such as an electric signal bringing an electric field between two opposite walls in the DRA will rearrange an amount of graphene oxide has been supported by simulations and measurements. Moreover, in order to achieve this alteration, the use of miniaturised metallic patches attached to the DRA walls and acting as electrodes has been carried out, proving that there is little affectation in the antenna performance despite the addition of small metallic parasitic elements at high frequencies for mm-wave applications. By benefitting from further investigation, the proposed DRAs can be fully suitable for 5G communications equipment as well as the base of future directions of frequency reconfigurable DRAs.

6.3. Future directions for the presented work.

Given the discussed and analysed devices designed in this thesis presented appropriate performances in terms of typical antenna metrics, there is the potential application for these devices in future mobile communications equipment ready to be used in the next generation 5G. Despite the proposed antennas presented appropriate numbers in terms of frequency responses and radiation patterns, suggested improvements are recommended to be carried out in order to achieve devices that will guarantee the minimal possible disadvantages for antenna metrics. The suggested recommendations discussing the improvement of shielding, refinement in the manufacture process and appropriate assessment of material properties are essential in the development of further work based on the devices presented in this Thesis.

The proposed triple-slotted antennas MIMO 1, 2 and 3 presented appropriate reflection coefficients and radiation patterns, however, for the diversity parameters, further improvement can be carried out, which can be an opportunity to refine the metrics by increasing the isolation between antennas with a view to reduce their correlations between antennas. Also, in order to obtain optimal correlation levels, one can extrapolate the triple slotted-antennas and develop the design of a board with four or more resonant slots operating at higher frequencies, having as precedent the assessed results in terms of correlation and diversity gains that have been observed in this Thesis.

Concerning the potentially reconfigurable dielectric resonator antenna, the use of PLA as dielectric resonant material has been proved. However, the use of more bioplastics or microwave-improved materials such as PTFE (commonly known as Teflon) could be a promising research opportunity to further development. Such material has been widely implemented in microwave engineering applications and is an available filament optimised for 3D-Printing production. Moreover, in terms of electrically tunable substances, the use of graphene oxide can be further investigated by specifying essential electric parameters aided by a proper characterisation of its fundamental metrics such as a good estimation of the dielectric constant or relative permittivity. Production variables such as concentration, presentation, or dispersion in certain solutions are equally important to specify prior to the development of future works. Graphene oxide is a promising material that will offer large amounts of technological solutions in the future when investigated more in depth. Although graphene oxide is an innovative modern and versatile material. A possible future direction for this project could be the use of other substances that alter their internal performance in presence of electric fields, ferromagnetic materials or liquid crystals can be investigated in the proposed devices delivered in this Thesis.

APPENDIX A: COMPARISONS BETWEEN SIMULATED AND MEASURED REFFLECTION COEFFICIENTS FOR MIMO 1, 2, 3 AND DRAS.

In this section, a compilation of graphs is presented comparing the simulations obtained with CST Microwave Studio against the measured data obtained in the facilities of the University of Sheffield, specifically, the reflection coefficients. These comparisons include the results for the three prototypes of 1×2 MIMO slot antennas discussed in Chapter 3 and the dielectric resonator antennas discussed in Chapter 5.

Tripe-slotted antennas MIMO 1, 2 and 3.

The reflection coefficients for Antennas 1 and 2 for each prototype comparing simulated vs measured results. Each of the following figures presents the simulated S_{11} or S_{22} parameters and their corresponding measured results. Overall, the agreement between simulations and measurements is good for each of the presented comparisons where the solid lines correspond to the simulated data and the dashed lines to the measured results.

MIMO 1

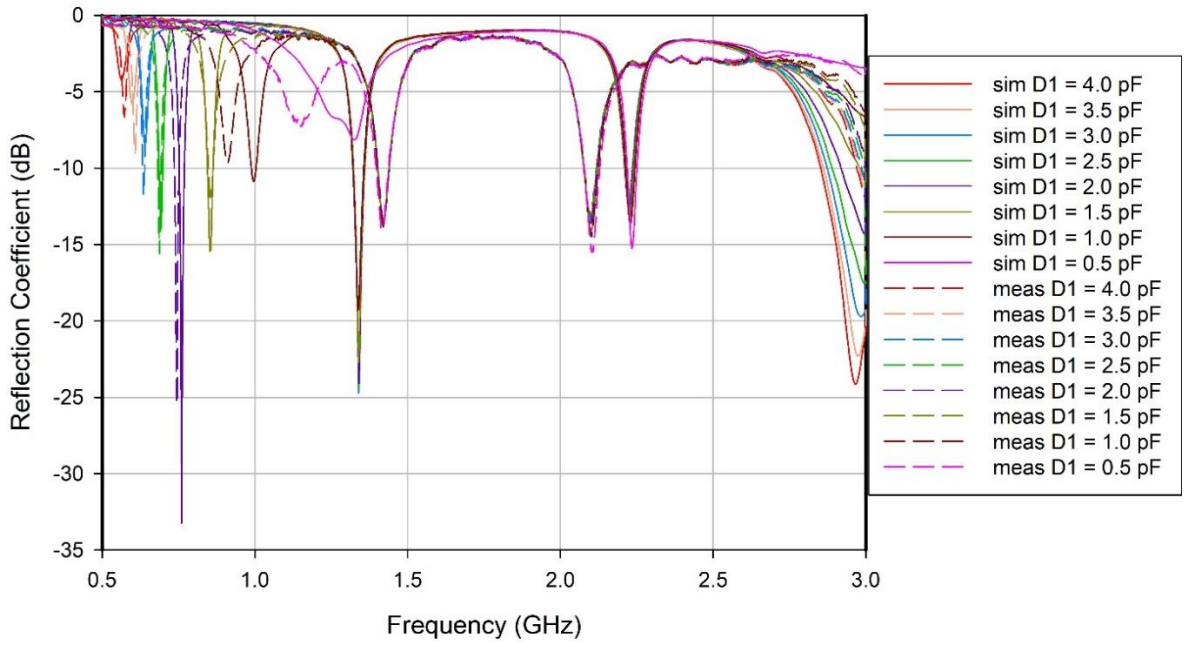

Fig. 152 Comparison between simulated and measured reflection coefficients for MIMO 1, Antenna 1 tuning D1.

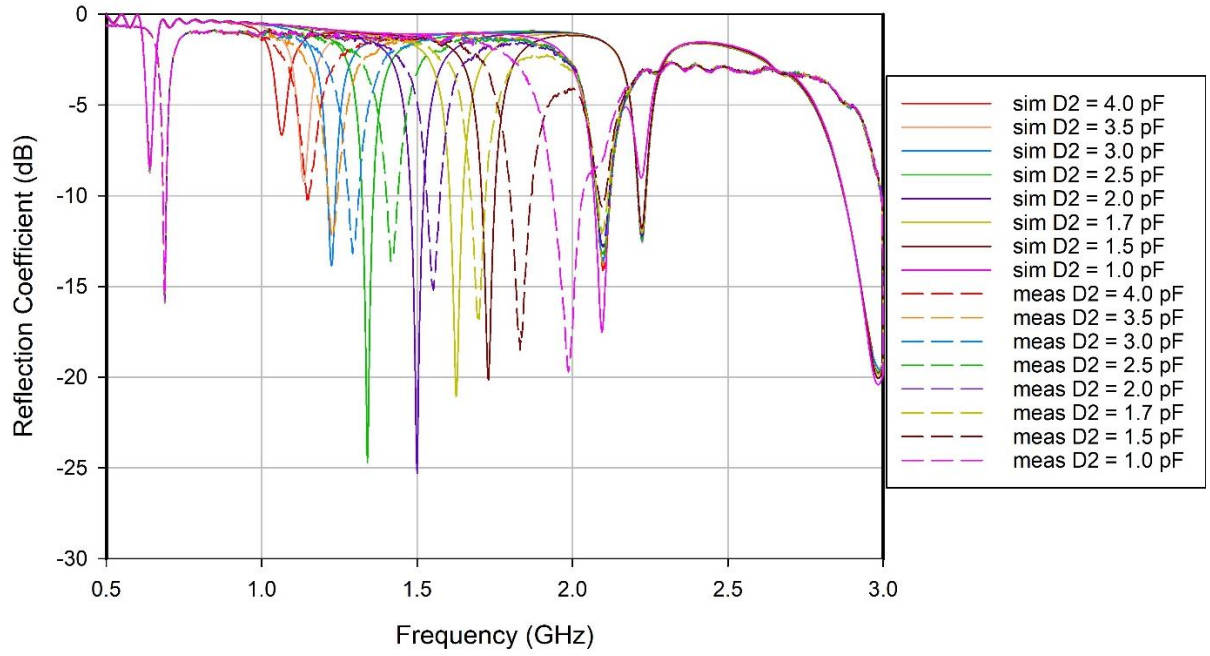

Fig. 153 Comparison between simulated and measured reflection coefficients for MIMO 1, Antenna 1 tuning D2.

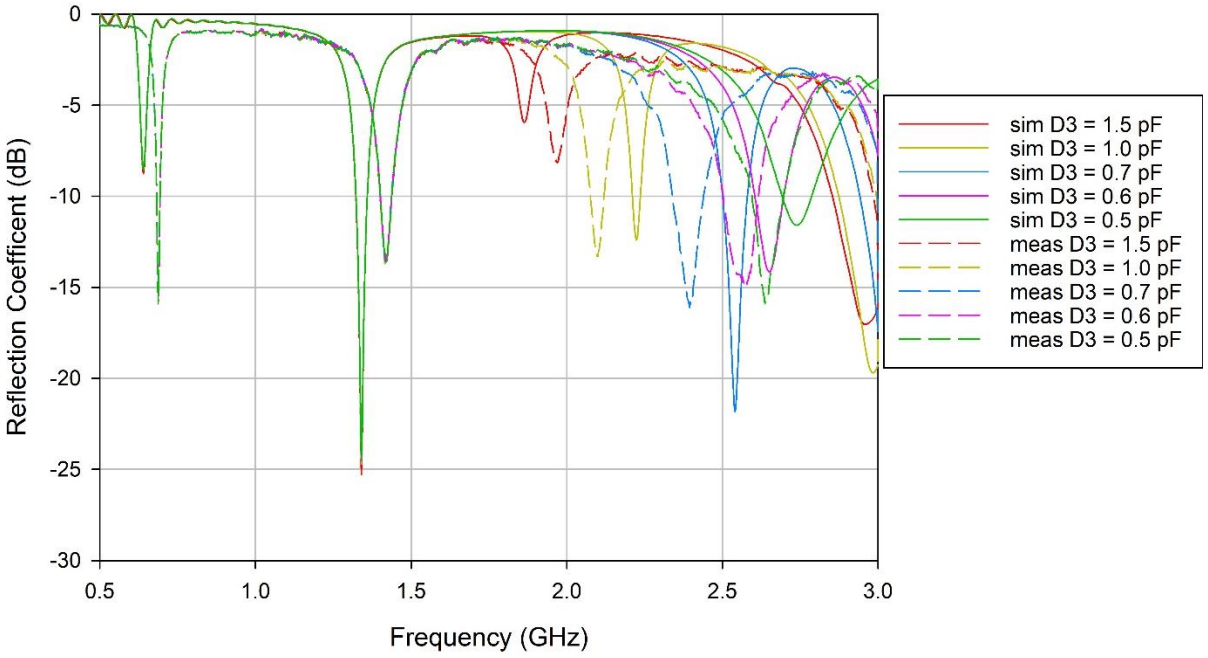

Fig. 154 Comparison between simulated and measured reflection coefficients for MIMO 1, Antenna 1 tuning D3.

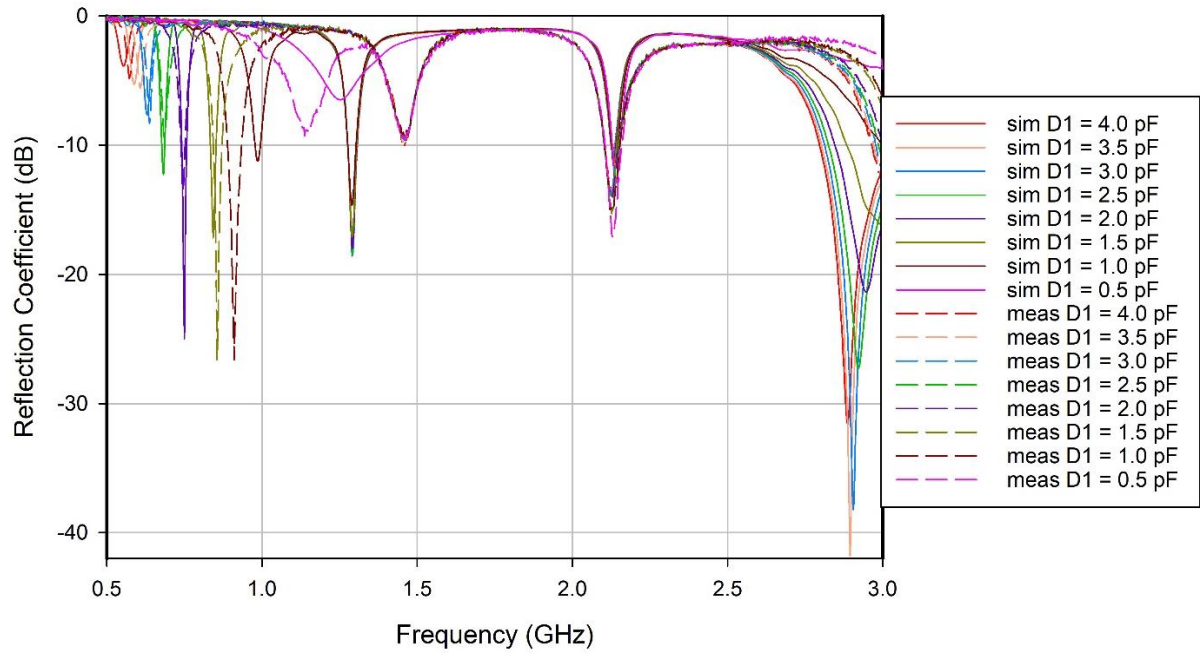

Fig. 155 Comparison between simulated and measured reflection coefficients for MIMO 1, Antenna 2 tuning D1.

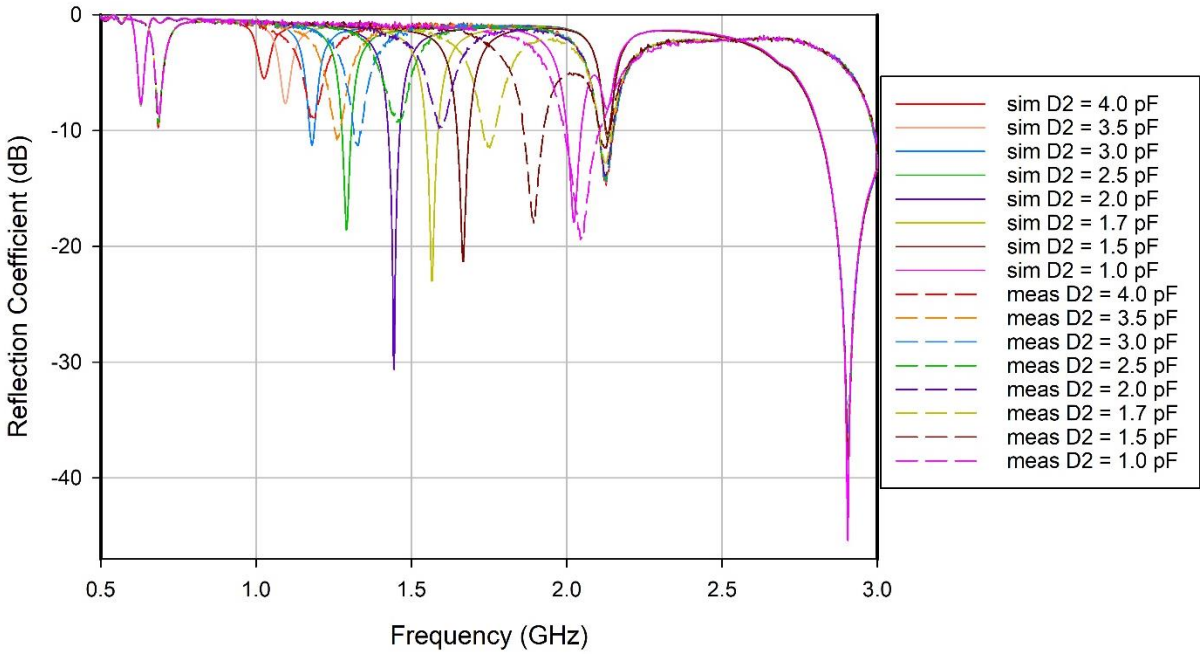

Fig. 156 Comparison between simulated and measured reflection coefficients for MIMO 1, Antenna 2 tuning D2.

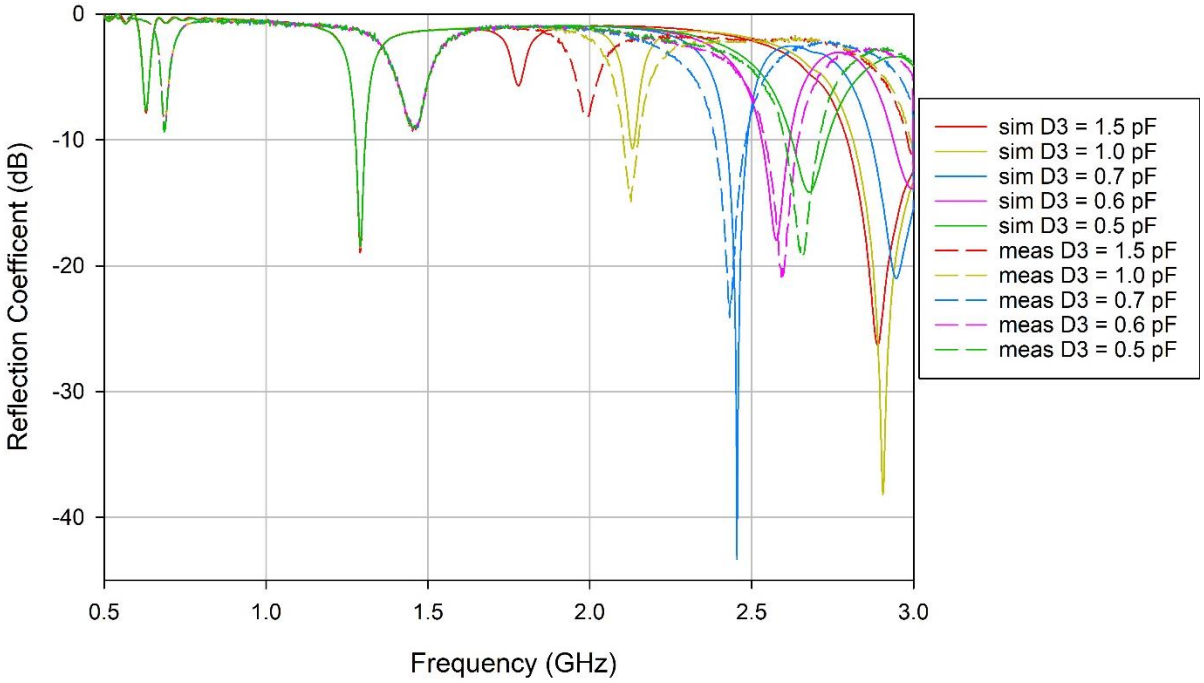

Fig. 157 Comparison between simulated and measured reflection coefficients for MIMO 1, Antenna 2 tuning D3.

MIMO 2

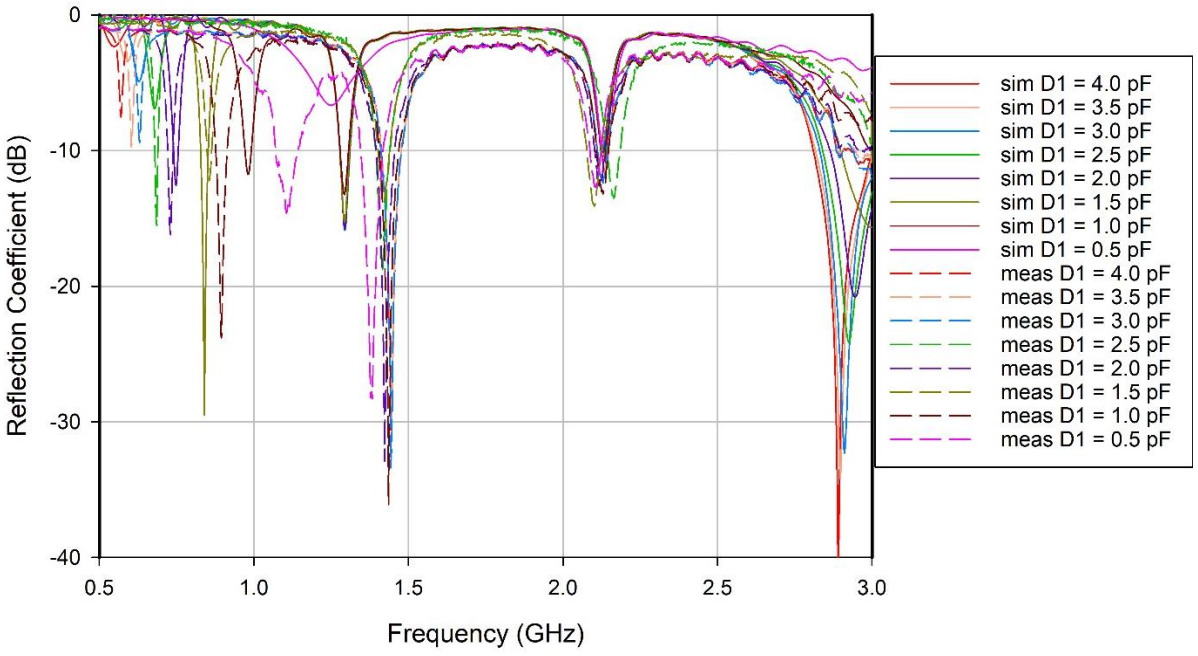

Fig. 158 Comparison between simulated and measured reflection coefficients for MIMO 2, Antenna 1 tuning D1.

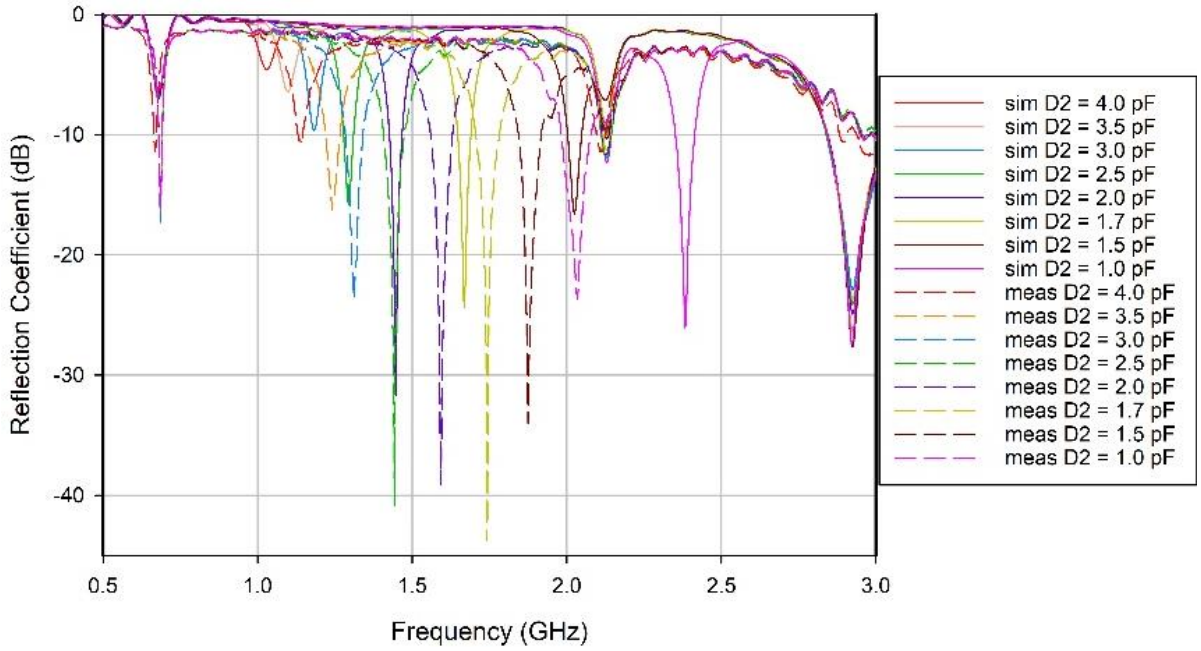

Fig. 159 Comparison between simulated and measured reflection coefficients for MIMO 2, Antenna 1 tuning D2.

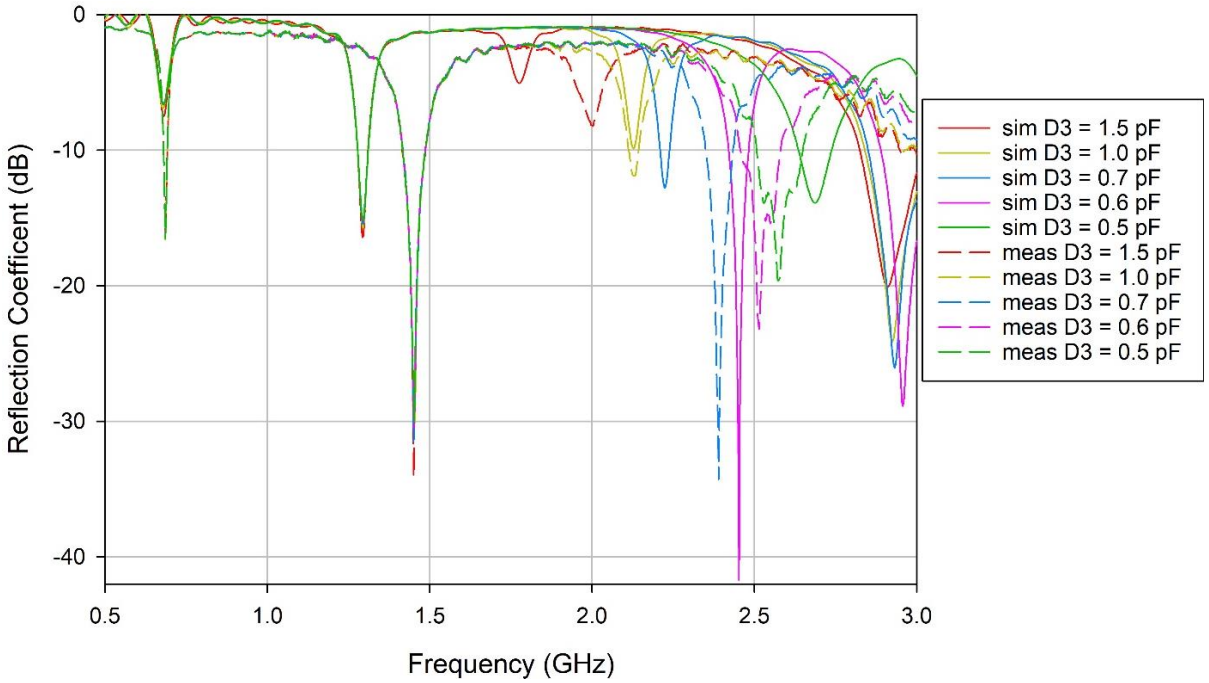

Fig. 160 Comparison between simulated and measured reflection coefficients for MIMO 2, Antenna 1 tuning D3.

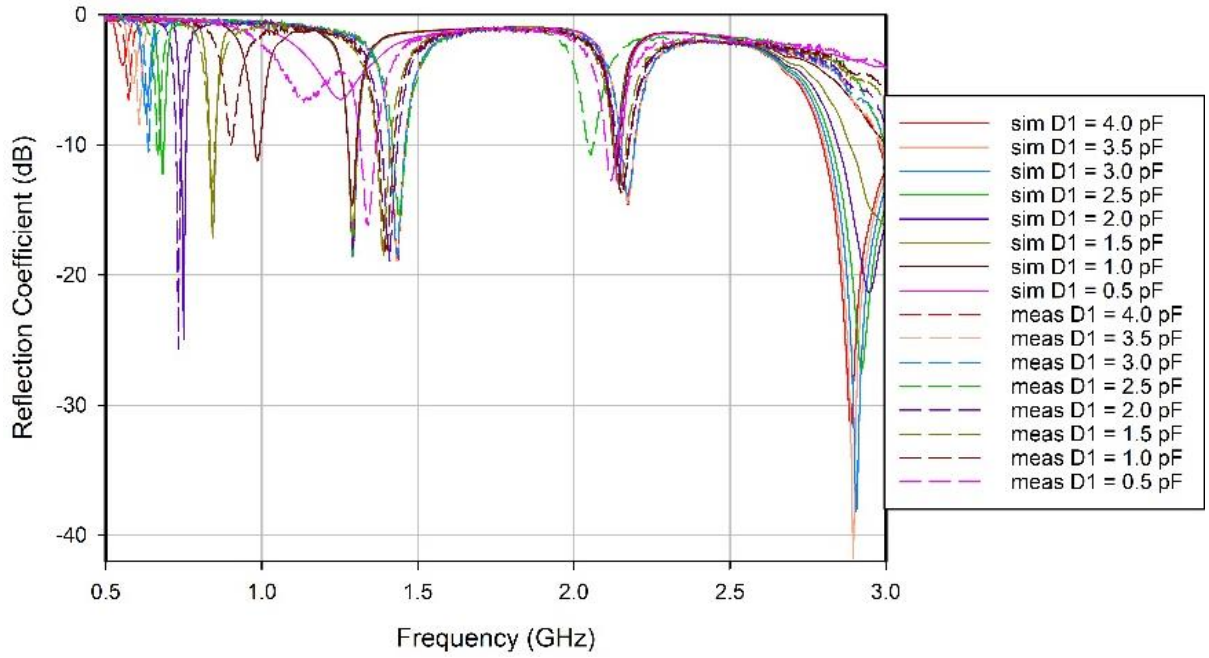

Fig. 161 Comparison between simulated and measured reflection coefficients for MIMO 2, Antenna 2 tuning D1.

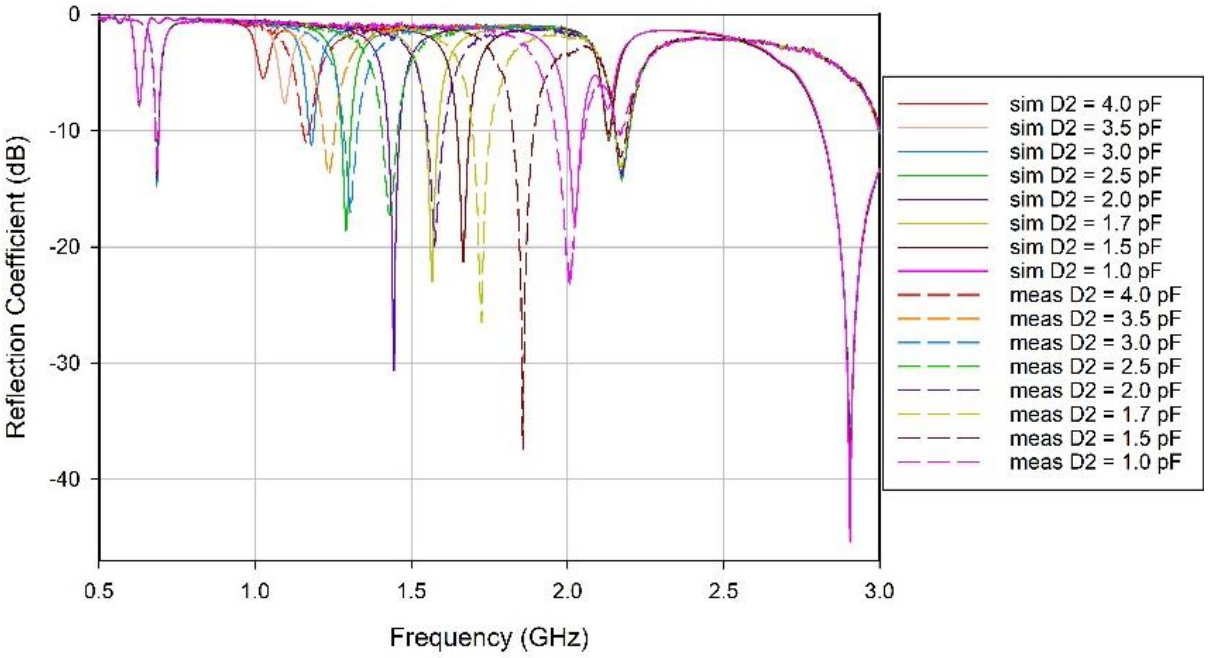

Fig. 162 Comparison between simulated and measured reflection coefficients for MIMO 2, Antenna 2 tuning D1.

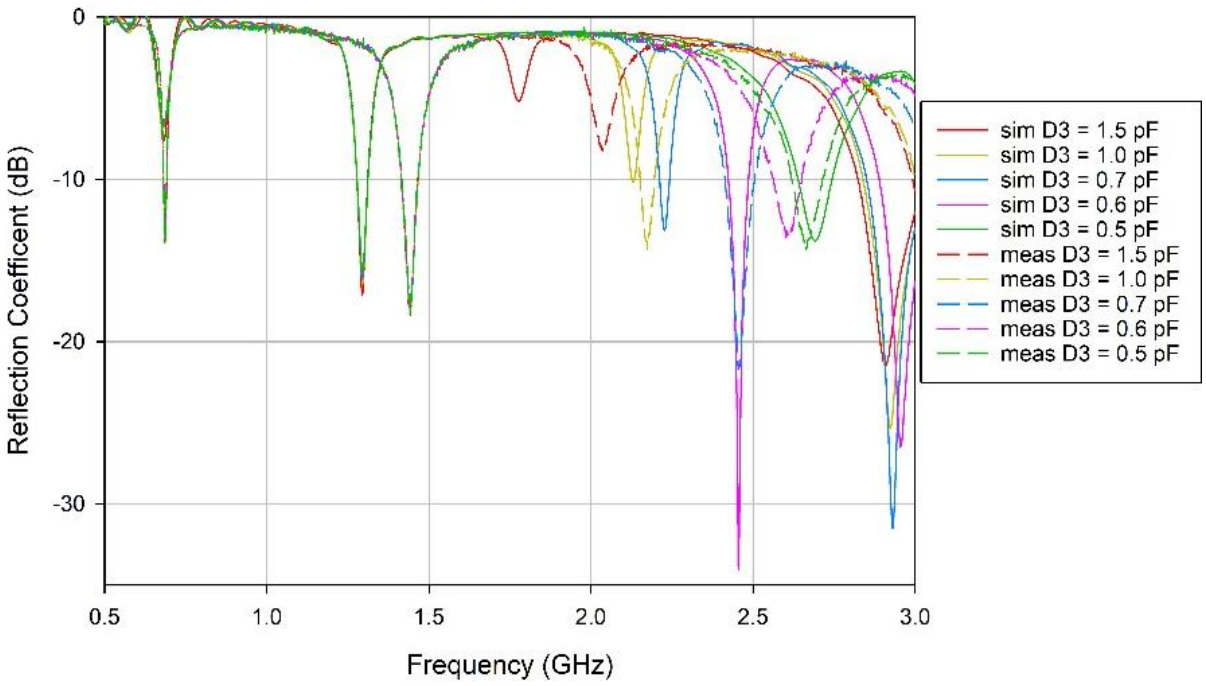

Fig. 163 Comparison between simulated and measured reflection coefficients for MIMO 2, Antenna 2 tuning D1.

MIMO 3

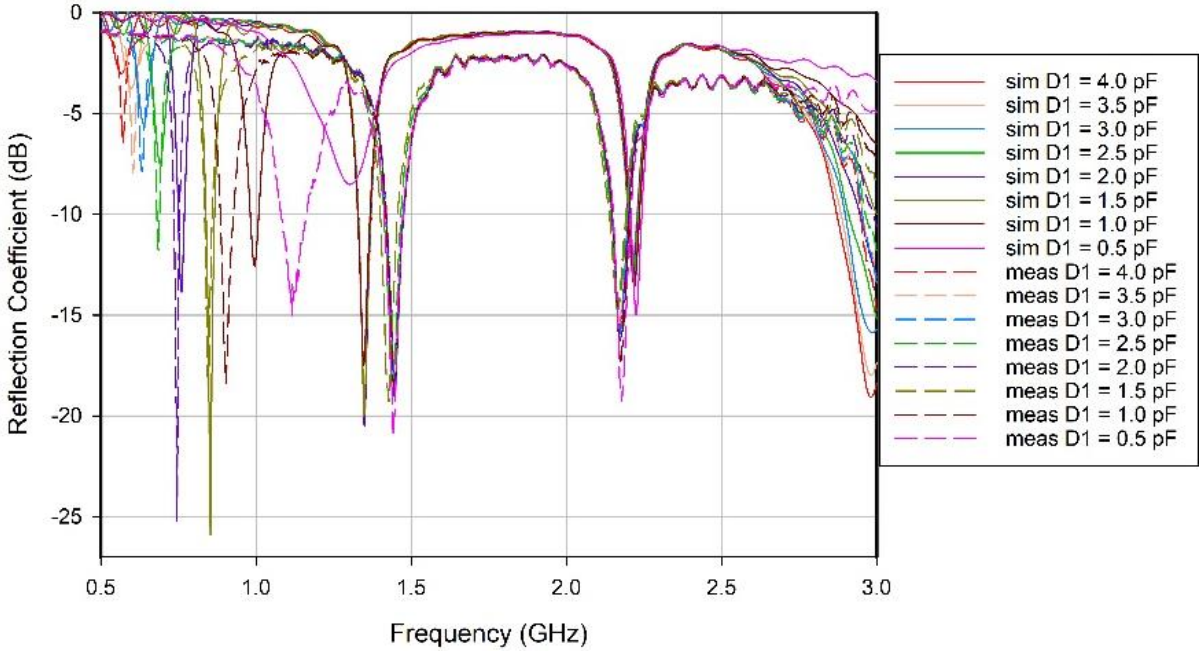

Fig. 164 Comparison between simulated and measured reflection coefficients for MIMO 3, Antenna 1 tuning D1.

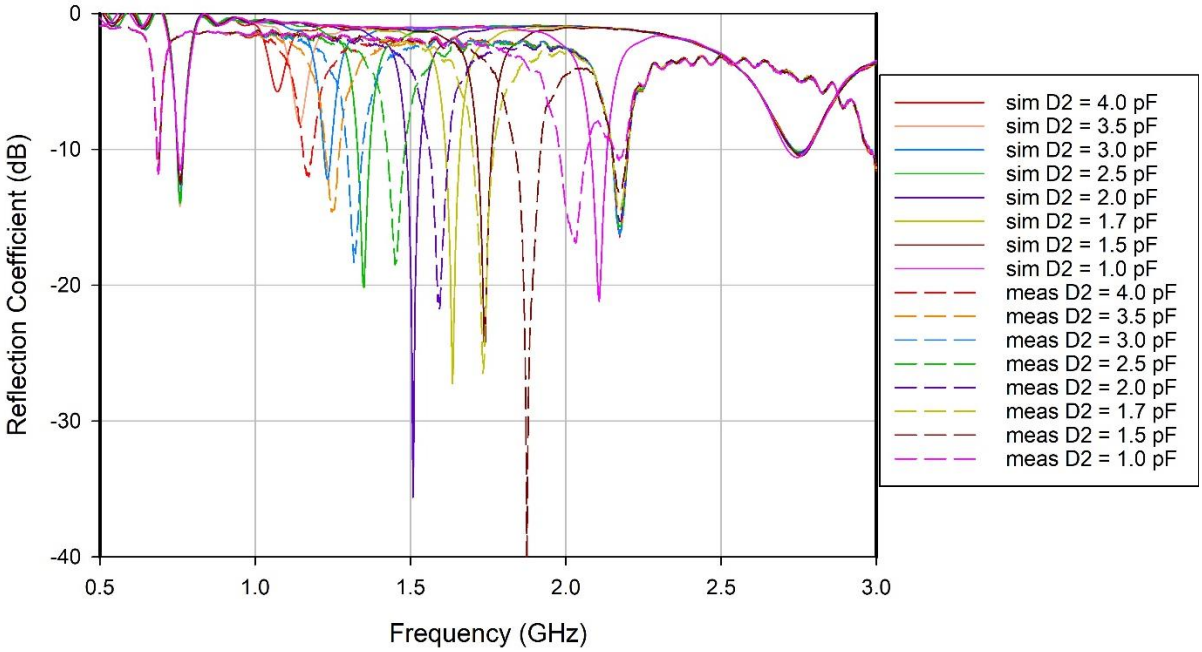

Fig. 165 Comparison between simulated and measured reflection coefficients for MIMO 3, Antenna 1 tuning D2.

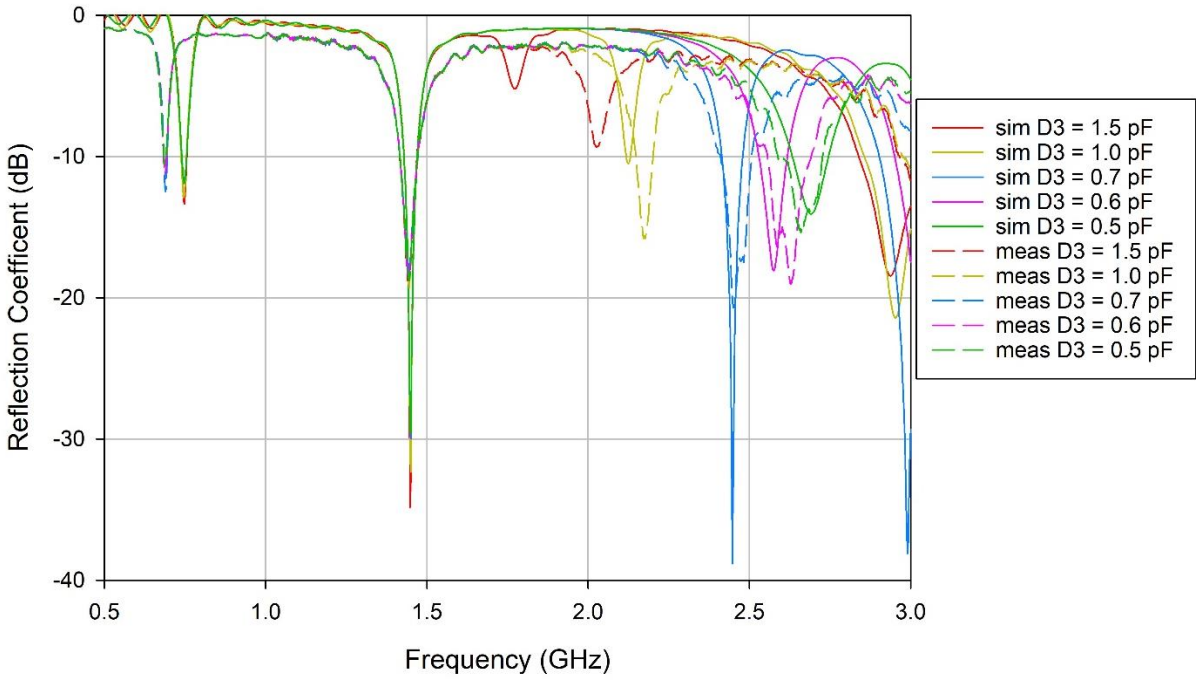

Fig. 166 Comparison between simulated and measured reflection coefficients for MIMO 3, Antenna 1 tuning D3.

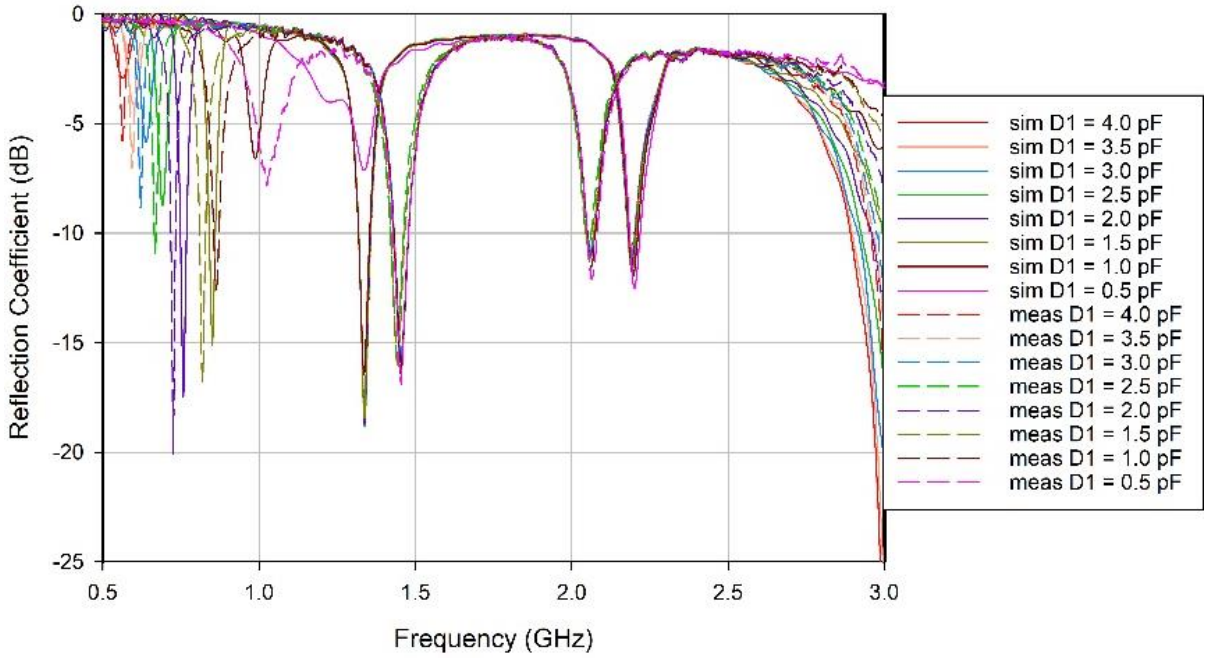

Fig. 167 Comparison between simulated and measured reflection coefficients for MIMO 3, Antenna 2 tuning D1.

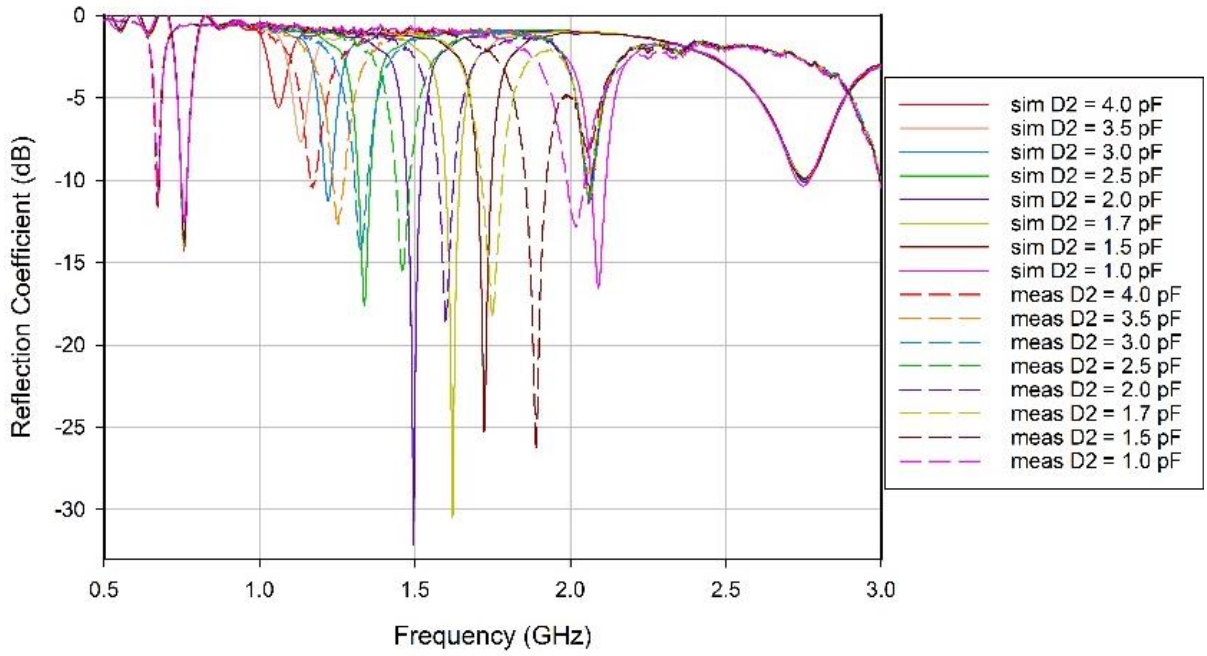

Fig. 168 Comparison between simulated and measured reflection coefficients for MIMO 3, Antenna 2 tuning D2.

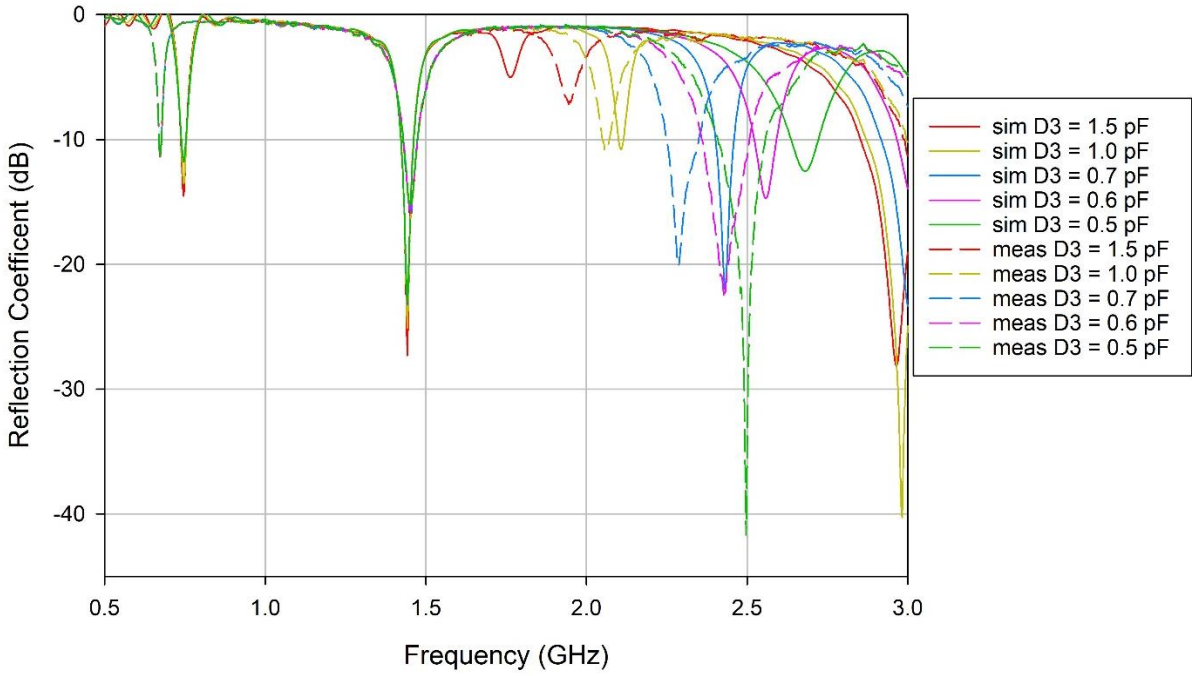

Fig. 169 Comparison between simulated and measured reflection coefficients for MIMO 3, Antenna 2 tuning D3.

Dielectric resonant antennas filled with different elements.

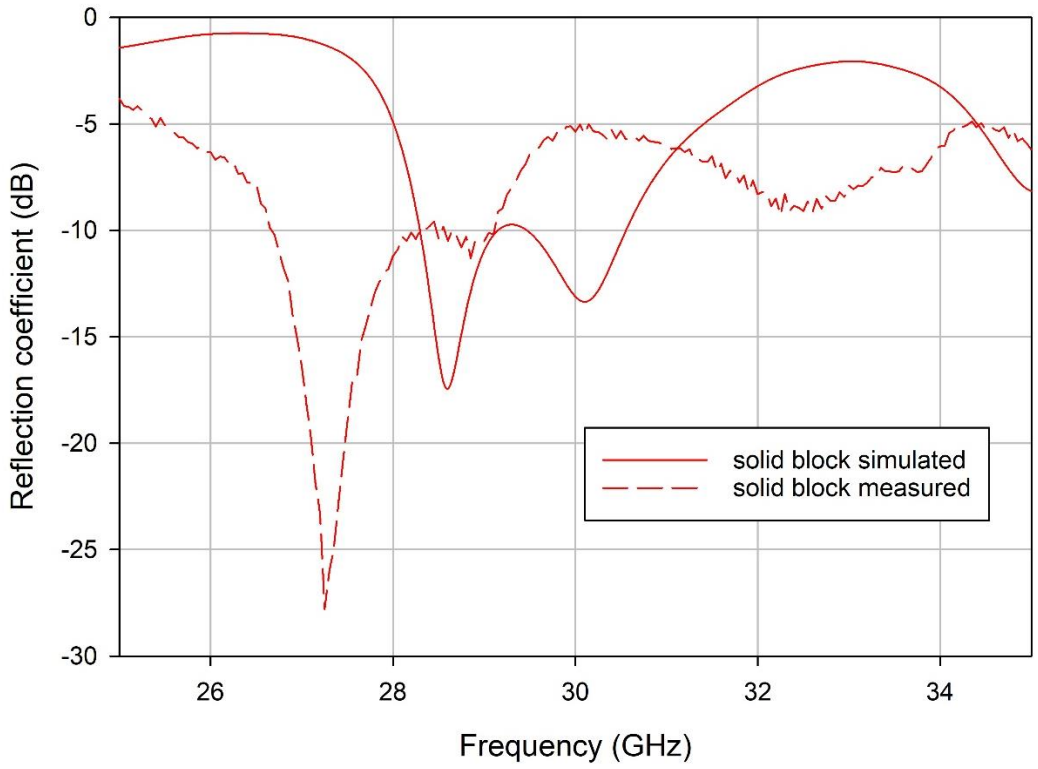

Fig. 170 Reflection coefficients simulated vs measured for solid DRA.

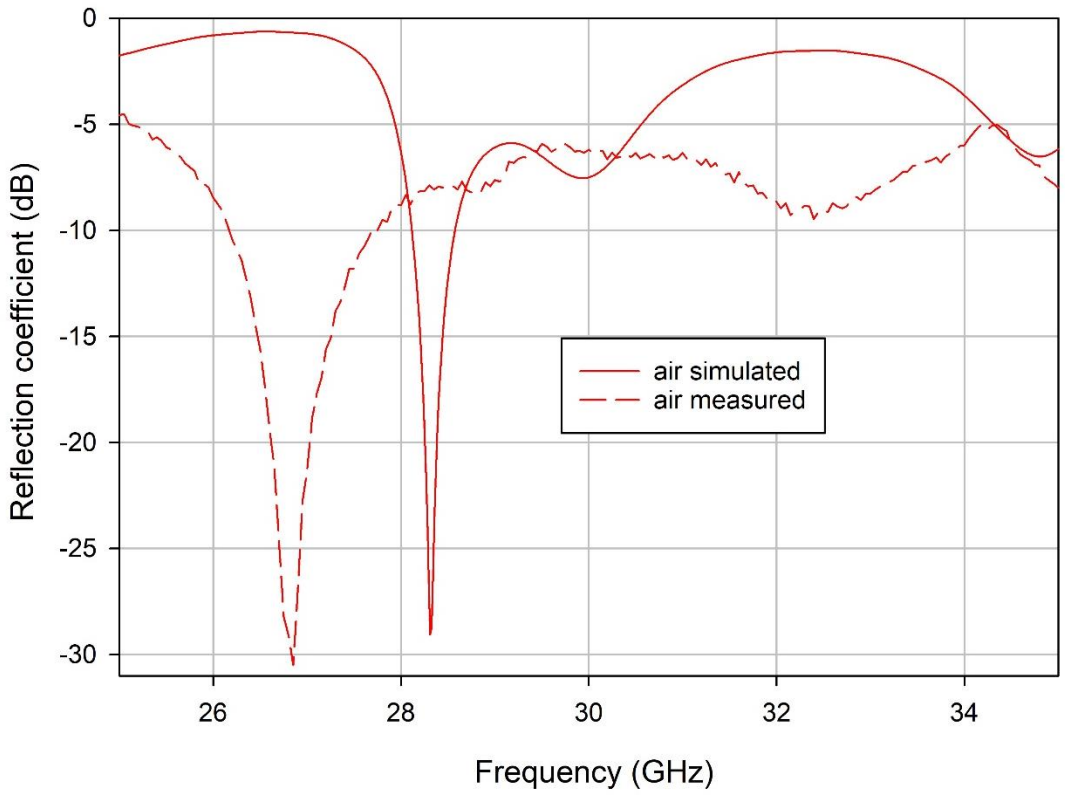

Fig. 171 Reflection coefficients simulated vs measured for hollowed DRA containing air.

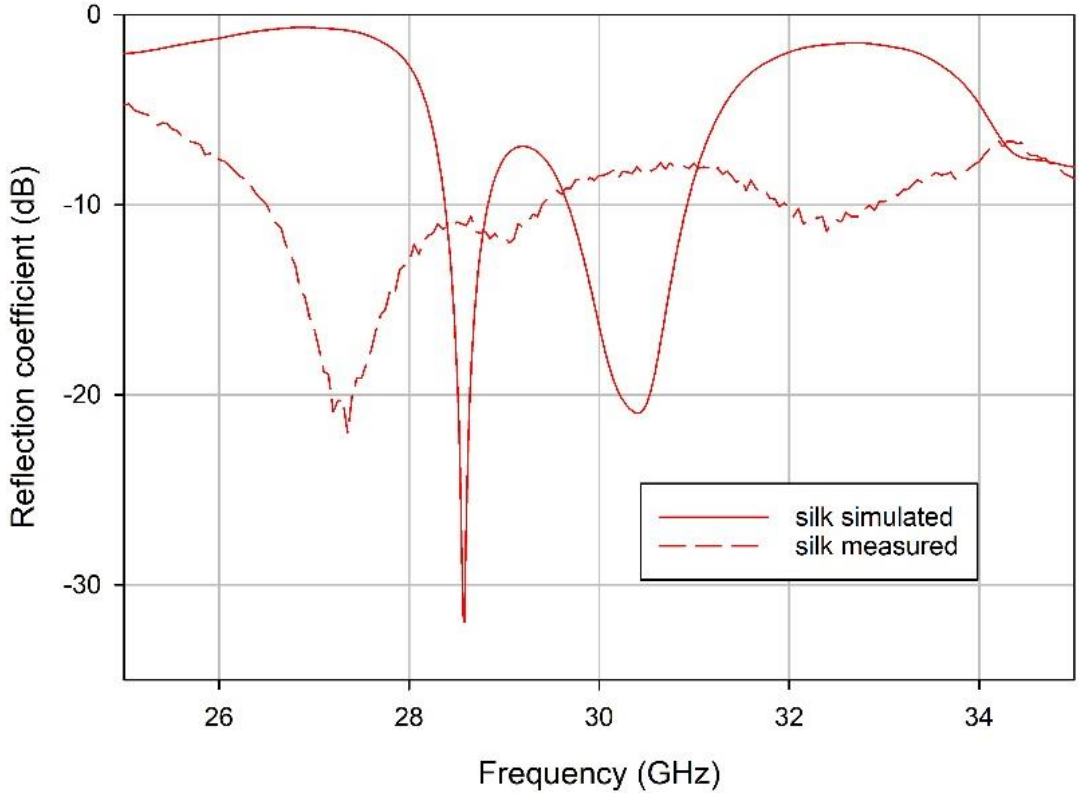

Fig. 172 Reflection coefficients simulated vs measured for hollowed DRA containing air.

APPENDIX B: PREPARATION OF SUBSTANCES AND DIELECTRIC RESONANT ANTENNAS PRIOR TO MEASUREMENTS.

Given the DRA discussed in Chapter 5 required additional preparations, in order to fill the cavity in the 3D-Printed dielectric resonator using some materials from the Chemical and Biological Engineering department of The University of Sheffield. The research group in silk materials provided the use of these substances with a view to contribute to this project.

The fabrication of the dielectric resonant antennas was carried out through 3D-prinintg in the silk materials lab of CBE department. The materials used for the manufacture of these DRAs were three different variants of Polylactic Acid (PLA) with three different relative permittivities consulted to the supplying company Colorfabb. In Fig. 173, the 3D-Printing of one of the studied DRAs using PLA is presented. The manufacture of both solid and hollowed DRAs was carried out by this process using a Ultimaker 3D printing system using exported STL files.

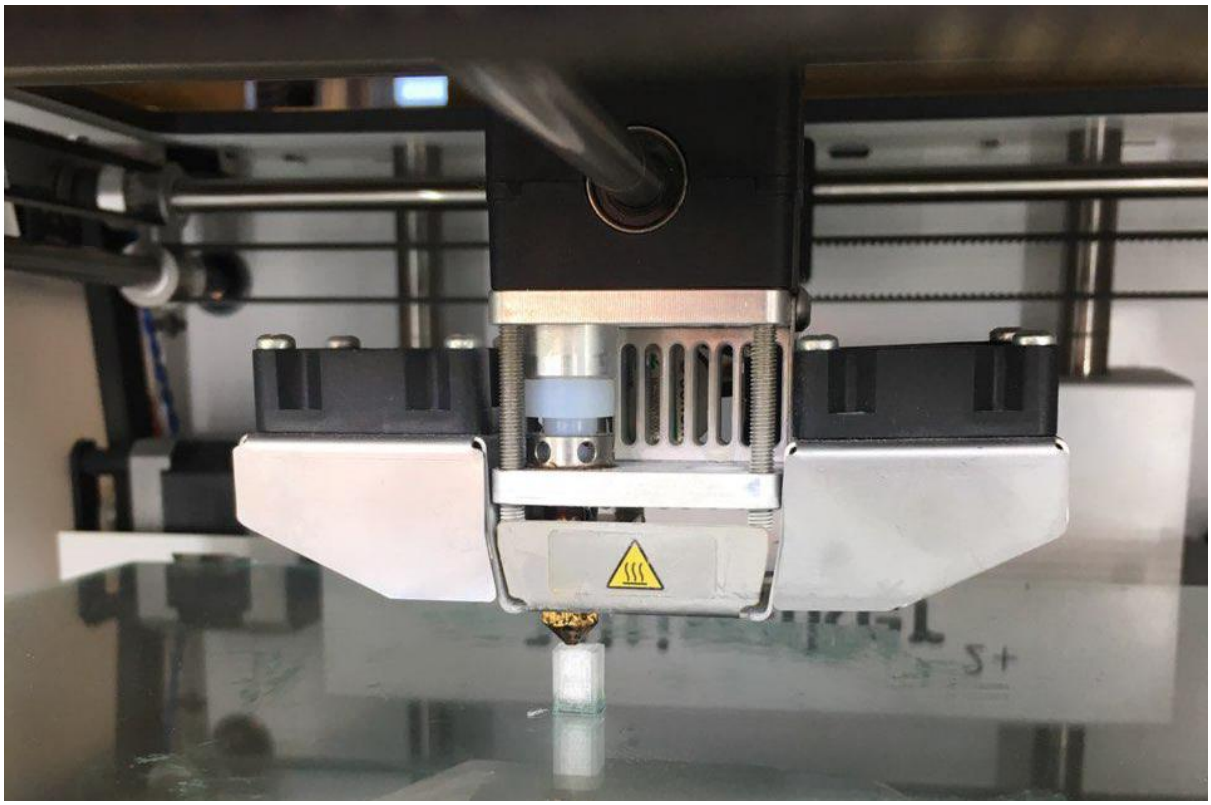

Fig. 173 3D-Printing process of a DRA using a polylactic acid filament.

The study of the solid and hollowed DRA containing only air did not require additional preparations for their performance characterisation measurements, however, for the DRAs filled with silk-sericin gel, graphene oxide gel and liquid preparations prior to their introduction to DRA cavity were required.

For the silk-sericin gel preparation, cocoons of *bombyx-mori* silkworm are cut into small pieces and submerged in water in a DURAN ® laboratory bottle. This is then autoclaved in a pre-programmed cycle on a machine controlling temperature and pressure in order to reach 121ºC and a pressure form 1.0 up to 2.17 Bar for sterilisation purposes. Once the cycle is finished, the remaining solid fibres are removed and then the liquid is the centrifuged. The supernatant containing the silk-sericin is collected after centrifugation. This solution is therefore stored at 4ºC in a fridge where gelation will take place. The gel is used straight from this final storage. In Fig. 174, the original cocoons in raw presentation in (a) and the final product silk-sericin gel in (b) are presented.

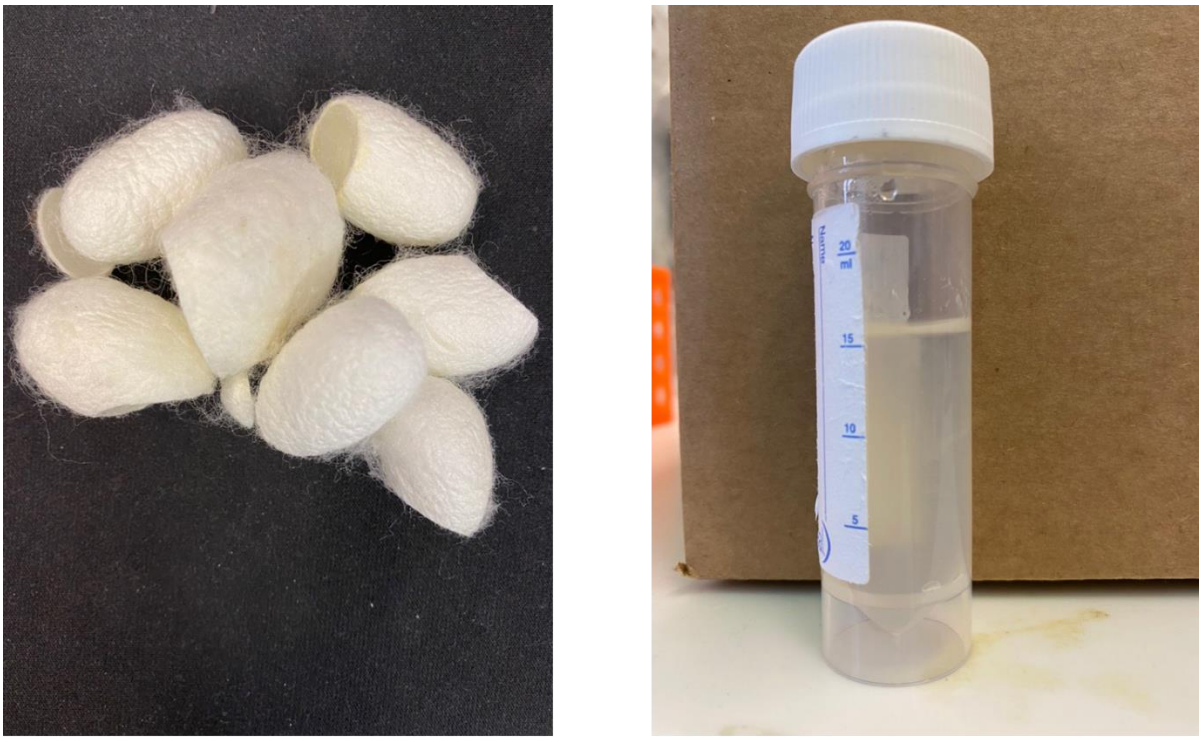

Fig. 174 Cocoons of bombyx-mori silkworm in pure state and (b) silk-sericin gel.

For the graphene oxide preparations, it was used firstly a liquid suspension of graphene oxide (GO) with a concentration of 0.5 mg/ml, then a few milligrams of gelatine are added to this suspension, this mixture is then heated and stirred until the dissolution of the gelatine and after a few minutes, the GO precipitates and is collected by filtering through filter paper. Both the suspension and gel were used in the dielectric resonant antennas previously 3D-Printed. These presentations of GO (gel and suspensions) as well as some DRAs filled with the discussed substances are presented in Fig. 175.

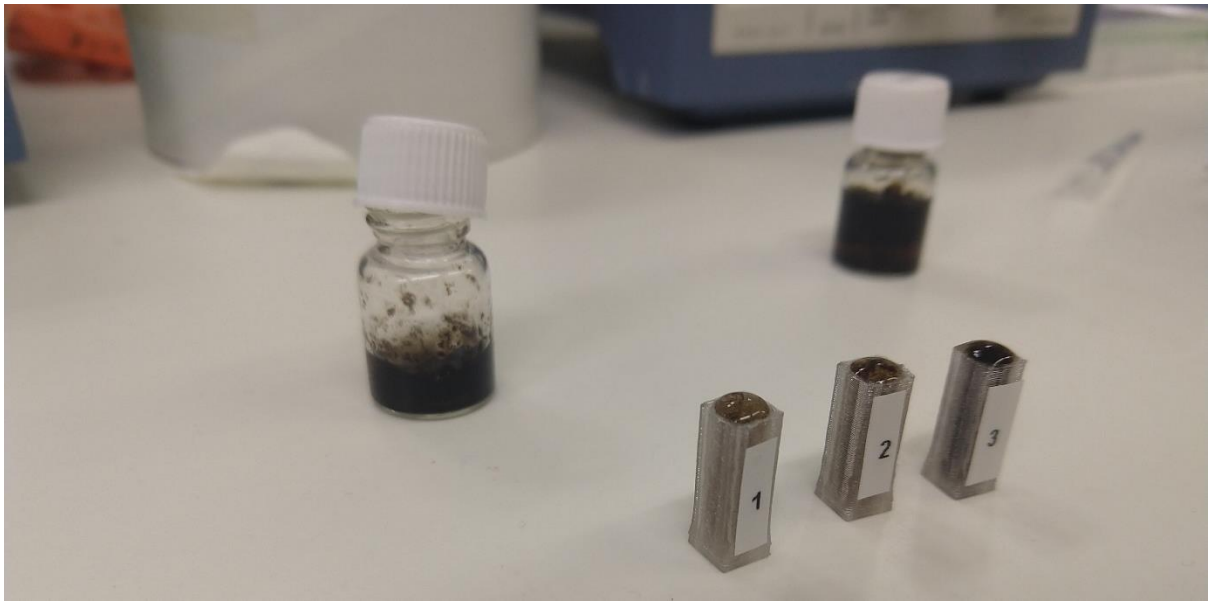

Fig. 175 Graphene oxide suspension and gel prepared in the CBE department.

As the prepared substances (silk-sericin and graphene oxide) are in liquid or colloidal presentations their containment in the cavity of the DRA risked leakages if moved during their measurement process. In order to avoid such undesired leakages, a layer of Para film was placed on top of the cavity of each DRA containing any of these substances. Para film is a very thin material that is widely used in biology and chemistry and provides a secure seal for recipients containing liquids that will be moved abruptly. As this material thickness is within the order of µm it was a suitable option to expect negligible effects on the antenna's performance during the measurements as well as protect the equipment. In Fig. 176, some DRAs filled with the prepared substances are presented, these are ready for their measurements and sealed by a layer of Para film, securing the substances in the cavity and avoiding leakages.

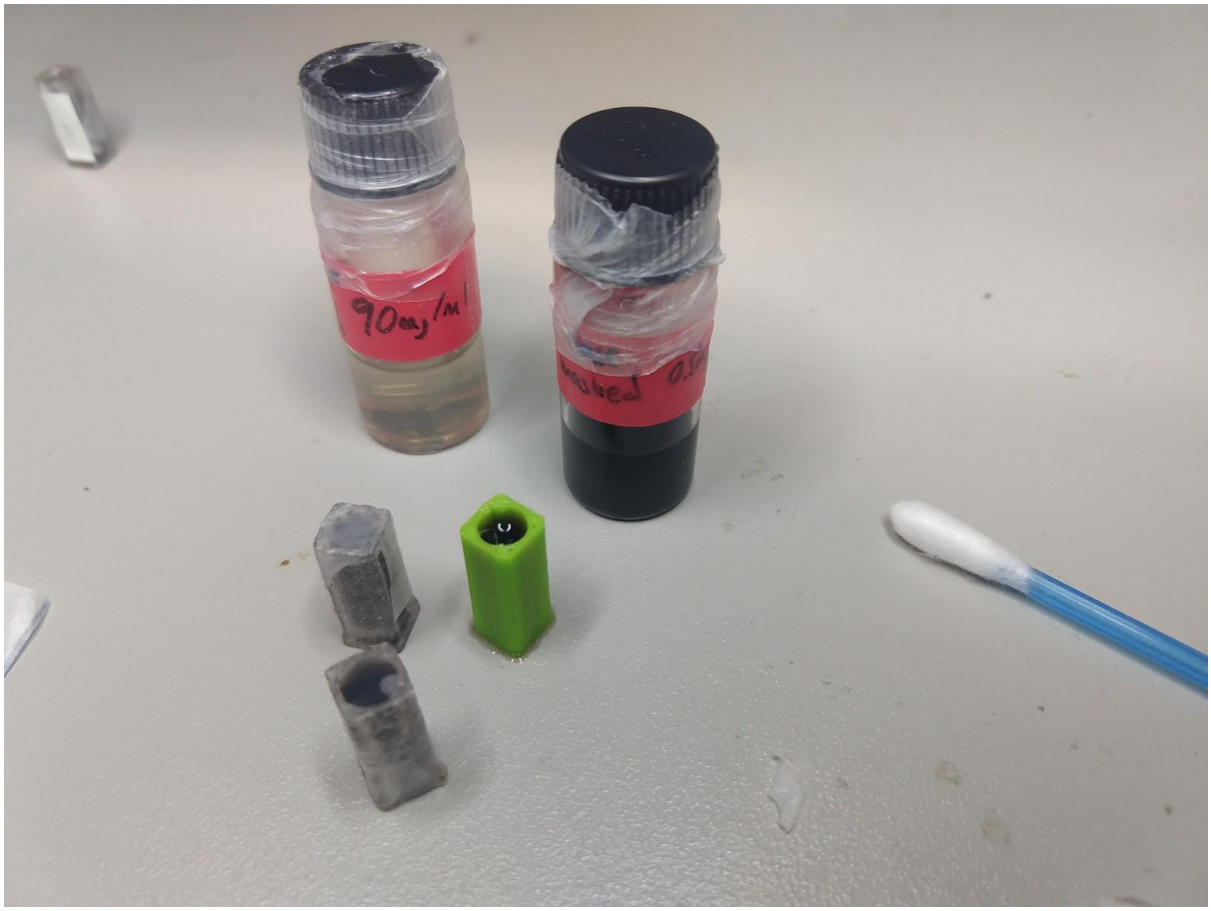

Fig. 176 Hollowed dielectric resonators filled with graphene oxide suspension and gel and silk-sericin gel and sealed by a layer of Para film.

The prepared DRAs were successfully connected to the corresponding equipment for their characterisation. The use of Para film ensured the containment of the DRAs filled with liquid and colloidal materials in order to analyse their effects in the system performance. For the measurement of the reflection coefficients of the antennas containing these substances the use of Para film did not affect the performance as tests were carried out for DRAs with and without a Para film seal. The results were practically identical and proved that the film has negligible effects on the antenna performances. In Fig. 177, a DRA being measured by a network analyser and containing graphene oxide suspension is presented, this prototype incorporated a Para film seal on top of it.

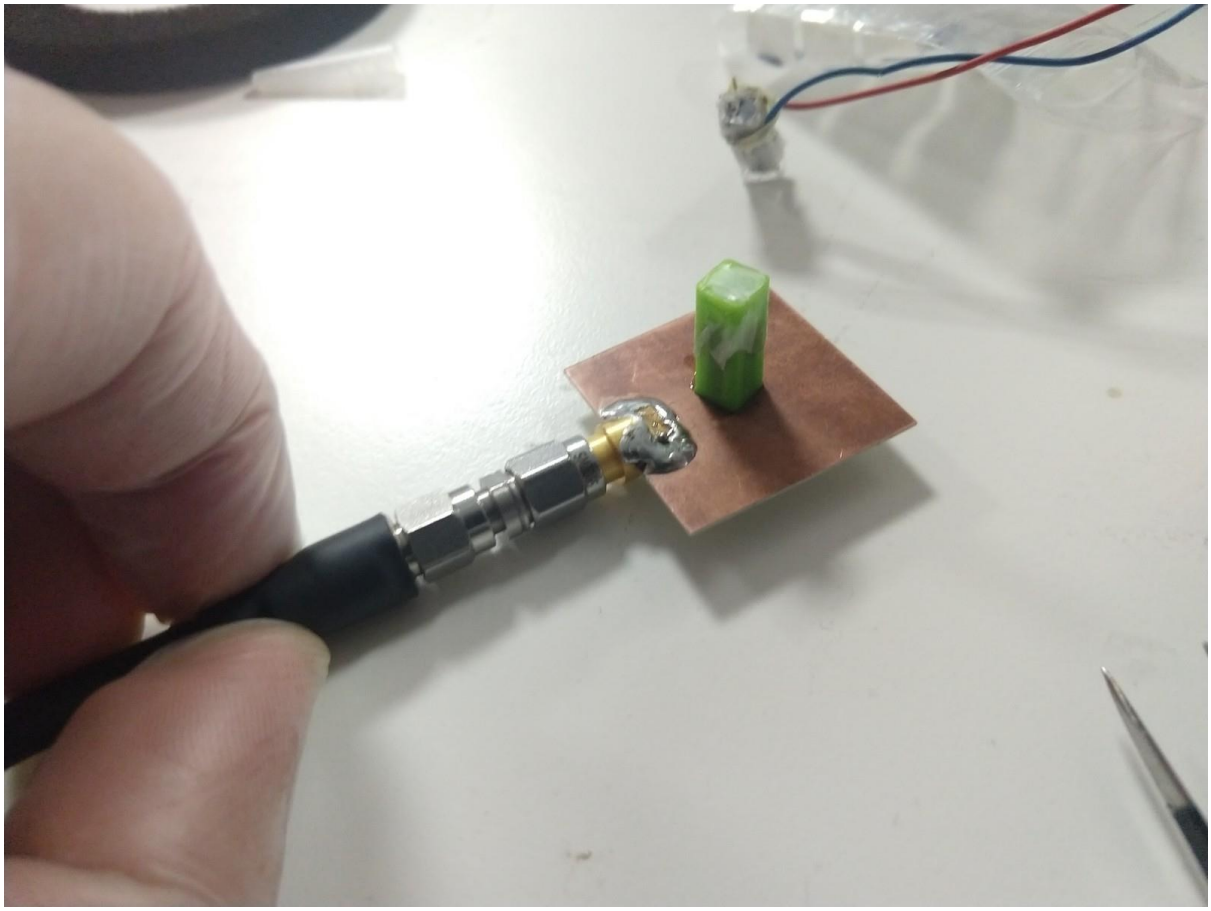

Fig. 177 DRA sealed with a layer of Para film on top of the cavity seating on the PCB that feeds it during measurements in VNA.

Similar to the measurements for reflection coefficients, in the mm-wave laboratory, the DRAs were kept sealed with their respective Para film layer. As the cutting-edge technology equipment of the laboratory requires a special treatment due to the sensitiveness of some of their elements, any external leakage from the DRAs would not only represent a potentially inaccurate measurement but also could damage the equipment. The Para film implemented previously for the reflection coefficient measurements proved to be effective for radiation pattern measurements in the anechoic chamber of the mm-wave laboratory. In Fig. 178, a DRA filled with silk-sericin gel and connected to the anechoic chamber of the mm-Wave laboratory is shown in order to measure its corresponding radiation patterns. As the effects of the Para film layer on the reflection coefficients were negligible the same method was carried out for this purpose, ensuring the containment of the substance and the safety of the equipment.

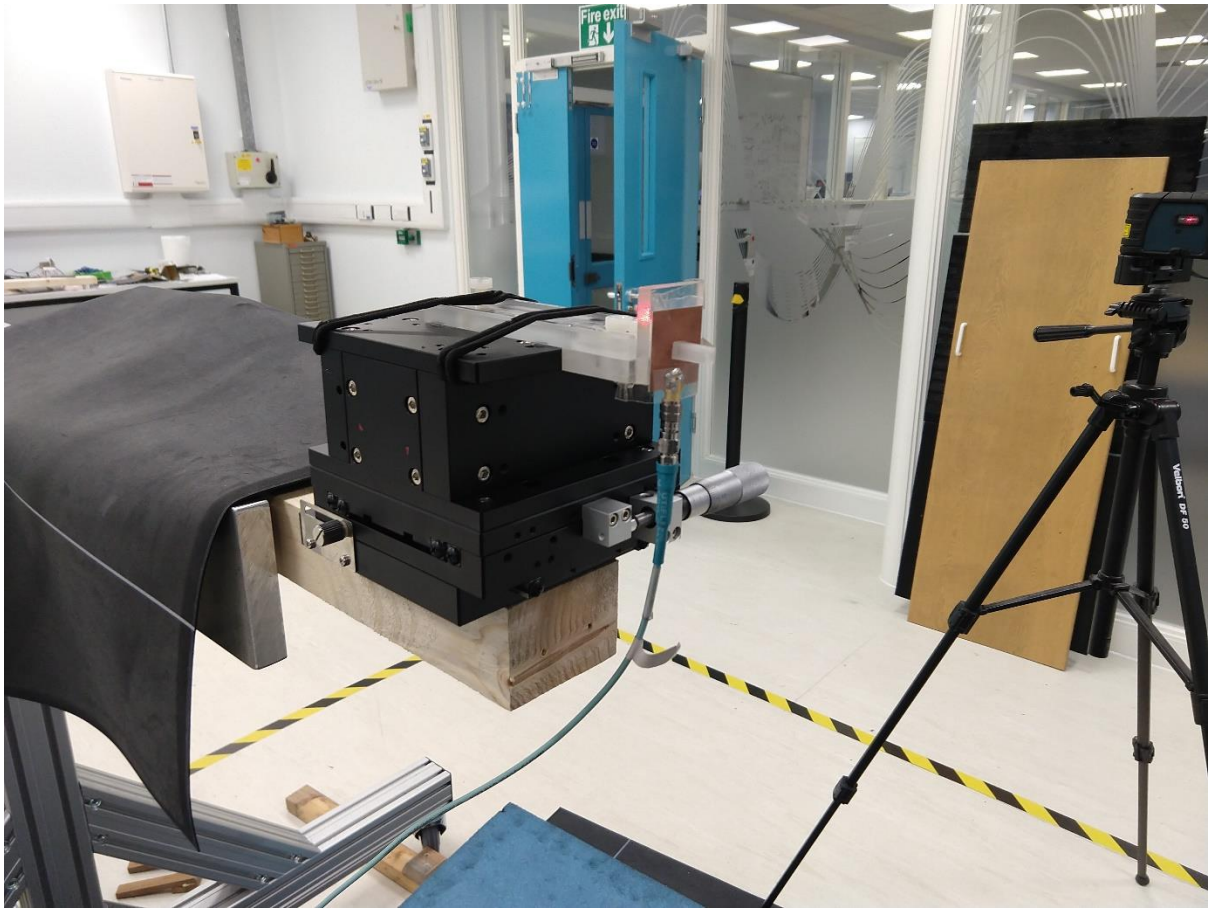

Fig. 178 DRA containing silk-sericin gel and sealed with Para film ready for measurements in mm-wave laboratory.

BILBIOGRAPHIC REFERENCES

[1] H. A. Majid, M. K. A. Rahim, M. R. Hamid, and M. F. Ismail, 'Frequency and Pattern Reconfigurable Slot Antenna', *IEEE Transactions on Antennas and Propagation*, vol. 62, no. 10, pp. 5339–5343, Oct. 2014.

[2] J. S. Sun, N. Kaneda, Y. Baeyens, T. Itoh, and Y.-K. Chen, 'Multilayer Planar Tunable Filter With Very Wide Tuning Bandwidth', *IEEE Transactions on Microwave Theory and Techniques*, vol. 59, no. 11, pp. 2864–2871, Nov. 2011.

[3] H. A. Majid, M. K. A. Rahim, M. R. Hamid, and O. Ayop, 'Reconfigurable wideband to narrowband antenna using tunable EBG structure', *Applied Physics A*, vol. 117, no. 2, pp. 657–661, Nov. 2014.

[4] Y. Kabiri, P. Gardner, and C. Constantinou, 'A novel approach for wideband tunable Electrically Small Antennas', in *The 8th European Conference on Antennas and Propagation (EuCAP 2014)*, The Hague, Netherlands, 2014, pp. 3633–3637.

[5] S. Chilukuri, Y. P. Rangaiah, A. Lokam, and K. Dahal, 'A Multi-Band Frequency and Pattern Reconfigurable Antenna for Wi-Fi/WiMAX and WLAN Applications : Frequency and Pattern Reconfigurable Antenna', in *2018 9th International Conference on Mechanical and Aerospace Engineering (ICMAE)*, 2018, pp. 208–212.

[6] A. Jouade, M. Himdi, A. Chauloux, and F. Colombel, 'Mechanically Pattern-Reconfigurable Bended Horn Antenna for High-Power Applications', *IEEE Antennas and Wireless Propagation Letters*, vol. 16, pp. 457–460, 2017.

[7] J. Wenjian, Z. Lanlan, W. Feng, S. Jinwen, and L. Yun, 'Structural design and realization of a mechanical reconfigurable antenna', in *2018 International Conference on Electronics Technology (ICET)*, 2018, pp. 349–353.

[8] T. Liu, H. Yang, L. Gu, F. Zhao, and W. Yin, 'An omnidirectional cylindrical DRA with a cone ground for WLAN applications', in *2015 IEEE Advanced Information Technology, Electronic and Automation Control Conference (IAEAC)*, 2015, pp. 415–418.

[9] P. A. Raju, N. Kumar, and S. K. Behera, 'Semi circular -semi hexagon microstrip antenna integrated with DRA for cognitive radio applications', in *2015 International Conference on Communications and Signal Processing (ICCSP)*, 2015, pp. 0031–0034.

[10] J. Nasir, Mohd. H. Jamaluddin, M. Khalily, M. R. Kamarudin, Irfanullah, and N. M. Nor, 'A dual-port MIMO DRA with high isolation for LTE application', in *2014 IEEE Asia-Pacific Conference on Applied Electromagnetics (APACE)*, 2014, pp. 55–58.

[11] M. Zou and J. Pan, 'Investigation of Resonant Modes in Wideband Hybrid Omnidirectional Rectangular Dielectric Resonator Antenna', *IEEE Transactions on Antennas and Propagation*, vol. 63, no. 7, pp. 3272–3275, Jul. 2015.

[12] M. Benisha, R. T. Prabu, and V. T. Bai, 'Requirements and challenges of 5G cellular systems', in *2016 2nd International Conference on Advances in Electrical, Electronics, Information, Communication and Bio-Informatics (AEEICB)*, 2016, pp. 251–254.

[13] A. Al-Dulaimi, X. Wang, and C. I, 'Standardization: The Road to 5G', in *5G Networks: Fundamental Requirements, Enabling Technologies, and Operations Management*, IEEE, 2018, pp. 691–708.

[14] and, 'MIMO multiantenna systems radiopropagation aspects', in *2014 IEEE Colombian Conference on Communications and Computing (COLCOM)*, 2014, pp. 1–6.

[15] M. D. Foegelle, 'MIMO device performance measurements in a wireless environment simulator', *IEEE Electromagnetic Compatibility Magazine*, vol. 1, no. 4, pp. 123–130, Fourth 2012.

[16] E. Biglieri, R. Calderbank, A. Constantinides, A. Goldsmith, A. Paulraj, and H. V. Poor, *MIMO Wireless Communications*. Cambridge University Press, 2007.

[17] M. H. Asghar, N. Mohammadzadeh, A. Negi, and T. Kazerouni, 'Principal ingredients and framework of Internet of Things (IoT)', in *2015 Twelfth International Conference on Wireless and Optical Communications Networks (WOCN)*, 2015, pp. 1–6.
[18] C.-G. Gheorghe, D. A. Stoichescu, and R. Dragomir, 'Latency requirement for 5G mobile communications', in *2018 10th International Conference on Electronics, Computers and Artificial Intelligence (ECAI)*, 2018, pp. 1–4.
[19] S. K. Routray, M. K. Jha, L. Sharma, S. Sarkar, A. Javali, and R. Tengshe, 'Energy Consumption Aspects of 5G Waveforms', in *2018 International Conference on Wireless Communications, Signal Processing and Networking (WiSPNET)*, 2018, pp. 1–5.
[20] W. H. Doherty, 'A New High Efficiency Power Amplifier for Modulated Waves', *Proceedings of the Institute of Radio Engineers*, vol. 24, no. 9, pp. 1163–1182, Sep. 1936.
[21] S. W. Wong, T. G. Huang, C. X. Mao, Z. N. Chen, and Q. X. Chu, 'Planar Filtering Ultra-Wideband (UWB) Antenna With Shorting Pins', *IEEE Transactions on Antennas and Propagation*, vol. 61, no. 2, pp. 948–953, Feb. 2013.
[22] D. S. Nagarkoti, Y. Hao, D. P. Steenson, L. Li, E. H. Linfield, and K. Z. Rajab, 'Design of Broadband Non-Foster Circuits Based on Resonant Tunneling Diodes', *IEEE Antennas and Wireless Propagation Letters*, vol. 15, pp. 1398–1401, 2016.
[23] S.-W. Wong and Z.-N. Chen, 'Ultra-wideband filtering antenna (invited paper)', in *2014 XXXIth URSI General Assembly and Scientific Symposium (URSI GASS)*, Beijing, China, 2014, pp. 1–4.
[24] E.-S. Jo *et al.*, 'A frequency reconfigurable slot dipole antenna using surface PIN diodes', in *2017 International Symposium on Antennas and Propagation (ISAP)*, 2017, pp. 1–2.
[25] P.-Y. Qin, F. Wei, and Y. J. Guo, 'A Wideband-to-Narrowband Tunable Antenna Using A Reconfigurable Filter', *IEEE Transactions on Antennas and Propagation*, vol. 63, no. 5, pp. 2282–2285, May 2015.
[26] T. Li, M. Shirazi, and X. Gong, 'S-band continuously-tunable slot-ring antennas for reconfigurable antenna array applications', in *2016 International Workshop on Antenna Technology (iWAT)*, 2016, pp. 18–19.
[27] W. Y. Sam and Z. Zakaria, 'The investigation of the varactor diode as tuning element on reconfigurable antenna', in *2016 IEEE 5th Asia-Pacific Conference on Antennas and Propagation (APCAP)*, 2016, pp. 13–14.
[28] T. Ikeda, S. Saito, and Y. Kimura, 'A dual-band frequency-tunable varactor-loaded single-layer multi-ring microstrip antenna', in *2016 International Symposium on Antennas and Propagation (ISAP)*, 2016, pp. 392–393.
[29] H. Lee, K. L. Ford, and R. J. Langley, 'Independently Tunable Low-Profile Dual-Band High-Impedance Surface Antenna System for Applications in UHF Band', *IEEE Transactions on Antennas and Propagation*, vol. 60, no. 9, pp. 4092–4101, Sep. 2012.
[30] Q. Bai, R. Singh, K. L. Ford, T. O'Farrell, and R. J. Langley, 'An Independently Tunable Tri-Band Antenna Design for Concurrent Multiband Single Chain Radio Receivers', *IEEE Transactions on Antennas and Propagation*, vol. 65, no. 12, pp. 6290–6297, Dec. 2017.
[31] B. Clerckx and C. Oestges, *MIMO Wireless Networks: Channels, Techniques and Standards for Multi-Antenna, Multi-User and Multi-Cell Systems*. Academic Press, 2013.
[32] L. Seddon, R. James, S. E. Day, F. A. Fernandez, P. Deo, and D. Mirshekar-Syahkal, 'Accurate modelling for the analysis and design of liquid-crystal-based microwave devices', in *2017 International Workshop on Electromagnetics: Applications and Student Innovation Competition*, London, United Kingdom, 2017, pp. 105–107.
[33] A. Manabe, 'Liquid crystals for microwave applications', in *2013 7th European Conference on Antennas and Propagation (EuCAP)*, 2013, pp. 1793–1794.

[34] M. A. Christou, N. C. Papanicolaou, and A. C. Polycarpou, 'A nematic liquid crystal tunable patch antenna', in *The 8th European Conference on Antennas and Propagation (EuCAP 2014)*, 2014, pp. 1875–1878.
[35] J. Yang *et al.*, 'Reflective liquid crystal terahertz phase shifter with tuning range of over 360°', *Antennas Propagation IET Microwaves*, vol. 12, no. 9, pp. 1466–1469, 2018.
[36] L. Liu and R. J. Langley, 'Liquid crystal tunable microstrip patch antenna', *Electronics Letters*, vol. 44, no. 20, pp. 1179–1180, Sep. 2008.
[37] M. Habib Ullah, W. N. L. Mahadi, and T. A. Latef, 'Aerogel Poly(butylene succinate) Biomaterial Substrate for RF and Microwave Applications', *Scientific Reports*, vol. 5, no. 1, Oct. 2015.
[38] P. A. Huidobro, M. Kraft, S. A. Maier, and J. B. Pendry, 'Graphene as a Tunable Anisotropic or Isotropic Plasmonic Metasurface', *ACS Nano*, vol. 10, no. 5, pp. 5499–5506, May 2016.
[39] M. Dragoman *et al.*, 'A tunable microwave slot antenna based on graphene', *Appl. Phys. Lett.*, vol. 106, no. 15, p. 153101, Apr. 2015.
[40] A. J. Sangster, *Compact Slot Array Antennas for Wireless Communications*. Springer, 2018.
[41] R. Waterhouse, *Printed Antennas for Wireless Communications*. John Wiley & Sons, 2008.
[42] H. Nakano and J. Yamauchi, 'Printed Slot and Wire Antennas: A Review', *Proceedings of the IEEE*, vol. 100, no. 7, pp. 2158–2168, Jul. 2012.
[43] C. A. Balanis, *Antenna Theory: Analysis and Design*. John Wiley & Sons, 2012.
[44] R. Q. Lee and R. N. Simons, 'Orthogonal feeding techniques for tapered slot antennas', in *IEEE Antennas and Propagation Society International Symposium. 1998 Digest. Antennas: Gateways to the Global Network. Held in conjunction with: USNC/URSI National Radio Science Meeting (Cat. No.98CH36)*, 1998, vol. 2, pp. 1172–1175 vol.2.
[45] Y.-C. Lee, J.-S. Sun, M.-H. Hsu, and R.-H. Chen, 'A New Printed Slot Loop Antenna With Tunable Strips for 2.4- and 5-GHz Wireless Applications', *IEEE Antennas and Wireless Propagation Letters*, vol. 8, pp. 356–358, 2009.
[46] S. C. Del Barrio, M. Pelosi, O. Franek, and G. F. Pedersen, 'Coupling element antenna with slot tuning for handheld devices at LTE frequencies', in *2012 6th European Conference on Antennas and Propagation (EUCAP)*, 2012, pp. 3587–3590.
[47] M. Shirazi, J. Huang, T. Li, and X. Gong, 'A Switchable-Frequency Slot-Ring Antenna Element for Designing a Reconfigurable Array', *IEEE Antennas and Wireless Propagation Letters*, vol. 17, no. 2, pp. 229–233, Feb. 2018.
[48] S. Swathi, G. Ujjwal, and S. Chilukuri, 'A Frequency Reconfigurable Antenna with slotted ground plane for Multi-band Applications', in *2018 IEEE Indian Conference on Antennas and Propogation (InCAP)*, 2018, pp. 1–5.
[49] G. Chen, X. Yang, and Y. Wang, 'Dual-Band Frequency-Reconfigurable Folded Slot Antenna for Wireless Communications', *IEEE Antennas and Wireless Propagation Letters*, vol. 11, pp. 1386–1389, 2012.
[50] Y. Chen, X. Liu, Y. Jiao, and F. Zhang, 'A frequency reconfigurable slot antenna', in *2007 International Symposium on Microwave, Antenna, Propagation and EMC Technologies for Wireless Communications*, 2007, pp. 516–518.
[51] S. Caporal Del Barrio and G. F. Pedersen, 'On the Efficiency of Capacitively Loaded Frequency Reconfigurable Antennas', *International Journal of Distributed Sensor Networks*, vol. 9, no. 7, p. 232909, Jul. 2013.
[52] P.-L. Chi, R. Waterhouse, and T. Itoh, 'Compact and Tunable Slot-Loop Antenna', *IEEE Transactions on Antennas and Propagation*, vol. 59, no. 4, pp. 1394–1397, Apr. 2011.

[53] H. Jiang *et al.*, 'Miniaturized and reconfigurable CPW square-ring slot antenna using thin film varactor technology', in *2011 IEEE MTT-S International Microwave Symposium*, 2011, pp. 1–4.
[54] E. Erfani, J. Nourinia, C. Ghobadi, M. Niroo-Jazi, and T. A. Denidni, 'Design and Implementation of an Integrated UWB/Reconfigurable-Slot Antenna for Cognitive Radio Applications', *IEEE Antennas and Wireless Propagation Letters*, vol. 11, pp. 77–80, 2012.
[55] S.-A. Yang, S.-C. Chiu, C.-P. Lai, and S.-Y. Chen, 'Polarization-reconfigurable slot loop antenna based on a novel varactor-loaded feeding network', in *2016 IEEE International Symposium on Radio-Frequency Integration Technology (RFIT)*, 2016, pp. 1–3.
[56] S. Riaz and X. Zhao, 'An Eight-Port Frequency Reconfigurable MIMO Slot Antenna with Multi-Band Tuning Characteristics', in *2018 12th International Symposium on Antennas, Propagation and EM Theory (ISAPE)*, 2018, pp. 1–4.
[57] R. Hussain, M. U. Khan, and M. S. Sharawi, 'Meandered H-Shaped Slot-line Quad-Band Frequency Reconfigurable MIMO Antenna', in *2019 13th European Conference on Antennas and Propagation (EuCAP)*, 2019, pp. 1–3.
[58] R. Hussain, M. U. Khan, and M. S. Sharawi, 'Frequency Reconfigurable MIMO Antenna using SRR for Multi-Band Operation', in *2019 13th European Conference on Antennas and Propagation (EuCAP)*, 2019, pp. 1–3.
[59] A. Ghalib, R. Hussain, and M. S. Sharawi, 'Low profile frequency agile MIMO slot antenna with TCM characterization', in *2017 11th European Conference on Antennas and Propagation (EUCAP)*, 2017, pp. 2652–2655.
[60] N. Behdad and K. Sarabandi, 'A varactor-tuned dual-band slot antenna', *IEEE Transactions on Antennas and Propagation*, vol. 54, no. 2, pp. 401–408, Feb. 2006.
[61] S. Long, M. McAllister, and Liang Shen, 'The resonant cylindrical dielectric cavity antenna', *IEEE Transactions on Antennas and Propagation*, vol. 31, no. 3, pp. 406–412, May 1983.
[62] L. G. H. Huxley, *A Survey of the Principles & Practice of Wave Guides*. CUP Archive, 1947.
[63] K. M. Luk and K. W. Leung, *Dielectric Resonator Antennas*. Research Studies Press, 2003.
[64] A. Petosa, 'Dielectric Resonator Antenna Handbook', p. 39.
[65] S. Keyrouz and D. Caratelli, 'Dielectric Resonator Antennas: Basic Concepts, Design Guidelines, and Recent Developments at Millimeter-Wave Frequencies', *International Journal of Antennas and Propagation*, 2016. [Online]. Available: https://www.hindawi.com/journals/ijap/2016/6075680/. [Accessed: 26-Feb-2019].
[66] K. W. Leung, X. S. Fang, Y. M. Pan, E. H. Lim, K. M. Luk, and H. P. Chan, 'Dual-Function Radiating Glass for Antennas and Light Covers—Part II: Dual-Band Glass Dielectric Resonator Antennas', *IEEE Transactions on Antennas and Propagation*, vol. 61, no. 2, pp. 587–597, Feb. 2013.
[67] M. Simeoni, R. Cicchetti, A. Yarovoy, and D. Caratelli, 'Plastic-Based Supershaped Dielectric Resonator Antennas for Wide-Band Applications', *IEEE Transactions on Antennas and Propagation*, vol. 59, no. 12, pp. 4820–4825, Dec. 2011.
[68] J. K. Plourde and Chung-Li Ren, 'Application of Dielectric Resonators in Microwave Components', *IEEE Transactions on Microwave Theory and Techniques*, vol. 29, no. 8, pp. 754–770, Aug. 1981.
[69] K.-L. Wong, N.-C. Chen, and H.-T. Chen, 'Analysis of a hemispherical dielectric resonator antenna with an airgap', *IEEE Microwave and Guided Wave Letters*, vol. 3, no. 10, pp. 355–357, Oct. 1993.

[70] Jung-Ick Moon and Seong-Ook Park, 'Dielectric resonator antenna for dual-band PCS/IMT-2000', *Electronics Letters*, vol. 36, no. 12, pp. 1002–1003, Jun. 2000.
[71] J. F. Legier, P. Kennis, S. Toutain, and J. Citerne, 'Resonant Frequencies of Rectangular Dlekctric Resonators', *IEEE Transactions on Microwave Theory and Techniques*, vol. 28, no. 9, pp. 1031–1034, Sep. 1980.
[72] R. K. Mongia, A. Ittibipoon, and M. Cuhaci, 'Low profile dielectric resonator antennas using a very high permittivity material', *Electronics Letters*, vol. 30, no. 17, pp. 1362–1363, Aug. 1994.
[73] J. Shin, A. A. Kishk, and A. W. Glisson, 'Analysis of rectangular dielectric resonator antennas excited through a slot over a finite ground plane', in *IEEE Antennas and Propagation Society International Symposium. Transmitting Waves of Progress to the Next Millennium. 2000 Digest. Held in conjunction with: USNC/URSI National Radio Science Meeting (C*, 2000, vol. 4, pp. 2076–2079 vol.4.
[74] R. A. Kranenburg and S. A. Long, 'Microstrip transmission line excitation of dielectric resonator antennas', *Electronics Letters*, vol. 24, no. 18, pp. 1156–1157, Sep. 1988.
[75] K. W. Leung, K. M. Luk, K. Y. A. Lai, and D. Lin, 'Theory and experiment of a coaxial probe fed hemispherical dielectric resonator antenna', *IEEE Transactions on Antennas and Propagation*, vol. 41, no. 10, pp. 1390–1398, Oct. 1993.
[76] Kwok-Wa Leung, Kwai-Man Luk, K. Y. A. Lai, and Deyun Lin, 'Theory and experiment of an aperture-coupled hemispherical dielectric resonator antenna', *IEEE Transactions on Antennas and Propagation*, vol. 43, no. 11, pp. 1192–1198, Nov. 1995.
[77] S. F. Mahmoud, *Electromagnetic Waveguides: Theory and Applications*. IET, 1991.
[78] A. Friedman, 'Mathematical Modeling of Dielectric Waveguides', in *Mathematics in Industrial Problems: Part 3*, A. Friedman, Ed. New York, NY: Springer, 1990, pp. 19–33.
[79] L. Lewin, *Theory of waveguides: techniques for the solution of waveguide problems*. Newnes-Butterworths, 1975.
[80] Y. Mitelman and E. Malov, 'Mathematical model for analysis of multilayered circular waveguides', 2016, pp. 1–4.
[81] S. Yakuno and T. Ishizaki, 'Novel cavity-type multi-mode filter using TEM-mode and TE-mode', in *2012 Asia Pacific Microwave Conference Proceedings*, 2012, pp. 376–378.
[82] A. Zettl, *Sturm-Liouville Theory*. American Mathematical Soc., 2012.
[83] S. Danesh, S. K. A. Rahim, M. Abedian, and M. R. Hamid, 'A Compact Frequency-Reconfigurable Dielectric Resonator Antenna for LTE/WWAN and WLAN Applications', *IEEE Antennas and Wireless Propagation Letters*, vol. 14, pp. 486–489, 2015.
[84] S. Danesh, M. R. Kamarudin, T. A. Rahman, M. Abedian, and M. Khalily, 'A wideband frequency reconfigurable rectangular dielectric resonator antenna', in *2016 10th European Conference on Antennas and Propagation (EuCAP)*, 2016, pp. 1–4.
[85] S. Danesh, S. K. A. Rahim, M. Abedian, M. Khalily, and M. R. Hamid, 'Frequency-Reconfigurable Rectangular Dielectric Resonator Antenna', *IEEE Antennas and Wireless Propagation Letters*, vol. 12, pp. 1331–1334, 2013.
[86] S. Khan, H. Ali, J. Nasir, L. Sieler, and C. Tanougast, 'A U-shaped Wide band frequency reconfigurable dielectric resonator antenna for 5G applications', in *2018 International Symposium on Networks, Computers and Communications (ISNCC)*, 2018, pp. 1–4.
[87] D. Aditya and R. Kumari, 'Aperture coupled frequency reconfigurable dielectric resonator antenna for wireless applications', in *2017 IEEE International Conference on Antenna Innovations Modern Technologies for Ground, Aircraft and Satellite Applications (iAIM)*, 2017, pp. 1–5.

[88] B. Liu, J. Qiu, N. Wang, C. Yang, and O. Denisov, 'Pattern reconfigurable conical dielectric resonator antenna with parasitic elements', in *2016 International Symposium on Antennas and Propagation (ISAP)*, 2016, pp. 816–817.
[89] S. P. Rodriguez-Albarran, S. M. Asif, K. L. Ford, R. J. Langley, and T. O'Farrell, 'Multiband tunable MIMO antenna', in *The Loughborough Antennas Propagation Conference (LAPC 2018)*, 2018, pp. 1–2.
[90] R. Vaughan, J. B. Andersen, and J. B. Andersen, *Channels, Propagation and Antennas for Mobile Communications*. IET, 2003.
[91] C. D. V. Rensburg, *Novel Spatial Diversity Techniques for Mobile Communications in Correlated Fading Environments*. University of California, Davis, 2001.
[92] A. Sibille, C. Oestges, and A. Zanella, *MIMO: From Theory to Implementation*. Academic Press, 2010.
[93] I. Ahamed and M. Vijay, 'Comparison of different diversity techniques in MIMO antennas', in *2017 2nd International Conference on Communication and Electronics Systems (ICCES)*, 2017, pp. 47–50.
[94] K. J. R. Liu, A. K. Sadek, W. Su, and A. Kwasinski, *Cooperative Communications and Networking*. Cambridge University Press, 2009.
[95] R. W. H. Jr and A. Lozano, *Foundations of MIMO Communication*. Cambridge University Press, 2018.
[96] M. M. da Silva, A. Correia, R. Dinis, N. Souto, and J. C. Silva, *Transmission Techniques for Emergent Multicast and Broadcast Systems*. CRC Press, 2010.
[97] Y. Dama, R. Abd-Alhameed, J. M. Noras, and N. Ali, 'An Exact Envelope Correlation Formula for Two-Antenna Systems Using Input Scattering Parameters and Including Power Losses', *International Journal on Communications Antenna and Propagation*, vol. 2, pp. 39–44, Feb. 2012.
[98] Y. a. S. Dama *et al.*, 'An Envelope Correlation Formula for (N,N) MIMO Antenna Arrays Using Input Scattering Parameters, and Including Power Losses', *International Journal of Antennas and Propagation*, 2011. [Online]. Available: https://www.hindawi.com/journals/ijap/2011/421691/. [Accessed: 30-Aug-2018].
[99] J. A. Garcia-Lopez and V. Casares-Giner, 'Optimum antenna separation for space diversity in l.o.s. radio links over flat ground', *Electronics Letters*, vol. 16, no. 18, pp. 717–718, Aug. 1980.
[100] S. Keyrouz and D. Caratelli, 'Dielectric Resonator Antennas: Basic Concepts, Design Guidelines, and Recent Developments at Millimeter-Wave Frequencies', *International Journal of Antennas and Propagation*, 2016. [Online]. Available: https://www.hindawi.com/journals/ijap/2016/6075680/. [Accessed: 06-Sep-2018].
[101] E. I. Simakov *et al.*, 'Fabrication of ceramic structures for MM-wave traveling wave tubes', in *2016 IEEE International Vacuum Electronics Conference (IVEC)*, 2016, pp. 1–2.
[102] V. K. Mishra and R. K. Chauhan, 'SIWG Filter at 25.75 GHz Using Rogers Duroid Substrate for 5G application', in *2018 IEEE International Students' Conference on Electrical, Electronics and Computer Science (SCEECS)*, 2018, pp. 1–3.
[103] Z. Ali, V. K. Singh, A. K. Singh, and S. Ayub, 'E-Shaped Microstrip Antenna on Rogers Substrate for WLAN Applications', in *2011 International Conference on Computational Intelligence and Communication Networks*, 2011, pp. 342–345.
[104] A. Sharma, K. Khare, and S. C. Shrivastava, 'Simple and Enhanced Gain Dielectric Resonator Antenna for Ku band Application', vol. 4, no. 9, p. 5, 2013.
[105] Y. Pan, K. W. Leung, and K. Luk, 'Design of the Millimeter-wave Rectangular Dielectric Resonator Antenna Using a Higher-Order Mode', *IEEE Transactions on Antennas and Propagation*, vol. 59, no. 8, pp. 2780–2788, Aug. 2011.

[106] Bin Li and Kwok Wa Leung, 'Strip-fed rectangular dielectric resonator antennas with/without a parasitic patch', *IEEE Transactions on Antennas and Propagation*, vol. 53, no. 7, pp. 2200–2207, Jul. 2005.
[107] L. T. Sin, A. R. Rahmat, and W. A. W. A. Rahman, *Polylactic Acid: PLA Biopolymer Technology and Applications*. William Andrew, 2012.
[108] Y. M. Pan and S. Y. Zheng, 'A Low-Profile Stacked Dielectric Resonator Antenna With High-Gain and Wide Bandwidth', *IEEE Antennas and Wireless Propagation Letters*, vol. 15, pp. 68–71, 2016.
[109] E. J. Reed, 'Effects of Microwave Radiation on Selected Mechanical Properties of Silk', UC Merced, 2013.
[110] D. Na, J. Choi, J. Lee, J. Jeon, and B. Kim, 'Commercial Silk-Based Electronic Yarns Fabricated Using Microwave Irradiation', *ACS Applied Materials & Interfaces*, vol. 11, Jul. 2019.
[111] Y. Iwai *et al.*, 'Field emission characteristics of graphite field emitters', in *2014 27th International Vacuum Nanoelectronics Conference (IVNC)*, 2014, pp. 44–45.
[112] M. Deka and D. Chowdhury, 'Tuning Electrical Properties of Graphene with Different π- Stacking Organic Molecules', *The Journal of Physical Chemistry C*, vol. 120, Feb. 2016.
[113] J. Park, Y. Cho, S. Sung, M. Byeon, S. J. Yang, and C. Park, 'Characteristics Tuning of Graphene-Oxide-Based-Graphene to Various End-Uses', vol. 14, pp. 8–21, Sep. 2018.
[114] X. Huang *et al.*, 'Graphene Oxide Dielectric Permittivity at GHz and Its Applications for Wireless Humidity Sensing', *Scientific Reports*, vol. 8, no. 1, pp. 1–7, Jan. 2018.
[115] X. Hong, W. Yu, and D. D. L. Chung, 'Electric permittivity of reduced graphite oxide', *Carbon*, vol. 111, pp. 182–190, Jan. 2017.
[116] A. Singh, N. Sharma, M. Arif, and R. Katiyar, 'Electrically reduce graphene oxide for photovolatic applications', *Journal of Materials Research*, Jan. 2019.